Improved Pulse Characteristics and Power Scaling of Drive Lasers for Laser-Wakefield Acceleration

by

Timo Felix Johannes Eichner

A Thesis Submitted to the Faculty of
Mathematics, Informatics and Natural Sciences
Department of Physics
for the Degree of

DOCTOR RERUM NATURALIUM

Universität Hamburg
July 2023

Gutachter der Dissertation: Dr. Andreas R. Maier
Prof. Dr. Franz X. Kärtner

Zusammensetzung der Prüfungskommission: Dr. Andreas R. Maier
Prof. Dr. Franz X. Kärtner
Prof. Dr. Jens Osterhoff
Prof. Dr. Nina Rohringer
Prof. Dr. Jochen Liske

Vorsitzende der Prüfungskommission: Prof. Dr. Jochen Liske

Datum der Disputation: 25. September 2023

Vorsitzender des Fach-Promotionsausschusses Physik: Prof. Dr. Günter H. W. Sigl

Leiter des Fachbereichs Physik: Prof. Dr. Wolfgang J. Parak

Dekan der Fakultät MIN: Prof. Dr.-Ing. Norbert Ritter

Eidesstattliche Versicherung / Declaration on oath

Hiermit versichere ich an Eides statt, die vorliegende Dissertationsschrift selbst verfasst und keine anderen als die angegebenen Hilfsmittel und Quellen benutzt zu haben.

Die eingereichte schriftliche Fassung entspricht der auf dem elektronischen Speichermedium.

Die Dissertation wurde in der vorgelegten oder einer ähnlichen Form nicht schon einmal in einem früheren Promotionsverfahren angenommen oder als ungenügend beurteilt.

Hamburg, den 20. Juli 2023

Timo Eichner

Abstract

Laser-wakefield acceleration (LWFA) is a promising, emerging technology for future accelerator-based X-ray light sources, which are essential tools in various fields of science, industry and medicine. In laser-wakefield acceleration, an intense laser pulse drives a plasma wave that supports high accelerating field gradients. This allows electrons to be accelerated over distances that are orders of magnitude shorter than in conventional radio-frequency-based particle accelerators. Driving high-brightness, accelerator-based X-ray sources requires lasers with a peak power around 100 TW, and well-controlled pulse properties, since of the quality of the accelerated electron beams is sensitive to the properties of the driving laser pulse. For LWFA to become truly competitive with current radio-frequency-based accelerators, the stability and pulse quality of the lasers must be further improved, and their repetition rate must be increased from the current few Hz to the kHz range, thereby raising the average power to the kW level. The challenges that need to be solved to achieve this lie in the design of the laser amplifiers, the pump lasers for those amplifiers, the final pulse compressor of chirped pulse amplification systems, and an overall improvement of the pulse quality and stability in all sub-components of the laser.

This thesis outlines a path towards future high repetition rate LWFA drivers by studying these challenges throughout the amplification chain of Ti:sapphire-based lasers. This starts with the generation of the seed pulse, which largely determines the properties of the final, fully amplified pulse. To deliver high quality seed pulses, a laser front-end based on optical parametric chirped pulse amplification (OPCPA) is presented. The technology can deliver pulses with high temporal contrast and flexible spectral properties, which make it an attractive option for seeding Ti:sapphire amplifiers. However, achieving high beam quality and stability is challenging for OPCPA. A thorough experimental and theoretical study of the saturation dynamics of OPCPA, and the use of advanced control methods, allow to combine these features and as a result, the present an OPCPA system exhibits both, unprecedented long-term stability and excellent spatio-temporal pulse quality.

Further, the thermal management of high average power Ti:sapphire amplifiers is investigated, leading to a conceptual design for a Joule-level amplifier that will provide a high quality beam for the first 100 Hz operation of a high energy laser wakefield accelerator. For future scaling to kHz repetition rates, the thesis further studies the high average power frequency doubling of ytterbium:doped multi-core fiber lasers, a highly scalable technology, which is a potential solution for providing the 10 kW-level average power pump beams required for future 100 TW, 1 kHz Ti:sapphire laser

systems.
Finally, the thermal limitations of gold-coated pulse compression gratings are studied, where absorption in the gold coating can cause thermal deformation of the gratings. A custom numerical model is developed to show that this deformation can degrade the spatio-temporal quality of the compressed pulses already at the few-Watt level, and as a result, other grating technologies will be required in future multi-kW drive lasers for laser-wakefield acceleration.

Zusammenfassung

Die Laser-Wakefield-Beschleunigung (LWFA) ist eine vielversprechende neue Technologie für beschleunigerbasierte Röntgenquellen, die ein wichtiges Werkzeug für verschiedene Bereiche der Wissenschaft, Industrie und Medizin sind. Bei der LWFA treibt ein intensiver Laserpuls eine Plasmawelle mit hohen elektrischen Feldstärken an, wodurch Elektronen auf um Größenordnungen kürzere Distanzen beschleunigt werden können als in konventionellen Hochfrequenz-Teilchenbeschleunigern. Der Betrieb von brillanten, beschleunigerbasierten Röntgenquellen erfordert Laser mit Spitzenleistungen von etwa 100 TW und gut kontrollierten Pulseigenschaften, da die Qualität der beschleunigten Elektronenstrahlen von den Eigenschaften des treibenden Laserpulses abhängt. Damit die LWFA mit konventionellen Beschleunigern konkurrieren kann, müssen die Stabilität und die Pulsqualität der Laser weiter verbessert und die Repetitionsrate von derzeit wenigen Hz auf kHz erhöht werden, wodurch die mittlere Leistung in den kW-Bereich steigt. Die Herausforderungen, die dazu gelöst werden müssen, liegen im Design der Laserverstärker, der Pumplaser für diese Verstärker, des finalen Pulskompressors von gechirpten Pulsverstärkersystemen und einer allgemeinen Verbesserung der Pulsqualität und -stabilität in allen Teilkomponenten des Lasers.

In dieser Arbeit wird ein Weg zu zukünftigen LWFA-Treibern mit hoher Repetitionsrate aufgezeigt, indem diese Herausforderungen in der gesamten Verstärkungskette von Ti:Saphir-basierten Lasern untersucht werden. Dies beginnt mit der Erzeugung des Seed-Pulses, der maßgeblich die Eigenschaften des finalen, vollständig verstärkten Pulses bestimmt. Um hochwertige Seedpulse zu erzeugen, wird ein Laser-Frontend auf der Grundlage der optisch parametrischen gechirpten Pulsverstärkung (OPCPA) vorgestellt. Diese Technologie kann Pulse mit hohem zeitlichen Kontrast und flexiblen spektralen Eigenschaften liefern, die optimal für das Seeden der nachfolgenden Verstärker geeignet sind. Das Erreichen einer hohen Strahlqualität und -stabilität ist jedoch eine Herausforderung für OPCPA. Eine gründliche experimentelle und theoretische Untersuchung der Sättigungsdynamik von OPCPA und der Einsatz fortschrittlicher Kontrollmethoden ermöglichen es, diese Eigenschaften zu kombinieren, so dass das vorliegende OPCPA-System sowohl eine bisher unerreichte Langzeitstabilität als auch eine exzellente räumlich-zeitliche Pulsqualität aufweist. Darüber hinaus wird das Wärmemanagement von Ti:Saphir-Verstärkern mit hoher mittlerer Leistung untersucht, was zu einem Konzept für einen Joule-Verstärker führt, der einen Strahl hoher Qualität für den ersten 100 Hz-Betrieb eines Hochenergie-Laser-Wakefield-Beschleunigers liefert. Im Hinblick auf eine zukünftige Skalierung auf kHz-Wiederholraten wird die Frequenzverdopplung der hohen mittleren Leistung von Ytterbium:dotierten Multi-Core-Faserlasern untersucht, eine hoch skalierbare Technologie, die eine potentielle Lösung für die Erzeugung von Pumpstrahlen mit einer mittleren Leistung von 10 kW darstellt, wie sie für zukünftige 100 TW, 1 kHz-Ti:Saphir-Lasersysteme benötigt werden. Schließlich werden die thermischen Grenzen von goldbeschichteten Pulskompressionsgittern untersucht, bei denen die Absorption in der Goldbeschichtung zu einer thermischen Verformung der Gitter führen kann. Mit Hilfe eines numerischen Modells wird gezeigt, dass diese Verformung die räumlich-zeitliche Qualität der komprimierten Pulse bereits bei wenigen Watt verschlechtern kann, so dass in zukünftigen LWFA-Treiberlaser andere Gittertechnologien erforderlich sein werden.

Yhteenveto

Laser-wakefield-kiihdytys (LWFA) on lupaava, kehittyvä tekniikka tulevaisuuden kiihdytinpohjaisia röntgenvalonlähteitä varten, jotka ovat tärkeitä työkaluja tieteen, teollisuuden ja lääketieteen eri aloilla. Laser-wakefield-kiihdytyksessä voimakas laserpulssi ajaa plasma-aaltoa, jossa on suuri kiihdyttävä kenttä. Tämä mahdollistaa elektronien kiihdyttämisen etäisyyksillä, jotka ovat kertaluokkia lyhyempiä kuin perinteisissä radiotaajuuspohjaisissa hiukkaskiihdyttimissä. Kirkkaiden, kiihdyttimiin perustuvien röntgenlähteiden ajaminen vaatii lasereita, joiden huipputeho on noin 100 TW, ja joilla on tarkasti hallittuja pulssiominaisuuksia, koska kiihdytettyjen elektronisäteiden laatu on hyvin herkkä ajavan laserpulssin ominaisuuksille. Jotta LWFA:sta tulisi todella kilpailukykyinen nykyisten radiotaajuuspohjaisten kiihdyttimien kanssa, lasereiden vakautta ja pulssin laatua on parannettava, ja niiden toistotaajuutta on nostettava nykyisestä muutamasta Hz:stä khz:n alueelle, jolloin keskimääräinen teho nousee kilowattitasolle. Haasteet, jotka on ratkaistava tämän saavuttamiseksi, liittyvät laservahvistimien, näiden vahvistimien pumppulasereiden ja lopullisen pulssikompressorin suunnitteluun sekä pulssin laadun ja vakauden yleiseen parantamiseen kaikissa laserin osakomponenteissa.

Tässä väitöskirjassa hahmotellaan tietä kohti tulevia korkean toistotaajuuden LWFA-ajolasereita tutkimalla Ti:safiiripohjaisten lasereiden keskeisiä haasteita, jotka tällä hetkellä rajoittavat niiden keskimääräistä tehoa ja pulssin laatua. Tämä lähtee alkupulssin luomisesta, jota varten esittelemme optiseen parametriseen pulssivahvistukseen (OPCPA) perustuvan laserin. Tekniikalla voidaan tuottaa pulsseja, joilla on suuri ajallinen kontrasti ja joustavat spektriset ominaisuudet, mitkä tekee siitä kiinnostavan vaihtoehdon Ti:safiirivahvistimien alkupulssin luomiseen. Korkean pulssin laadun ja vakauden saavuttaminen on kuitenkin haastavaa OPCPA:ssa. Esittelemme OPCPA-järjestelmän, joka täyttää molemmat vaatimukset, tutkimme perusteellisesti vahvistettujen pulssien spektraalista ja tilallista laatua ja esittelemme kehittyneitä säätömenetelmiä, jotka mahdollistavat tällaisen laserjärjestelmän ennennäkemättömän pitkän ajan vakauden. Tutkimme myös suuren keskitehon Ti:safiirivahvistimien lämpöhallintaa ja esittelemme suunnitelman Joule-tason vahvistimelle, joka tuottaa korkealaatuisen säteen suurienergisen laser-wakefield-kiihdyttimen ensimmäiseen 100 Hz:n toimintaan. Tulevaisuuden skaalausta varten kHz:n toistotaajuuksiin tutkimme lisäksi ytterbium: seostettujen moniytimisten kuitulasereiden suuren keskitehon frekvenssimuunosta, joka on mahdollinen ratkaisu 10 kW:n pumppusäteiden luomiseen, joita tarvitaan tulevissa 100 kW:n, 1 kHz:n Ti:safiirilaserjärjestelmissä. Lopuksi tutkimme tavanomaisesti käytettyjen kultapinnoitettujen pulssikompressiorhilojen lämpörajoitteita. Simulaatioiden avulla

näytämme, että absorptio kultapinnoitteessa voi aiheuttaa hilojen termisiä muodonmuutoksia, jotka heikentävät kompressoitujen pulssien laatua. Osoitamme että tämän seurauksena tulevissa usean kilowatin ajolasereissa tarvitaan toista hilateknologiaa.

Contents

Introduction **19**

Publications **23**

1 Drive Lasers for Laser-Wakefield Acceleration **25**
- 1.1 Brief Introduction to Laser-Wakefield Acceleration 25
  - 1.1.1 Laser-Wakefield Acceleration 25
  - 1.1.2 Required Drive Laser Properties 30
- 1.2 Typical Setup of LWFA Drive Lasers 32
- 1.3 Demands for Future Laser Systems and Potential Laser Technologies . 36

2 Stable, High-Quality Pulses from an OPCPA-Based Seed-Laser **43**
- 2.1 Introduction to OPCPA 44
  - 2.1.1 Fundamentals of Nonlinear Optical Processes 44
  - 2.1.2 Optical Parametric Amplification 46
  - 2.1.3 Broadband Parametric Amplification 52
  - 2.1.4 Second Harmonic Generation 57
  - 2.1.5 Stability of OPCPA-Systems 57
  - 2.1.6 Angular and Spatial Dispersion in OPCPA 63
- 2.2 The MALCOLM Laser System 65
  - 2.2.1 Optical Design 66
  - 2.2.2 Mechanical Design & Implementation 70
  - 2.2.3 Performance 72
- 2.3 Spatio-Spectral Couplings in Saturated OPCPA 78
  - 2.3.1 Simulation of Beam Degradation in Saturated OPCPA 79
  - 2.3.2 Measurement of STCs with Insight 80
  - 2.3.3 Spatial Filtering of Saturated OPCPA Pulses 83
  - 2.3.4 Concluding Remarks on Spatio-Spectral Couplings in OPCPA 86
- 2.4 Numerical Optimisation and Automated Tuning 87
  - 2.4.1 Overview of Suitable Optimisation Techniques 87
  - 2.4.2 Implementation in MALCOLM 89
  - 2.4.3 Self-Tuning from a Random Initial State 90
  - 2.4.4 Improved Day-to-Day Reproducibility 92
- 2.5 Full-State Feedback Stabilisation of an OPCPA 93
  - 2.5.1 Overview of State Space Control 94

2.5.2 Linear Performance Model of MALCOLM 96
2.5.3 Calculating Stabilization Gains 98
2.5.4 Results of Full-State-Feedback-Stabilization 99
2.6 Long-Term Stability of MALCOLM 100
2.7 Conclusion and Future Improvements on MALCOLM 101

3 Scaling Ti:Sapphire Amplifiers Towards High Average Power 105
3.1 Overview of Ti:sapphire Lasers 105
3.1.1 Amplification in Ti:sapphire 105
3.1.2 Pumping Ti:sapphire 106
3.2 High Average Power Pump Generation 108
3.2.1 Brief Overview of the Multi-Core Fiber (MCF) Concept 109
3.2.2 Simulations and Experimental Results on MCF-Based SHG . . 111
3.2.3 Frequency Conversion of a 2.5 kW MCF Fiber Laser 118
3.2.4 Outlook on High Average Power Pump Generation 121
3.3 High Average Power Ti:sapphire Amplifiers 121
3.3.1 High Average Power Amplification in Ti:sapphire 122
3.3.2 COLIMA: Concept for a 100 Hz, 1 J Ti:sapphire Amplifier . . . 126
3.3.3 Proposed Optical Layout 133
3.3.4 Concluding Remarks and Outlook towards first Experimental Results 136
3.3.5 Scaling to Higher Repetition Rates 136

4 Heat-Induced Deformation and Thermal Management of Diffraction Gratings 141
4.1 Thermal Expansion of Compressor Gratings 142
4.1.1 Simulation of Grating Deformation 142
4.1.2 Spatio-Spectral Phase 144
4.2 Case Study of the ANGUS Laser System 146
4.3 Comparison of Substrate Materials 149
4.4 Mitigation Strategies 151
4.5 Conclusion and Outlook 154

5 Conclusion 157

Bibliography 163

List of Figures

1.1 Laser-driven plasma wake in the bubble regime. 26
1.2 Overview of the basic principle of CPA 33
1.3 Overview of the ANGUS laser system 34
1.4 Comparison of high average power ultrafast laser results 40

2.1 Evolution of pulse energies in OPA with pump depletion 49
2.2 Index ellipsoid 52
2.3 Walk-offs in non-collinear broadband phase matching 56
2.4 Phase matching efficiency in LBO crystal 56
2.5 Pulse energy stability in presence of input fluctuations in OPA 59
2.6 Pulse energy stability for fluctuating Gaussian intensity profiles 60
2.7 Evolution of the signal bandwidth in saturated OPCPA. 62
2.8 Origin of spatial chirp and pulse from tilt in NOPA 64
2.9 Angular chirp from un-optimised phase matching angles in NOPA . . 65
2.10 Optical layout of the OPCPA frontend 66
2.11 SHG conversion efficiency in BBO and KDP 68
2.12 Phase matching efficiency in collinear LBO 69
2.13 Rendering of the mechanical setup of the MALCOLM laser system. . . . 70
2.14 Example of modular design of the MALCOLM laser system. 71
2.15 Short term energy stability of the OPCPA 73
2.16 Typical spectrum of the OPCPA output 73
2.17 Typical spectral stability of the OPCPA 74
2.18 Compressibility of the OPCPA output 75
2.19 Temporal contrast on a short term scale 76
2.20 Temporal contrast of the OPCPA frontend 76
2.21 Measured pulse duration stability 77
2.22 Beam profiles of the OPCPA output 78
2.23 Simulated degradation of spatio-spectral beam quality in OPCPA . . . 80
2.24 Zernike coefficients of saturation-induced wavefront aberrations 81
2.25 Measured vs. simulated beam properties in saturated OPCPA 82
2.26 Spectrally resolved Zernike coefficients of a saturated OPCPA beam . 82
2.27 Overview of the measured beam quality improvement after spatial filtering 84
2.28 M^2 measurement of the OPCPA output 85
2.29 Stability improvement of saturated OPCPA with spatial filtering . . . 86
2.30 Overview of the stages and control system of the MALCOLM laser system 90
2.31 Pulse properties during optimisation from a random initial point . . . 91
2.32 Snapshots of spectrum during optimisation from a random initial point 91
2.33 Reproducibility of daily optimisation 93
2.34 Overview of the linear OPCPA-performance model 97

2.35 Stabilized and un-stabilized laser parameters of MALCOLM 99
2.36 Long term stability of the OPCPA seeder 100
2.37 OPA signal energy with pump recycling 103
2.38 Comparison of a linear and nonlinear model. 104

3.1 Emission and absorption cross-sections of Ti:sapphire 106
3.2 Schematic overview of the Q-switched multi-core fiber laser. 109
3.3 Beam profile of the tapered multicore fiber output 110
3.4 Farfield profile of the tapered multicore fiber output 111
3.5 Caustic of the relay imaged MCF output 112
3.6 Schematic overview of the SHG simulation steps 114
3.7 Simulated conversion efficiency of the MCF-based SHG 115
3.8 Measured conversion efficiency of an MCF-based SHG 115
3.9 Temporal profile of the MCF lasers output pulse. 116
3.10 Simulated evolution of the second harmonic pulse energy 117
3.11 Beam profiles of the frequency doubled MCF output 117
3.12 Caustic of the relay imaged MCF output for 10 mJ pulses 118
3.13 Simulated conversion efficiency of a high energy MCF-based SHG . . . 119
3.14 Temperature distribution in a an SHG crystal at 2.5 kW input power . 120
3.15 Temperature dependent SHG phase matching efficiency with NCPM . 120
3.16 Overview of the first development stage of KALDERA 122
3.17 Overview of slab and disk amplifier geometries. 124
3.18 Thermal conductivity of pure and doped sapphire 125
3.19 Evolution of pulse energy and B-integral in COLIMA 128
3.20 Beamprofiles in COLIMA 128
3.21 Evolution of spectrum in COLIMA 129
3.22 Transverse gain in COLIMA 130
3.23 Overview of the crystal cooling assembly of COLIMA 131
3.24 Local heat-load in the COLIMA crystal 131
3.25 Temperature distribution in the pumped COLIMA Ti:sapphire crystal . 132
3.26 Simulated caustic after a pass through the amplifier crystal 132
3.27 Wavefront map after single pass through COLIMA 133
3.28 Optical layout of the relay imaging multipass setup. 134
3.29 Caustic through the relay imaged multipass amplifier 135
3.30 Scaling of thermal focal length 137
3.31 Overview of a possible adaptation of COLIMA for kW average power 138
3.32 Thermal focal length for one-sided vs two-sided cooling 138

4.1 The layout of the ANGUS compressor 143
4.2 Spatio-temporally deformed pulse profiles 146
4.3 Beam parameters as a function of average power in gold-based compressors147
4.4 Peak intensity as a function of laser average power 148

4.5 Spatio-temporal pulse profiles at optimal average power 149
4.6 Peak intensity as a function of average power for different grating materials 150
4.7 Grating surface temperature as a function of average power 151
4.8 Grating geometry with active cooling on top and bottom edges 152
4.9 Illustration of grating geometry with active cooling 153
4.10 Peak surface temperature of a cooled compression grating 153

List of Tables

3.1 Parameters of the sapphire at cryogenic and room temperature 126

4.1 Parameters of the ANGUS lasers pulse compressor 143
4.2 Thermal properties of grating substrate materials 149

Introduction

Since its invention [1] and first experimental demonstration [2] in 1960, the laser has become an indispensable tool for science: It has revolutionised the experimental methods for understanding the inner workings of atoms and molecules [3–6], the universe on an astronomical scale [7–10], and the behaviour of matter under the most extreme conditions [11–13].

A few decades later, these methods were augmented by the development of bright X-ray sources driven by particle accelerators [14]. Their short wavelength makes it possible to probe the structure and dynamics of matter at atomic resolution. Through further development of these two tools, lasers and accelerator-based light sources have continued to push the boundaries, allowing to study matter at ever shorter length and time scales down to sub-Ångström [15] and attosecond [16] resolution, enabling a wide range of scientific applications [17–22].

However, modern accelerator-based X-ray sources are expensive and large instruments, that are only available at national-lab-scale facilities. Due to the scarcity of such facilities, access to high-brightness X-ray sources is limited. A compact and more affordable alternative to conventional radio-frequency (RF)-based particle accelerators could help to make these tools more accessible, opening the way to a breadth of research that is not possible with current instruments.

The invention of laser-wakefield acceleration (LWFA) by Tajima and Dawson in 1979 [23] promised a potential route towards compact accelerators with properties that made them highly suitable for driving bright X-ray sources [24]. The principle is based on exciting plasma waves that support strong electric fields, that are about 3-4 orders of magnitude larger than what is reachable in conventional accelerators. As a result, the acceleration distance required for driving X-ray sources can be reduced from the 100 m-scale to centimeter distances. The proposed method for exciting such plasma waves was to use high-power laser pulses with an intensity on the order of $10^{18}\,\mathrm{W/cm^2}$, further interweaving the paths of these two technologies.

Laser systems capable of delivering such high-intensity pulses only became realistic in the mid-1980's with the invention of chirped pulse amplification (CPA) [25] and titanium-doped sapphire (Ti:sapphire) as a laser medium [26], which enabled the generation of laser pulses with Joule-level energy and femtosecond duration. After further refinement, these laser technologies enabled the first experimental demonstration of laser-wakefield acceleration in 2004 [27–29].

Since then, the technique and quality of the accelerated electron beams have continued to improve, leading to the development of LWFA-driven X-ray sources [30–35] and ultimately to the demonstration of an LWFA-based free-electron laser [36, 37]. While demonstrating the potential of laser-wakefield acceleration to become an important tool for future scientists, the progress has so far mostly been achieved in few-shot, proof-of-principle experiments, and LWFA-based X-ray sources are not yet competitive with sources driven by conventional accelerators.

The main limitation in this regard is the high-energy laser systems that drive the laser-plasma interactions. The repetition rate of these laser systems needs to be increased from the current few-hertz level, the stability of the laser pulse properties must to be improved, and a high degree of control over the spatial and spectral pulse properties is required to achieve electron beam quality and stability, similar to that of conventional RF-based accelerators. For reference, experiments at free-electron lasers driven by conventional accelerators operate with around 100 X-ray pulses per second, with state-of-the-art superconducting accelerators typically delivering up to a few thousand pulses per second to an individual experiment [38].

Raising the repetition rate of laser-driven accelerators to the kHz-level would have two distinct consequences that play a crucial role in making them competitive with RF-based accelerators. First, the high repetition rate simply results in a comparable number of pulses per second and therefore a similar acquisition time for high statistics and precise measurements. In addition, a higher repetition rate allows fast feedback control, which can compensate most of the lasers – and therefore electrons – fluctuations, further reducing the disturbances in measurements and improving the experimental conditions for X-ray users. The majority of these fluctuations are typically caused by thermal drifts and convective air-flow, as well as mechanical and acoustic vibrations. The typical timescale on which these disturbances occur is on the order of a few milliseconds or slower, and they could therefore be compensated by feedback loops in lasers running at kHz repetition rates.

The KALDERA project at DESY aims to overcome these current limitations in laser-wakefield acceleration and to construct a laser system that will drive a GeV-level laser-wakefield accelerator at a repetition rate of 1 kHz. A first development stage of KALDERA will consist of a Ti:sapphire system operating at a repetition rate of 100 Hz. This allows to take advantage of the favorable properties of Ti:sapphire and the decades of experience with the technology, but will also push the average power of such lasers into a new regime. This is particularly difficult with Ti:sapphire, as a large fraction of the average power is converted to heat, which can cause the quality of the amplified pulses to degrade. To ensure the high pulse quality that is required for LWFA, the sources of such degradation need to be well understood, and the laser system – and all of its subcomponents – must be carefully designed to prevent it.

This thesis has been completed in the context of this first stage of development of KALDERA and we will address key challenges throughout the amplification chain of high energy laser systems, that currently limit their spatio-temporal pulse quality, stability and average power.

In *Chapter 1* we will first review the underlying physics of laser-wakefield accelerators and derive fundamental laser properties that are required to produce the high quality, GeV-level electron beams that are needed for bright, LWFA-based X-ray sources. In an overview of the state of the art of high-intensity lasers, we will compare different technologies and motivate that, despite challenges, Ti:sapphire is indeed the most feasible option for scaling the repetition rate of such accelerators to the kHz-level within the next few years.

We will then highlight the key components in the amplification chain of Ti:sapphire laser systems that are crucial for high quality LWFA, and in particular the problems that arise in those components, when increasing the average power towards the kW-level: 1) the generation of stable, high-quality seed pulses, 2) heat management in the actual Ti:sapphire amplifiers, 3) the generation of pump pulses with kW-level average power, and finally 4) the compression of ultrafast laser pulses at high average power.

In the following chapters we will then take a closer look at these key components and present solutions to their specific challenges.

In *Chapter 2* we explore the generation of seed pulses using optical parametric chirped pulse amplifiers (OPCPA) [39, 40]. The seed pulses largely determine the properties of the final, fully amplified pulses, so it is important to generate them in a way that allows a high degree of control over their properties. Especially in LWFA, they must also have high spatio-temporal quality and stability. OPCPA offers a high degree of flexibility in pulse properties, with high single pass gain and an inherently high temporal contrast, which in principle allows to generate high-quality seed pulses in a compact setup. However, delivering such high quality pulses in a stable and controlled manner has historically been challenging for OPCPA. The main reasons for this are an inherent trade-off between stability and spatio-temporal beam quality, and a high degree of coupling between different pulse properties. We will present a laser system – MALCOLM – that combines these features and provides stable seed pulses with high beam quality and a high degree of control, which is enabled by a deep understanding of the pulse degradation in saturated parametric amplification, and the use of machine learning methods to optimise and control the working point of MALCOLM. The laser system delivers 50 μJ pulses with a Fourier-limited pulse duration of 25 fs and a wavelength of 800 nm, with excellent spatio-temporal pulse quality and unprecedented long-term stability.

In *Chapter 3* we'll focus on the main amplifiers of high average power Ti:sapphire lasers. The main challenges are the generation of high average power pump beams and the thermal management of the Ti:sapphire amplifier itself. Future kW-level Ti:sapphire laser systems will require high brightness pump pulses with an average power on the order of 10 kW. As a possible solution for reaching this level, we'll present a multi-core fiber (MCF) based approach that has been developed at Helmholtz-Institut Jena, and we will focus on the specific challenges of the frequency conversion of the MCF lasers output to the 500 nm range that is required for pumping Ti:sapphire lasers.
We will further present a conceptual design of COLIMA, the 100 Hz, 1 J ultrafast Ti:sapphire amplifier that will be the final amplifier for the first development stage of KALDERA. The large quantum defect of Ti:sapphire and the resulting large heat load in the amplifier crystal, make it difficult to scale such amplifiers beyond the current few-hertz level. We'll present strategies for efficient heat extraction and the mitigation of thermal lensing, as well as simulations of the amplifiers gain dynamics.

In *Chapter 4* we will finally explore the limitations of the gold-coated diffraction gratings that are used in the pulse compressors of all current large Ti:sapphire systems due to the large diffraction bandwidth that they support. The gold coating of these gratings absorbs a few percent of the incident laser beam, leading to a heating that can cause the gratings to deform and lead to complex spatio-temporal couplings of the compressed laser pulses. We will study this phenomenon using numerical simulations to reproduce and understand the effects observed in the ANGUS laser system, a few-hertz, 200 TW, Ti:sapphire system at DESY. Finally, we'll present mitigation strategies for use in future high average power laser systems and investigate the average power limits up to which conventional gold-based grating technology can be used.

Publications

The following peer-reviewed publications are closely related to the contents of this thesis, and parts of them are reproduced in extended form in the following chapters.

1. **T. Eichner**, T. Hülsenbusch, J. Dirkwinkel, T. Lang, L. Winkelmann, G. Palmer, and A.R. Maier, *Spatio-spectral Couplings in Saturated Collinear OPCPA*, Opt. Express **30**, 3 (2022) [41]
2. **T. Eichner**, T. Hülsenbusch, G. Palmer, and A.R. Maier, *Evolutionary Optimisation and Long-Term Stabilisation of a Multi-Stage OPCPA System*, Opt. Express **31**, 22 (2023) [42].
3. C. Aleshire, **T. Eichner**, A. Steinkopff, A. Klenke, C. Jauregui, G. Palmer, S. Kuhn, J. Nold, N. Haarlammert, W. Leemans, T. Schreiber, A.R. Maier, and J. Limpert, *Frequency-Doubled Q-switched 4x4 Multicore Fiber Laser System*, Opt. Lett. **48**, 8 (2023) [43]
4. V. Leroux, **T. Eichner**, A.R. Maier., *Description of Spatio-Temporal Couplings from Heat-Induced Compressor Grating Deformation*, Opt. Express **28**, 6 (2020) [44]

Other publications that are only remotely related to this thesis, are the following.

5. V. Leroux, S. W. Jolly, M. Schnepp, **T. Eichner**, S. Jalas, M. Kirchen, P. Messner, C. Werle, P. Winkler, and A. R. Maier, *Wavefront degradation of a 200 TW laser from heat-induced deformation of in-vacuum compressor gratings*, Opt. Express **26**, 13061 (2018) [45]
6. N. Delbos, C. Werle, I. Dornmair, **T. Eichner**, L. Hübner, S. Jalas, S. Jolly, M. Kirchen, V. Leroux, P. Messner, M. Schnepp, M. Trunk, P. Walker, P. Winkler, and A. Maier, *Lux – A laser–plasma driven undulator beamline*, Nucl. Instrum. Methods Phys. Res. A, **909**, 318 (2018) [46]
7. A. R. Maier, N. M. Delbos, **T. Eichner**, L. Hübner, S. Jalas, L. Jeppe, S. W. Jolly, M. Kirchen, V. Leroux, P. Messner, M. Schnepp, M. Trunk, P. A. Walker, C. Werle, and P. Winkler, *Decoding Sources of Energy Variability in a Laser-Plasma Accelerator*, Phys. Rev. X **10**, 031039 (2020) [47]

8. M. Kirchen, S. Jalas, P. Messner, P. Winkler, **T. Eichner**, L. Hübner, T. Hülsenbusch, L. Jeppe, T. Parikh, M. Schnepp, and A. R. Maier, *Optimal Beam Loading in a Laser-Plasma Accelerator*, Phys. Rev. Lett. **126**, 174801 (2021) [48]
9. S. Jalas, M. Kirchen, C. Braun, **T. Eichner**, J.B. Gonzalez, L. Hübner, T. Hülsenbusch, P. Messner, G. Palmer, M. Schnepp, C. Werle, P. Winkler, W.P. Leemans, and A.R. Maier *Tuning curves for a laser-plasma accelerator*, Phys. Rev. Accel. Beams **26**, 071302 (2022) [49]
10. C. Werle, C. Braun, **T. Eichner**, T. Hülsenbusch, G. Palmer, A.R. Maier *Out-of-plane multilayer-dielectric-grating compressor for ultrafast Ti:sapphire pulses*, Opt. Express **31**, 23 (2023) [50]

Finally, the following publications are not related to the contents of the thesis.

11. S.W. Jolly, N.H. Matlis, F. Ahr, V. Leroux, **T. Eichner**, A.L. Calendron, H. Ishizuki, T. Taira, F.X. Kärtner, and A.R. Maier, *Spectral phase control of interfering chirped pulses for high-energy narrowband terahertz generation*, Nat. Commun., **10**, 2591 (2019) [51]
12. N.H. Matlis, F. Ahr, A.-L. Calendron, H. Cankaya, G. Cirmi, **T. Eichner**, A. Fallahi, M. Fakhari, A. Hartin, M. Hemmer, W.R. Huang, H. Ishizuki, S.W. Jolly, V. Leroux, A.R. Maier, J. Meier, W. Qiao, K. Ravi, D.N. Schimpf, T. Taira, X. Wu, L. Zapata, C. Zapata, D. Zhang, C. Zhou, and F.X. Kärtner, *Acceleration of electrons in THz driven structures for AXSIS*, Nucl. Instrum. Methods Phys. Res. A, **909**, 27 (2018) [52]

1 Drive Lasers for Laser-Wakefield Acceleration

The aim of this chapter is to derive fundamental properties required from current and future drive lasers for laser-wakefield acceleration (LWFA). To understand these requirements, we will first review the fundamental physics of laser-wakefield acceleration to motivate the use of high-quality laser pulses with Joule-level energy and tens of femtosecond duration. We will then compare commonly discussed laser technologies in terms of their specific suitability for meeting these requirements, and explain why Ti:sapphire-based lasers are currently the most feasible option. Using the ANGUS laser as an example, we will introduce the typical layout of a state-of-the-art Ti:sapphire-based LWFA drive laser and illustrate the key challenges that need to be addressed in future systems: The stable and flexible generation of high quality seed pulses, the generation of kW-level pump beams for Ti:sapphire amplifiers, the thermal management in these amplifiers, and finally the compression of ultrafast laser pulses at kW-level average power.

1.1 Brief Introduction to Laser-Wakefield Acceleration

1.1.1 Laser-Wakefield Acceleration

The central process in laser-wakefield acceleration is the excitation of plasma waves with a highly intense laser pulse [53, 54]. A common analogy to describe this mechanism is that of a speed-boat that moves through water and – due to the shape of its hull – pushes water away from its path. After the boat has passed a certain point, the water rushes back towards the boat's axis of propagation, creating a wave that co-propagates with the boat behind its stern.

Very similarly, a laser pulse propagating through a plasma pushes electrons out of its path by the so-called ponderomotive force [56]

$$\vec{F}_p = -\frac{e^2}{4m_e\omega^2}\vec{\nabla}(\vec{E}^2), \tag{1.1}$$

which can be understood as a force caused by a radiation pressure pushing electrons towards regions of lower intensity. In this equation, ω is the angular frequency of the oscillating laser field, m_e is the electron mass, e is the electron charge, and $\vec{E}^2$ is the

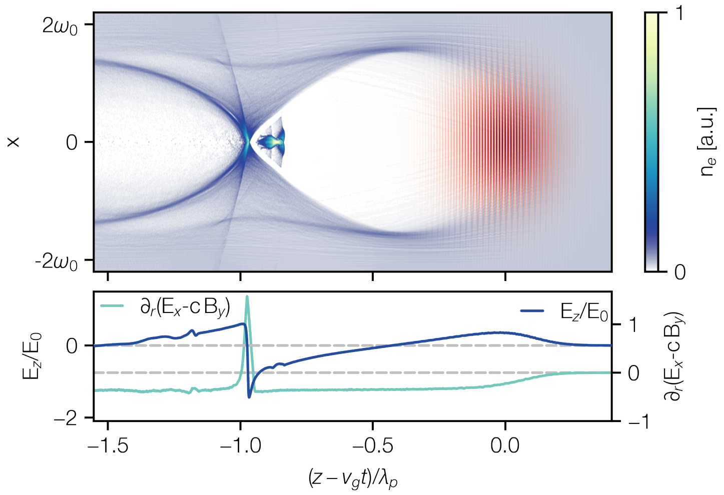

Figure 1.1 – A laser-driven plasma wake in the bubble regime. The top pane shows the local electron density of a plasma wake in the blowout regime, with an electron bunch at the rear end of the bubble. The red shows the local electric field strength of the driving laser. The bottom pane shows the axial, accelerating electric field E_z/E_0 and the focusing field $\partial_r(E_x - cB_z)$ (a.u.). The simulation was done using FBPIC [55] assuming a plasma density of $n_e = 1 \times 10^{18}\,\mathrm{cm}^{-3}$, $a_0 = 4$, a spotsize of $w_0 = 10\,\mu\mathrm{m}$ and a pulse duration of 32 fs.

squared electric field strength, which is directly proportional of the local intensity of the laser pulse. As we will see later in this section, the laser intensity required to excite such plasma waves is well above the ionisation threshold of the gases in which the interaction takes place. As a result, the gas is ionized and can be considered to be a plasma, with the electrons and ions being only loosely coupled through their Coulomb-interaction. However, due to their much higher mass, the ions can be considered stationary and it is sufficient to consider only the motion of the electrons in the following paragraphs.

The charge separation caused by the laser pulse pushing the plasma electrons away from its axis of propagation, leads to an electrostatic field which results in a restoring force acting on the displaced electrons. As a result, these electrons begin to oscillate around their initial position at the characteristic plasma frequency $\omega_p \propto \sqrt{n_e}$. The collective motion of all displaced plasma electrons forms waves in the electron density n_e that follow the laser pulse as a wake-field, as it is shown in figure 1.1.

The resonant excitation of waves at the plasma frequency can lead to large amplitude waves in electron density that can sustain electric fields of strength [57, 58]

$$E_0[\mathrm{V/m}] \simeq 96\sqrt{n_e[\mathrm{cm}^{-3}]}, \tag{1.2}$$

which is also called the non-relativistic wave-breaking limit. At experimentally well accessible plasma densities of $10^{18}\,\mathrm{cm}^{-3}$, E_0 can be on the order of 100 GV/m, which is around three to four orders of magnitude larger than electric fields typically reached by conventional accelerator technology [59]. This already hints at the large potential of plasma based acceleration, if one would be able to resonantly excite such waves and use these large-scale electric fields for the controlled acceleration of charged particles.

Such plasma waves are resonantly excited if the transverse and temporal dimensions of the laser pulse match half a plasma wavelength $\lambda_p = 2\pi c/\omega_p \simeq 3.3 \times 10^{10}\mu\mathrm{m}/\sqrt{n_e[\mathrm{cm}^{-3}]}$. To understand this resonance condition, we shall take a look at the temporal intensity profile of a laser pulse. On the leading edge of the pulse, the intensity gradient of the rising edge of the pulse pushes electrons away from the axis of propagation through the ponderomotive force, exciting an oscillation of the electrons. As the falling edge of the laser pulse exhibits an opposite intensity gradient to the leading edge, the sign of the ponderomotive force is reversed and electrons are pulled back towards the axis of propagation. If this push and subsequent pull are properly timed with respect to the natural oscillation of the electrons, i.e. $\tau_{\mathrm{laser}} \simeq 0.5\lambda_p/c$, the plasma wave is excited resonantly. This relation also applies to the transverse dimension of the laser, where the diameter of the laser should be matched to the plasma wavelength: $2w_0 \simeq \lambda_p$. At the previously mentioned typical plasma density of $10^{18}\,\mathrm{cm}^{-3}$, the plasma wavelength would be $33\,\mu$m and the required spotsize and pulse duration thus $66\,\mu$m and 55 fs respectively.

Depending on strength of the ponderomotive kick that the electrons experience, the plasma wake may have very different behaviour. For relatively low intensity laser pulses, the electrons behave in a simple non-relativistic manner and the resulting waves can be described as a sinusoidal low-amplitude modulation of the electron density.

If the wave excitation is however strong enough such that the ponderomotive force of the laser directly accelerates electrons to relativistic energies, one speaks of the nonlinear regime. In this regime, the electrons motion is strongly influenced by relativistic effects, resulting in a distortion of the plasma wave, steepening the density modulation of the electrons.When further increasing the strength of the wave excitation, the modulation of the electron density may become strong enough to lead to a largely depleted electron density right behind the driving laser pulse, commonly called the plasma bubble (see figure 1.1 for an exemplary depiction). This regime is thus called the bubble or blowout regime and is generally desired for acceleration of electrons as it provides the highest accelerating field gradients and an efficient transfer of energy from the wakefield to the electron bunch, resulting in higher achievable electron energies over a shorter acceleration length and at a lower laser pulse energy [56]. The laser intensity needed for the transition from the linear to the nonlinear regime can be conveniently described by the lasers normalized peak vector potential [56]

$$a_0 \simeq 0.86\,\lambda_0\,[\mu\mathrm{m}]\,\sqrt{I_0[10^{18}\mathrm{W/cm^2}]}. \tag{1.3}$$

Whenever $a_0 < 1$, the electrons behave in a non-relativistic manner, while for $a_0 > 1$ the plasma waves behave non-linearly. The bubble-regime is reached when further increase the laser intensity such that $a_0 \gg 1$. From equation 1.3 we can already derive a first demand on the drive laser: for efficient acceleration in the nonlinear regime with $a_0 > 1$, a laser peak intensity on the order of at least $10^{18}\mathrm{W/cm^2}$ is needed – assuming a laser wavelength of approximately $1\,\mu$m around which a large number of high intensity laser technologies exist.

The bottom pane of figure 1.1 illustrates the accelerating and focusing fields in the bubble regime. In order to use the large-amplitude longitudinal electric fields for acceleration of electrons, one needs to inject a short electron bunch ($\mathrm{L_{bunch}} \ll \lambda_p$) into the plasma bubble at a phase where the electrons simultaneously experience an accelerating, and a focusing field that prevents an electron bunch from being dispersed, i.e. where both fields shown in figure 1.1 have a negative sign. This imposes strict limits on the distance between the electron bunch and the driving laser pulse, but several methods for controlled injection at a suitable phase of the wakefield have been developed and experimentally demonstrated [56, 60–63].

Scaling Laws and Acceleration Limits

The energy that an electron gains when accelerated in a wakefield can be written as

$$W \simeq eE_{\mathrm{avg}}L_{\mathrm{acc}}, \tag{1.4}$$

where L_{acc} is the length over which acceleration takes place and E_{avg} is the average accelerating field gradient given by [56]

$$E_{\mathrm{avg}} = E_0\left(\frac{a_0^2}{2}\right)\left(1+\frac{a_0^2}{2}\right)^{-\frac{1}{2}}. \tag{1.5}$$

The acceleration length L_{acc} – typically on the order of a few millimeters to a centimeter – is practically limited by one of three dominant effects: 1) diffraction of the laser pulse, 2) depletion of the laser energy, or 3) dephasing of the electrons [56].

While diffraction is typically the overall limiting factor if it is left uncompensated, a number of methods have been developed to prevent it by optically guiding the laser pulse [64]. This is typically done by introducing a radial density gradient in the plasma that results in a radially decreasing refractive index which focuses the laser and thus counteracts diffraction. This has been shown experimentally to be effective enough for the other limiting effects – depletion and dephasing – to ultimately limit the achievable electron energy [65]. In the following, we will therefore focus on the limitations imposed by the latter two effects.

The process of pump depletion simply describes the transfer of energy from the laser pulse to the plasma wave. After a certain amount of propagation of the laser through the plasma, the laser loses a significant fraction of its energy, leading to a decrease in peak intensity that prevents a further wakefield excitation.

The third effect – electron dephasing – describes the process of the electrons catching up with, or even out-running, the laser pulse. As the laser pulse propagates through the plasma, its group velocity is lowered by the refractive index of the plasma, while the electrons quickly achieve relativistic velocities close to the vacuum speed of light. They may therefore catch up with the driving laser pulse and exit the accelerating phase of the wakefield, effectively stopping the acceleration process.

In the nonlinear regime, dephasing and depletion occur after a similar acceleration distance [56]

$$L_d \simeq \frac{\lambda_p^3}{2\lambda^2}\frac{\sqrt{2}}{\pi}a_0 \propto n_e^{-3/2}. \tag{1.6}$$

By combining this acceleration length with the accelerating field gradient – and more specifically its proportionality to $\sqrt{n_e}$ (see eq. 1.2) –, we find that the total energy gain in the electric field is proportional to n_e^{-1}, i.e. higher electron energies require lower plasma densities [56].

However, a lower plasma density also implies a larger plasma wavelength ($\lambda_p \propto n_e^{-1/2}$). As described earlier, this in turn means that the duration and beam diameter of the driving laser pulse must be increased according to $\propto n_e^{-1/2}$, in order to resonantly excite the wakefield. This would correspond to a decrease in the lasers peak intensity, which must be compensated by an increase in pulse energy to maintain a constant intensity – or correspondingly a_0 – and remain in the nonlinear wakefield regime. The scaling between the required laser energy and the plasma density thus follows $E_L \propto n_e^{-3/2}$.

In summary, we can derive the general relationship between the maximum electron energy and the laser energy:

$$W \propto E_L^{3/2}, \tag{1.7}$$

which is valid for an optimal case where the laser diffraction is handled such that the acceleration length is limited by electron dephasing and laser depletion, and an efficient acceleration is ensured by resonant excitation of a nonlinear wakefield.

Correspondingly, one can derive a similar relationship between the optimal pulse duration and the required laser pulse energy:

$$\tau_{\text{Laser}} \propto E_L. \tag{1.8}$$

These scaling laws imply that there is ideal relationship between pulse energy, spot size, and pulse duration of the driving laser pulse, that results in an efficient acceleration of electrons to a given electron energy. While the spotsize can be easily adjusted in experiments, the relationship between pulse energy and pulse duration has far-reaching implications for whether or not a certain laser technology is suitable for laser-wakefield acceleration.

Electron Bunch Charge

In addition to the electron energy, the bunch charge – i.e. the number of electrons N_{max} that are accelerated in a bubble – is also important for many applications. The effect that ultimately limits the bunch charge is beam loading, which occurs when the bunch has enough charge to generate its own electric field of comparable magnitude to the fields present in the accelerating bubble. The electron bunch's own field then distorts the prevailing accelerating and focusing field gradients, possibly to the extent that no further electrons can be contained in the bubble. In the nonlinear regime, this limit for the number of electrons can be estimated as [56]

$$N_{\text{max}} \simeq 3.1 \times 10^9 \lambda_0[\mu\text{m}]\sqrt{P_L[\text{TW}]} \tag{1.9}$$

where P_L is the lasers peak power. However, operation near this limit would degrade electron beam quality, and typical experimental values for the beamloading efficiency (the achieved fraction of N_{max}) are on the order of ten percent [56].

1.1.2 Required Drive Laser Properties

A key application of particle accelerators is the generation of X-ray pulses that can be used for imaging and spectroscopy in various scientific disciplines. Today, the brightest X-ray pulses are provided by large-scale free-electron laser [66] facilities such as the European XFEL [67], LCLS [68], SACLA [15], FERMI [69] or FLASH [70]. To drive such light sources, electron beams with an energy around 1 GeV and a bunch charge on the order of 500 pC, as well as high beam quality in terms of low energy spread and emittance would be required [71, 72], which is well within the reach of laser-wakefield accelerators [73–77].

Using the relationships derived in the previous sections, we can estimate what laser parameters would be required to provide the necessary electron energy and bunch charge.

Starting from equation 1.9, we can estimate that a laser with a peak power around 100 TW is needed to provide a bunch charge in the relevant range – when using a laser with a wavelength around $1\,\mu$m, at which a large number of high power laser technologies are available. In addition, equation 1.8 implies that – for efficient acceleration – such a peak intensity should not simply be achieved through excessive shortening of the pulse duration, but rather through a moderate pulse duration combined with a high pulse energy. For plasma densities that allow acceleration to 1 GeV (around $1 - 3 \times 10^{18}\,\mathrm{cm}^{-3}$ [78]), this would imply a pulse duration around 30-50 fs and a corresponding pulse energy of 3-5 J.

In addition, the pulses should have a high quality in terms to their temporal and spatial shape. Our simple considerations of resonant excitation of plasma waves in section 1.1.1 were based on idealized Gaussian intensity profiles in the spatial and temporal dimension of the laser pulses. In reality, however, there are a number of effects in a laser system that can degrade this 3-dimensional pulse profile. The most common and impactful are spatio-temporal couplings and poor temporal contrast.

With respect to the spatial pulse profile of the laser, in particular deformations that deviate from a radial symmetry can lead to an asymmetry of the ponderomotive forces and thus to a deformation of the plasma bubble. This leads to transverse field components in the plasma bubble that can lead to unwanted steering or oscillations of the electrons [79, 80]. As a result, the stability of the bunch properties and the focusability of the electron bunches can be severely degraded. Besides wavefront aberrations, also spatio-temporal couplings (STCs) can cause such an asymmetry. A very common first-order STC is pulse front tilt (PFT), which can be caused by angular dispersion of the laser pulses [81, 82], and can easily be introduced in all stages of a laser system, but especially the dispersive sections of the laser such as the stretcher and compressor of a CPA system [83, 84]. The effect of pulse front tilt on the electron properties has been thoroughly investigated both theoretically [85] and experimentally [86–88]. Besides such a direct influence on the plasma dynamics, a low spatio-temporal beam quality also reduces the peak intensity and thus increases the needed pulse energy to achieve the same amplitude of the plasma wake.

While distortions of the spectrally integrated wavefront and temporal properties of a pulse can be compensated to some extent using adaptive optics or programmable dispersive devices, compensating spatio-temporal couplings is much more difficult.

Minimizing their sources throughout the laser system is therefore an important task in the design of any laser system, but especially those dedicated to laser-wakefield acceleration.

The temporal contrast of high intensity laser systems is another important factor to consider in the laser design. A particularly important aspect is the post-pulse intensity on a <500 fs timescale, as this would correspond to a laser field that can interact with electrons trailing the laser pulse in the bubble. Such a pedestal around the main pulse is inherent in many laser architectures and its mitigation requires special measures throughout all stages of the laser chain. While there are a number of methods to actively enhance the temporal contrast, they are often only feasible for low-intensity pulses, have a low energy transmission or provide only a small improvement that may not be sufficient to prevent a perturbation of the electrons [89–92]. Ensuring such a high temporal contrast must therefore also be considered throughout the entire laser chain [93–100].

Finally, for applications using the electron- or X-ray beams, it is important to have a high degree of control and repeatability of the beam properties. Due to the direct and highly nonlinear connection between the electron properties and the laser properties, this ultimately means that the fluctuations of the driving laser pulses must be as small as possible to ensure that the fluctuations of the electron properties are also small. This direct connection between the electron properties and laser pulse fluctuations has been investigated experimentally in [47] and [48], where it was found that besides the stability of the laser energy, also the stability of the pulse duration and the laser wavefront of typical high intensity laser systems can limit the electron stability. As a result, the laser system has to be built in a way that ensures exceptional reliability, and stability in all beam properties.

1.2 Typical Setup of LWFA Drive Lasers

Experiments on laser-wakefield acceleration only became possible after the invention of the chirped pulse amplification (CPA) technique [25] and its combination with titanium-doped sapphire [26] as a gain medium. Both of these key laser technologies are now indispensable in the generation of >10 TW laser pulses with durations of tens of femtoseconds.

Especially the invention of CPA in 1985 has led to a leap in the ever-increasing peak power of laser systems. Without this technology, the intensity of the laser pulses in TW-level systems would be sufficient to damage optical components of the laser, and nonlinear interactions between the laser pulses and the optical components would result in degradation of the laser beam quality. Figure 1.2 shows the basic principle of CPA: a short, low-energy seed pulse is generated and stretched in time – chirped

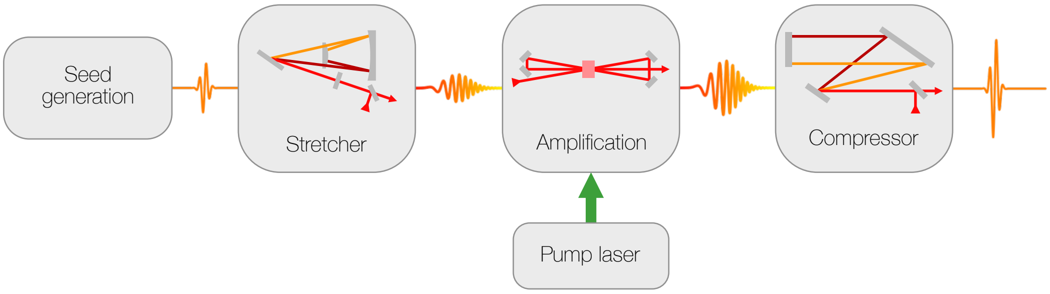

Figure 1.2 – Basic principle of chirped pulse amplification (CPA): 1) A broadband, high quality seed pulse is generated 2) It is temporally stretched to reduce the peak intensity 3) it is amplified to high pulse energy and finally 4) it is re-comrpessed to short duration and high peak power.

– before amplification. This reduces the peak intensity of the pulses and thereby prevents damage of optical components during the subsequent amplification. After amplification, the pulses are compressed to finally achieve the peak intensity required for experiments. In high energy laser systems, the chirping and recompression are typically performed using highly dispersive optical assemblies based on diffraction gratings. CPA is ubiquitous in all high intensity laser systems that are capable of producing pulses suitable for laser-wakefield acceleration.

The key property of Titanium-doped sapphire (Ti:sapphire) is its large emission bandwidth centered around 800 nm, which allows amplification of pulses with Fourier-limited pulse durations well below 50 fs [26]. In addition, the material properties allow for an efficient energy extraction and thus the amplification to pulse energies of several tens of Joules[1].

One such Ti:sapphire-based CPA laser system is the Angus system at DESY, which is used to drive the Lux laser-wakefield accelerator [46]. The main achievements at Lux include the continuous operation of the laser-wakefield accelerator over unmatched durations >30 h and with unprecedented long-term stability [47]. In addition, experiments at Lux have enabled substantial advances in the reproducible generation of high-quality electron bunches [48], partly with the help of machine learning methods [101]. Enabling such advances, Angus can be considered a prime example of a state-of-the-art LWFA drive laser, and we will therefore use it to review a typical setup of such laser systems.

Angus is a Ti:sapphire laser system with a double CPA [95] architecture that delivers pulses with up to 6 J energy and 30 fs duration at a repetition rate of up to 5 Hz. However, for reasons discussed later in this section, the repetition rate is typically limited to 1 Hz. The amplification chain of the system – shown in figure 1.3 – starts

---

[1] See chapter 3 for more details on Ti:sapphire.

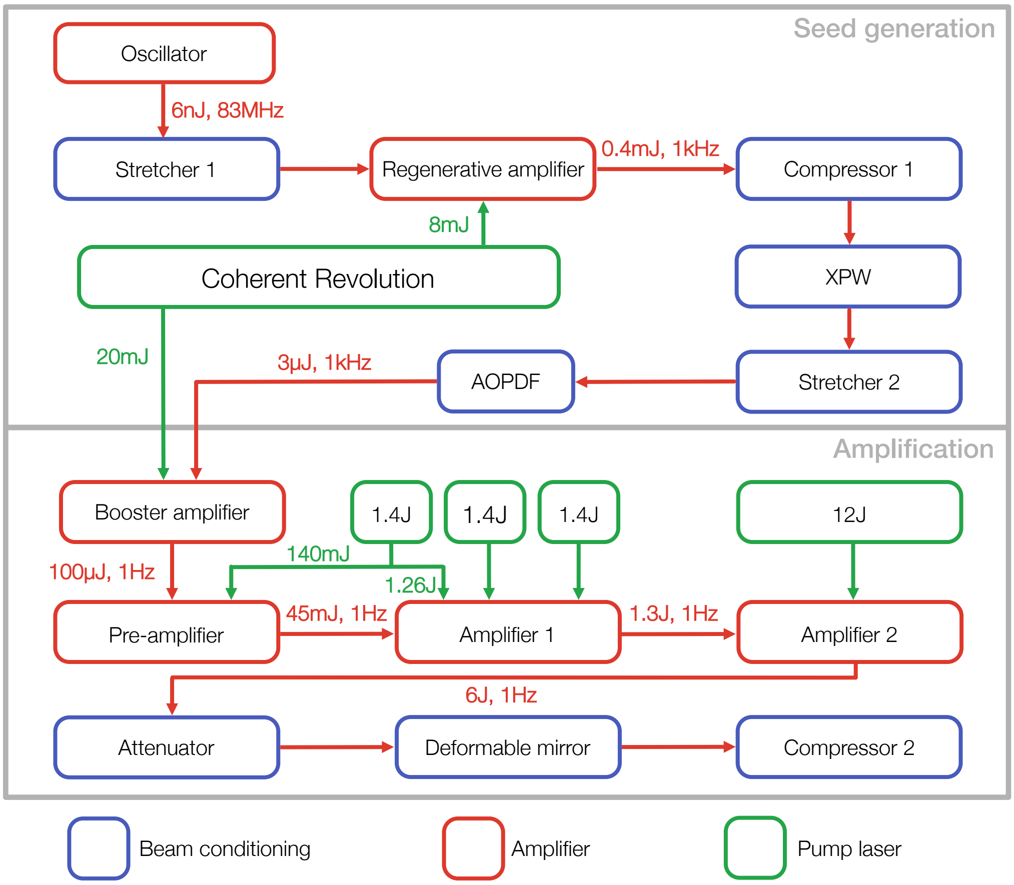

Figure 1.3 – Overview of the amplifier chain of the ANGUS laser system

with a Kerr-lens mode-locked Ti:sapphire oscillator, producing 6 nJ pulses with a 12 fs Fourier limit at 83 MHz repetition rate. The pulses are stretched to a duration of approximately 220 ps duration and then picked down to a 1 kHz repetition rate through selective incoupling into a regenerative amplifier that amplifies the pulses to 400 μJ. After this first amplifier, the pulses are recompressed and sent into a cross-polarised wave generation (XPW)-based pulse cleaner that enhances the temporal contrast of the pulses by suppressing the low intensity background on a ns-timescale that is inherent to regenerative amplifiers by roughly three orders of magnitude [89]. A subsequent Öffner-type stretcher and two-pass booster amplifier prepare the pulses for the subsequent high energy amplifier section. The pulse duration after the stretcher is roughly 400 ps, but varies between 260 ps and 440 ps in the later amplifiers as a consequence of spectral shaping that is caused by gain narrowing and red-shifting in the high-gain Ti:sapphire amplifiers [102]. An acousto-optical programmable dispersive filter (AOPDF) [103], DAZZLER, is used to partially pre-compensate gain narrowing through active spectral shaping, and to fine-tune the spectral phase of the pulses after recompression. The booster amplifier raises the energy from 3 μJ to about 100 μJ, before a Pockels-cell-based pulse picker reduces the repetition rate to the final 1-5 Hz.

The high energy amplification is started by a 5-pass preamplifier that increases the pulse energy to 45 mJ, which is then amplified to about 1.3 J in a first power amplifier, Amp1. The final amplifier, Amp2, boosts the energy to 6 J with a pump energy of 12 J.

All pulsed pump lasers are frequency doubled, Q-switched neodymium-doped lasers. The pump laser for the regenerative and booster amplifiers is a diode pumped solid stage laser – Coherent Revolution – emitting at 527 nm. The high energy pump lasers for the later, low repetition rate amplifiers are flashlamp pumped Nd:YAG lasers emitting at 532 nm.

After the final amplifier, an attenuator based on a waveplate and thin-film polarisers allows to adjust the on-target pulse energy. A deformable mirror allows the correction of errors in the lasers wavefront. Finally, a two-grating in-vacuum compressor recompresses the pulses close to the 30 fs Transform-limited pulse duration, producing the >100 TW peak power required for LWFA experiments.

Special care has been taken to diagnose relevant pulse characteristics such as energy, spectral shape, beam position, beam pointing and beam profiles after each of the described amplification stages. The online diagnostics and monitoring of the laser performance is enabled by a far reaching integration into the accelerator control system DOOCS (Distributed Object-Oriented Control System) [104, 105], which has been extended for use in laser systems. The beam position and pointing diagnostics are also used for drift compensation after each amplifier.

The 30 W average power that would be achieved at the lasers full 6 J, 5 Hz operation already leads to significant degradation of the beam quality in particular after the compressor where a fraction of the incident average power is absorbed in the gold coated in-vacuum diffraction gratings. This heatload leads to a deformation of the grating substrates, that – due to the spatial dispersion on some of the grating passes – leads to a spectrally dependent wavefront deformation that can not be precompensated with the deformable mirror. A thorough investigation of this behaviour will be given in chapter 4.

Similar thermal issues are also observed in other sections of the laser system, where heatload on optomechanics leads to a deformation of mechanics and subsequent drifts in beam pointing. These pointing drifts are largely compensated by the previously described beam stabilisation after each amplifier, but drifts within individual amplifier stages are not compensated, leading to potential drifts in other coupled laser parameters such as the pulse energy. While this active monitoring and drift compensation of the lasers performance has enabled successful operation of LUX over durations >30 hours, there are still challenges that need to be handled for future long-term accelerator operation.

In particular drifts in spectral properties originating from the XPW-based frontend are difficult to compensate in the current setup due to the lack of tuning knobs and the nature of the material degradation of the BaF_2 that is used for the XPW process.

1.3 Demands for Future Laser Systems and Potential Laser Technologies

Although there has been rapid progress in the quality of electron beams from laser-wakefield accelerators, they are not yet competitive with conventional accelerator technology. In order to bring the capabilities towards a regime, in which they are interesting for user applications, a number of key challenges need to be overcome. In particular, the repetition rate, stability and quality of the driving laser pulses need to be improved. These requirements are to some extent in conflict with one another, since an increased repetition rate also results in an increased average power and thermal load on laser components, which in turn can lead to a degradation of beam quality, similar to that observed in ANGUS. However, a high spatio-temporal beam quality can be ensured through an appropriate choice of laser technology and the optical design of the laser system.

A major improvement to the overall stability of such high energy laser systems can be achieved by actively stabilizing laser properties using feedback loops. However, their effectiveness is limited in today's few-hertz laser systems, because most fluctuations occur on time-scales much shorter than the time between laser pulses and therefore cannot be easily compensated. The most common causes of such unwanted changes in laser properties are drifts induced by temperature changes within the laser system, convective airflow due to temperature differences around the lasers beampath, as well as mechanical and acoustic vibrations of the mechanical structure of the laser system. Most optomechanical components have resonant frequencies of a few hundred Hertz, above which the vibrations are passively dampened. As a result, the most sources of laser fluctuations could be compensated with feedback loops that operate at a repetition frequency above a few hundred Hertz. With a repetition repetition rate of 1 kHz, a feedback speed close to the Nyquist frequency of 500 Hz is in principle possible, such that the repetition rate of future laser systems should ideally be at or above 1 kHz.

Incidentally, a laser repetition rate of 1 kHz also pushes the number of accelerated electron bunches to a level that is comparable to the number of bunches available at a single experiment at modern superconducting free-electron laser facilities [38], thus providing comparable experimental conditions for users of such a facility.

While Ti:sapphire has until now been the architecture of choice for the generating the highest peak power pulses with pulse durations below 50 fs duration, there are significant challenges in scaling Ti:sapphire technology towards high average power. The key drawback of Ti:sapphire in this regard is the quantum defect of roughly 30%, which is caused by the ratio of the required pump wavelength near 500 nm and the center wavelength of the gain spectrum at roughly 800 nm. This is much larger than in other common gain materials that are doped with for example with ytterbium (Yb) or neodymium (Nd). The large quantum defect implies that roughly 30% of the incident pump power is converted directly into a heat load in the amplifier crystal, which must be extracted from the crystal to prevent effects such as thermal lensing that could degrade the beam quality. The high thermal conductivity of the host sapphire crystal helps to remove heat efficiently to some extent, but the thermal load still remains the main limitation for scaling Ti:sapphire technology to high average power.

In addition, the short upper-state lifetime of only $3.2\,\mu$s and the required pump wavelength in the blue-green spectral range make Ti:Sapphire difficult to pump. Any energy contributing to the gain must be delivered in a time much shorter than the fluorescence lifetime. Direct diode pumping would be the most efficient way to pump Ti:sapphire, but due to the limited peak power of commercially available laser diodes at a wavelength close to the required 500 nm, this approach is only feasible in low-energy, high-repetition rate laser systems. Instead, high-energy Ti:sapphire systems are typically pumped using frequency doubled, Q-switched Nd-lasers that are pumped by flashlamps. While this method can indeed provide high energy pump pulses capable of driving PW-laser systems, it is inefficient and limited to low repetition rates. A better alternative would be to use diode pumped Nd- or Yb-laser systems, but these would also need to be scaled up to deliver the 10 kW-level pump power needed in future 1 kHz, 100 TW Ti:sapphire lasers.

More details on the thermal limitations and pump generation will be given in chapter 3, but as a consequence of them, it is worth considering alternative technologies to circumvent the disadvantages of the Ti:sapphire-technology. The most promising such alternatives are spectrally broadened, high average power Yb-systems, OPCPA based amplifiers and thulium-based laser amplifiers. However, each of these technologies have its own unique challenges that also prevent them from being immediately viable as LWFA drive lasers.

Post-Compression of Yb-based Laser Systems

While Yb-based laser systems are capable of delivering very high average power beams – up to 10 kW in low energy, coherently combined fiber lasers [106] – they face two major challenges: The pulse energies above 1 J, that are required to drive laser plasma accelerators have only recently been achieved at kHz repetition rates [107], and such high energy Yb-lasers only support pulse durations of around 1 ps or longer, which raises the need for post-compression of the pulses to the sub-50 fs range. While this is possible [108], it becomes increasingly difficult at higher pulse energies due to practical limitations in the damage thresholds and peak intensities that multi-pass post-compression cells can support [109]. In addition, pulses from such nonlinear post-compression schemes typically have a degraded temporal contrast [110, 111] – especially on the < 1 ps-timescale – which can lead to low electron beam quality and stability. Nevertheless, this technology has been shown to have great potential as a complementary method for applications that demand very high repetition rate electron beams at slightly lower energy than is achievable with Ti:sapphire based laser systems. It is expected that the capabilities of these two technologies will converge over the next few years, making them complementary approaches for different applications.

This role as a driver laser for lower energy, high repetition rate accelerators can be supported by the use of coherently combined fiber lasers, which have been shown to be scalable to extremely high repetition rate and average power [106], but scaling in pulse energy is a challenge for fiber technology. The highest pulse energy currently achieved in such a laser system is 32 mJ [112] at a repetition rate of 20 kHz. Such coherently combined fiber lasers are typically also able to support pulse durations well below 500 fs, which reduces the required amount of pulse shortening and thus simplifies the post-compression to suitable pulse durations.

Optical Parametric Chirped Pulse Amplification (OPCPA)

While OPCPA [39] can support an exceptionally large amplification bandwidth – and correspondingly short pulse durations – as well as very low thermal load in the amplifier crystals, there are a number of key challenges that make scalability to high pulse energy difficult. Most importantly, the generally low pump-to-seed conversion efficiency leads to a need for pump pulses with even higher energy than in Ti:sapphire laser systems. However, some schemes, such as OPCPA using spatially and temporally shaped pump pulses, or recent developments involving the elimination of idler photons during amplification, enable conversion efficiencies of approximately 40% [93, 113, 114]. Such approaches would bring parametric amplifier technology to similar efficiencies as Ti:sapphire, but stricter demands on the pump lasers in terms of pulse duration, timing stability and beam quality, nevertheless make pumping of OPCPA more challenging than in the case of Ti:sapphire. Indeed, these factors have limited the demonstrated average power of OPCPA-based lasers to the 100 W-level (see figure 1.4), despite the OPCPA-technology itself having the potential to scale well into the kW regime [115].

In addition, OPCPA has an inherently high tendency to introduce complex spatio-temporal couplings, which are undesirable in laser-wakefield acceleration [116], and the benefit gained from the additional gain bandwidth is largely deminished by the scaling laws described in chapter 1. This means that, while still a potentially viable option overall, the additional technical requirements for the pump lasers combined with the negligible benefits in terms of bandwidth, make OPCPA a less interesting option for LWFA drive lasers than Ti:sapphire – at least as a high-energy amplifier. The strengths of this technology in terms of spectral flexibility and excellent temporal contrast, make it an ideal option for generating high quality seed pulses in hybrid OPCPA/Ti:sapphire laser systems [117, 118].

Thulium-Based Laser Systems

In the case of the final much-discussed option, thulium-doped lasers, high-energy amplification has only recently been demonstrated [119, 120]. Important milestones such as simultaneous short pulse and high energy operation remain to be demonstrated. In addition, high energy experiments have so far only been demonstrated at sub-Hz repetition rates – apart from a recent result on a burst-mode operation with an average power of 3.6 kW during a 5 ms-long burst [120]. A major advantage of the technology is the possibility of direct diode-pumping, which contributes to a much higher wall-plug efficiency compared to technologies such as Ti:sapphire or OPCPA [121]. In addition, the longer wavelength of around 1.9 μm leads to an increased ponderomotive potential compared to Ti:sapphire- or Yb-based lasers, and therefore to more efficient excitation of a plasma wake. A disadvantage of thulium based lasers is their narrower amplification bandwidth that only supports pulse durations above approximately 100 fs [122], limiting usability of the technology in electron acceleration, although the longer wavelength slightly relaxes the required pulse duration. If necessary, the pulse duration could be reduced well below 100 fs either by post compression [123, 124], similar to Yb-lasers, or, as suggested in [122], by Tm,Ho-codoping. However, the suitability of these approaches to high energy amplifiers is questionable, as post-compression suffers from the same scalability problems as in Yb-lasers and the use of Tm,Ho-codoping has so far only been demonstrated in low energy systems, with a lack of research into the scalability of this approach.

Furthermore, the lower demand for optical components and diagnostics in the 2 μm-wavelength range has resulted in lower availability and lower maturity of such sub-components compared to the 1 μm spectral range, where a wide range of optics and diagnostics is commercially available.

In summary, thulium-based laser systems have several advantages over current laser technologies around 1 μm, that make it a very promising option on longer timescales and for future compact accelerators, but the reduced gain bandwidth, reduced availability and maturity of auxiliary components, and the novelty of the technology, make it unlikely to deliver the workhorse-like performance, that is required by LWFA, within the next few years. In the long term, thulium technology may however play a key role in mature laser-wakefield accelerators that function as dedicated "science machines" and need to fulfil requirements beyond the ones described in this chapter, such as a low operating cost and therefore high wallplug-efficiency.

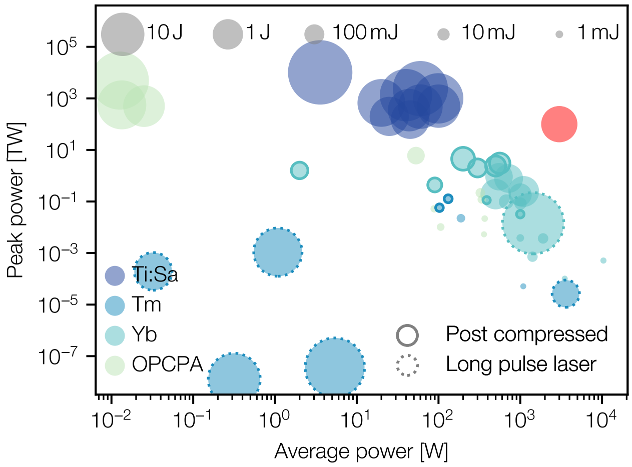

Figure 1.4 – Comparison of high average power ultrafast laser results from Ti:sapphire, thulium- and ytterbium-doped lasers as well as OPCPA systems. The red circle marks the desired parameters of 100 TW peak power, 3 J pulse energy and a repetition rate of 1 kHz. Dotted edges indicate long pulse laser systems with a pulse duration >10 ps, while solid edges mark laser systems with nonlinear post compression of pulses. [107, 108, 110, 119, 120, 123–147]

The parameter ranges in which these different technologies operate are visualized in figure 1.4. It can be seen that although post-compressed Yb-lasers and Ti:sapphire technology currently come closest to the laser parameters desired for a 100 TW, kHz-laser system, neither technology is currently able to deliver both the required peak power and average power.

For Yb-lasers, the key challenges can be summarised to two main points: Scaling up the energy of ultrafast laser systems to the 3-5 J range, and developing the technology to compress such pulses to the 30-50 fs range that would be required for LWFA. In Ti:sapphire, these pulse parameters are routinely achieved and even exceeded in a large number of TW and PW-class laser systems, but the main challenge is to scale up the repetition rate to the kHz range. Despite this challenge, Ti:sapphire currently comes closest to the desired performance at kHz repetition rates. This is especially true when additional factors that are not shown in figure 1.4 are considered, such as the pulse quality. By combining Ti:sapphire amplifiers with other technologies that we have discussed here, Ti:sapphire-based lasers are expected clearly outperform Yb-based lasers, especially in these secondary performance characteristics. Examples of such a combined approach include OPCPA-based seed generation for Ti:sapphire amplifiers – which can result in excellent temporal contrast – and Yb:fiber-based high average power pump lasers – which can potentially solve the challenge of pumping Ti:sapphire.

As a result, such a hybrid approach built around Ti:sapphire amplifiers, is currently the most feasible option for driving high-energy laser-wakefield accelerators at the kHz-level within the next few years. This conclusion is shared by a number of independent reviews and roadmaps on steps towards next generation laser-wakefield accelerators [121, 148–150].

Following this conclusion, we will therefore further explore the hybrid OPCPA-Ti:sapphire approach in the first phase of KALDERA and address many of the remaining challenges in this thesis.

The first of these challenges stems from the flexibility of OPCPA, which is enabled by a large number of adjustable amplifier parameters, that may however also present weak points as they can be difficult to control. To avoid potentially unreliable operation or poor pulse quality, a good understanding of the technology and a high degree of control over the adjustable parameters are required.

Other challenges, of course, are the thermal management of the Ti:sapphire amplifiers themselves and the generation of the required high average power pumped beams. One possible approach to this is the use of Yb:fiber technology, which has been used to demonstrate exceptionally high average power. Multi-core fibers in particular, further promise scalability to a large number of amplifiers in a compact footprint, which in combination can potentially deliver Joule-level pulse energy. Even if such scalability is successful, frequency conversion to the 500 nm-region of such a multi-aperture, high average power beam is not trivial. The challenges in this regard are discussed in the chapter 3.

Finally, the wavefront degradation due to heating of the gold-coated compressor gratings, which already limits the performance of the low repetition rate ANGUS laser system. This effect is expected to worsen as we move toward the desired kW average power, so the degradation needs to be well understood and mitigated, and the limitations of the gold-based technology need to be evaluated. This will be done in chapter 4.

2 Stable, High-Quality Pulses from an OPCPA-Based Seed-Laser

Parametric amplification of optical photons [151] is a well established method for generating ultrafast laser pulses. Unlike more conventional laser technology, which uses energy storage in the electronic structure of certain atoms or ions, parametric amplifiers rely on an instantaneously induced polarisation in a material that is driven by a strong optical field. Due to the nonlinear nature of this induced polarisation, it can decay into optical fields different from the driving field, and can be used for frequency conversion or amplification of optical pulses. The lack of energy storage means that very little energy - for most practical purposes a negligible amount - is absorbed in the gain medium, and thus there is very little thermal stress in the gain material, making it interesting for high-power applications. In addition, the optical properties of many nonlinear materials make it possible to amplify very large optical bandwidths, which are needed to generate ultrashort pulses. Furthermore, the large gain bandwidth allows a high degree of flexibility that allows the spectral characteristics of the OPCPA output to be optimally tuned for a specific application – for example, by pre-compensating for spectral narrowing in other amplifiers.
The instantaneous and nonlinear nature of OPCPA further results in an inherently high temporal contrast of the amplified pulses, which is not given in most other laser technologies. Finally, the highly nonlinear amplification allows such high quality pulses to be amplified in a remarkably compact package.

While the technology indeed has some great advantages over Ti:sapphire technology, there are also significant challenges that make scalability to high energy more difficult than for the more conventional laser technology. Nevertheless, the advantages outweigh the challenges in the low-energy frontend section of high energy laser systems [117, 118] and a hybrid architecture, in which an OPCPA-based seeder is combined with conventional high energy amplifiers, has been widely used in various high intensity systems [152–156].
Stable, high quality pulses are essential for seeding any laser system, since the properties of the fully amplified laser pulses are largely determined by the properties of the seed pulse. The high temporal contrast and spectral flexibility of pulses from an OPCPA are two important properties of seed pulses, as it is difficult to achieve these properties in the high-energy amplifier section of a laser system. However, achieving high spatio-temporal beam quality is usually challenging for OPCPAs due to the complex dynamics

of the amplification process. In addition, the highly nonlinear amplification can easily introduce unwanted fluctuations in the pulse characteristics. To understand and mitigate these drawbacks, and to take advantage of the beneficial properties, we will use this section to first theoretically explore the fundamental physics of OPCPA, followed by a presentation of the MALCOLM, a seed laser for high-energy Ti:sapphire systems based on OPCPA technology, that has been designed to meet the particularly strict stability and beam quality requirements of LWFA.

2.1 Introduction to OPCPA

To understand the strengths and challenges of parametric amplifiers, in particular with respect to the requirements of laser-wakefield acceleration, we will first review some basic concepts of nonlinear optics that make parametric amplification possible in the first place, followed by the implications of these concepts for the generation of highly stable pulses with high spatio-spectral beam quality.

The introduction to nonlinear optics and parametric amplification largely follows the derivations in [157], [158] and [159].

2.1.1 Fundamentals of Nonlinear Optical Processes

The propagation of optical fields and their interaction with media can be fully described by Maxwell's equations. A feature described by these equations, which is of particular interest when dealing with high intensity optical fields, is the polarisation that is induced in a medium whenever an electro-magnetic wave passes through it [160]. In most everyday scenarios, this polarisation can be viewed as a linear function $\mathbf{P} = \epsilon\chi\mathbf{E}$ of the externally applied field strength $\mathbf{E}$, where χ is the electric susceptibility of the material [161], which in layman's terms, describes the tendency of the material's electrons to react to an externally applied electric field, and is determined by the strength of the interaction between the electrons and ions in the material [160, 162]. When dealing with high intensity laser fields, the linear approximation loses its validity and one must expand the equation to a power series that represents its full nonlinear nature:

$$\mathbf{P} = \epsilon_0(1+\chi)\mathbf{E} = \epsilon_0(\mathbf{E} + \mathbf{E}\chi^{(1)} + \mathbf{E}^2\chi^{(2)} + \mathbf{E}^3\chi^{(3)} + \dots) \tag{2.1}$$

Because of the small values of the higher order susceptibilities $\chi^{n>1}$ (e.g. $\chi^{(2)}$ is typically on the order of pm/V), higher order terms of the polarisation become relevant only when the medium is excited by strong electric fields that are comparable to the atomic electric field of $\sim 10^{11}$ V/m [157]. When such strong fields are present, the electron displacement is not only determined by the external electric field and the fields of an single ion to which the electron is bound, but also by the surrounding ions, resulting in a nonlinear response of the electron to the external field [162]. Electric fields that induce such a nonlinear response are routinely achieved in ultrafast laser pulses and thus these nonlinear properties of the material need to be taken into account. In particular, the second and third order terms become relevant, where the second order susceptibility describes the tendency of a material to support frequency mixing processes such as difference frequency generation (DFG), sum frequency generation (SFG), or second harmonic generation (SHG), and the third order term that describes phenomena such as the intensity dependent refractive index and resulting self-focusing and self-phase modulation that is utilised in nonlinear spectral broadening [157].

In the wave-picture of optical fields, the nonlinear nature of the polarisation can be viewed as a superposition of multiple optical fields with different frequency components – ω_1, ω_2 and ω_3: If a polarisation is induced by a pump at frequency ω_3 and a seed (ω_1) is simultaneously present in the material, then the superposition of the two frequencies results in a modulation of the total electric field, where the modulation corresponds to the presence of the third wave – the idler – at the difference frequency ω_2. This process can be used to transfer energy from the exciting high intensity field to less intense fields, and thereby amplifying optical pulses. As with all phenomena in nature, the conservation of energy and momentum must be fulfilled also in these processes. Therefore the photon energies must satisfy the equation $\hbar\omega_3 = \hbar\omega_2 + \hbar\omega_1$ and the photon momenta have to fulfill $\hbar k_3 = \hbar k_2 + \hbar k_1$, where k_i are the wave vectors of the interacting beams [158]. The latter condition is equivalent to the phase matching condition $\Delta k = k_3 - k_2 - k_1 = 0$, which we will discuss in more detail later on.

In order to understand this phenomenon in a way that allows accurate modeling of parametric amplifiers and frequency converters, it is useful to look at the phenomenon in a more quantitative way. To do this, we will start with the wave equation

$$\frac{\partial^2 \mathbf{E}(\mathbf{r},t)}{\partial \mathbf{r}^2} - \mu_0 \frac{\partial^2 \mathbf{D}(\mathbf{r},t)}{\partial t^2} = \mu_0 \frac{\partial^2 \mathbf{P}_{NL}(\mathbf{r},t)}{\partial t^2}, \tag{2.2}$$

which describes the evolution of an electric field according to Maxwell's equations [159]. Again we see the interaction of the externally applied electric field $\mathbf{E}$, the linear displacement field $\mathbf{D}$ and $\mathbf{P}_{NL}$, the nonlinear components of the induced polarisation. In the case of low intensity and therefore weakly interacting fields, the right-hand side of the equation is "0" and one speaks of purely linear propagation of the electric field E. However, when the fields are strong enough for $\mathbf{P}_{NL}$ to become non-negligible, the right-hand side acts as a source term in the wave-equation, again indicating the formation of field components that are different from the driving electric field, and one speaks of a nonlinear parametric process taking place [159]. While solving equation 2.2 would fully describe the phenomena that we want to understand, this is not a trivial task and many methods have been proposed aiming at solutions under specific boundary conditions. We will do the same in the following derivation of parametric amplification and second harmonic generation, and start by restricting the nonlinear polarisation to the relevant second order while neglecting higher order terms, that depend on E^3 and higher orders. Under this assumption, the nonlinear polarisation can be written as

$$P_{NL} = \epsilon_0 \chi^{(2)} E^2(z,t) = 2\epsilon_0 d_{eff} E^2(z,t), \tag{2.3}$$

where d_{eff} is the effective nonlinear coefficient and depends on the specific components of the tensor $\chi^{(2)}$ that are involved in the interaction [157]. In addition, we will first consider an idealised electric field that is a superposition of three monochromatic waves at frequencies $\omega_1 < \omega_2 < \omega_3$:

$$E(z,t) = \frac{1}{2}\left(A_1(z)e^{j(\omega_1 t - k_1 z)} + A_2(z)e^{j(\omega_2 t - k_2 z)} + A_3(z)e^{j(\omega_3 t - k_3 z)}\right) + c.c., \tag{2.4}$$

where A_i describes the amplitude of the respective wave [159]. Using equation 2.3 we can calculate the nonlinear polarisation P_{NL} that results from the excitation by $E(z,t)$. We observe that when we square $E(z,t)$, polarisation terms emerge, that depend on $2\omega_1$, $2\omega_2$, $2\omega_3$, $\omega_1+\omega_2$, $\omega_1+\omega_3$, $\omega_2+\omega_3$, as well as $\omega_3-\omega_1$, $\omega_3-\omega_2$, and $\omega_2-\omega_1$. The first six of these frequency mixing terms describe sum frequency generation (SFG), while the last three represent difference frequency generation (DFG) [159].

In particular the processes of optical parametric amplification (OPA) and second harmonic generation (SHG), which can be considered special cases of DFG and SFG respectively, are relevant for this thesis. Therefore, we will use the following sections to take a closer look at the interactions that lead to optical parametric amplification (the following section 2.1.2) and at second harmonic generation (2.1.4).

2.1.2 Optical Parametric Amplification

If we consider a case where only interactions between all three waves fulfill the phase matching condition, the relevant interactions are reduced to $\omega_3-\omega_1=\omega_2$, $\omega_3-\omega_2=\omega_1$ and $\omega_1+\omega_2=\omega_3$ and we can write the nonlinear polarisation in a reduced form [159]

$$\begin{aligned}P_{NL}(z,t) &= \epsilon_0 d_{eff} A_2^*(z) A_3(z) e^{j(\omega_1 t-(k_3-k_2)z)} \\ &+ \epsilon_0 d_{eff} A_1^*(z) A_3(z) e^{j(\omega_2 t-(k_3-k_1)z)} \\ &+ \epsilon_0 d_{eff} A_1(z) A_2(z) e^{j(\omega_3 t-(k_1+k_2)z)} + c.c.\end{aligned} \tag{2.5}$$

This polarisation again consists of three different waves oscillating at the frequencies ω_1, ω_2 and ω_3, but the main difference to the driving electric field $E(z,t)$ is firstly that the amplitude of the polarisation at one frequency is determined by the product of the amplitudes at the other two frequencies, indicating that the waves are nonlinearly coupled, and secondly that the wavenumber of a given polarisation component does not automatically match its frequency. This means that a polarisation component is excited, and thus energy transfer between the waves is efficient, only when the phase matching condition is fulfilled [159].

If we apply a slowly varying envelope approximation to the wave equation 2.2 and use it to look at the evolution of the individual components of the nonlinear polarisation P_{NL}, we get the coupled wave equations [159]

$$\begin{aligned}\frac{\partial A_1}{\partial z} &= -j\sigma_1 A_2^* A_3 e^{-j\Delta kz}, \\ \frac{\partial A_2}{\partial z} &= -j\sigma_2 A_1^* A_3 e^{-j\Delta kz}, \\ \frac{\partial A_3}{\partial z} &= -j\sigma_3 A_1 A_2 e^{j\Delta kz},\end{aligned} \tag{2.6}$$

where $\sigma_i = d_{eff}\omega_i/c_0 n_i$. $n_i = \sqrt{\epsilon}_{ri}$ is the refractive index and $\Delta k = k_3 - k_2 - k_1$ is the previously introduced wavevector mismatch.

Parametric amplification now takes place when we let a pump wave at ω_3 interact with a seed at frequency ω_2, that has a much smaller amplitude $A_2 \ll A_3$. The amplitude A_3 of the pump will decrease during the interaction, transferring energy to the seed A_2 and resulting in the generation of the third wave with amplitude A_1 at $\omega_1 = \omega_3 - \omega_2$.

Exponential Amplification

Assuming initial conditions with $A_2(0) = 0$ and neglecting the depletion of the pump energy, i.e. $A_3 \approx const.$ and $\partial A_3/\partial z \approx 0$, one can solve the coupled wave equations for the intensity of the signal and idler beams after an interaction length L [159]:

$$
\begin{aligned}
I_1(L) &= I_1(0)\left(1 + \left[\frac{\Gamma}{g}\sinh(gL)\right]^2\right) \\
I_2(L) &= I_1(0)\frac{\omega_1}{\omega_2}\left[\frac{\Gamma}{g}\sinh(gL)\right]^2,
\end{aligned}
\tag{2.7}
$$

where $g = \sqrt{\Gamma^2 - \Delta k^2/4}$ is the small signal gain, $\Gamma^2 = \frac{2d_{eff}^2\omega_1\omega_2}{c_0^3\epsilon_0 n_1 n_2 n_3} I_3$ and $I_i = 1/2n\epsilon_0 c_0 |A_i|^2$ is the intensity of the respective waves. Using these equations, one can then define the parametric gain as the signal intensity relative to its initial value at $L = 0$ [159]:

$$
G(L) = \frac{I_1(L)}{I_1(0)} = 1 + \left[\frac{\Gamma}{g}\sinh(gL)\right]^2. \tag{2.8}
$$

We can see that the gain is mainly affected by two parameters: The wavevector mismatch Δk, which is ideally eliminated, and the pump intensity I_3.

In the large-gain limit, where $gL \gg 1$, the intensities and the gain converge towards

$$
\begin{aligned}
I_1(L) &\simeq I_1(0)\left(\frac{\Gamma}{g}\right)^2\frac{e^{2gL}}{4} \\
I_2(L) &\simeq I_1(0)\frac{\omega_1}{\omega_2}\left(\frac{\Gamma}{g}\right)^2\frac{e^{2gL}}{4} \\
G(L) &\simeq \left(\frac{\Gamma}{g}\right)^2\frac{e^{2gL}}{4}
\end{aligned}
\tag{2.9}
$$

and we find that a parametric amplifier provides exponential gain at the signal wavelength as long as pump depletion can be neglected. This exponential gain is made possible by a feedback mechanism that involves all three interacting waves: The initial difference frequency generation between pump and signal leads to the generation of the idler wave, which in turn supports the generation of signal photons through DFG of the idler and pump beams. The presence of more signal photons then leads to the generation of more idler photons, resulting in a positive feedback and an exponential amplification of the signal intensity.

Considering a realistic scenario of amplifying a signal wavelength of 800 nm in a BBO crystal with a 515 nm pump beam with intensity of 65 GW cm^{-2}, equation 2.8 yields a gain of approximately 10^6 after an interaction length of only 2 mm. This illustrates the potential of OPA for building remarkably compact high gain amplifiers.

Saturated Amplification

The equations 2.9 were derived for a simplified case assuming a constant pump intensity. In realistic OPA systems, however, the pump depletion quickly becomes relevant and thus the exponential gain predicted by the equations saturates. In this case, the exact description of the amplification process becomes much more complex and elaborate analytical models involving various assumptions [163] are required. As a more general alternative that e.g. also includes other nonlinear processes, a numerical solution of the coupled wave equations [164, 165] would be necessary. In the later sections of this chapter, we will present results of such numerical calculations using the chi3D simulation tool [166].

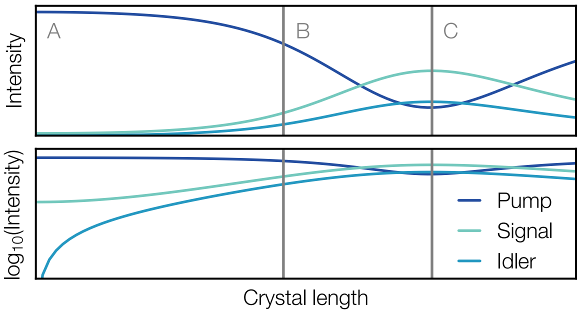

Figure 2.1 – Numerically simulated evolution of the signal pulse energy in the presence of pump depletion (inspired by [158])

For a qualitative understanding pulse energy evolution including pump depletion, we can look at figure 2.1. The amplification process can be divided into three phases: In section A the depletion of the pump can still be neglected, the signal intensity is small compared to the pump, and the amplitude of the idler wave is small compared to the signal wave. The evolution of the wave amplitudes is thus well described by the exponential amplification that we have derived analytically. Once the signal and idler waves reach similar amplitudes, the positive feedback mechanism is interrupted because the idler intensity becomes large enough that the difference frequency generation between pump and signal roughly balance out with the sum frequency generation between signal and idler [158]. This interrupts the exponential evolution of the signal energy and a roughly linear gain regime is reached (section B). Once the total intensity of signal and idler becomes much larger than the intensity of the pump, the sum frequency generation process between signal and idler dominates the overall interaction. The energy flow from the pump to the signal saturates and even reverses in this backconversion regime (C).

We can derive two important insights from this behaviour: first, the gain and efficiency of parametric amplifiers can be greatly enhanced by eliminating the idler photons from the interaction and thus keeping the amplification process in the exponential gain regime for as long as possible, and second, fluctuations of the signal energy caused by fluctuations of the signal or pump intensities can be minimized by carefully balancing the SFG and DFG processes in the backconversion regime. We will discuss the second point in more detail in section 2.1.5, as it is particularly interesting for applications that are sensitive on the intensity of the laser pulses, such as in laser-wakefield acceleration.

Parametric Phase

So far we have only considered the evolution of the intensity of the interacting waves. Especially in the backconversion regime, the evolution of the phase of the amplified pulses also becomes relevant and can lead to a change of the phase of the signal waves. This evolution can be calculated by solving the imaginary part of the coupled wave equations. After a propagation length L, the phases ϕ_i of the three waves can then be written as [167]:

$$\begin{aligned}
\phi_1(z) &= \phi_1(0) - \frac{\Delta k z}{2} + \frac{\Delta k z \gamma_1^2}{2} \int_0^z \frac{\mathrm{d}z}{f + \gamma_1^2}, \\
\phi_2(z) &= \phi_3(0) - \phi_1(0) - \frac{\pi}{2} - \frac{\Delta k z}{2}, \\
\phi_3(z) &= \phi_3(0) - \frac{\Delta k z}{2} \int_0^z \frac{f \mathrm{d}z}{1 - f},
\end{aligned} \tag{2.10}$$

where $f = 1 - I_3(z)/I_3(0)$ is the degree of pump depletion and $\gamma_1^2 = \frac{\omega_3}{\omega_1} \frac{I_1(0)}{I_3 0}$ is the squared ratio of the initial photon numbers of signal and pump.

These equations have several implications for the phase of the signal ϕ_1. First of all it is not influenced by the pump and thus any phase aberrations of the pump beam can not be transferred to the signal. If such aberrations exist, they are entirely transferred to phase of the idler beam ϕ_2, which adapts to the phase of the signal and pump to ensure optimal energy flow from the pump to the signal and idler. If the matching condition $\Delta k = 0$ is fulfilled, the phase of pump and signal remain unchanged during the amplification. If a wavevector mismatch $\Delta k \neq 0$ does however exist, the interacting waves accumulate an additional phase difference of $\Delta k z/2$ during propagation. This additional phase is particularly pronounced if the amplifier is saturated and the pump depleted. The resulting phase change imprinted onto the signal is called parametric phase and is influenced by the pump intensity, the degree of pump depletion and the wavevector mismatch. The parametric phase can have detrimental implications for the beam quality of the amplified beam, especially in broadband parametric amplifiers, where guaranteeing perfect phase matching over the full signal spectrum is challenging, as we will discuss in section 2.1.3.

Due to the locally varying intensity in realistic 3-dimensional pump pulses, the gain and pump depletion varies spatially and temporally, which can lead to a spatially and temporally varying intensity and wavefront of the amplified signal pulses. We will study this phenomenon in detail in section 2.3.

Phase Matching

In order to take full advantage of the high gain amplification enabled by parametric processes and to ensure high efficiency, it is important to find a way to satisfy of the phase matching condition. To do this, we shall start with the notation $k = \omega n / c_0$ of the wavevector, which allows us to write the phase matching condition as [159]

$$n_3\omega_3 - n_2\omega_2 - n_1\omega_1 = 0. \tag{2.11}$$

In this form, it becomes clear that for a given set of interacting wavelengths, one possible way to fulfill the phase matching condition, is to adjust of the refractive index of the interacting waves. Considering that in our case $\omega_3 > \omega_2 > \omega_1$, we would need a material with $n_3 < n_2 < n_1$ to satisfy the condition. However, in the visible and near infrared region around $1\,\mu$m, all known isotropic materials exhibit positive dispersion, meaning that $\partial n / \partial \omega > 0$ and thus the condition for the refractive indices can not be satisfied [159]. The most common way to get around this problem is to use birefringent, i.e. non-isotropic materials, where the refractive index depends on the directions of polarisation and propagation with respect to the optical axes of the material. For example, uniaxial crystals have two different frequency dependent refractive indices: the ordinary refractive index n_o and the extraordinary refractive index n_e, corresponding to different polarisation directions of the incident light wave. The extraordinary index n_e can also be adjusted with the angle θ between the direction of propagation and the optical axis of the crystal, resulting in the refractive index $n_e(\theta)$ that is given by [159]

$$\frac{1}{n(\theta)^2} = \frac{\cos^2\theta}{n_o^2} + \frac{\sin^2\theta}{n_e^2}. \tag{2.12}$$

In many birefringent materials it is possible to find a configuration of polarisations of the interacting beams, where θ can be tuned to satisfy the phase matching condition.

Index matching based angle tuning in birefringent crystals is also called critical phase matching, as opposed to non-critical phase matching [157]. In non-critical phase

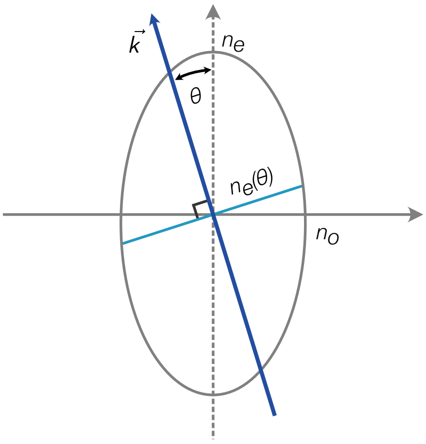

Figure 2.2 – Index ellipsoid to illustrate the parameters used in equation 2.12 (reproduced from [159])

matching, the temperature dependence of the refractive index of is used to achieve phase matching. In this case, the angle θ is kept at "0" so that at least one of the interacting beams propagates along the extraordinary axis of the crystal and the refractive index is adjusted by tuning the temperature of the nonlinear crystal. For example, second harmonic generation of 1030 nm beams can be achieved in the XZ-plane of LBO at a temperature of about 190°C. An advantage of this method is much better angular acceptance of the phase matching compared to critical phase matching, i.e. strong divergence or pointing changes of the input beams do not lead to a change of the phase matching efficiency.

The decrease in efficiency that is caused by imperfect phase matching is also described by the so-called phase matching efficiency, which can be derived from the 2.8 as [157]

$$\eta = \frac{G(L,\Delta k)}{G(L,\Delta k = 0)} = \left[\frac{\sin(\Delta k L/2)}{\Delta k L/2}\right]^2. \tag{2.13}$$

2.1.3 Broadband Parametric Amplification

For the sake of simplicity, all considerations up to now have been based on the interaction of monochromatic beams. When amplifying ultrafast pulses, however, this assumption loses its validity and the dispersive properties of the waves – i.e., the frequency-dependence of the refractive index, and thus of $k(\omega) = \frac{n(\omega)\omega}{c_0}$ must be take into account.

This has several consequences: First of all, the phase matching condition must be extended to all amplified wavelengths, making its fulfillment more complex, and second, the temporal overlap and walk-off between the individual pulses must be considered.

Temporal Overlap of Pulses

The most important consequence of the dispersion is the difference in group velocities between the interacting pulses. Especially in the case of ultrashort laser pulses, this can lead to a separation of the signal and idler from the pump pulses, which would stop the amplification completely. To prevent this, the interaction length must be kept well below the so-called pulse splitting length [159]

$$l_{i,3} = |\tau / \delta_{i,3}| = \left| \tau \middle/ \left(\frac{1}{v_{gi}} - \frac{1}{v_{g3}} \right) \right| \tag{2.14}$$

where $i = 1, 2$ denotes the index of the idler and signal pulses, v_{gi} is the group velocity of the respective pulses, and $\delta_{i,3}$ the group velocity mismatch (GVM) between them and the pump pulse. τ is the FWHM of the pulse duration. In practice, the GVM of the pulses is determined by the dispersive conditions defined by the chosen phase matching configuration and cannot be influenced very much. The only possible free parameter to maximize the pulse splitting length is the pulse duration τ, which can be increased by temporal chirping of the signal pulses. Especially in high energy OPA systems, this is often done anyway leading to the OPCPA scheme: optical parametric *chirped pulse* amplification, which is analogous to the conventional chirped pulse amplification done in high energy laser systems described in chapter 1 [39].

In OPCPA, the temporal overlap of pump and seed pulses leads to a trade-off: On the one hand, the reduced pump intensity at the leading and trailing edges of the pulses leads to a reduced gain in the edges of the signal spectrum. The resulting gain-dependent spectral narrowing could be avoided by minimizing the ratio τ_s/τ_p between the duration of signal and pump pulses, although the benefit of shortening the seed becomes negligible below a ratio of $\tau_s \approx \tau_p/3$ [168]. Following this rule of thumb, large fractions of the pump envelope do not interact with the signal wave and therefore do not contribute to the amplification, limiting the efficiency of the amplification. As we will discuss in more detail in 2.1.5, the unseeded regions of the pump may instead amplify optical parametric fluorescence (OPF), which would degrade the temporal contrast and stability of the amplifier output [168]. To avoid OPF and to ensure efficient extraction of the pump energy, one would prefer to have the entire pump envelope overlap with the seed. For the pulse durations, this would mean that $\tau_s/\tau_p > 1$, which contradicts the maximisation of the amplified bandwidth.

This trade-off has been studied in detail by Moses *et al.* [168], who found that a good compromise can be achieved by maximizing the product of gain and amplified bandwidth $G\Delta\omega$, which is achieved at a ratio of

$$(\tau_s/\tau_p)_{opt} \approx 2.1\sqrt{-2\ln[1-1/\ln(2E_p/E_s)]}, \tag{2.15}$$

where E_p and E_s are the initial energies of the pump and signal pulses, respectively. Note that for relatively low gain amplifiers, where the ratio of pump and seed energies is less than about 10^4, the optimal duration of the signal pulse is actually longer than the pump duration and one would lose significant amounts of bandwidth in the amplified signal pulses. While maximising $G\Delta\omega$ is generally indeed a good goal in the design of an OPCPA system, it is also necessary to consider other desired pulse characteristics into account, e.g., if maximum bandwidth is required.

In addition the temporal overlap of the individual pulses, the dispersion can also affect the shape of the pulses themselves due to the different phase velocities of the spectral components within the pulse. A full treatment of the nonlinear interaction of broadband pulses in a dispersive environment has to be considered in the coupled wave equation 2.6 and an accurate modeling of the interaction requires a numerical solution of the equations.

Broadband Phase Matching

In addition to the temporal evolution of the interacting pulses, the larger bandwidth also has severe consequences for the wavevector mismatch Δk of all interacting wavelengths and it is therefore helpful to consider the maximum bandwidth $\omega_i \pm \Delta\omega$ over which phase matching is actually satisfied. To do this, it is helpful to remember that typical OPA laser systems use pump pulses that have a much smaller bandwidth than the signal. To calculate $\Delta\omega$ we can therefore still consider a monochromatic pump at ω_3 and only consider the effects of the broadened signal. To satisfy the conservation of energy, a broadband signal must result in the generation of a broadband idler, which we will also consider. One approach to understand the influence of dispersion on phase matching is to consider the first-order Taylor expansion of $k(\omega)$ around the center frequency $\overline{\omega_1}$ of the signal. In the broadband case, the signal frequency then changes to the spectrum $\overline{\omega_1} + \Delta\omega$ and similarly, the idler then forms the spectrum $\overline{\omega_2} - \Delta\omega$. The wavevector for the two frequencies can then be written as [159]

$$\begin{aligned} k(\overline{\omega_1}+\Delta\omega) &\approx k(\overline{\omega_1}) + \frac{\partial k}{\partial\omega}|_{\omega_1}\Delta\omega \\ &= k(\overline{\omega_1}) + \frac{1}{v_{g1}}\Delta\omega \\ k(\overline{\omega_2}-\Delta\omega) &\approx k(\overline{\omega_2}) - \frac{\partial k}{\partial\omega}|_{\omega_2}\Delta\omega \\ &= k(\overline{\omega_2}) - \frac{1}{v_{g2}}\Delta\omega \end{aligned} \tag{2.16}$$

If phase matching at the central frequencies is satisfied, i.e. $\Delta k = k(\omega_3) - k(\omega_2) - k(\omega_1) = 0$, the remaining wavevector mismatch is

$$\Delta k \approx \left(\frac{1}{v_{g1}} - \frac{1}{v_{g2}}\right)\Delta\omega = \delta_{12}\Delta\omega, \tag{2.17}$$

where δ_{12} is the group velocity mismatch (GVM) between the idler and signal pulses [159]. From this, we can already conclude that the phase matching of a broadband parametric amplifier is optimal, when the group velocities of the signal and idler pulses are matched.

By inserting this wavevector mismatch into the parametric gain equation 2.8, one can derive an approximate expression for the FWHM bandwidth that a given OPA can support [159]:

$$\Delta\omega \approx 4\sqrt{\ln 2}\sqrt{\frac{\Gamma}{L}}\frac{1}{|1/v_{g1} - 1/v_{g2}|}, \tag{2.18}$$

This tells us, that the phase matching bandwidth $\Delta\nu$ is limited by the group velocity mismatch between the idler and seed pulses, and that high bandwidth pulses can be amplified with appropriate group velocity matching.

Such group velocity matching can be achieved in the aforementioned non-collinear phase matching geometry, by tuning the non-collinear angle α such that the condition

$$v_{g1} = v_{g2}\cos\Omega \tag{2.19}$$

is satisfied, where Ω is the angle of propagation between the idler and signal pulses [159], as is shown in figure 2.3. Parametric amplifiers using this configuration are also called non-collinear optical parametric amplifiers (NOPA).

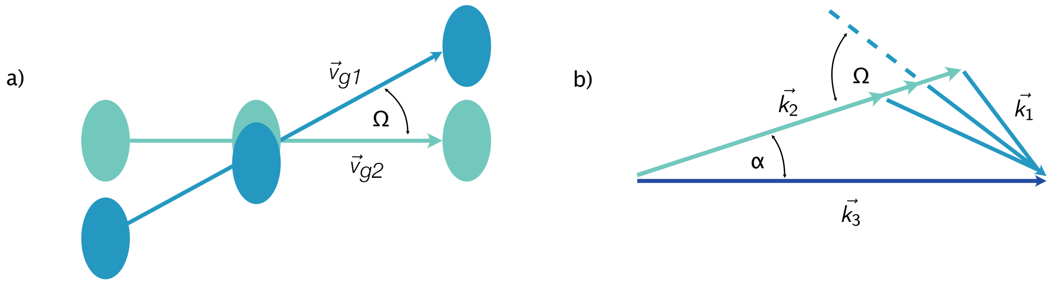

Figure 2.3 – Broadband non-collinear phase matching. a) Walkoff between idler and signal pulses with matched group velocity v_{gi} and b) depiction of the resulting angular dispersion of the idler.

It is important to remember that equation 2.18 was derived assuming only the first order Taylor expansion of $k(\omega)$. When the group velocities v_{g1} and v_{g2} are matched, the gain bandwidth becomes large enough, that this first order approximation is no longer valid and higher-order dispersion terms limit the phase matching bandwidth. Nevertheless, the increase in the gain bandwidth is remarkable: For example, in lithium triborate (LBO) it is possible to approximately quadruple the FWHM phasematching bandwidth as is shown in figure 2.4.

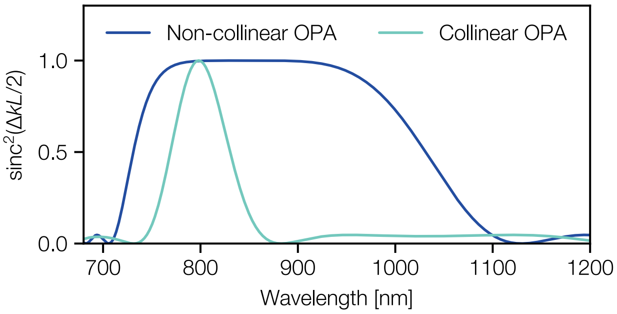

Figure 2.4 – Phase matching efficiency in a 3 mm long LBO crystal for a non-collinear phase matching geometry including group velocity compensation between signal and idler ($\theta = 16.5°$, $\alpha = 1.6°$), and a collinear phase matching configuration ($\theta = 11.7°$, $\alpha = 0°$)

In addition to increasing the phase matching bandwidth, non-collinear phase matching also introduces a frequency dependent angle of propagation in the idler, i.e., the introduction of angular dispersion. As we will discuss in more detail in section 2.1.6, the realisation of this phase matching scheme while ensuring excellent pulse quality is challenging because the scheme has a high tendency to also introduce angular dispersion or pulse front tilt to the signal.

For practical purposes it is therefore necessary to consider whether the benefits of the additional spectral bandwidth that can be amplified in non-collinear amplifier outweigh the potential drawbacks of potentially lower spatio-spectral beam quality. Depending on the application for which the OPCPA system will be used, factors other than the phase matching bandwidth may be have a greater influence on which phase matching geometry is best to use.

2.1.4 Second Harmonic Generation

In the derivation of the second order nonlinear polarisation in section 2.1.1, we already noted the emergence of polarisation components oscillating at $2\omega_i$, twice the frequency of the respective interacting fields. If we additionally consider a special case where $\omega_1 = \omega_2 = \omega$, the nonlinear polarisation is simplified to include fewer interacting terms, and the resulting coupled wave equations can be reduced to the two equations

$$\begin{aligned} \frac{\partial A_{2\omega}}{\partial z} &= -\frac{j\omega d_{eff}}{n_{2\omega}c_0} A_\omega^2 e^{j\Delta k z}, \\ \frac{\partial A_\omega}{\partial z} &= -\frac{j\omega d_{eff}}{n_\omega c_0} A_{2\omega} A_\omega^* e^{-j\Delta k z}, \end{aligned} \tag{2.20}$$

where $\Delta k = k(2\omega) - k(\omega)$, and A_ω and $A_{2\omega}$ are the respective amplitudes of the fundamental and second harmonic [157].

In the limit of negligible depletion of the fundamental A_ω, one can find the solution

$$I_{2\omega}(z) = \frac{2\omega^2 d_{eff}^2}{n_{2\omega} n_\omega^2 c_0^3 \epsilon_0} z^2 I_\omega^2 \left[\frac{\sin^2(\Delta k z/2)}{\Delta k z/2}\right]^2 \tag{2.21}$$

for the intensity $I_{2\omega}$ of the second harmonic after distance z [157]. We can see that in contrast to parametric amplification there is no exponential gain but instead the second harmonic intensity scales only with the square of the crystal length.

While general solutions for the evolution of the intensities with depletion of the fundamental exist in the form of Jacobi elliptic functions [169], a more general approach is – as in the case of OPA – the numerical solution of the wave equations. In that case also dispersive effects and the full three-dimensional intensity profile of the interacting pulses can be taken into account.

2.1.5 Stability of OPCPA-Systems

In the introduction to laser plasma acceleration in chapter 1, we noted that stable drive pulses are crucial for optimal operation of the accelerator. The highly nonlinear nature of OPCPA makes parametric amplifiers sensitive to a number of different noise sources,

resulting in typically higher fluctuations of the output parameters than in conventional laser amplifiers. In addition, different pulse characteristics are coupled in complex ways, making it even more difficult to guarantee stability of specific properties.
The sources of fluctuations in OPAs can be broadly divided into three categories: environmental influences such as changes in ambient temperature, humidity or convection of the surrounding air, input fluctuations of the pump and signal pulses, and lastly quantum noise in the form of amplified optical parametric fluorescence.

While the environmental influences can be greatly reduced by the design of the laser hardware – which we will discuss in more detail in section 2.2.2 –, the prevention of parametric fluorescence and the damping of input fluctuations can be achieved by appropriate design of the parametric amplifier itself. We will therefore use this section to look at the specific influence of input fluctuations on the stability of output energy and spectrum of the signal pulses, and briefly discuss optical parametric fluorescence and strategies for its mitigation.

Energy Stability

In our investigation of the gain regimes of OPAs in section 2.1.2, we found that at saturated gain, back-conversion of idler and signal photons to the pump wavelength counteracts the further amplification of the signal beam. It is possible to find a crystal length where the two interactions are balanced, such that fluctuations of the input intensities are damped and a stable signal intensity is emitted from the OPA [170–172].

As an idealised example using spatially and temporally flat input pulses, 2.5 shows the variation of the signal energy as a consequence of variations of the initial pump and signal intensities, with each having a respective relative peak-to-peak variation of 20 %. In a) and b) it can be seen that variations of the initial pump intensity can result in larger overall fluctuations than those of the initial seed intensity (especially in the exponential gain regime), but both kinds of input fluctuations can be almost completely suppressed when the amplifier is operated in saturation. When both beams have independent fluctuations, such an effective suppression of noise transfer from the input to the output of the amplifier is not possible, since a perfect balance between amplification and back-conversion cannot be achieved anymore. This behaviour is illustrated in figure 2.5 c), where we can also see that, independent of the pump fluctuation, a decrease in the relative fluctuations of the signal beam is possible when the amplification is pushed into the back-conversion regime.

However, when a single pump laser system is used to provide both the pump and seed pulses, the input fluctuations of the two pulses are strongly correlated, i.e., if one pulse has an above-average intensity, the other pulse tends to do so as well, and vice

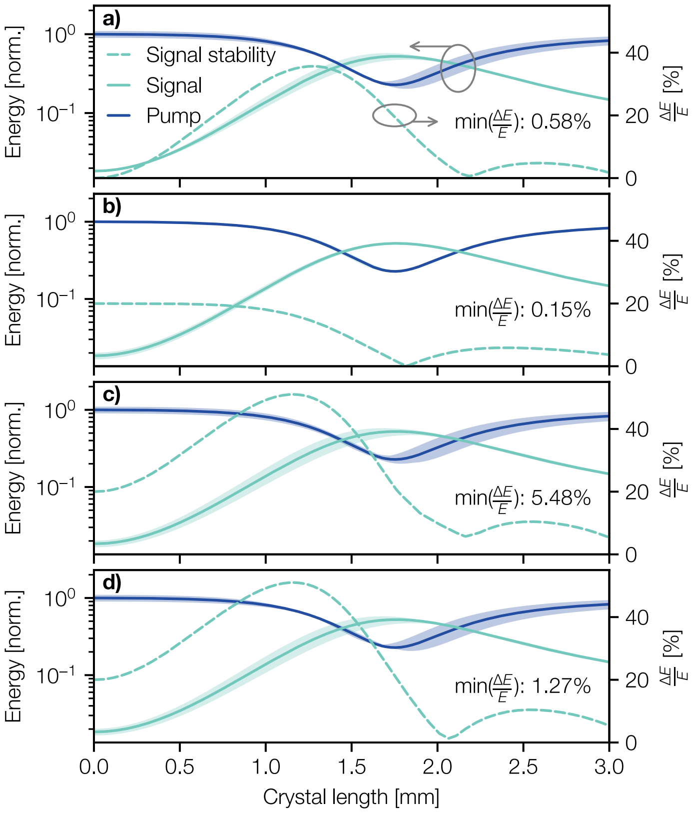

Figure 2.5 – Numerically simulated evolution of the signal pulse energy for variations in the initial pump and signal energies for idealised spatially and temporally flattop pulses. $\frac{\Delta E}{E}$ denotes the peak-to-peak variation of the signal energy normalized to the mean energy, and the shaded areas illustrate this relative peak-to-peak variation around the respective pulses. In a) the initial pump intensity was varied by ±10%, in b) only the initial seed intensity was varied, and in c) both, pump and seed energy were varied, assuming uncorrelated fluctuations of both. In d) also both input intensities were varied, but assuming a mutual source such that fluctuations are correlated. The pulse energy in all plots is normalised to the initial mean pump energy.

versa. In such a scenario (shown in Fig. 2.5 c)), the resulting output fluctuations again resemble cases a) and b) and the input fluctuations can be suppressed much more effectively than when the fluctuations are not correlated. It can therefore be concluded that the use of a mutual driver for pump and seed generation is highly advantageous for the energy stability of parametric amplifiers.

For realistic OPCPA systems, it should be noted that the pump and seed pulses can of course not have the same wavelength, so in order to use a mutual source of pump and signal, at least one of the pulses needs to be subjected to some sort of wavelength conversion scheme. Since such processes are also intensity dependent, the noise characteristics can be modified so that the fluctuations at the input of the OPA do not have the same amplitude. If one of the pulses has significantly larger fluctuations than the other, the resulting noise suppression converges back to cases a) or b) and the input fluctuations can be suppressed.

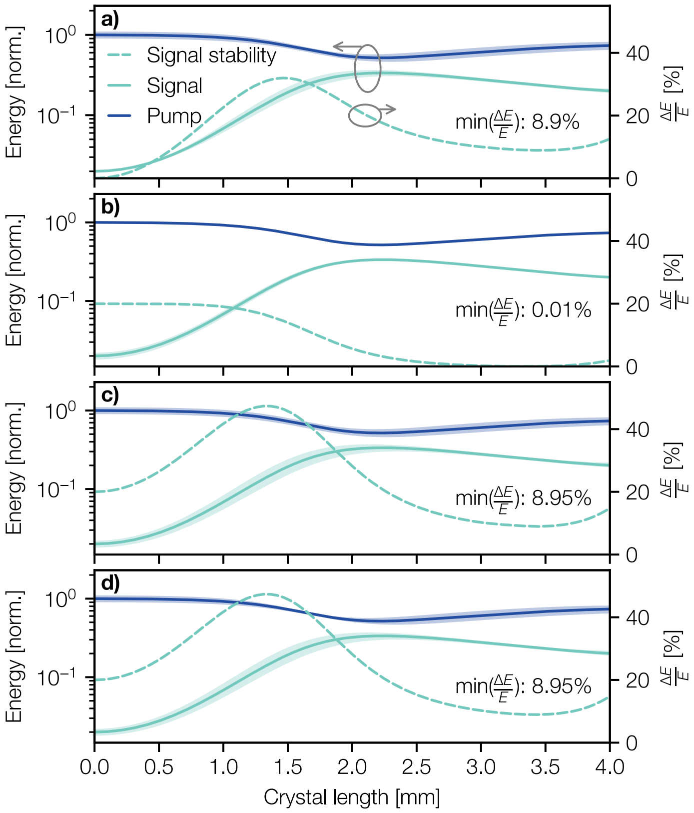

Figure 2.6 – Equivalent of figure 2.5, using spatially and temporally Gaussian intensity profiles of pump and signal.

Since the evolution of the signal energy strongly depends on the initial intensity of the pump and seed pulses, the degree of saturation can vary locally within the three-dimensional intensity profile, if the pulses do not correspond to the idealised flattop profiles used in figure 2.5. This also has a strong influence on the transfer of input fluctuations to the output, and the behaviour is quite different for Gaussian pump and seed intensity profiles, as shown in figure 2.6.

We see that the transfer of pump fluctuations to the output can no longer be suppressed, and these pump fluctuations determine the overall stability in OPAs where both, pump and seed intensities fluctuate. The advantage of using a mutual source laser for pump and seed pulses is largely diminished and a highly stable pump beam must be provided in order to have a stable OPA output.

Although the consequences of saturation on the spatio-temporal beam properties will be discussed in detail in section 2.1.6, we should mention here, that the locally varying degree of saturation present in amplifiers using Gaussian pulse profiles, also leads to a degradation of the spatio-temporal beam quality of the signal pulses.

Spectral Stability

The chirp of the seed pulses has a direct influence on the stability of the spectral properties of an OPCPA. Two key parameters that are relevant for the application as a seed laser, are the center wavelength and the spectral bandwidth, which defines the compressed pulse duration of the signal pulses.

The central wavelength is particularly sensitive to the relative timing of the pump and signal pulses, as changes in timing cause the temporal peak of the pump intensity to overlap with different spectral components of the seed. The sensitivity of the center wavelength to timing can be minimised by using longer pump pulses and strongly chirped seed pulses so that any given timing variation is small compared to the seed duration. However, to achieve an intensity that is sufficient for efficient, saturated amplification in low energy μJ-level OPCPA systems, it is necessary to use sub-picosecond pulses, which requires femtosecond-level synchronisation between the pump and seed pulses.
If separate laser systems are used for pump and seed generation, such synchronisation would have to be done electronically, which is difficult to achieve. The few femtosecond synchronisation required for stable operation of an OPCPA with sub-ps pump pulses is possible [173], but with considerable technical effort. A much more robust approach would again be to use a single drive laser to generating of both pulses, which are then passively synchronised [174]. Even with such a laser architecture, maintaining synchronisation at a femtosecond-level is difficult and a mechanically robust laser setup that passively minimises perturbations to the timing of the pump and signal pulses is therefore important.

Bandwidth stability is primarily determined by the stability of the pulse durations of pump and signal, and the relative gain that different spectral components experience during the amplification. Since changes in timing can be viewed as changes to the group delay and thus the first-order temporal phase of signal and pump, minimising timing perturbations within an OPA also minimises higher-order phase fluctuations, that would influence the pulse duration of signal and pump and thus have a direct effect on the amplified bandwidth.

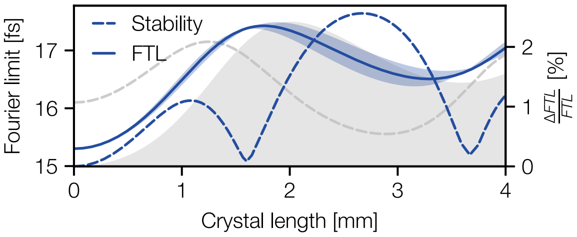

Figure 2.7 – The Fourier limit (solid line) as function of crystal length in a saturated collinear OPCPA, as well as its stability (dashed line) for correlated fluctuations of the pump and signal intensity, similar to figure 2.6. The grey shaded area and line indicate the qualitative evolution of the corresponding signal energy as a reference.

Thus, if the timing of signal and pump pulses is well controlled, the remaining contribution is the gain experienced by different spectral components, which – especially in saturated OPCPA and with Gaussian pump pulses – can lead to a coupling of the pump intensity and the amplified bandwidth, which is illustrated in figure 2.7. Note that the degree of saturation that minimises the energy stability is not the same as the degree of saturation that would minimize fluctuations of the spectral bandwidth. While the influence of the intensity fluctuations on the signal energy is greater than on the bandwidth, the coupling still needs to be considered when optimising of the degree of saturation.

Optical Parametric Fluorescence (OPF)

The high gain of parametric amplifiers allows to amplify phase matched photons from vacuum fluctuations resulting in the phenomenon of optical parametric fluorescence [175, 176]. The quantized, random nature of vacuum fluctuation leads to high relative fluctuations of initial photon numbers, which are further amplified by the exponential gain of the parametric amplifier, resulting in a noisy output of the amplifier. In particular in saturated OPAs, where the signal pulse experiences only linear gain or is even back converted, the exponential gain of the noise photons can result a degradation of the signal-to-noise ratio of the amplifier output [177]. Practically, a poor signal-to-noise ratio has two consequences for the amplifier performance: 1) the fluctuating photon numbers of the noise lead to a fluctuation of the total energy emitted from the amplifier [175, 178] and 2) the amplified OPF forms an incoherent and therefore uncompressible background of noise photons that degrades of the temporal contrast of the laser pulse [175–177], similar to amplified spontaneous emission in conventional laser systems.

Of course, these consequences can only become relevant if the simultaneous amplification of OPF and signal-photons is possible at all, and if the OPF experiences substantial gain. However, the simultaneous amplification can be prevented by ensuring that the entire pump pulse can interact with phase matched seed photons. Since the initial number of seed photons will always be higher than the number of noise photons, the seed will experience a higher gain than the noise, resulting in a suppression of its amplification. In practice, this is achieved by matching the dimensions of the signal pulse in space and time to those of the pump. As discussed in section 2.1.3, temporal matching of pump and signal pulses in OPCPA can lead to a narrowing of the of the signal bandwidth, which may not be desired. Another method to limit the gain of the OPF is therefore to limit the overall gain of the amplifier. In order to still achieve a certain output energy, the total gain can be distributed over several amplification stages with high seed energy and a gain below 10^3 [176], which also contributes to an increase of efficiency and bandwidth of the OPCPA system [168]. Furthermore, the random nature of the OPF background leads to strong phase fluctuations and spatial frequencies that result in different propagation characteristics of the noise and signal beams. Therefore, a large fraction of the noise can be eliminated after amplification by spatially filtering the amplifier output.

We can thus conclude that if the OPF content in the amplifier output is limited by matching the dimensions of the pulses and maintaining a low gain, fluctuations of the input pulses to the OPCPA system remain the main source of output noise of the amplifier system besides environmental drifts. Furthermore, it is highly advantageous for stable OPCPA to use spatially and temporally flat input pulses instead of profiles with locally varying intensity, and to use a mutual drive laser for the generation of signal and pump pulses. If spatially and temporally flat pulses are not available, output fluctuations will be dominated by fluctuations of the pump intensity. As an additional benefit, spatio-temporally flat pump pulses allow for higher efficiency of the amplification [179].

2.1.6 Angular and Spatial Dispersion in OPCPA

As discussed in chapter 1, spatio-spectral couplings can have detrimental effects on the properties of the electron bubble driven by a given laser pulse and thus have a negative influence on the quality of the accelerated electrons. While all spatio-spectral couplings have a negative effect on the peak intensity of a laser pulse, in particular deformations of the laser pulse that break a radial symmetry, such as angular and spatial dispersion, can lead to an asymmetry of the plasma bubble and therefore to unwanted steering of the accelerated electrons.

In particular the non-collinear phase-matching geometry of OPCPA is inherently prone to generation of spatial and angular dispersion in the amplified signal pulse, which limits its applicability for the application in particle acceleration. The two main causes of this inherent tendency are the spatio-temporal overlap between the pump and seed pulses that may introduce a spatial chirp in the amplifier crystal [116], and unoptimised phase-matching angles, which can lead to the generation of angular chirp [180].

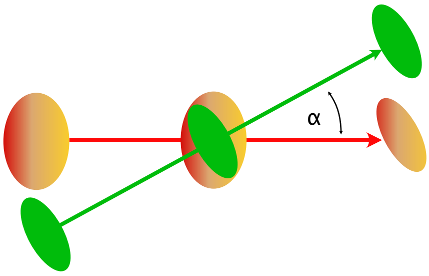

Figure 2.8 – Depiction of the introduction of spatial chirp and pulse front tilt in non-collinear parametric amplifiers due to the spatio-temporal overlap of pump and signal pulses and subsequent locally varying gain. The pump is depicted in green, while the chirped seed is shown in red/orange.

Figure 2.8, illustrates the spatial overlap between pump and chirped seed pulses that leads to a spatially and temporally selective amplification of the signal. As a result, the wavelengths that experience the highest gain vary over the spatial coordinate of the seed, resulting in a shift of the center wavelength in the amplified beam. In addition, the chirped pulses have a pulse front tilt corresponding to the non-collinear angle, which disappears when the pulses are compressed. The remaining spatial chirp, however, can be converted to angular chirp by further propagation or by focusing the beam, which then again leads to a pulse front tilt. The spatially and spectrally selective amplification can be mitigated to some extent by adjusting the spatial and temporal extent of the pump pulses, as well as the temporal chirp of the seed, so that the gain variations across the seed pulse are minimized [116]. To completely eliminate this effect, the pulse fronts of pump and signal must be matched in the amplifier, which can be done by introducing angular dispersion in the pump beam, e.g. by transmission through a prism or grating [181, 182].

In addition, the phase matching conditions themselves can lead to an angularly selective amplification of spectral components in the seed, resulting in an angular chirp of the amplified seed [180]. This is illustrated in figure 2.9, where the angularly and spectrally resolved phase-matching efficiency in LBO is shown for three different phase matching angles. If the angle is not ideal, the highest phase matching efficiency is achieved at different non-collinear angles α for different wavelengths, effectively resulting in angular dispersion of the amplified pulses. Optimising the phase matching angle can only minimize the angular dispersion over a limited spectral range and for spectral components below approximately 800 nm – to where the desired seed

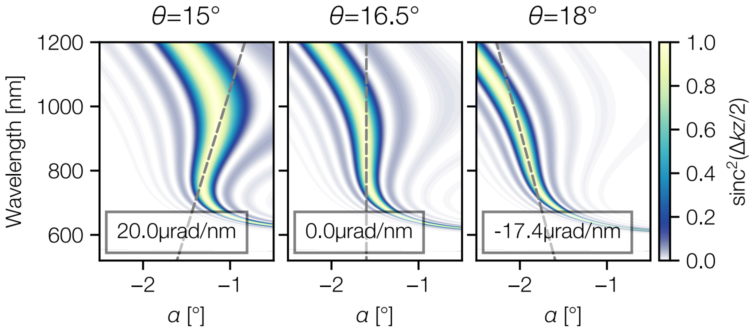

Figure 2.9 – Phase matching conditions in non-collinear OPA with optimised phase matching angle (center pane) and misaligned phase matching angles by -1.5° and +1.5°. The dashed lines are a linear fit to the maximal phase matching efficiency and thus corresponds to the linear components of the angular chirp imprinted on the signal. The respective slopes are shown in the panels. The curves are calculated for a 515 nm pump beam and the XY-plane of a 2 mm long LBO-crystal.

spectrum for Ti:sapphire amplifiers extends –, a small amount angular dispersion is present regardless of the phase matching angle. To make things more complicated, the residual angular dispersion is not purely linear, making it difficult to compensate in later stages of the amplification chain.

Both of these effects can be mitigated, but add complexity of the OPCPA setup, which is in contrast to the principle of maximising system reliability by minimising complexity and number of components. As an alternative, it may therefore be useful to consider collinear phase matching, which has neither of the problems described in this section.

2.2 The Malcolm Laser System

Malcolm is an OPCPA based seed laser for the high energy amplifiers of a Ti:sapphire based LWFA drive laser. Such amplifiers require a central wavelength of 800 nm, a pulse energy of $> 50\,\mu$J and a bandwidth corresponding to a Fourier transform limited pulse duration of 20-30 fs. These specifications were for Malcolm to replace the existing Ti:sapphire-based frontend of the Angus laser system (see section 1.2). However, these parameters are typical for Ti:sapphire systems, and thus Malcolm should also be suitable for other Ti:sapphire systems, such as kaldera.

For the Ti:sapphire laser to optimally meet the requirements of the LWFA, already the frontend must already provide a high stability and spatio-temporal pulse quality, as these properties are largely determined by the seed pulse. In this section we will present the optical design of the laser that allows to meet these requirements, followed by an overview of the mechanical hardware that was designed to ensure stable environmental conditions around the beampath. Finally, we will give a brief overview of the general performance, before taking a closer look at the two most important characteristics – beam quality and long term stability – in the following sections.

2.2.1 Optical Design

As derived in section 2.1.5, a mutual source for the pump and seed pulses of parametric amplifiers is highly desirable for the overall stability of the system and this defined the primary architecture of the Malcolm laser system: A white-light seeded OPA. White-light seeding allows a single ultrafast laser system to be used for both pump and seed pulse generation.

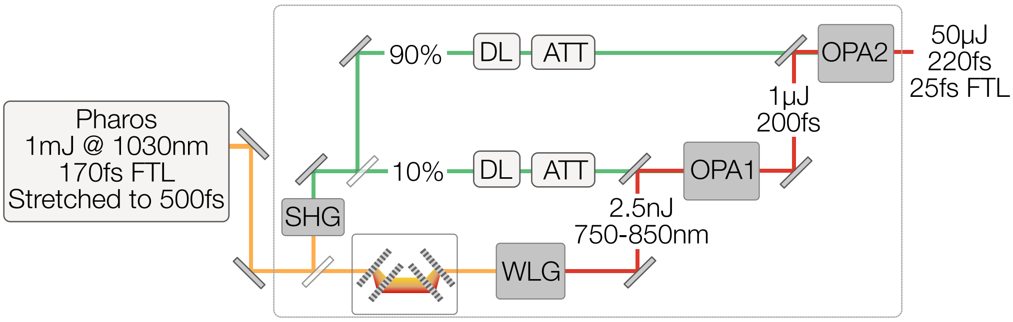

Figure 2.10 – Optical layout of the OPCPA frontend. DL: Delay line, ATT: Variable attenuator

Drive Laser

The selection of a suitable pump laser for such an OPCPA system is an important first step in its development, but it is constrained several desired performance characteristics. A short pulse duration < 500 fs is advantageous for stable white light generation [183], and commercial laser systems supporting such pulse durations are widely available at a wavelength of 1030 nm. The required seed energy for the Ti:sapphire amplifiers (50 μJ) and a typical overall OPA efficiency of $E_{800\text{nm}}/E_{1030\text{nm}} \approx$ 5-10 % gives a required pulse energy of around 1 mJ. In addition, high pulse-to-pulse stability and long term reliability are needed to minimise the input fluctuations to the OPA. At the time of the start of the development of Malcolm, the commercial laser that best fulfilled these requirements was the Pharos laser system from Light Conversion. Pharos is an industrial Yb:doped laser system consisting of a Kerr-lens modelocked oscillator and a regenerative amplifier operating at up to 6 kHz for an output energy of 1 mJ. The compressed pulse duration of Pharos is 170 fs and the rms pulse-to-pulse energy stability of Pharos has been measured to be 0.3% over 30 s. To drive our OPCPA system, we operate the laser at a repetition rate of 1 kHz.

Seed Generation

White light generation (WLG) [184] in bulk material driven at 1030 nm allows to generate a supercontinuum with a – compared to other white light sources – relatively high energy of multiple nJ contained in the 750-850 nm range. This is sufficient for seeding OPAs while suppressing the amplification of parametric fluorescence and thus enabling a high signal-to-noise ratio [176]. Furthermore, bulk WLG driven by 1030 nm-pulses can be tuned to have high energy stability of the spectral content around 800 nm due to a suppression of input fluctuations in the filamentation process [183, 185, 186]. In the WLG setup of MALCOLM, approximately 1 μJ of the 1030 nm-pulse is compressed and focused into a YAG crystal for generating the seed of the parametric amplifiers. YAG was chosen for its robustness and proven long term reliability. The available seed energy in the relevant spectral range is approximately 2.5 nJ.

Further details on the WLG setup and in particular its optimisation for spectral stability of the OPCPA stages can be found in [187] and [188].

Pump Generation

The second harmonic of Pharos at 515 nm is suitable for pumping 800 nm amplifiers as broadband OPA phase matching of these wavelengths is possible in various nonlinear crystals. A clear disadvantage of all commercially available ultrafast laser systems in the ≈1 mJ-pulse energy is their Gaussian beam profile, which is defined by the internal design of those lasers. As discussed in section 2.1.5, a stable pump intensity is particularly important with such a beam profile.

For reasons that we will discuss later, the pump duration for the OPAs was set to be 500 fs, which means that a slightly stretched output of the Pharos was used to drive the SHG. To limit the long-term degradation of optics, the peak intensity is kept below 50 GW cm^{-2} on all crystals throughout the laser – i.e. roughly a factor of two below the laser induced damage threshold of the anti-reflection coatings.

The SHG is done in a BBO crystal that has been cut for Type I SHG phase matching ($\theta = 23.4°$) and reaches a conversion efficiency of 44 %, resulting in an available pump energy of approximately 440 μJ. The length of the crystal has been chosen to operate in the back-conversion regime, where intensity fluctuations of the input pulses are suppressed, thus providing the highest possible pump stability in the subsequent amplifiers.

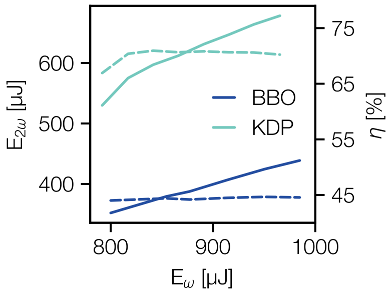

Figure 2.11 – Measured SHG conversion efficiency in BBO and KDP. The solid line shows the pulse energy of the second harmonic, while the dashed line represents the conversion efficiency.

The conversion efficiency of the SHG is primarily limited by the bandwidth of the 1030 nm pulses, which is large compared to the phase matching bandwidth of the BBO. As an alternative material that would support the conversion of the full spectrum, KDP (Type I, θ=41°, ϕ=90°) was considered and indeed a conversion efficiency of up to 71% has been measured using the same beam parameters of the fundamental as with the BBO crystal. The high nonlinear refractive index n_2 of KDP and the required crystal length of approximately 7 mm led to substantial Kerr-lensing of the 515 nm beam and consequently poor pump beam quality in the parametric amplifiers. As is visible in figure 2.11, the SHG is strongly saturated so that some optimisation of the crystal length is possible to avoid Kerr-lensing. Nevertheless, BBO was chosen instead of KDP because the strong hygroscopicity of KDP would lead to a long-term degradation of the SHG energy.

The rms energy stability of the SHG output with the BBO crystal was measured to be 0.12% over 30 s, confirming of the suppression of input fluctuations by the saturated conversion of the SHG.

Amplifier Layout

To maintain a simple – and therefore more reliable – optical layout, while at the same time eliminating sources of angular dispersion, the collinear phase matching geometry was chosen over the non-collinear one. As discussed in section 2.1.6, this eliminates the need for pulse front matching and thus output pulses free of angular or spatial dispersion can be achieved with a greatly simplified optical design.

Among commercially available nonlinear crystals, only BBO and LBO [189, 190] have a sufficient phase matching bandwidth to support the amplification of sub-30 fs pulses. Of these two, LBO was chosen due to its higher damage threshold, smaller spatial walk-off angle and, most importantly, its roughly 20 % larger phase matching bandwidth at the same OPA gain, which corresponds to 65 nm FWHM for a 2 mm long crystal. The corresponding phase matching efficiency as a function of wavelength and non-collinear angle α is shown in figure 2.12. The slight disadvantage over BBO in terms of its susceptibility to environmental influences (e.g. temperature sensitive phase matching and hygroscopicity), has not been observed to cause problems when temperature control and appropriate housing of the laser system are provided.

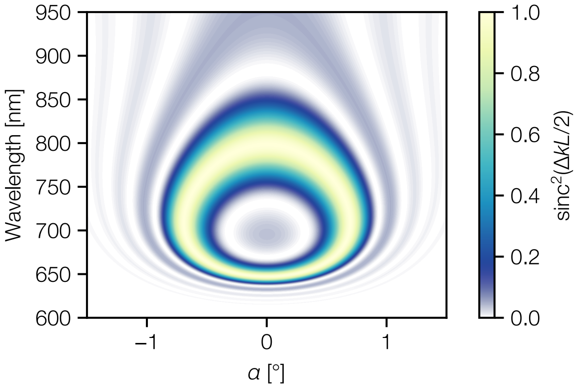

Figure 2.12 – DFG phase matching efficiency LBO as a function of the wavelength and non-collinear angle α. The pump has a wavelength of 515 nm, the phase matching angle is $\theta = 11.7°$ and the crystal length is 2 mm.

The total gain of the OPA system that is required to achieve the output energy of >50 μJ, is 50μJ/2.5 nJ= 2×10^4. In order to avoid the amplification of optical parametric fluorescence and stay below a single stage gain of $10^2 - 10^3$, the amplification is split into two amplification stages with the first stage having a gain of approximately 600 and the second stage having gain of 33. The low gain of the second stage allows for fast saturation and therefore improved extraction efficiency of the pump energy and improved stability.

The crystal lengths of the SHG and the two OPA stages were numerically optimised using (3+1)D start-to-end simulations with chi3D [165], that included the SHG, the OPAs, and the beam transport between the SHG and OPAs. The goal of the optimisation was to minimize the influence of intensity fluctuations of the 1030 nm drive pulses on the stability of the energy and bandwidth of the OPA output, while meeting the minimum performance requirements in terms of output energy and bandwidth, and minimising the absolute deviation of the spectrally integrated beam profile from a Gaussian. The resulting crystal lengths were then used as a starting point for tests tests with slightly varied crystal lengths in the actual laser setup and finally lengths within a few hundred μm of the simulated optima were used.

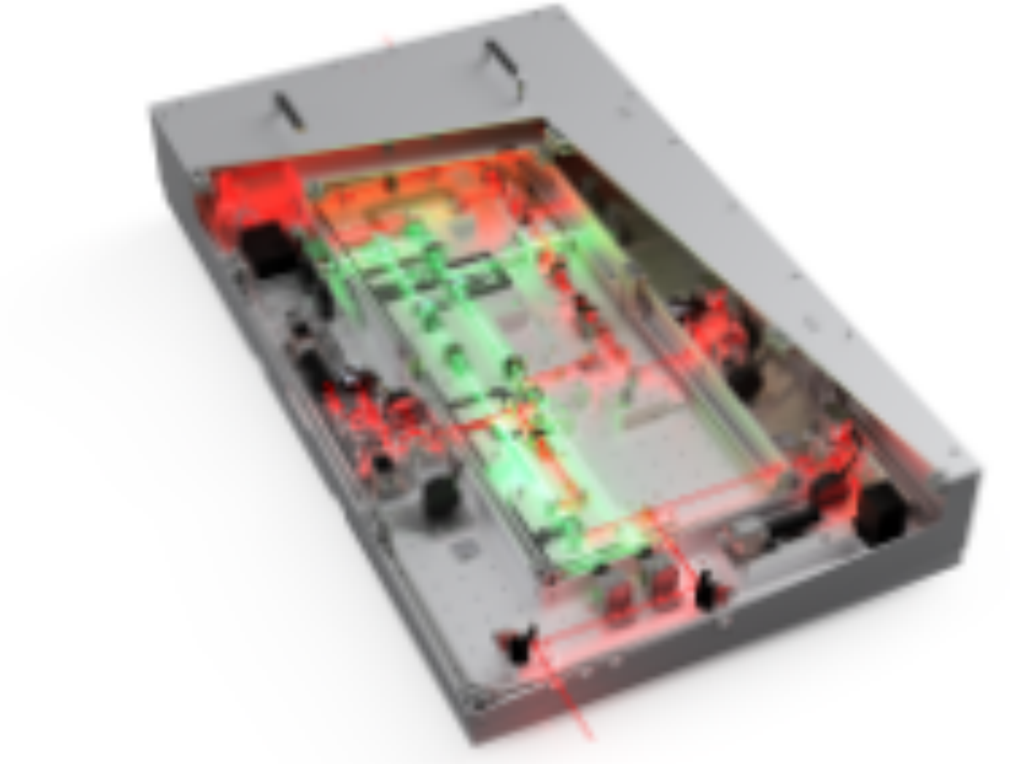

Figure 2.13 – Rendering of the mechanical setup of the MALCOLM laser system. Parts of the outer and inner housing are cut out for improved visibility of sub components.

2.2.2 Mechanical Design & Implementation

The optical design of the laser system with beam and crystal parameters described above was first tested in a simple breadboard prototype. The desired beam quality and performance was already achieved in this prototype, but for permanent operation and integration into the amplification chain of the high energy Ti:sapphire laser systems, a more advanced housing and mechanical setup was designed, to further improve the stability and reliability.

The mechanical design of the laser system aims to provide a compact and rigid environment that allows to operate the laser independent of external disturbances such as mechanical vibrations or temperature changes. At the same time, a certain degree of flexibility must be maintained to allow for future upgrades of subcomponents of the laser system.
To ensure thermal and mechanical stability, an aluminium plate, that can be temperature-controlled, was chosen as the base. To thermally isolate the base plate from the optical table, a layer of PTFE is placed between them. The components on top of the base plate are housed in a two layer, sheet metal enclosure, the inner compartment of which

contains the OPCPA system itself (see figure 2.13). All diagnostic devices and potential heat sources are contained in the outer compartment to minimize temperature gradients within the amplifier section that could cause convection and thus disturb the beam. These heat sources include electronic devices and dumps for all waste beams, such as the idler or residual pump after the OPCPA stages. Diagnostic devices that generate significant heat – such as cameras – are thermally isolated from the breadboard and water cooled to efficiently dissipate their heat and prevent a heating of the lasers mechanics.

The laser system itself is divided into modules (see figure 2.14), each of which contain a sub-system of the laser – incoupling of the 1030 nm-beam, SHG, white-light generation, and the two OPCPA modules. Each module consists of an aluminium base with pre-milled mounting locations for optics mounts and actuators to maximise mechanical rigidity by maintaining a low beam height and short optical path lengths. The modules are interchangeable to allow for future upgrades of individual sub-systems.

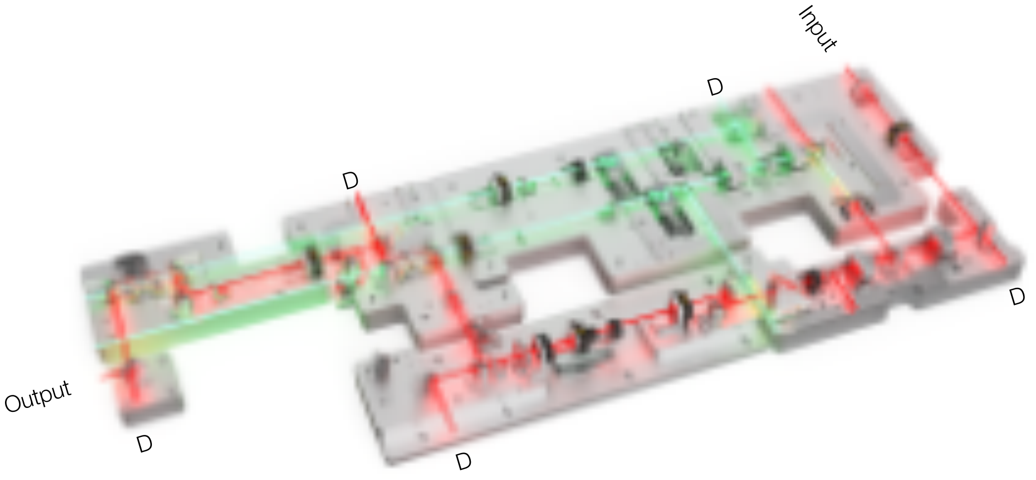

Figure 2.14 – Modular main amplification and frequency conversion section of the MALCOLM laser system. Auxilliary beams marked "D" are used for diagnostic purposes.

For each of the sub-systems, a dedicated diagnostic module is located n the outer compartment, allowing to monitor relevant beam parameters such as beam position, pointing, energy and spectrum at all stages of the laser. As a result, the sources of problems during operation can be quickly pinpointed, minimizing maintenance time.

The optical path resembles a Mach-Zehnder interferometer (see also figure 2.10), which minimizes the optical path lengths over which the seed and pump pulses propagate independently and thus reduces relative fluctuations between the two. In addition, the Mach-Zehnder setup results in parallel propagation of the beams, so that thermal expansion of the breadboard results in equal path length differences in the pump and seed arms. In addition, both arms have an equal number of reflections, so that fluctuations in the input pointing result in minimal relative beam movement of the beams in OPA crystals. The input IR beam is additionally controlled by a high-bandwidth piezo-actuator-based beam stabilisation.

The relative delay between the pump and signal pulses in the OPA stages can be adjusted with motorized delay lines in the respective pump beams. Motorized rotation stages allow adjustment of the phase matching angle of the OPA and SHG crystals, and attenuators consisting of a $\lambda/2$ waveplate and thin film polarizer allow for fine tuning of the pump energy in the respective amplifier stages.

2.2.3 Performance

The MALCOLM laser system typically delivers approximately $50\,\mu$J pulses at a repetition rate of 1 kHz, although up to $60.5\,\mu$J have been achieved by sacrificing spectral bandwidth. The typical rms shot-to-shot energy stability is around 0.15 %, measured with a photodiode-based, calibrated energy head (Ophir, PD-10C). However, due to the inherent noise of the photodiode based measurement[1], this measured value of the rms stability is largely dominated by measurement noise and the value should be considered an upper limit of the true stability.

A more accurate estimate of the stability can be made by using the integrated counts of 1D or 2D detectors such as spectrometers or cameras, where the noise of individual pixels is averaged, reducing the overall noise level. Using single shot spectra recorded at 1 kHz, we were indeed able to measure a fluctuation of the integrated counts of 0.07 % rms (see figure 2.15), which limits the true value of the energy stability to the sub-permille-level. This could be confirmed using the integrated counts of single shot camera images (0.08 % rms fluctuation over 1 minute), which however could only be recorded at a repetition rate of 10 Hz.

The rms stability of the driving Pharos laser system was measured to be 0.3 % rms, demonstrating the effectiveness of reducing input fluctuations through strong saturation of the SHG and OPCPA stages. The pulse energy available as a seed for the second OPA stage is around $1.5\,\mu$J with a typical rms stability of approximately 0.2 %.

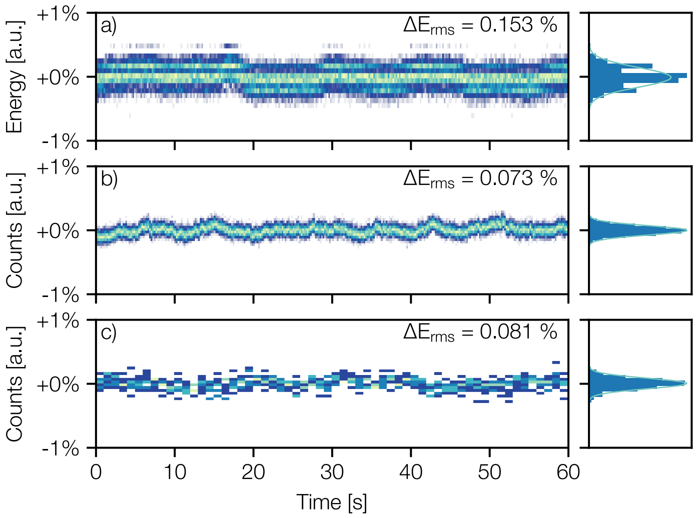

Figure 2.15 – Short term energy stability of the OPCPA. a) shows a measurement done with a photodiode-based calibrated energy head. b) shows a measurement using the integrated counts of single shot spectra sampled at 1 kHz, and c) shows a measurement using the integrated counts of single shot camera images, sampled at 10 Hz. The measurement done with the energy head is dominated by the repetability and noise of the measurement system itself, for more details see footnote [1]. The light blue line in the histograms indicate a Gaussian fit to the respective energy distribution. The three measurements were not done simultaneously.

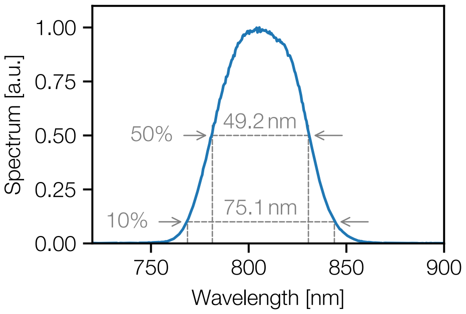

Figure 2.16 – Typical spectrum of the OPCPA output. The FWHM bandwidth is 45 nm and the spectrum supports a Fourier limited pulse duration of 24.9 fs.

Spectrum

The spectrum of the laser is centered at approximately 800 nm with a FWHM bandwidth of approximately 45 nm, supporting a Fourier limited pulse duration of 24.9 fs. The center wavelength is tunable from approximately 792 nm to 810 nm without sacrificing bandwidth. Beyond this range the spectrum is clipped due to the reflectivity curves of the dielectric mirrors used throughout the laser system. A typical output spectrum is shown in figure 2.16.

The spectrum is slightly narrowed in the last amplification stage, with the first OPA stage supporting a Fourier limit of approximately 18 fs.

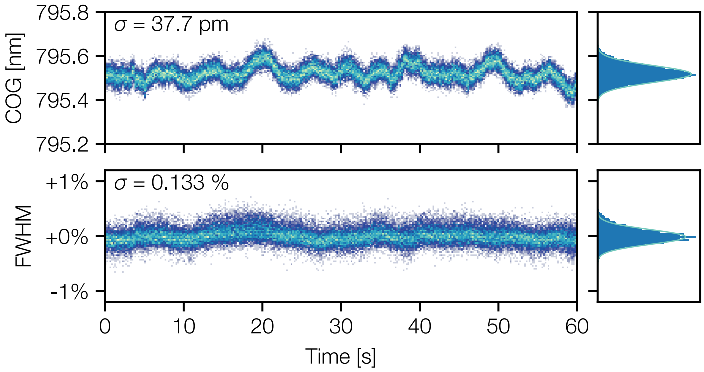

Figure 2.17 – Typical stability of the center of gravity wavelength as well as the FWHM bandwidth of the OPCPA output.

The stability of the center of gravity wavelength and FWHM bandwidth of the spectrum is shown in figure 2.17, indicating an rms stability of the center wavelength of less than 40 pm, and a stability of the FWHM bandwidth of 0.15 %. These stability measurements were made on the early breadboard prototype of the laser system, and in particular the center wavelength stability is strongly affected by airflow in the laser's beam path, which causes drifts on a timescale of a few seconds. This problem has been solved in the second, engineered version of the laser hardware, resulting in a short term wavelength stability of approximately 20 pm rms, which is also reflected in the long-term measurements that we will show in section 2.6. A thorough analysis of the spectral stability and the improvements to the laser hardware is be given by Thomas Hülsenbusch in [188].

---

[1] The noise level of the used Ophir PD-10C energy head is specified to be 0.25 %. Experimentally, we could however observe slight differences between individual energy heads of the same type, and depending on operating conditions, the measured noise levels ranged between 0.15-0.25 %. In any case, the stability values measured using the energy heads are strongly influenced by the repeatability and resolution of the energy heads and should be considered a mere upper limit of the actual value.

Compression and Temporal Contrast

As discussed in the introductory sections, saturation of the final amplifier stage can lead to suboptimal temporal pulse characteristics due to the accumulation of parametric phase and the formation of a pedestal of parametric fluorescence around the main peak. To check whether such a degradation is visible in MALCOLM, the output pulses were compressed using a chirped mirror compressor and a pair of fused silica wedges to fine-tune of the spectral phase. The total GDD added to the pulse by the dispersive mirrors and fused silica is -1590 fs^2.

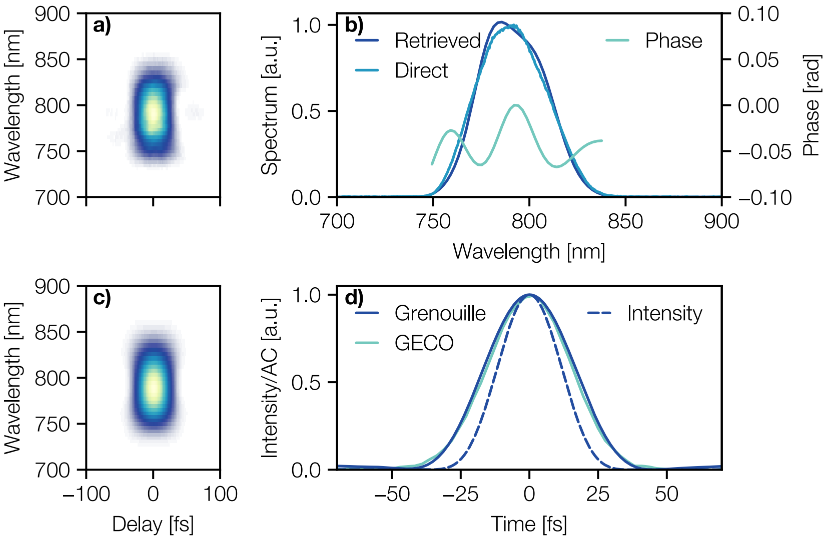

Figure 2.18 – Measurements of the pulse duration and spectral phase of the compressed OPCPA output. a) and c) show the measured and retrieved FROG traces. b) Shows the spectral phase and spectrum retrieved from the FROG measurement, as well as an direct measurement of the spectrum for reference. d) Shows the respective autocorrelation traces measured with FROG (Grenouille, SwampOptics) and a scanning intensity autocorrelator (GECO, Light Conversion), as well as the retrieved intensity profile from the FROG measurement.

The pulse duration and temporal shape were measured with an intensity autocorrelator and Grenouille, both of which indicate a 26 fs FWHM duration at a 25 fs Fourier limit. Only a small amount of symmetric higher order spectral phase is observed, which is attributed to the parametric phase resulting from the temporally symmetric depletion of the pump pulse.

The small amount of higher order phase does not lead to significant pre- or post-pulses, which was verified with Self-Referenced Spectral Interferometry (SRSI, Wizzler), which provides a higher dynamic range than the autocorrelation measurements shown above. The measured temporal profile in figure 2.19 shows the absence of significant side-peaks of the temporal profile of the pulse, with the relative intensity of the pulse dropping below the specified dynamic range of 40 dB within approximately 100 fs of the main peak.

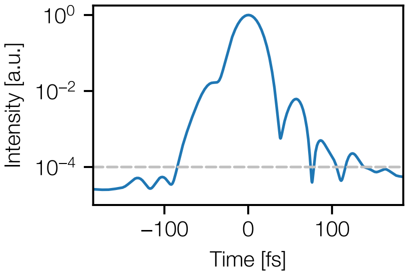

Figure 2.19 – Temporal contrast on a short term scale

The temporal contrast on a > 100 fs timescale was measured using a Tundra third-order autocorrelator. The pulse energy after compression with the chirped mirror compressor was 43 μJ, which is below Tundra's specified minimum input energy of 50μJ [191], resulting in a slightly reduced dynamic range of the measurement. Nevertheless, a dynamic range of nearly 10^{12} was achieved, which is sufficient to demonstrate the excellent temporal contrast of the OPCPA system and to verify that it fulfills the requirements as a seed laser.

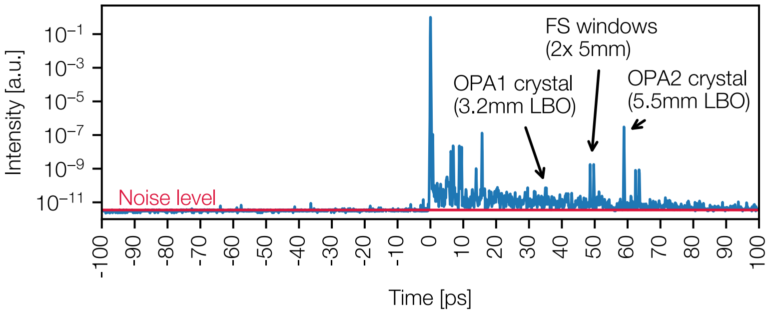

Figure 2.20 – Temporal contrast of the OPCPA frontend

A relative intensity $< 10^{-11}$ is reached only 500 fs before the arrival of the main pulse, while some post-pulses and a pedestal is observed after the main peak. This is consistent with the assumption that optical parametric fluorescence can only be amplified in the presence of pump intensity, which (with the FWHM pump duration of 500 fs) restricts the amplification to a few hundred fs window around the main pulse. The OPF-content of the pulses was measured to be $< 3.5 \cdot 10^{-6}$ by measuring the output energy of the OPA with a blocked seed, providing an upper bound for the relative OPF-content.

The post-pulses do not exceed a relative amplitude of 10^{-6} and most could be traced back to the plane-parallel optics such as amplifier crystals and windows used for dispersion tuning in the laser. The post pulse pedestal is attributed to multiple reflections in the plane-parallel optics.

The pulse duration and contrast measurements were done in the early prototype of the OPCPA system with a simplified mechanical setup, but since the optical setup is identical and all relevant optical components and beam properties are the same in the final engineered setup, the measurement is expected to be representative of the temporal contrast in the final, mechanically robust setup as well.

In the subsequent sections of the Ti:sapphire laser system, a degradation of the contrast is expected. Most importantly, a ps-pedestal is expected to form due to unavoidable surface imperfections in the stretcher optics, and spectral modulation and nonlinear couplings in the high energy amplifiers should result in a mirroring of post-pulses to pre-pulses [94]. To limit nonlinear coupling, the B-integral in these subsequent amplifiers must to be kept to a minimum.

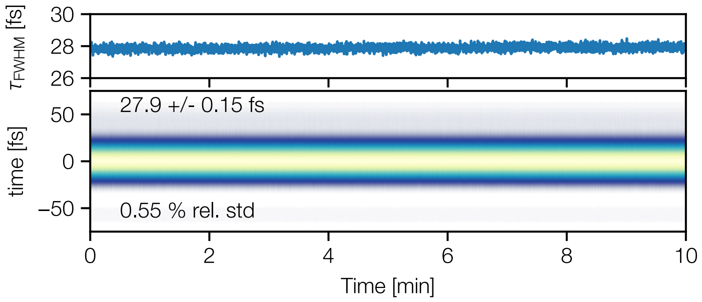

Figure 2.21 – Pulse duration stability measured with SRSI. The individual measurements are single shot taken at a 10 Hz measurement rate.

The stability of the pulse duration was measured to be around 0.5 % using single shot SRSI measurements. Since the Wizzler's typical repeatability of the reconstruction of the temporal profile from the SRSI trace is also around 0.5%, this value should be considered as an upper limit for the actual pulse duration stability. The relative bandwidth stability of 0.15 % mentioned above also suggests at potentially much higher pulse duration stability than what was measured. The stability measurement was done at a slightly different working point of the OPCPA system, resulting in an increased pulse duration of 27.9 fs compared to the previously discussed autocorrelation measurements. However, the difference in working point is not expected to affect the stability of the system.

Beam Quality

As a consequence of the strong saturation of OPA2 with a roughly Gaussian pump profile, a clear degradation of the beam profile is visible. Figure 2.22 shows the collimated and focused beam profiles after the OPCPA and a flattening of the beam profile due to back-conversion is clearly visible in the collimated beam. As we will show in section 2.3.3, a pristine Gaussian beam profile is recovered later on.

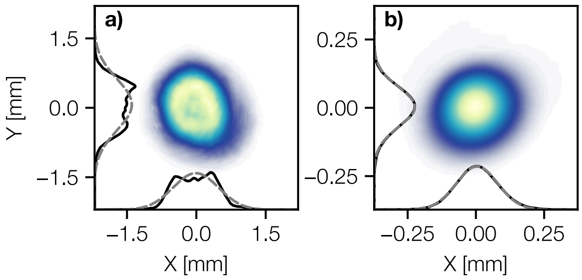

Figure 2.22 – Beam profiles in the collimated (a) and focused (b) beam. An f=500 mm achromatic lens was used for focusing the beam.

2.3 Spatio-Spectral Couplings in Saturated OPCPA

The results presented in this section have previously been published in [41]

At various points throughout our discussion of saturated OPCPA, we have seen suggestions that locally varying degrees of saturation in the spatio-temporal beam profiles of the seed pulses can lead to a degradation of the beam quality of the amplified pulses. This becomes evident also in the beam profiles shown in figure 2.22, and numerical investigations by Giree *et al.* have shown that these beam profile aberrations can vary across the spectrum [192]. Giree has shown that this can have a detrimental effect on the achievable Strehl ratio, and thus the peak intensity of the compressed and focused output of non-collinear OPCPAs, but the same concept should also apply to collinear OPCPA – especially in a system such as Malcolm, where strong saturation is used to ensure the highest possible output stability. In the following sections, we will take a detailed look at these aberrations first with the help of simulations and then with measurements of the Malcolm output using the Insight technique [193]. We will also show that the saturation results in the generation of distinct spatial frequencies in the beam that can filtered with only a small loss of energy.

2.3.1 Simulation of Beam Degradation in Saturated OPCPA

To understand the saturation dynamics in the second OPA stage, we modeled the stage using chi3D [165]. As inputs to the simulation, spatially and temporally Gaussian pump and seed pulses were used, which approximate the profiles measured in the laser. Otherwise, the pulse properties were the same as the ones as in the laser system described in section 2.2.1. The LBO was operated at a phase matching angle of $\theta = 11.8°$.

Figure 2.23 shows the evolution of the pulse energy (and its variation δE for a 1 % pump energy fluctuation) in the second amplifier stage, as well as the spectral dependence of the beam profile and wavefront in the plane of the birefringent walk-off at three snapshots along the propagation through the amplification crystal.

Since there is no visible effect of the birgefringent walk-off between the pump and the seed in LBO crystal and the beam remains symmetric with respect to the axis of propagation, the pulse properties can be considered rotationally symmetric for now, and the slices shown in the figure are indicative of the entire beam profile.

Figure 2.23 further shows, that the pulse energy stability improves only once the pulse energy starts to saturate. A crystal length where the tolerance towards pump fluctuations is optimal, is reached at 5.2 mm, i.e. at a value slightly beyond the working point with highest output energy [171]. The 5.2 mm crystal length was therefore chosen for OPA2.

While the pulse energy stability improves during the amplification, the beam profile degrades strongly and becomes wavelength dependent. At wavelengths near the center of the spectrum – which, due to its chirp, also corresponds to the temporal center of the pulse – the pump and seed intensities are highest, and the phase matching curve shows the highest relative conversion efficiency. Due to the combination of these factors, the central part of the spectrum reaches the back-conversion regime first. This back-conversion in the central high-intensity part of the pulse then leads to (i) a change in the beam profile, and (ii) the introduction a spatially varying parametric phase [194, 195]. In contrast to that, the edges of the pulse have less favorable conversion conditions, thus reach the back-conversion regime later during the amplification, and therefore maintain a higher beam quality until the end of the amplification.

Due to the coupling of the wavelength and temporal profile of the pulse, the parametric phase shift and the change of the beam profile lead to a wavelength dependent wavefront and beam profile of the pulse, that is inherent to saturated OPCPA with pulses that have a temporally varying intensity (such as e.g. Gaussian pulses).

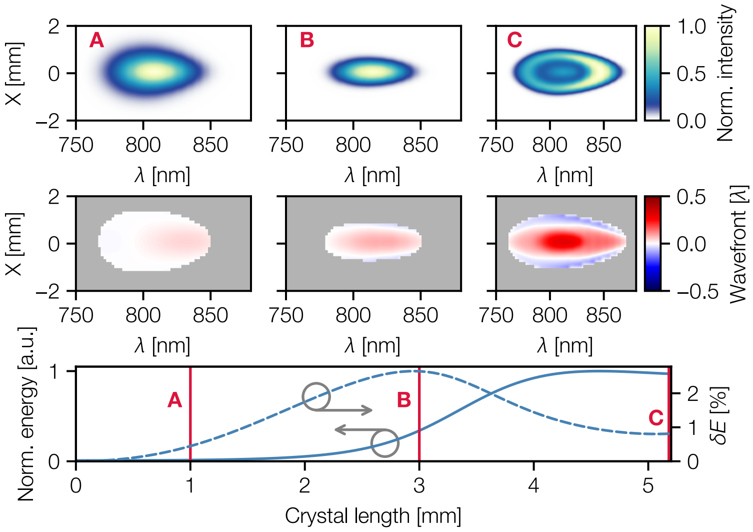

Figure 2.23 – Top row: snapshots of the spectrally dependent slices of the beam profile, middle: spectrally dependent slices of the wavefront error (limited to region with intensity larger than 10% of the peak intensity), bottom: the evolution of the seed energy (solid line) during propagation through the LBO crystal. To indicate the stability with respect to pump fluctuations, the relative variation in output energy (dashed line) is plotted on the right axis for a pump energy variation of 1%. A minimal variation of 0.8% (i.e. better than the pump stability) is reached at the exit of the crystal. The 5.2 mm crystal length, where the optimal pulse energy stability is reached, is also used as the working point for the OPCPA system. All results shown in this figure are simulated using chi3D.

From a Zernike analysis of the wavefront of the amplified pulses, it can be seenn that the wavefront distortion introduced by the saturation mostly has a rotational symmetry and can therefore be described by aberrations such as defocus and spherical aberration. This can be seen in figure 2.24, where the Zernike coefficients of the fully saturated wavefront are shown. This rotational symmetry of the aberrations is due to the collinear propagation of seed and pump pulses, and the resulting symmetry of the amplification process. The minor contribution of 4th order coma that is visible in figure 2.24 is attributed to the slight breaking of the symmetry due to the small spatial walkoff. The analysis of the Zernike composition of the wavefront was done using the tools described in [44, 196].

2.3.2 Measurement of STCs with Insight

The aberrations expected from the simulations of the previous sections were experimentally characterized using the Insight technique [193]. This method is based on

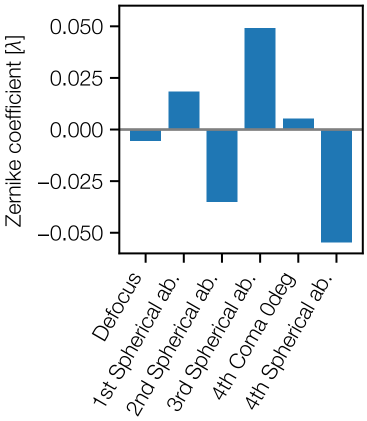

Figure 2.24 – Simulated amplitude of the Zernike polynomials of the spectrally integrated wavefront. Only values with an amplitude larger than $\lambda/200$ and up to the 66th polynomial are shown. The amplified pulse primarily features rotationally symmetric aberrations.

two dimensional Fourier spectroscopy combined with a phase retrieval approach to reconstruct the full spatio-spectral electric field of the laser pulse. The method allows to identify complex spatio-spectral couplings in both the intensity and phase profiles of the pulse, and is therefore ideally suited to investigate the previously described aberrations [197].

For the Insight measurements, the output surface of the OPA2 crystal was imaged with a 4f telescope consisting of two $f = 500\,\mathrm{mm}$ achromatic lenses. A third achromatic lens with a focal length of 200 mm in the image plane was then used to focus the beam into the measurement device.

The near-field (NF) beam profiles that were reconstructed using the INSIGHT technique, are shown in the top of figure 2.25 and agree with the simulated beam profiles in the bottom row. The reconstructed NF beam profile also agrees with the directly measured NF beam profile shown in figure 2.22, indicating that the residual error of the reconstruction is low. This agreement is also quantified by a 6.7 % rms deviation between the retrieved and measured in-focus (far-field, FF) intensity profiles.

The same features in the FF and NF profiles are visible when comparing the measured and simulated beams. The beam profile strongly deviates from a Gaussian profile near the center of the spectrum, resulting in characteristic side-lobes in the far-field, while the edges of the spectrum maintain a high beam quality. In the amplifier crystal (i.e. near the NF plane), the center of the pulse is depleted as a consequence of back-conversion, resulting in a dip in the beam profile. The spectrally integrated beam profile shows a flat top shape that is expected from the simulation. As expected from the collinear design of the OPA system, no spatial or angular dispersion is observed in

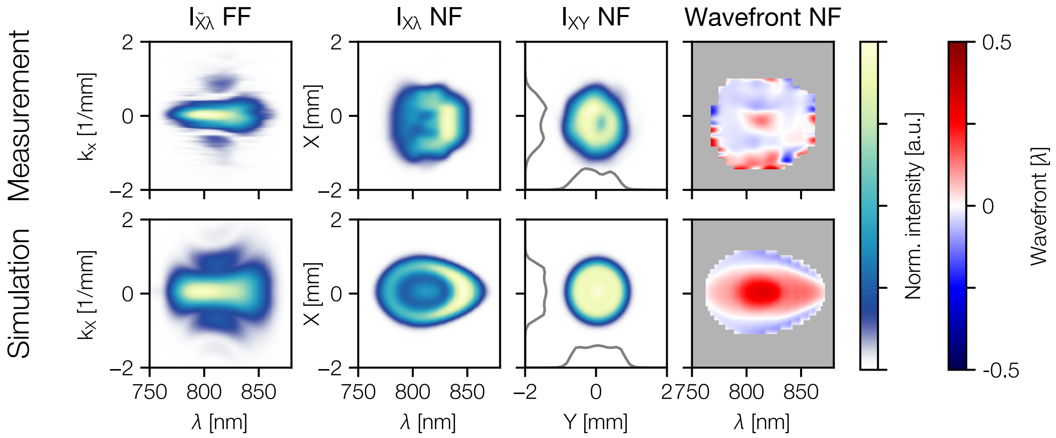

Figure 2.25 – Comparison of measured (top) and simulated (bottom) spectrally resolved beam profiles and wavefront. The top row shows the reconstructed spectrally resolved intensity profiles in the far-field (FF) and the near-field (NF), as well as the reconstructed beam profile of the NF beam imaged at the output surface of the OPA crystal. The last column shows the corresponding wavefront error in the near field as a function of wavelength (limited to region with intensity larger than 10% of peak intensity). The bottom row shows the corresponding profiles determined with the numerical simulations described in the previous section.

the beam. In the wavefront, a strong phase shift is visible in the regions of the pulse where back-conversion occurs, resulting in the expected radially symmetric wavefront aberrations. The discrepancy between the measured and simulated wavefronts is attributed to Kerr-lensing in the pump pulse, which leads to a sharper intensity peak than the Gaussian assumed in the simulation. This sharper peak leads to the more localized distortion of the wavefront visible in figure 2.25. For the same reason, the side lobes visible in figure 2.25 are more localised towards the center of the spectrum.

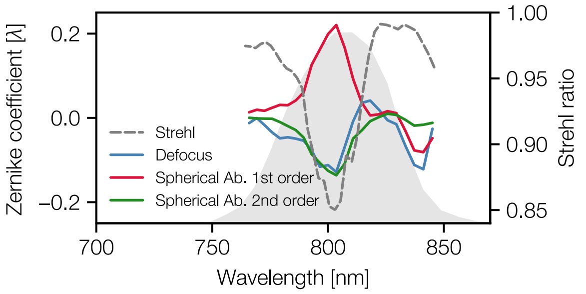

Figure 2.26 – Spectrally resolved magnitude of main aberrations, i.e. defocus and spherical aberration. The spectrally dependent aberrations result in a strong variation of the Strehl ratio across the spectrum.

Further examination of the Zernike coefficients corresponding to these aberrations reveals the strong spectral dependence of the amplitude of the aberration (see figure 2.26). This spectral dependence leads to a degradation of the Strehl ratio across the spectrum, resulting in a Strehl-ratio of 0.85 at 803 nm, while the edges of the spectrum have a high wavefront quality with a Strehl-ratio of above 0.98.

When calculating the full spatio-spectral Strehl ratio S_{full} as it was suggested by Giree *et al.* [192], one can see that the wavefront aberrations lead to a reduction in achievable peak intensity to 67 % compared to an aberration-free pulse. In contrast to the spectrally averaged Strehl ratio $S_{\langle\omega\rangle}$, S_{full} is calculated by comparing the achievable intensity of the full spatio-spectral electric field of the distorted pulse with that of the spectrally and spatially averaged field, which corresponds to a pulse with a clean phase. In this way, spectrally dependent phase aberrations such as chromatic aberration are accounted for in the calculation of the Strehl ratio, while they are omitted when spectrally averaging the single wavelength Strehl ratios to calculate $S_{\langle\omega\rangle}$. We calculate $S_{\langle\omega\rangle}$ by integrating

$$S_{\langle\omega\rangle} = \int I_{\text{norm}}(\omega) e^{-\sigma_\phi(\omega)^2} d\omega, \tag{2.22}$$

where $I_{\text{norm}}(\omega)$ is the normalized spectral intensity and $\sigma_\phi(\omega)$ denotes the standard deviation of the wavefront in a 4σ aperture of the beam [198] at the frequency ω.

$S_{\langle\omega\rangle}$ is calculated to be 0.92, indicating that the major influence on the degradation of the beam quality is due to the chromaticity introduced by the saturation of the OPCPA process. This degradation of the achievable peak intensity is a clear drawback of operating the OPCPA in saturation.

2.3.3 Spatial Filtering of Saturated OPCPA Pulses

To summarise the results so far, we can conclude that strong saturation leads to a severe degradation of the beam quality, which manifests itself as a spectrally dependent deformation of the beam profile and wavefront of the output pulses, but allows a high energy stability, which was measured to be around 0.15 %.

A possible approach to recover a high beam quality and homogeneity of the beam properties across the spectrum, is spatial filtering. In particular filtering out the side-lobes visible in the far-field beam profile in figure 2.25 is expected to help. In addition, such a scheme is easy to implement in the beam transport to the next section of the amplification chain of the high energy laser system that is to be seeded. For the measurements shown in the below, a pinhole was placed in the Fourier plane of the transport towards the INSIGHT device that was described above.

Already with a pinhole diameter of $\text{D}_{\text{pinhole}} = 1.42\, w_0$ (1000 μm) and a high transmission through the filter of T = 92%, an immediate effect on the spectrally dependent

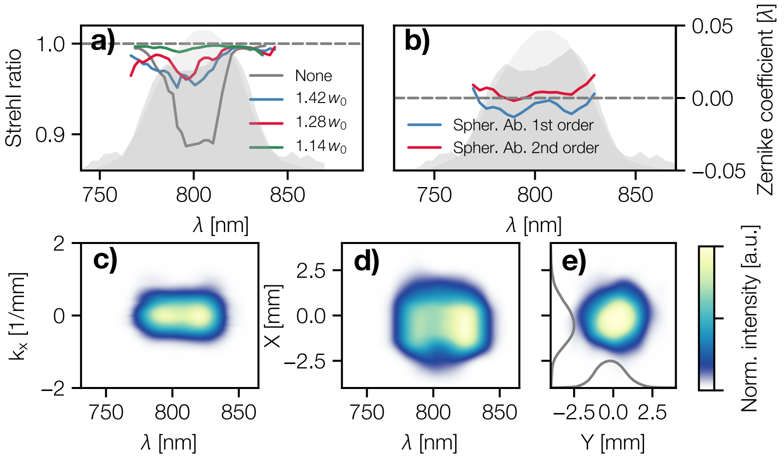

Figure 2.27 – Overview of the measured beam quality improvement after spatial filtering. Compared to figure 2.25, a great improvement in the homogeneity and the overall quality of the pulse is visible. a) shows the Strehl ratio across the spectrum for pinhole diameters from 1.14 w_0 to 1.42 w_0, as well as in the unfiltered case. w_0 is the 4σ beam diameter at the pinhole position. b) shows the residual wavefront error after filtering with the 1.14 w_0 pinhole and the bottom row shows the spectrally dependant beam profile in the far-field (c)) and the near-field beam (d)), as well as the NF beam profile (e) that corresponds to the collimated beam). The spectrum shown as an overlay in a) and b) is that of the beam filtered with the 1.14 w_0 pinhole, with the unfiltered spectrum shown in lighter grey in the background. The spectral wings visible around 750 nm and 850 nm in a) and b) are an artefact of the INSIGHT retrieval.

Strehl ratio is visible (see figure 2.27). With a pinhole diameter of around 1.14 w_0 (800 μm), the Strehl ratio is above 0.98 over the entire spectrum, while the transmission is still at 85%. The full spatio-spectral Strehl in this filtered case is $S_{\text{full}} = 0.85$, while the spectrally averaged Strehl is $S_{\langle\omega\rangle} = 0.99$. Comparing these values with those of the unamplified seed ($S_{\text{full}} = 0.92$ and $S_{\langle\omega\rangle} = 0.94$), one can conclude that while the beam quality of individual spectral components is preserved or even slightly improved, there is some chromaticity introduced by the saturation that is not completely eliminated by the spatial filter.

However, as shown in figure 2.27, the spectral variation of the spherical aberrations is largely eliminated and an overall homogeneous spatio-spectral beam profile is achieved. This is visible in the FF and NF beam profiles, which are both close to a Gaussian profile across the entire spectrum, and the first and second order spherical aberrations maintain an amplitude below $\lambda/75$ and $\lambda/38$ respectively over the entire spectrum. In the unfiltered case the corresponding values were $\lambda/4.5$ and $\lambda/7$. The M^2 of the filtered beam was measured to be 1.178 and 1.219 in the horizontal and vertical planes respectively (see figure 2.28).

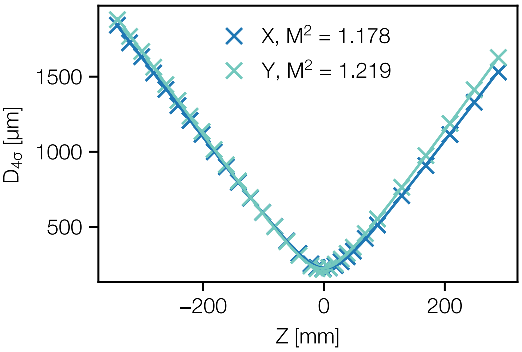

Figure 2.28 – Beam caustic of the OPCPA output after filtering of beam profile.

In addition to the improvement of the wavefront properties of the pulse, the shape of the spectrum is slightly changed, since part of the energy in the distorted, central part of the spectrum is not transmitted through the spatial filter. This leads to a flattening of the spectral shape (see figure 2.27), but has no significant influence on the spectral bandwidth or the Fourier limit.

Stability Improvement

Besides the improvement in beam quality, spatial filtering reduces the 30 second energy jitter of the laser system by 20 % from 0.17 % rms to 0.14 % rms. These values are again close to the inherent noise and resolution limits of the diode based energy measurement and therefore provide an upper limit of the true stability. This further improvement in energy stability is also observed in simulations (see figure 2.29) and is attributed to the fact that once the back-conversion regime is reached, the input fluctuations primarily result in a fluctuation of the center of the beam profile, where the back-conversion occurs. When the beam is propagated to the Fourier plane, the small fluctuating central part of the pulse (corresponding to higher spatial frequencies) is mapped to the side-lobes of the FF beam profile. By filtering these out, a significant fraction of the remaining energy fluctuations is eliminated. An equivalent pinhole-based concept has been developed for suppressing spatial mode fluctuations in gravitational wave detectors [199], although cavity-based mode filters are typically preferred over pinhole-based setups for that application.

In the simulated setup, the achievable stability improvement for the configuration of the final amplifier of MALCOLM is 30 % at a pinhole diameter of $0.88\,\omega_0$. At a pinhole diameter of $1.14\,\omega_0$ that was used in the experiment, the simulation showed a suppression of energy fluctuations by 28 %, while 89 % of the energy could be transmitted.

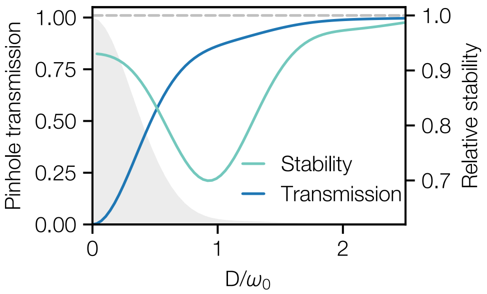

Figure 2.29 – Simulated pinhole transmission and relative stability as a function of the pinhole diameter normalize to the 4σ beam diameter. The relative stability is defined as the stability of the filtered beam compared to the stability of the unfiltered beam. The minimum relative stability is 0.7 at a pinhole diameter of $0.88\,\omega_0$. The transmission in that case is 83 %. The shaded area shows a lineout of the focused beam profile.

The trade-offs of the spatial filtering scheme are the energy loss mentioned above (typically 10-20% depending on the exact configuration) and an increased sensitivity of the laser performance to pointing fluctuations of the laser system. The improvement of short-term jitter is therefore only achievable if the laser has a sufficient pointing stability. In the case of our specific laser system, the output pointing was measured to deviate well below 10 μrad over several hours, which is stable enough for the fluctuation suppression to work, but they could still explain the slightly worse measured performance compared to the simulations.

In addition, special care must be taken to limit the in-focus intensity to avoid additional nonlinearities that could degrade the pulse quality. However, this problem can be solved by using long focal lengths and potentially an in-vacuum spatial filter. Neither problems with pointing jitter of the laser, nor nonlinearities in the focal area were observed in our setup.

2.3.4 Concluding Remarks on Spatio-Spectral Couplings in OPCPA

While this work focused on collinear OPAs, the studied aberrations are also expected to occur in non-collinear OPAs. However, due to the additional walk-off between the pump and seed pulses, the aberrations are not expected to be limited to the radially symmetric ones, but additional aberrations such as coma should be present – in particular in the non-walkoff compensating phase matching scheme. We further focused on pulses with an spatial and temporal intensity close to a Gaussian profile. While this is typical for many OPA systems, an improvement in performance is expected by using spatio-temporally flat-top pump pulses, as they would lead to a more homogeneous saturation of the parametric amplification and therefore to a more homogeneous wavefront and beam profile. This would, however, require special measures for temporal and spatial beam shaping in the pump laser, which would add complexity to the laser system.

2.4 Numerical Optimisation and Automated Tuning

Optical parametric chirped pulse amplifiers are versatile tools, in which the flexibility of pulse properties makes them an excellent source for a wide range of applications. However, we have already seen in the introduction of this chapter, this flexibility comes with the problem that the properties of the amplified pulses are coupled in a complex way. Due to this, adjusting one input parameter, such as the energy of a pump pulse, can simultaneously affect many parameters, such as the energy, bandwidth, and spectral shape of the amplified pulse. This complexity is caused by an intricate and often non-intuitive interplay of the of different nonlinear and dispersive effects and is greatly increased when parameters are added by combining multiple amplification stages to achieve higher overall gain. While this interplay provides a large number of tunable parameters that allow flexibility of the output parameters, it also makes it difficult to ensure an optimally tuned laser. Environmental influences, such as a warm-up of the laser hardware, can further reduce the reproducibility of performance, and the success of manual tuning to recover it, often depends on the operator's knowledge of the intricacies of the laser system. To be independent from such factors, an automated tuning and control procedure would be desirable.

Machine learning based control of the laser is one approach to do this. The successful application of machine learning methods has already been demonstrated in several areas of photonics [200]. In particular, the application to the self-tuning, optimization and mode-locking of ultrafast fiber lasers [201, 202] and the application of deep reinforcement learning to optimization of nonlinear processes such as white-light generation [203] demonstrate the potential benefits of machine learning techniques in the generation and amplification of ultrafast laser pulses. However, to our knowledge, such methods have not been applied to complex multi-stage laser systems. As a possible solution, we will therefore use this section to explore the application of numerical optimisation and control methods, which are widely used in other engineering disciplines, to the optimisation and stabilisation MALCOLM.

2.4.1 Overview of Suitable Optimisation Techniques

Since laser systems are inherently noisy and not all parameters of the laser system can be measured with sufficient accuracy, and environmental changes can lead to slight changes of the lasers state on a day-to-dy basis, one typically does not have an analytical model that fully describes the entire laser system. Many black-box optimisation algorithms, which do not rely on any knowledge of the system state, have been developed to optimise the performance of systems similar to laser systems. For example, Bayesian optimisation has been successfully used LWFA experiments at LUX [101], which overall pose a similar optimisation problem. However, such surrogate-based methods have the disadvantage of limited scalability to high-dimensional problems – i.e. problems with a large number of input variables, and computationally expensive fitting of a surrogate model, which makes this approach most feasible in applications where the time between taking samples is long.

Evolutionary algorithms, such as genetic algorithms or evolutionary strategies, do not rely on building a surrogate model of the function that is being optimised, and can therefore outperform surrogate-based methods in applications where sampling the function is fast [204] – as in the case of high repetition rate laser systems, where a measurement of the systems state can be done in a fraction of a second. In addition, many such algorithms scale well towards large numbers of input variables [204]. Within the realm of evolutionary algorithms, evolutionary strategies are particularly well suited for optimisation in continuous parameter spaces [205].

A versatile and commonly used evolutionary strategy is the Covariance Matrix Adaptation Evolutionary Strategy (CMA-ES) [206], which works particularly well with relatively few sampled points, ill-conditioned problems and non-separable problems [207], meaning that the input variables are highly interdependent, as is the case in OPCPA systems.

The optimisation process in CMA-ES is initiated from a randomly picked point X_0 within the search space. A normally distributed population of N points – called x_i – with a standard deviation of σ_0 around the mean X_0 is then sampled to determine the local variation of the fitness $f(x_i)$ of the function that is to be optimised. In the case of a laser system, the fitness can be determined by some performance characteristic, such as e.g. the output energy and the sampled point x_i can be a set of input parameters. In its most simple implementations, the sampled points are then ranked according to their fitness and the covariance matrix of the μ best points is used to determine the mean X_1 and width σ_1 of the distribution of points of the next iteration. Newly sampled points within this updated distribution are then added to the population to form the next generation of the evolutionary process. Over several such iterations, the mean of the population converges towards a global optimum, with the width of the distribution decreasing once the optimum lies within the sampled distribution [207].

In more advanced implementations, the distance between two subsequent populations can be influenced by additional parameters. For example, the mean value of a subsequent population can be not only determined by the best points of the previous population, but their relative influence may be weighted by their rank within the population. Alternatively, a user-defined learning rate can reduce the step-size from generation to generation [208]. In general, however, the algorithm performs well without extensive parameter tuning for the specific application, making it easy to implement in a wide variety of applications [209].

Due to its inherently statistical treatment of sampled points, CMA-ES tends to perform better than many other evolutionary methods in the optimisation of noisy functions [210]. However, there is a trade-off between speed and noise-robustness, as increased robustness is achieved by increasing the number of sampled points per generation.

For the work presented in this chapter, CMA-ES was chosen because of its robustness in noisy and ill-conditioned problems and therefore a high expected reliability in the presence of laser fluctuations – especially at non-optimal working points. In noise-free environments, some other algorithms – in particular NEWUOA [211] – have however been shown to outperform CMA-ES [212], and for stable laser systems such as the OPCPA system presented here, the noise-level may be small enough that it is worth investigating the feasibility of these algorithms in future work.

2.4.2 Implementation in Malcolm

In the MALCOLM laser system, all phase matching angles, delay lines and attenuators of the pump beams are motorised by piezo crawler stages and can be controlled through the DOOCS control system [104, 105]. This results in a total of 7 parameters that can be adjusted in order to optimise the output performance of the laser. As the optimiser, an open source implementation of CMA-ES [213] runs on a python layer that can read values from the online-diagnostics and actuate the motorised stages through the control system. An overview of the layout of the control system is shown in figure 2.30. All diagnostics operate at a repetition rate of 10 Hz, resulting in a 100 ms time window over which the diagnostic values are averaged, providing additional robustness against fluctuations in the measured values. Due to limitations in the speed of the used actuators, the stage positions could only be updated at a rate of 1 Hz. In this configuration, the potential speed of the evolutionary strategies algorithm could therefore not be fully exploited, but we still used this approach to ensure scalability in future systems with upgraded hardware.

We used a population size of 9 and defined boundaries for the input parameters that were chosen to avoid damage to the laser system due to collisions of the actuators or a pump intensity that could lead to damage of components. The respective input variables are normalised to these limits.

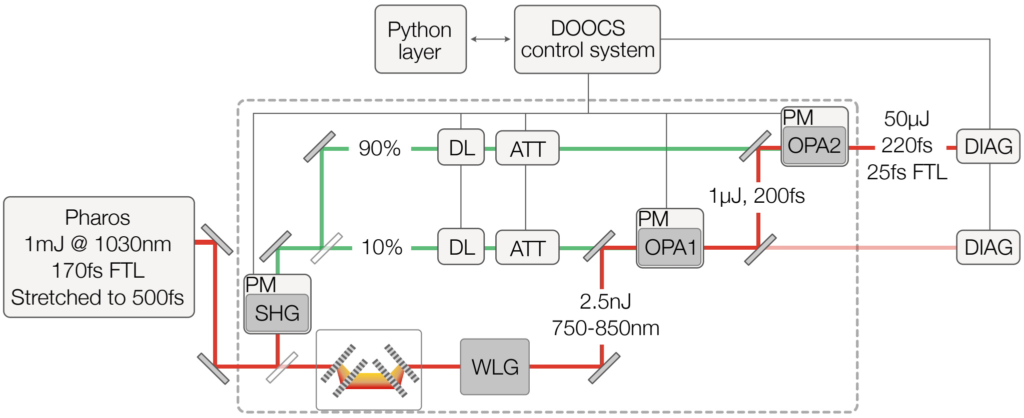

Figure 2.30 – Overview of the stages and control system of the MALCOLM laser system that were used for the optimisation and stabilisation of the laser.

2.4.3 Self-Tuning from a Random Initial State

A useful and desirable goal when seeding a Ti:Sapphire laser system is to maximize the bandwidth and energy of the seed laser, while ensuring that the spectrum is centered at a wavelength that is suitable for pre-compensate the red-shift of the spectrum in the subsequent Ti:Sapphire amplifiers. We can use these desired parameters to formulate a fitness function that describes the quality of the laser output in a single value. For this particular objective we chose

$$f = \Delta\lambda \cdot E - C(\lambda_{\mathrm{COG}} - \lambda_0)^2, \tag{2.23}$$

where $\Delta\lambda$ is the FWHM bandwidth of the output spectrum, E is the output energy, λ_{COG} is the center of gravity wavelength of the output spectrum and λ_0 is the desired center wavelength. C is an experimentally determined weighting constant. The product of the spectral bandwidth and the output energy is roughly proportional to the peak power of the fully compressed pulses of the OPCPA, which we want to maximize.

Figure 2.31 shows the evolution of the fitness function, the pulse energy, the bandwidth and the central wavelength over the duration of an optimisation run, that was started from a random configuration within the safety limits of the motorised stages. We can see that initially there is no amplification in the OPA stages and only after around 40 generations of random sampling of the parameter space, a configuration with a low output energy is found (compare also figure 2.32). The optimiser then starts to move the laser configuration towards a state with significant output energy. After around 200 iterations, the optimizer converges to an optimal value, with further searches leading to smaller improvements, with no further significant improvements occurring

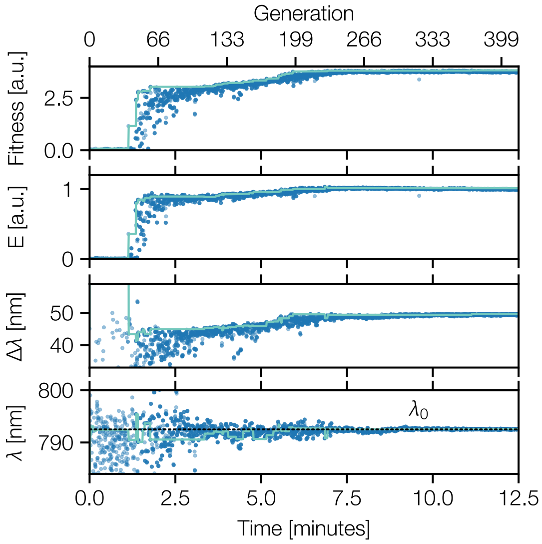

Figure 2.31 – Evolution of pulse properties during optimisation from a random initial point. The first row shows the fitness calculated according to eq. 2.23. Below that are the normalised output energy, the FWHM bandwidth $\Delta\lambda$ and the center of mass wavelength of the output spectrum. The target wavelength of 792 nm is marked by the dashed line. The light blue lines show the respective values best configuration that has been found so far.

after about 6 minutes of optimization. The evolution of the spectrum is also visible in figure 2.32.

This is not only significantly faster than manual tuning, but typically results in a 5-10% increase in output power and bandwidth. While the comparison is somewhat subjective, it underlines the potential of automated tuning procedures.

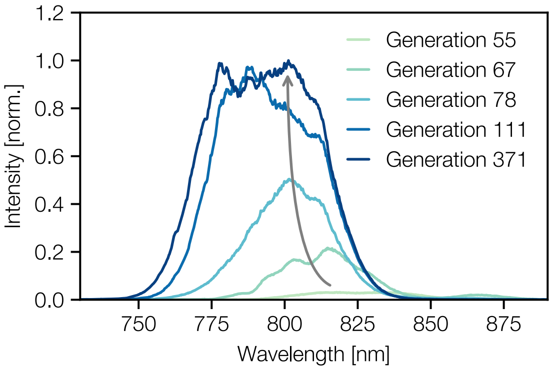

Figure 2.32 – Snapshots of the output spectrum at different stages during optimisation. The arrow indicates the direction of evolution of the spectrum.

The optimizer not only adjusts the parameters of the final OPCPA stage, whose output is considered in the fitness function, but also actively adjusts the properties of the seed and pump pulses to ensure an optimal phase matching angle of the pump – which, due to the narrow phase matching bandwidth, also has a significant influence on the spectral and temporal shape of the pump – as well as an optimal seed pulse. This includes the energy of the seed pulse, but also the bandwidth and, most interestingly, the center wavelength of the seed, which is shifted toward shorter wavelengths by about 10 nm to pre-compensate a red shift due to temporal walk-off in the final OPA stage.

In our specific laser system, the spatial overlap of the pump and seed beams cannot be adjusted in an automated way, but an iterative tuning procedure with alternating manual alignment of the mirrors and automated tuning of delays, pump energies and phase matching angles can nevertheless lead to an overall acceleration of the alignment of the laser system, where changes in the spatial alignment can also influence the spectral properties, e.g. due to changes in the optical path length of the pump and seed pulses.

2.4.4 Improved Day-to-Day Reproducibility

While the previously described approach works well to maximize the performance at any given time, changes in the surrounding lab conditions can affect the achievable performance. To ensure the highest possible repeatability of performance from day to day, it may be better to use a different fitness function. An initial optimization can indeed be done with the fitness function described above, but with slightly adjusted limits of the parameter space, in order to leave some room for compensation of drifts in performance. This is especially necessary in the case of the pump energies, since these are typically limited by the conversion efficiency and only decrease with changes in the system. Once an optimal working point is reached, the output spectrum can be stored as a reference for future optimization runs.

By defining a fitness function that characterises the deviation of the output spectrum from the un-normalized reference, one can reach the same spectral shape and amplitude on a daily basis. The fitness function we minimized to achieve this can be written as

$$f = \text{mean}\left[(I(\lambda) - I_{\text{ref}}(\lambda))^2\right] . \tag{2.24}$$

Figure 2.33 shows the performance of the laser system over a five day period with daily fine-tuning of the operating point of the laser system. The fine-tuning consisted of minimising equation 2.24, starting from the current operating point and with the initial spread of the population limited to 5% of the safety limits. This restricts the optimization to a small search space and allows faster convergence, which is typically achieved in around 2 minutes. To ensure convergence, we stop the optimizer after 3 minutes.

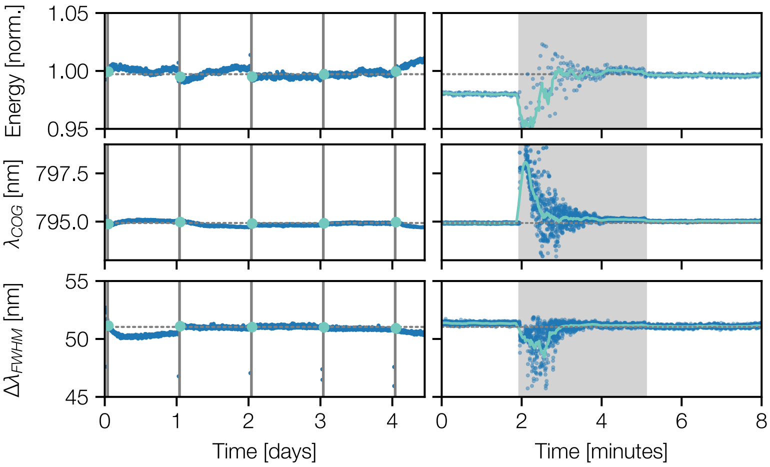

Figure 2.33 – Reproducibility of daily optimization over a 4.5-day period. The vertical lines show the periods of the daily optimization. The dots in the left column show the respective optimisation outcomes. The right column shows a zoom into an example of one of the 3-minute-long optimisation periods, with the solid line showing a rolling mean of the respective pulse porperties.

From 2.33 we can also see that while the operation point is successfully recovered at each optimization, there are some drifts in laser performance between the tuning times. To compensate for these drifts, the working point of the laser system needs to be adapted more frequently, which would be possible with a feedback loop that stabilizes the relevant laser parameters.

2.5 Full-State Feedback Stabilisation of an OPCPA

While we will introduce a few basic concepts of state-space models and feedback control that are necessary to understand the work done in this chapter, we advise the reader to turn to text books such as [214], [215] and [216] for a more complete introduction of linear control theory, which also heavily influenced the introductory sections of this chapter.

Stabilising a complex system faces a similar challenge as optimising the system: The output properties are strongly coupled, and multiple output properties can be influenced by a single actuator. As a result, independent feedback loops based on conventional single-input-single-output (SISO) feedback loops that aim to stabilize separate laser properties can interfere with each other, potentially leading to resonances and unwanted fluctuations in some of the laser parameters.

One approach to avoid such interference is to use a centralised controller that stabilizes the overall state of the laser system, that is defined by the set of monitored output parameters. Stabilization of multiple-input multiple-output (MIMO) systems is a common problem throughout engineering, and a widely used solution is full-state feedback (FSF) control. This is based on a linear state-space representation of the system for which an analytical solution exists, that brings the system to a desired state.

2.5.1 Overview of State Space Control

State space control relies on a simple linear model of the system that is to be controlled. Since the 10 Hz operating frequency of the control system naturally introduces discrete time steps, we will use the discrete-time formulation to describe the temporal evolution of the laser system. A general state-space model can then be written as

$$\begin{aligned} x_{k+1} &= Ax_k + Bu_k, \\ y_k &= Cx_k + Du_k, \end{aligned} \tag{2.25}$$

where $x_k \in \mathbb{R}^n$ is the state vector of the system at time k, which describes the current state of the system by n different values. $A \in \mathbb{R}^{n\times n}$ is the so-called state matrix, which describes the evolution of the system in the absence of external inputs, $u_k \in \mathbb{R}^p$ is a vector of external inputs from p actuators to the system, and $B \in \mathbb{R}^{n\times p}$ is the input matrix, which describes the influence of a given input on the state of the system. $y_k \in \mathbb{R}^q$ is the output vector, which typically consists of measurable quantities of the system, $C \in \mathbb{R}^{q\times n}$ is the output matrix, which describes the relationship between the internal state and the q measurable quantities, and $D \in \mathbb{R}^{q\times p}$ is a so-called feedthrough matrix, which is only relevant if inputs to the system have a direct influence on the measurement without affecting the internal state of the system.

This rather general description can be greatly simplified for our laser system if we assume that the state of the system is completely described by the measurable quantities (i.e. $C = \mathbb{I}^n$ with the n-dimensional identity matrix $\mathbb{I}^n$), that there is no direct feedthrough ($D = 0$), and that the laser system – in general – remains in a given state without external inputs ($A = \mathbb{I}^n$). In this case, the laser system can be described as

$$\begin{aligned} &x_{k+1} = x_k + Bu_k,\ y_k \\ &= x_k, \end{aligned} \tag{2.26}$$

where $x_k = x_{k,\mathrm{sp}} - x_{k,\mathrm{absolute}}$ is a vector of the deviations of the current absolute values $x_{k,\mathrm{absolute}}$ of measurable quantities (e.g., output energy or center wavelength) from their respective setpoints $x_{k,\mathrm{sp}}$, and u_k describes the relative changes in actuator positions within the laser system.

In our specific case, the absolute state-vector

$$x_{k,\mathrm{absolute}} = \begin{bmatrix} \mathrm{E}_{\mathrm{OPA1}} \\ \mathrm{E}_{\mathrm{OPA2}} \\ \lambda_{\mathrm{OPA2}} \\ \Delta\lambda_{\mathrm{OPA2}} \end{bmatrix} \tag{2.27}$$

is given by the output energy of both OPA stages, as well as the center wavelength and bandwidth of the second OPA, while the input vector

$$u_k = \begin{bmatrix} \tau_{\mathrm{OPA1}} \\ \tau_{\mathrm{OPA2}} \\ \mathrm{E}_{\mathrm{P,OPA1}} \\ \mathrm{E}_{\mathrm{P,OPA2}} \end{bmatrix} \tag{2.28}$$

consists of the pump delays τ and the pump energies E_{P} of the two OPA stages, respectively.

For such a system to be fully controllable by inputs u_k, it must satisfy the controllability condition, which can be written as [214]

$$\mathrm{rank}([B\ \ AB\ \ A^2B\ \ \ldots\ \ A^{n-1}B]) = n. \tag{2.29}$$

This means that for the system to be movable to any state x_{k+1} for which the state space model is valid, the different axes of the system must be linearly independent. For a system in which each input influences only a single output parameter, this condition is always satisfied, since each input-output relation is independent. However, for systems in which individual inputs affect multiple outputs – such as the OPCPA systems we described earlier – this is not so trivial, and controllability must be evaluated.

If controllability is given, the system can also be stabilized. To do this, one would like to eliminate any deviation of the system from its setpoint, which can be achieved by making the inputs of the system dependent on the current state and thus creating a feedback loop.

$$x_{k+1} = (\mathbb{I}^n + BK)x_k, \tag{2.30}$$

where K is the feedback matrix. To stabilize the system, i.e. to set $x_{k+1} \overset{!}{=} 0$, we have to solve this equation and calculate the required feedback gains K.

2.5.2 Linear Performance Model of Malcolm

A first step in solving equation 2.30 is to determine B, the influence of given change of the actuators on the output of the laser. During the daily optimization described in section 2.4.3, around 1000 different actuator positions around the optimized working point of the laser are explored on a daily basis. We have recorded these actuator positions along with the corresponding values measured by the online diagnostics of the laser system, resulting in a dataset that contains the necessary relationships between inputs and outputs of the laser. For small deviations from the optimum, i.e. for data points close to the optimal working point, the relationship can be approximated to be linear and the input matrix B can be calculated by multivariate linear regression.

We performed the linear regression on the FWHM bandwidth, pulse energy, and center wavelength of the two OPA stages, using the 650 data points with the best fitness value according to equation 2.24. This restricts the data set to points closest to the working point, which ensures a linear relationship between the parameters by omitting points heavily influenced by the nonlinear behavior of the laser system. We further modify the measured values by subtracting their mean and normalize them by their standard deviation to scale the parameters to a similar magnitude and allow meaningful statistical analysis.

Since the most relevant parameters to stabilize are the output parameters of OPA2, namely its output energy, center wavelength, and spectral bandwidth, we left the spectral properties of OPA1 unstabilized to not over-constrain the system. As a result, we have four stabilized output parameters: The center wavelength, the spectral bandwidth of OPA2, and pulse energy of OPA2 and OPA1. We found that these parameters are mainly influenced by the respective pump energy and pump pulse delay in the two OPA stages.

Therefore, we limited our linear regression to these sets of four input and output parameters. The measured values output values as well as the predictions of the respective actuator positions are shown in figure 2.34, along with the the coefficient

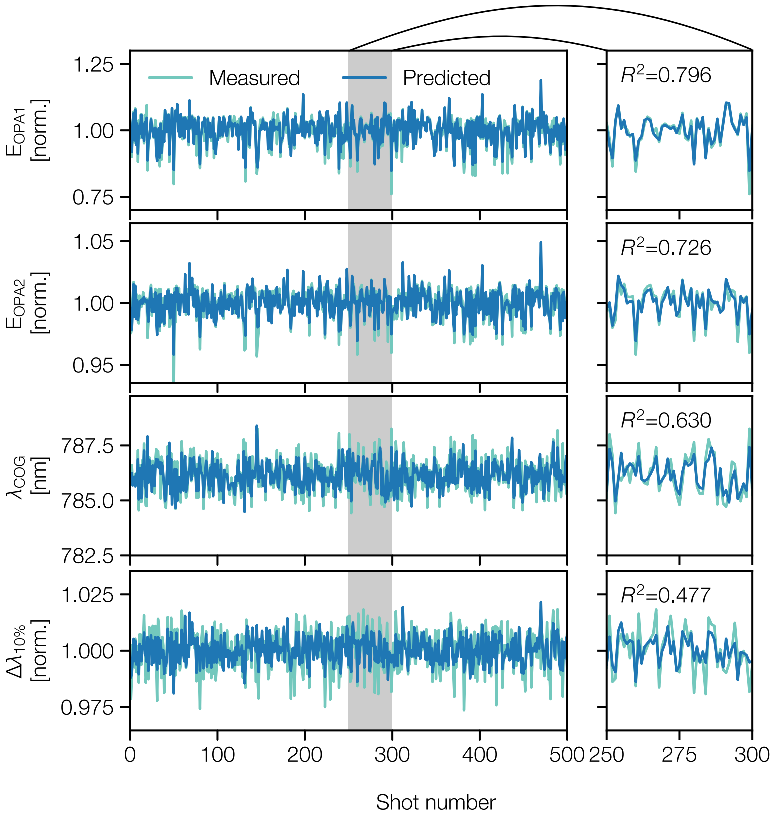

Figure 2.34 – Measured performance parameters – pulse energy, center of mass wavelength λ as well as FWHM bandwidth $\Delta\lambda$ of laser system, as well as the corresponding predictions by the linear model based on the stage positions at the respective laser shot.

determination, R^2, of the respective output parameters. We can see that a large part of the output variations are determined by the four input parameters. In particular, the output energy of OPA stages 1 and 2, and center wavelength of the second OPA stage are well represented by the model with coefficients of determination of 0.8, 0.73, and 0.63, respectively. In the case of the 10%-bandwidth, the coefficient is 0.48, which is reasonable considering the complex couplings in the OPCPA that affect the bandwidth.

We can further see the respective importance of the individual input parameters by looking at the significance level of the observed correlations correlation, which is described the p-value

$$p = \begin{array}{c} \\ \mathrm{E_{OPA1}} \\ \mathrm{E_{OPA2}} \\ \mathrm{CWL_{OPA2}} \\ \mathrm{BW_{OPA2}} \end{array} \begin{array}{c} \begin{array}{cccc} \tau_{\mathrm{OPA1}} & \tau_{\mathrm{OPA2}} & \mathrm{E_{P,OPA1}} & \mathrm{E_{P,OPA2}} \end{array} \\ \begin{pmatrix} 0.00 & 0.84 & 0.08 & 0.09 \\ 0.00 & 0.00 & 0.15 & 0.03 \\ 0.00 & 0.00 & 0.67 & 0.33 \\ 0.00 & 0.00 & 0.00 & 0.00 \end{pmatrix} \end{array} \tag{2.31}$$

Lower p-values indicate that the observed correlation is more likely to be caused by actual changes in the inputs rather than by random causes. For our application, we have defined a cut-off of $p = 0.1$, above which we consider a correlation as spurious. The corresponding elements in equations 2.31 and 2.32 are marked in red.

As an example, we can see from the low p-values in the bottom row of matrix 2.31, that the bandwidth of OPA2 is determined by all of the four input parameters (pump delays τ_{OPA1} and τ_{OPA2}, as well as pump energies $\mathrm{E_{P,OPA1}}$, $\mathrm{E_{P,OPA2}}$) – again highlighting the complex couplings in OPCPA that influence this particular parameter –, while the center wavelength of OPA2 is determined only by the pump delays of the two OPA stages.

To ensure the controllability of the system and to eliminate spurious correlations from influencing the feedback loop, we simplify matrix B by eliminating parameters with $p < 0.1$:

$$B = \begin{array}{c} \\ \mathrm{E_{OPA1}} \\ \mathrm{E_{OPA2}} \\ \mathrm{CWL_{OPA2}} \\ \mathrm{BW_{OPA2}} \end{array} \begin{array}{c} \begin{array}{cccc} \tau_{\mathrm{OPA1}} & \tau_{\mathrm{OPA2}} & \mathrm{E_{P,OPA1}} & \mathrm{E_{P,OPA2}} \end{array} \\ \begin{pmatrix} -0.88 & \cancelto{0}{-0.01} & 0.04 & 0.03 \\ -0.75 & -0.49 & \cancelto{0}{0.01} & 0.08 \\ 0.37 & 0.66 & \cancelto{0}{0.04} & \cancelto{0}{0.03} \\ -0.32 & 0.62 & 0.10 & 0.11 \end{pmatrix} \end{array} \tag{2.32}$$

Despite this simplification, the overall coefficient of determination of our model remains at 0.66, indicating that the high predictability of the model is maintained. The resulting matrix now has a rank of 4 and thus satisfies the controllability condition (eq. 2.29). Note that the values in the input matrix B (eq. 2.32) are in normalized units.

2.5.3 Calculating Stabilization Gains

While equation 2.30 can be solved unambiguously now that we know the system response to a given input, the direct solution of the equation generally does not provide a feedback matrix K that has any tolerance to model inaccuracy or measurement noise – both of which are present in real-world implementations.

An alternative method for the calculation of K that results in a more cautious response to changes of the system is pole placement [214]. In this method, the eigenvalues s of the closed-loop system $(1 - BK)$ are chosen to be $-1 < |s| < 1$. An eigenvalue of $s = 0$ would correspond to an aggressive response of the system that aims to eliminate the entire deviation from the setpoint within a single time-step. For values of $s \neq 0$, the response is more cautious, with convergence to a stabilized state occurring over $1/|1 - s|$ time steps. This provides an opportunity to tune the response of the system and to include some tolerance to an imperfect representation of the laser dynamics by the model.

In our specific case, we found $s = 0.8$ to be a reasonable compromise between a fast response to external perturbations of the system and tolerance to noise in the measured laser properties, as well as towards drifts of the model over time.

2.5.4 Results of Full-State-Feedback-Stabilization

Figure 2.35 demonstrates the successful simultaneous stabilization of the energy, bandwidth, and center wavelength of the laser system of the system over 5 hours.

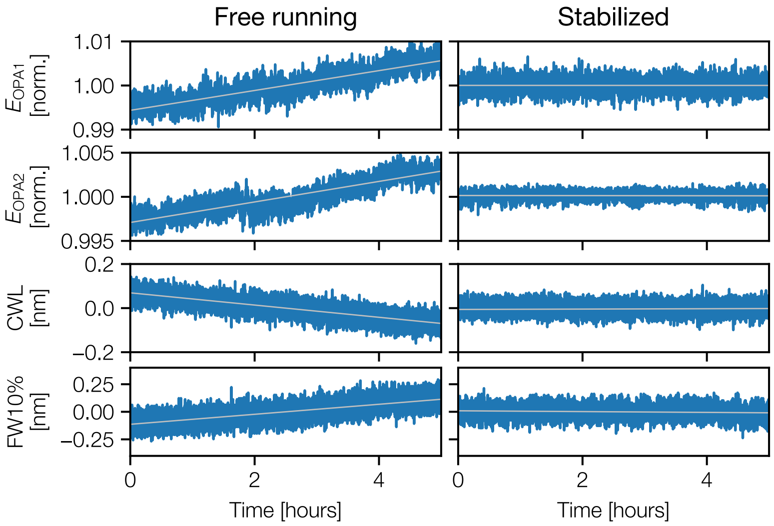

Figure 2.35 – Stabilized and un-stabilized laser parameters, using full-state feedback control. The grey lines show a linear fit of the respective trands.

Due to the limited response time of the actuators used in the laser system, the stabilization was implemented as a simple drift compensation with the feedback loop operating at a rate of 0.5 Hz.

In particular the stabilization of the bandwidth demonstrates the ability of model-based control to influence certain output parameters without the presence of an individual actuator that directly influence the property. Instead, a combination of all actuators is used, with major components being the saturation level of both amplifier stages and the timing of the pump pulses in the two OPA stages. This is also reflected in the matrices 2.31 and 2.32.

2.6 Long-Term Stability of Malcolm

To verify the long term stability of MALCOLM, the laser was operated over period of 50 hours with the stabilization running. The resulting trends in output energy, center wavelength, and bandwidth are shown in figure 2.36. All measurements were done using independent diagnostics that were not used in the feedback loop. For the energy measurement, all shots were recorded at the full repetition rate of 1 kHz, while the spectra were recorded at a rate of 1 Hz integrating over a single shot.

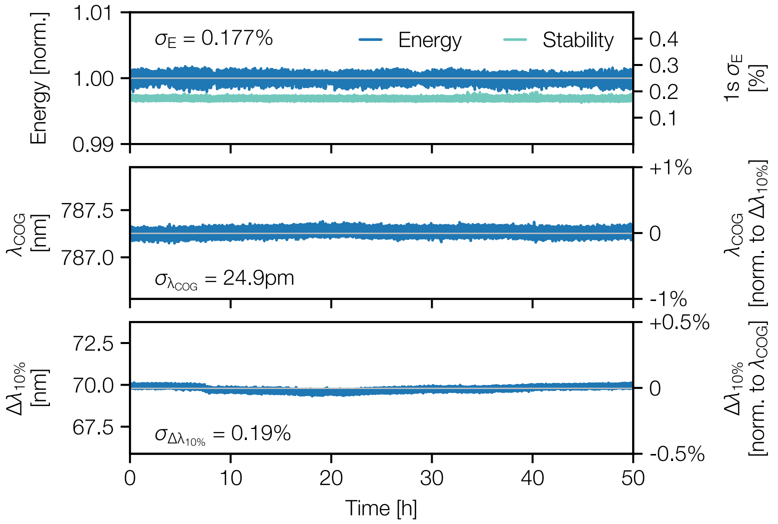

Figure 2.36 – Long term stability of the OPCPA seeder, measured with out-of-loop diagnostics. The grey lines show the respective mean values to guide the eye.

The pulse energy stability was measured to be 0.18 % rms over the entire 50 hour measurement, while the wavelength stability was measured to be 25 pm rms. The bandwidth at 10 % intensity level was measured to vary by 0.19 % rms. The short-term energy jitter – over 1 second – remains below 0.19 % throughout the entire measurement, with an average of 0.17 %. The energy values

The slight drifts in the spectral properties could be traced back to a pointing drift within the laser system which is coupled to the spectral shape through the incoupling into the used spectrometers.

As already described in section 2.2.3, the measured energy stability is largely limited by the resolution of the used photodiode-based energy heads, and in fact the rms variation of the integrated counts of the single-shot spectra is only 0.13% over the entire 50-hour measurement. The integration over many spectrometer pixels results in higher resolution in counts and lower relative intrinsic noise than with the energy heads. Nevertheless, the value obtained from the spectrometer counts should be taken as an indication only, since the spectra are only recorded at 1 Hz. However, short-term measurements of the spectrum at the full 1 kHz repetition rate, show no difference in stability compared to measurements at 1 Hz, except for additional small drifts in the long-term measurement due to the aforementioned slow changes in coupling into the spectrometer.

2.7 Conclusion and Future Improvements on Malcolm

In summary of this chapter, we have constructed a highly stable OPCPA-based seed laser for high energy Ti:sapphire systems. Optimised working points of the laser system can be reached in an automated and reproducible way, which contributes to a flexible and yet user-friendly operation of the system. The excellent short term stability of energy and spectrum (e.g. an rms energy stability below 0.15 %) could be maintained over multiple days of operation with the help of a full-state feedback control. During continuous operation over 50 hours, we measured an overall energy stability of 0.177 % rms, a single shot wavelength stability of 25 pm, and 0.19 % rms variations in the bandwidth of the output spectrum. In both the short and long term, the measured energy stability is is largely determined by the inherent noise of the measurement setup, with measurements using the integrated counts of single shot spectra or camera images indicating a stability around 0.1 %. The excellent short term stability is largely achieved through passive stability of the system through saturation the gain in the OPA stages, which leads to spatio-spectral couplings that adversely affect the pulse quality. We have thoroughly characterised this saturation-induced degradation by measuring the full 3-dimensional spatio-spectral electric field of the pulses and could use these measurements to filter out degraded portions of the pulse and retrieve yield an excellent beam quality. The resulting pulse have excellent wavefront quality quantified by a full spatio-spectral Strehl ratio of 0.85 and a M^2 of 1.2.

Nevertheless, there is still room for improvement in the lasers system's characteristics – in particular, the output energy, which only barely meets the requirements for seeding the subsequent Ti:sapphire amplifiers without much headroom in case of a power degradation. We will therefore look at some potential improvements in the following.

SHG Improvement

A primary limitation of the overall efficiency of the OPCPA system – and thus its output energy – is the efficiency of the SHG-based pump generation. In section 2.2.1 we already hinted at the potential 1.5x improvement in efficiency by using KDP as a nonlinear crystal instead of BBO. However, due to the hygroscopicity and therefore poor lifetime of KDP, we decided to use the more robust BBO for the time being.

In order to prevent degradation of the KDP, it must be operated in a dry environment, which can be achieved either by placing the crystal in a hermetically sealed housing or by operating it at an elevated temperature compared to the environment. To eliminate any potential convection in the laser housing, all heat sources have been removed from it and adding a crystal heater to the KDP crystal would be counterproductive. Sealed housings, on the other hand, have an input and output window through which the beam is transmitted, resulting in the accumulation of B-integral, which has already been observed to cause a degradation of the pump beam quality.

A possible solution to this problem would be to adapt the housing design so that the humidity inside the housing can be maintained at a safe level of <20 %. If the lifetime and degradation rate of the KDP crystals is well characterized, the full state feedback control could also be adjusted to compensate for the decrease in pump energy. However, this would mean that the pump energy used would initially have to be severely restricted in order to have sufficient headroom in the control, which would slightly reduce the desired benefit of using KDP.

OPA Efficiency Upgrade

Another way to increase the output energy of the laser is to adapt the parametric amplifier design to increase the efficiency of the pump-to-signal conversion. Several approaches have been proposed in the literature [113, 217–219], all of which rely on eliminating the idler photons from the amplification process. The most feasible such setup in Malcolm would be the installation of a third amplifier stage in which the signal and the residual pump from OPA2 would again overlap, resulting in additional extraction of energy from the pump pulse. However, the total crystal length in such a scenario would become comparable to the pulse splitting length between pump and signal, and the group delay difference between pump and signal would have to be compensated between the crystals. First numerical simulations of such a setup (see figure 2.37) suggest an increase in signal energy of up to 2x.

Due to the high ratio of signal to pump pulse energy, the third amplifier stage would quickly reach the back-conversion regime and thus only a short amplifier crystal would be needed. Furthermore, the length of the first crystal could be reduced from the current length of OPA2, so that the highly saturated amplification takes place primarily in the third crystal. As a consequence of shortening both crystals, the phase matching of the amplifier (OPA2+3) would have a larger spectral and angular acceptance than the currently installed OPA2, resulting in a slightly increased bandwidth of the amplified pulses.

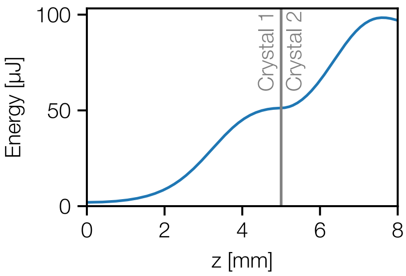

Figure 2.37 – OPA signal energy with recycling of the residual pump energy in a third OPA crystal. The final amplifier would then consist of two OPA crystals: Crystal 1 and Crystal 2.

If the group velocity difference is not compensated between the OPCPA crystals, a slightly lower energy increase of around 1.5x can still be expected, but the benefits in terms of increased angular and spectral acceptance are largely diminished by sub-optimal temporal overlap of the pump and signal pulses, which makes a longer interaction length of the pulses necessary to reach the same gain.

As a conservative estimate, the overall increase in output energy of the OPCPA – if both the SHG and the final parametric amplifier are upgraded – could be on the order of 2x, resulting in an output energy of approximately 100 μJ.

Machine Learning-Assisted Control

The results on automated tuning and full-state feedback that have been presented in this chapter are a promising first step and are transferable also to other ultrafast and high-energy laser systems. They demonstrate a possible method for achieving the high degree of control and stability that will ultimately be required from future LWFA drive lasers. However, these results are based on simple time-invariant linear models, which have their limitations, especially if wide tunability is required, or if high-precision stabilization should be implemented over long time scales, during which the system may change, causing the validity of the models to decrease with time.

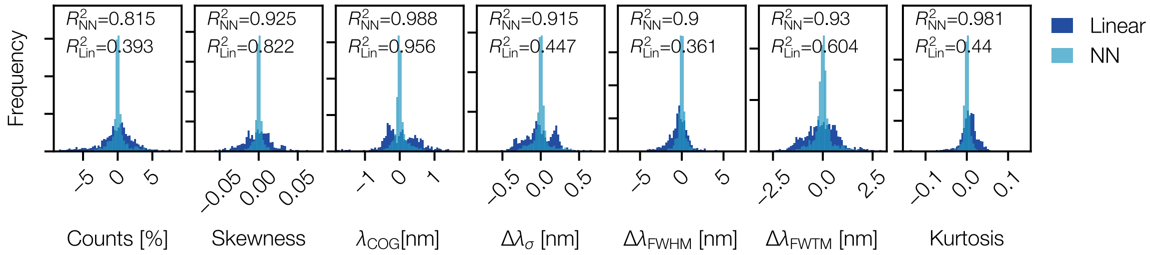

Figure 2.38 – Histograms of the error of the prediction of spectral properties of the second OPA stage, by a linear and a neural network-based model. The vertical tick-separation corresponds to 100 datapoints.

More complex, continuously updated and non-linear models are expected to provide a better description of the laser dynamics, and initial results indeed confirm that e.g. neural network based models can describe the laser dynamics in a more reproducible way and over a larger parameter space where the assumed linearity of a state space model is no longer given. A comparison between a linear and a non-linear model is shown in figure 2.38. The nonlinear model in this case consists of a neural network with an input layer (7 units), a single hidden layer of 64 units with a rectifier activation, and an output layer of 7 units with a linear activation. For training the neural network, we used all 7 actuators of the laser system (phase matching angles of both OPA stages and SHG, pump delays of both OPA stages as well as pump energy of both OPA stages), in contrast to the reduced set of input parameters used for the full state feedback stabilisation described earlier in this chapter. The dataset consisted of a total of approximately 12000 data points collected during the daily optimisation routine over a period of 1 month. Unlike the data used to fit the linear model for FSF stabilisation, we did not restrict the data to points with a high objective function, but used the full data set. The data set was split into a training and a test set in a 90/10 ratio. Due to the slightly different setting of the experiment, the R^2-values of the linear model in figure 2.38 are not directly comparable to the results we showed previously in section 2.5.2. Nevertheless we can see that without the restriction to a small, asymptotically linear parameter space, the nonlinear model clearly outperforms the linear model and the predictions have a smaller deviation from the measured values.

3 Scaling Ti:Sapphire Amplifiers Towards High Average Power

A key challenge in scaling the average power of ultrafast laser sources lies in the scalability of the main amplifiers pump sources and the thermal management of the final high-energy amplifiers themselves. Both of these factors are particularly challenging in the case of Ti:sapphire based laser systems, that are currently the only technology capable of routinely producing peak powers higher than 100 TW, which is needed to accelerate electrons to the GeV range. The challenges of scaling to higher average power at repetition rates in the 0.1 to 1 kHz range, arise from inherent properties of the Ti:sapphire material. In the following section, we will give a brief overview of the specifics of Ti:sapphire as an amplifier medium, followed by two sections of which the first addresses a scalable solution for generating high average power beams, and the second shows the conceptual design of a 100 Hz, Joule-level Ti:sapphire amplifier.

3.1 Overview of Ti:sapphire Lasers

The origin of all advantages of Ti:sapphire relevant to high-intensity pulse generation and the challenges in scaling to high average power operation can be traced back to its spectroscopic properties. These properties allow femtosecond pulses to be efficiently amplified to Joule-level energies, but also result in the generation of comparably large amounts of excess heat and a short excitation lifetime, which makes pumping of Ti:sapphire more challenging than for many other laser materials. The following two sections will provide a detailed overview of these properties in order to provide a context for the following sections on the generation of suitable high repetition rate pump pulses and a high average power Ti:sapphire amplifier.

3.1.1 Amplification in Ti:sapphire

Ti^{3+}:Al_2O_3 (Ti:sapphire) is a quasi-4-level laser material with an unusually large emission bandwidth, which makes it interesting for various applications in spectroscopy and ultrafast laser science. The broad emission (see figure 3.1) supports the generation of 5 fs laser pulses in Kerr-lens mode-locked oscillators [220] or tuneable lasers that

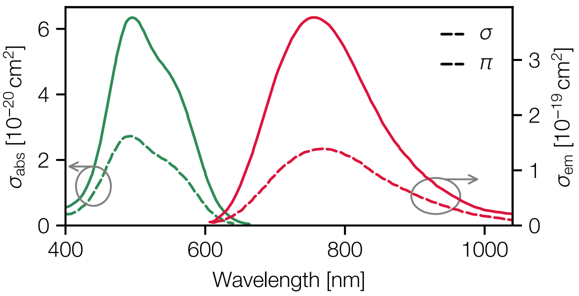

Figure 3.1 – Emission (σ_{em}) and absorption cross-sections (σ_{abs}) of Ti:sapphire in π- and σ-polarisation at room temperature [26, 222]

cover a spectral range from < 700 nm to > 1000 nm [221], with the highest efficiency at wavelengths around 800 nm. The peak emission cross-section of $\sigma_{\text{em}} = 3.77 \times 10^{-19}$ cm^2 yields a saturation fluence of $J_{\text{sat}} = h\nu/\sigma_{em}$ =0.7 J cm^{-2}, which allows for an efficient energy extraction at moderate fluences, making it possible to construct efficient high energy amplifiers. Amplifiers with tens to hundreds of joules of output energy have been demonstrated at multiple facilities [156]. Combined with typical pulse durations of 20-30 fs, this results in multi-PW peak powers and excellent suitability for LWFA-based electron acceleration.

While the thermal properties of sapphire make it an excellent host material for high average power laser systems, heat management of Ti:sapphire amplifiers is challenging due to the high heat-load that comes with the high quantum defect of roughly 35%. This means that roughly a third of the incident pump power is directly converted into heat that must be removed from the amplifier crystal to prevent thermal effects such as thermal lensing from degrading the beam quality of the amplified beam. As a result, the Joule-level Ti:sapphire amplifiers typically operate at a repetition rate below 10 Hz – far from the kHz level repetition rate that is desired for future laser-wakefield accelerators.

3.1.2 Pumping Ti:sapphire

As shown in figure 3.1, the absorption band of Ti:sapphire is centered around 490 nm [223], which means that also the pump source should have a wavelength in the blue/green spectral region. Typically, frequency doubled, Q-switched neodymium (Nd) or ytterbium (Yb) lasers have been used for this purpose. After frequency doubling, these lasers can deliver pulses at wavelengths around 510-532 nm, close to the peak absorption of Ti:sapphire crystals. Historically, mostly Nd-based lasers have been used because the low saturation fluence of Nd-based gain media allows efficient energy extraction and comparatively simple generation of high energy pulses. These lasers have been pumped by flashlamps, which – while providing very large amounts of energy for up to MJ laser systems [156] – have two key problems that prevent their use at high repetition rate: first, the electronics that provide the pulsed current for flashlamp operation are typically limited to repetition rates well below 100 Hz (although operation up to 100 Hz is possible in some special cases [224]). Due to the short lifetime of flashlamps of a few tens of millions to around a hundred million shots, the high repetition rate shortens the maintenance intervals to impractical durations. Second, the ratio of the of extremely broad emission bandwidth of the flashlamps to the narrow absorption band of Nd-based laser materials, leads to percent-level efficiency and thus to an unreasonable wall-plug efficiency of the overall laser system.

Diode-pumped solid state lasers (DPSS) are much more reasonably scalable to high repetition rates, but have only become relevant for pumping high energy Ti:sapphire systems in in the last decade. A prominent example of the use of this technology is the HAPLS laser system [225] developed at Lawrence Livermore National Lab with a specified peak power of 1 PW at 10 Hz repetition rate. However, there are also other examples of higher repetition rate at reasonably high pulse energies (e.g. >200 mJ at 100 Hz [226]), and mJ-level pulses are routinely available at kHz repetition rates in various commercial Ti:sapphire laser systems. From these observations, one can quickly come to the conclusion that diode pumped solid state lasers are an excellent option for simultaneous high energy and high repetition rate pump sources for Ti:sapphire lasers. With the increase in repetition rate that is made possible by diode pumping, the average power of pump lasers also increases. The particularly low quantum defect of Yb-based lasers makes them in certain aspects even more interesting for high average power operation than Nd-based lasers. However, Yb-based lasers have the disadvantage of high saturation fluences, which make the efficient extraction of high pulse energies more difficult than in the case of neodymium.

A further improvement of the wall-plug efficiency of Ti:sapphire amplifiers could be achieved by direct diode pumping of the Ti:sapphire [227, 228], eliminating the intermediate Nd- or Yb-doped solid-state laser and subsequent frequency conversion from the near-infrared to the absorption band of Ti:sapphire. However, this approach is currently limited to high repetition rate, low energy lasers, despite rapid progress in the development of laser diodes in the 500 nm range in recent years. The challenge for this technology lies in the limited brightness of currently available laser diodes around 500 nm and the short upper-state lifetime of only around 3.2 μs in Ti:sapphire. Any pump energy contributing to the gain must be delivered in a time significantly shorter than this lifetime, which, even in the case of state-of-the-art 2 kW-level laser diodes [229], is in the sub-10 mJ range. In addition, the highest average power laser diodes are currently only available at comparatively short wavelengths below approximately 470 nm [230], which has often been observed to contribute to induced absorption at the seed wavelength of 800 nm, significantly degrading the pump-to-signal efficiency of the Ti:sapphire amplifier [231].

This makes diode pumped Yb:doped or Nd:doped laser, delivering high energy pulses with nanosecond duration, currently the best available option for high average power Ti:sapphire pumping.

3.2 High Average Power Pump Generation

For a targeted pulse energy of 3 J out of a Ti:sapphire amplifier, one can estimate the required pulse energy from a Q-switched Yb-based laser that would provide the pump pulses. A typical optical-to-optical efficiency of saturated Ti:sapphire amplifiers is about 40%, resulting in a required pump energy of 7.5 J at 500 nm, and a corresponding average power of 7.5 kW at the desired repetition rate of 1 kHz. Adding an estimated 60% efficiency in converting the Yb laser wavelength of 1030 nm to 515 nm by second harmonic generation (SHG), we can conclude that about 12.5 J of energy from the Yb laser will be needed to amplify 3 J in the Ti:sapphire amplifier. At a repetition rate of 1 kHz, this corresponds to an average power of 12.5 kW, which in itself presents challenges that require careful engineering and thermal management of the Yb laser system.

Three main approaches for generating such high average power beams have been established over the past decades: Thin disk amplifiers, slab amplifiers, and fiber lasers. In all three approaches, the geometry of the gain medium is modified to provide optimal heat extraction. We discuss the first two in more detail in section 3.3.1, and for now discuss fiber lasers as a potential, highly scalable approach to pump generation for Ti:sapphire lasers.

The high aspect ratio of an optical fiber results in a large surface area, that allows for efficient heat extraction, enabling the operation of fiber amplifiers at kW-level average power without complex cooling concepts. As an additional benefit, the inherent guiding of the beam in the fiber core leads to a mechanically robust design with a long interaction length between the pulse and the gain medium, resulting in a compact single pass amplifiers with high average power. The maximum energy that a single fiber core can support is strongly limited, but the approach can be highly parallelized, so that a large number of fibers cores could be used to provide a combined energy of several Joule, while the individual fiber cores carry only moderate pulse energy and average power.

This method has been used to demonstrate average powers in excess of 10 kW with excellent beam quality [106]. An additional factor that further improves the compactness and therefore scalability of the laser is the combination of multiple amplifier cores in a single fiber, as it is done in the multi-core fiber approach pioneered at the Helmholtz Institute Jena [232].

3.2.1 Brief Overview of the Multi-Core Fiber (MCF) Concept

The laser system described in this subsection was developed Christopher Aleshire et al. at the Helmholtz-Institut Jena and Fraunhofer Institut Jena, with no contributions from the author of this thesis. The description is included to illustrate applicability of the laser for pumping high energy Ti:sapphire systems, and the specific challenges presented by the lasers architecture for pumping Ti:sapphire amplifiers. Further details of the laser system can be found in [233].

The key feature of the multi-core fiber design is the combination of multiple doped amplifier cores in a single cladding that is used to guide the beam of a pump source. Due to the significantly larger core diameter of the cladding, the pump source does not need to have a high beam quality and e.g. highly multimode diode lasers can be used, which are available with average power in the tens of kW range. The pump is uniformly absorbed in all Yb-doped amplifier cores, through which a seed beam propagates and is amplified. Currently, the typical number of cores per fiber is around 16, but designs with square core arrays of $16 \times 16 = 256$ cores have been envisioned, and 10×10 fibers have been studied as feasible with moderate technical difficulty [234]. Due to the high aspect ratio geometry of the amplifier cores, the advantageous thermal properties and efficient heat dissipation of fiber lasers are largely preserved, while the overall setup is greatly simplified, as components for fiber cooling and potential free-space beam routing between amplification stages can be handled in the same way as with a single beam from a single-core fiber.

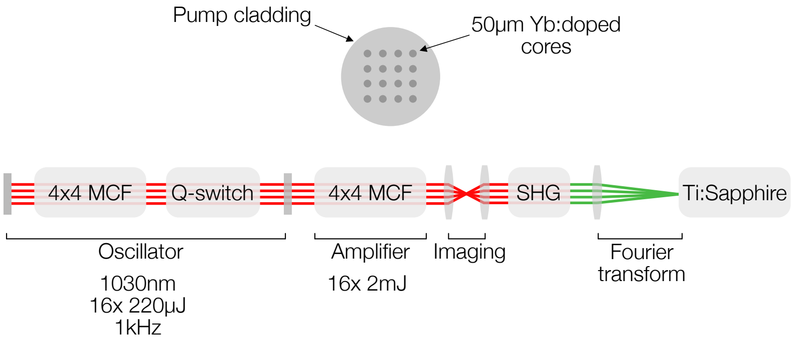

Figure 3.2 – Schematic overview of the Q-switched multi-core fiber laser. The top image shows the end-facet of a 4x4 core multicore fiber. The oscillator and amplifier of the laser system shown in the bottom have previously been reported on in [233].

The scalability of this technology to kW-level average power has been demonstrated in the case of coherently combined ultrafast lasers [235] and recently also the operation of a Q-switched system delivering nanosecond pulses with up to 49 mJ of combined energy out of 16 cores has been demonstrated [233].

This latter high-energy laser system was used in the the experiments that we'll discuss later in this section. It consists of a MOPA design with an oscillator cavity that is Q-switched using a Pockels cell. The amplifying module in the cavity is a $4 \times 4 = 16$ core Yb-doped fiber with a core diameter of 50 μm. The oscillator output – with a pulse duration around 20 ns and an energy of 220 μJ per core – is imaged into a subsequent 98 cm long amplifier fiber. The fiber input is tapered with the core diameter increasing from 19 μm to 50 μm over a distance of 20 cm to suppress higher order mode content and thus improve the amplified beam profile. The seed beam is amplified to up to 3 mJ at a 1 kHz repetition rate, although at the time of the experiments presented in this chapter, only up to 2 mJ were available. The resulting beam profile is shown in figure 3.3. The slight radial dependence of the beam profiles of the individual cores is due to refractive index changes due to small thermal gradients in the multicore fiber.

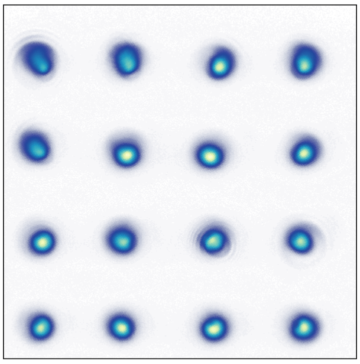

Figure 3.3 – Beam profile of the tapered multicore fiber output.

The combination of this technology with large mode diameters, in combination with a further increase in core count can pave the way towards Joule-class fiber laser technology that would be an excellent candidate for pumping high energy Ti:sapphire laser systems with kW average power. Individually these two features have been demonstrated, with single core nanosecond fiber lasers delivering pulse energies on the order of 100 mJ [236–238], and studies on multi-core fibers showing scalability to large core-counts [234]. While Joule-level MCF-lasers thus seem to be technically feasible, another challenge lies in dealing with the multi-aperture profile of the beams amplified in an MCF fiber and transforming it into a single aperture that would be needed in a Ti:sapphire amplifier crystal. Due to the collinear nature of the individual MCF cores, a propagation to the Fourier plane – as can be done with a single lens – yields a uniform beamprofile that consists of the superposition of all individual beams with a Gaussian intensity distribution, as shown in figure 3.3.

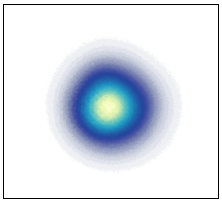

Figure 3.4 – Beam profile of the tapered multicore fiber output, propagated to the Fourier plane with a single lens.

Converting the 1 μm fiber lasers output to the 500 nm range can be done through second harmonic generation. Due to the tens of nanosecond range – 20 ns in the case of the 49 mJ-system from Jena – relatively small beams are needed to reach an intensity on the GW/cm^2 level, that allows efficient SHG. Such intensities can easily be achieved in the imaged, multi-aperture MCF-output, which also has the advantage of parallel propagation of the beamlets (which is particularly important in critical phase matching with limited angular acceptance). We will therefore pursue this approach in the following sections. As suggested previously, the multi-aperture beam can then be converted to its single-aperture, far-field version, as it is also indicated in figure 3.11.

3.2.2 Simulations and Experimental Results on MCF-Based SHG

The simulations presented in this subsection were performed by the author of the thesis in preparation of the experiments, which were carried out in close collaboration with Christopher Aleshire, Arno Klenke, Cesar Jauregui and Jens Limpert at Helmholtz-Institut Jena. The experimental results have been published in [43].

In order to use the output of the MCF-laser for pumping Ti:sapphire, the 1030 nm output needs to be converted to the absorption band around 500 nm by SHG. For this purpose, the individual fiber cores are imaged onto a nonlinear crystal. To ensure a high conversion efficiency, a high intensity and high phase matching efficiency are required. Typical damage thresholds of AR-coatings at ns pulse duration are around 1 GW/cm^2, and to stay below the LIDT by a safety margin of 2, the 20 ns, 2 mJ output of the fiber needs to be imaged onto the nonlinear crystal with a magnification of approximately 3.75x to a beam diameter of around 187 μm.

For such small beams, a nonlinear crystal with low walk-off – possibly even eliminating walk-off through non-critical phase matching – is required to ensure high conversion efficiency. In addition, the crystal should have low absorption and high damage threshold to ensure safe operation at high average power, and should be commercially available in large dimensions to ensure scalability to high energy systems. LBO fulfills all these requirements and was therefore chosen as the nonlinear material and has been used in numerous high energy and high average power applications [107, 239–243].

For comparison, the commonly used BBO would not be suitable due to its larger walk-off angle of 57 mrad compared to 8.16 mrad in LBO. At an intensity of 1 GW/cm^2, a crystal length of 17 mm would be required to maximize conversion efficiency. After this distance, the spatial walk-off would be about 1 mm – much larger than the beam size and thus preventing efficient frequency conversion.

KTP is also often used for frequency doubling of nanosecond lasers. However, its lower damage threshold of about 0.3-0.6 GW/cm^2 would mean that one would have to operate with a large beam diameter (1.5-2 times larger than that required for LBO). The resulting walk-off relative to beam size and maximum achievable conversion efficiency is comparable to LBO when using critical type 1 or type 2 phase matching. However, it has a significantly higher absorption coefficient (typically around 50-100 ppm/cm), which makes it less favorable than LBO for high average power applications. In addition, KTP does not support non-critical phase matching, which – as mentioned above – is possible with LBO [244]. As a consequence, we LBO is the preferred material for an experimental implementation of such a frequency conversion setup.

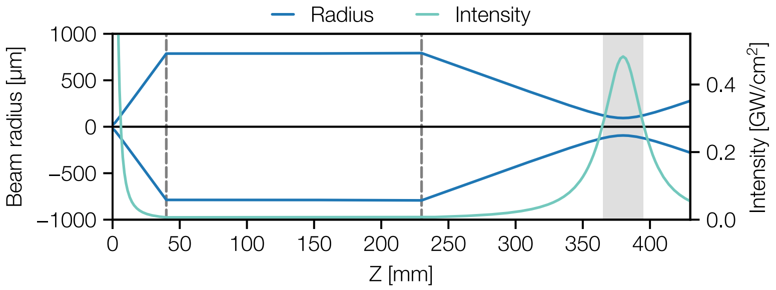

Figure 3.5 – Radius (1/e^2) of an individual beamlet in the relay imaging from the output facet of a fiber to the SHG. The beam radius at the fiber output is 25 μm, with the M=3.75 magnification resulting in a 93.75 μm minimal radius in the SHG crystal. The dashed lines indicate the locations of the f=40 mm collimation lens and the f=150 mm focusing lens. The shaded area indicates the location of a 30 mm long crystal. The turquoise line indicated the intensity of the fundamental beam, with a peak of 450 MW/cm^2

Figure 3.5 shows the caustic of a beam relay imaged with f=40 mm and f=150 mm lenses, corresponding to the desired 3.75x magnification and 1 GW/cm^2 peak intensity. Typical crystal lengths for nanosecond SHG setups are on the order of 2-3 cm and it is clearly visible in figure 3.5 that over marked the 30 mm area around the focus, the beam has a strongly varying size and divergence angle with a maximum of 3.2 mrad (internal angle in LBO). This would result in a significantly reduced phase matching efficiency if such a beam were focused into a critically phase matched LBO which has an FWHM angular tolerance of 6.8 mrad·cm. It is therefore better to use non-critical phase matching, which is possible at a temperature of 190°C. However, even in that case, the beam size and intensity (see fig. 3.5) strongly varies during propagation through the typically few-centimeter long LBO crystal. To accurately study the frequency conversion, numerical simulations are necessray.

Numerical simulation of second harmonic generation of nanosecond pulses

Most established simulation tools are not suitable for simulating the second harmonic generation of small-diameter, nanosecond pulses, as e.g. the commonly used SNLO software [245] does not take into account the natural diffraction of the beam. chi3D on the other hand – which we used for the short pulse OPCPA simulations in chapter 2 – would be able to describe the pulse propagation correctly. However, its algorithm requires sampling of the full electric field from the sub-wavelength scale to the full nanosecond pulse duration, resulting in impractical memory requirements for long-pulse simulations. For our application, we have therefore developed a custom tool to simulate the second harmonic generation of small beam nanosecond pulses.

The first step is to define the electric field amplitude of the input pulse. In our application to narrow-band nanosecond pulses, it is sufficient to consider a monochromatic beam and neglect dispersive effects. In our specific example, this can be seen by comparing the 0.5 nm bandwidth of the MCF-laser with the 2.3 nm acceptance bandwidth of an LBO crystal with a typical length of 30 mm.
As a result, we will use a description of the electric field amplitude of our pulse that only considers the spatial and temporal amplitude variations as $A(x, y, t)$. This amplitude can be derived from the assumed intensity profile of the input pulse – in an idealized case, for example, a simple 3-dimensional Gaussian profile, or from user-defined intensity profiles derived, e.g. determined from measured data.

In section 2.1.4 we have already introduced the differential equations that describe the nonlinear propagation of the fundamental and the formation of the second harmonic pulse:

$$\begin{aligned} \frac{\partial A_{2\omega}}{\partial z} &= -\frac{j\omega d_{eff}}{n_{2\omega}c_0} A_\omega^2 e^{j\Delta kz}, \\ \frac{\partial A_\omega}{\partial z} &= -\frac{j\omega d_{eff}}{n_\omega c_0} A_{2\omega} A_\omega^* e^{-j\Delta kz}, \end{aligned} \tag{3.1}$$

In addition, linear propagation and natural diffraction of both pulses must be considered. This behavior is well described in the Fourier domain, where the intensity profile after propagation of length z can be calculated by multiplying the amplitude with a transfer function according to [246]

$$A(x,y,t)|_{z=z} = \mathcal{F}_{x,y}^{-1}\left[\mathcal{F}_{x,y}\left[A(x,y,t)|_{z=0}\right]\exp\left(i2\pi z\sqrt{\frac{1}{\lambda^2} - f_x^2 - f_y^2}\right)\right], \tag{3.2}$$

where $\mathcal{F}_{x,y}$ is the two-dimensional spatial Fourier transform, $\mathcal{F}_{x,y}^{-1}$ is the inverse Fourier transform, and $f_{x,y} = k_{x,y}/2\pi$ are the transverse spatial frequencies.

To combine the nonlinear and linear propagation in a single algorithm, a split-step Fourier approach is used. This means that the propagation through the nonlinear crystal is divided into N steps of length $dz = l_{\text{crystal}}/N$, in which the linear and nonlinear propagation are evaluated alternatingly. The nonlinear propagation step over the distance dz consists of solving the differential equations (3.1) using a 4th order Runge-Kutta method. The linear step, on the other hand, is performed in the Fourier domain according to the equation 3.2. The figure 3.6 illustrates the iterative algorithm and the corresponding Python code is available at [247].

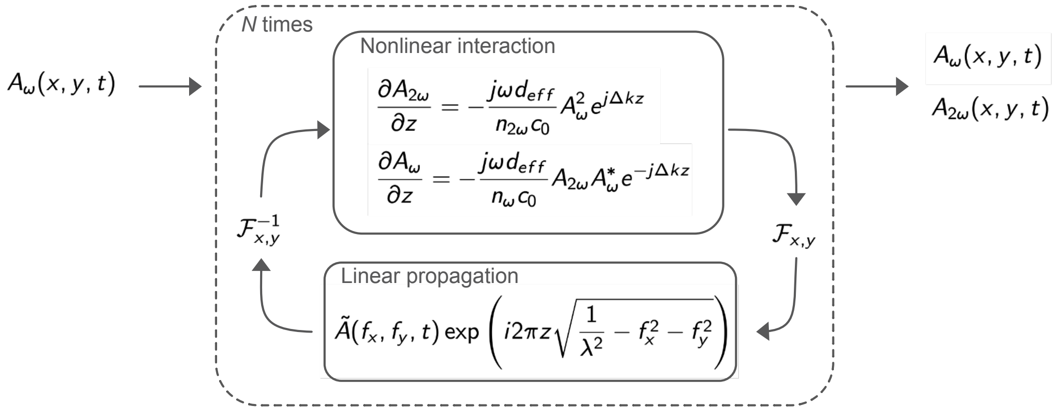

Figure 3.6 – Schematic overview of the SHG simulation steps

The results of this approach have been verified to agree with measurements of large-beam SHG setups and simulations of similar large-beam, long-pulse SHG setups using SNLO [245]. As we will see later in this section, the frequency conversion of small beams with significant diffraction – such as the MCF output – could also be reliably reproduced.

Using this approach, we can thus calculate the evolution of the MCF-lasers output pulse and its frequency doubled counterpart as it propagates through the second harmonic crystal. Figure 3.7 shows the SHG energy for a 2 mJ fundamental pulse with the previously described 20 ns duration and 187 μm beam diameter. The spatial and temporal intensity profiles are assumed to be perfectly Gaussian. After a propagation distance of 30 mm, a peak conversion efficiency of 77% is reached.

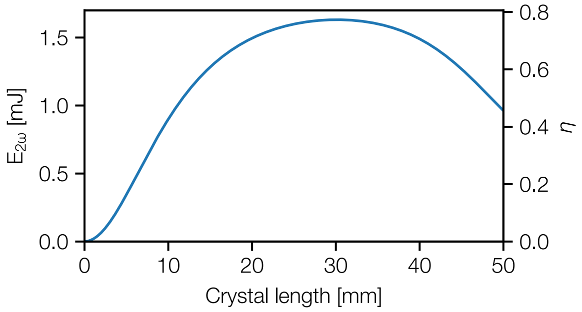

Figure 3.7 – Conversion efficiency of second harmonic generation in non-critically phase matched LBO with a peak intensity of 450 MW/cm^2 in the nonlinear crystal. The pulse energy of the fundamental is 2 mJ, the pulse duration is 20 ns FWHM and the $1/e^2$ beam radius is 93.75 μm.

First experimental results in frequency doubling of the MCF output

The 30 mm long crystal was therefore used to experimentally verify the conversion efficiency. For this purpose, the beam was focused into a 6x6x30 mm LBO crystal, which was set to the non-critical phase matching temperature of 190°C. The fundamental and second harmonic beams were separated immediately after the LBO crystal using dichroic mirrors that reflect the second harmonic. Figure 3.8 shows the resulting output power and the calculated conversion efficiency with a maximum of 51.7%, corresponding to a power of 17 W at 515 nm.

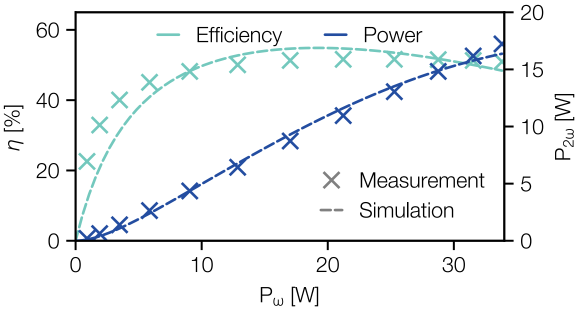

Figure 3.8 – Measured conversion power of the second harmonic, as well as conversion efficiency of the MCF-pumped SHG. The dashed curves show the simulated conversion efficiency and output power, using measured spatial and temporal intensity profiles as simulation inputs.

This measured efficiency is of course significantly lower than the previously estimated 77%. However, using the real intensity profiles of the fundamental that were present in the experiment (see figure 3.3 for the spatial profiles and figure 3.9 for the temporal shape), the calculated conversion efficiency decreases to only 52.5% at the input energy of 1.58 mJ, where the highest conversion efficiency of 51.7% was measured in the experiment. As can be seen from the overall trend of the output power in Figure 3.8, the simulations are in excellent agreement with the measurements.

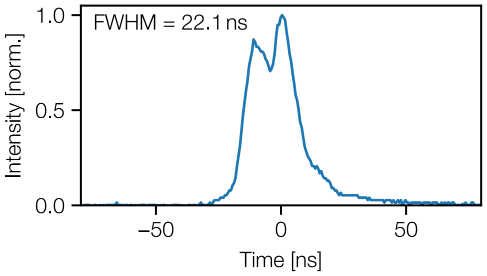

Figure 3.9 – Temporal profile of the MCF lasers output pulse that was used as an input for numerical simulations. The profile is measured using a fast photodiode.

Figure 3.10 compares the conversion of the idealized Gaussian pulses with that of the measured spatial and temporal intensity profiles. We can again see that the use of the real beam profiles has a significant impact on the simulated conversion efficiency. Furthermore, the conversion is sensitive to the exact focus position of the focus, and excellent agreement with the measurements is obtained by setting the focus position to 12.8 mm from the crystal input surface and by assuming a small temperature deviation of 0.2 K from the perfect phase matching temperature. Both adjustments are well within tolerance of the experimental parameters. Finally, we can see that an increase of the conversion efficiency to more than 65% should be possible in the experiment by optimizing the experimental setup, especially with respect to the crystal length.

The beam profile of the converted beam is shown in the figure 3.3. The right panels of the figure show the Gaussian far-field profile of the incoherently combined beams. The resulting single aperture intensity profile is suitable for pumping a Ti:sapphire amplifier. However, the Gaussian shape is not ideal for efficient energy extraction from a Ti:sapphire amplifier. To improve this, an intermediate beam profile can be used between the near-field and far-field planes, resulting in a flat-top intensity profile that is much more suitable for pumping high-energy amplifiers. As a consequence of the square arrangement of the fiber cores, the resulting flat-top beam profile is also square, but this can be made round by a suitable arrangement of the fiber cores [248].

Critical phase matching was tested in a 25 mm LBO crystal, but resulted in a conversion efficiency of only 40 %, which is expected to be caused by the above mentioned angular sensitivity of critical phase matching and spatial walk-off.

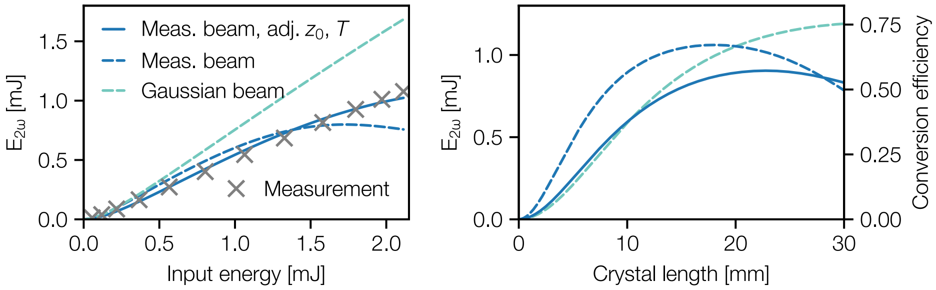

Figure 3.10 – Simulated output energy of the SHG. The left panel shows the output energy for different input beam properties: Gaussian pulses with optimized focus position and perfect phase matching, the same using measured spatial and temporal profiles, and finally measured profiles with adapted focus position z_0 and crystal temperature T to optimize the agreement with the measurement. The right panel shows the pulse energy along the propagation through the LBO crystal for the respective scenarios and at an input pulse energy of 1.58 mJ, where the highest conversion efficiency was observed in the experiment.

These first experimental results are a promising first step towards demonstrating the feasibility of multicore fiber lasers as a potential pump for Ti:sapphire-based laser systems.

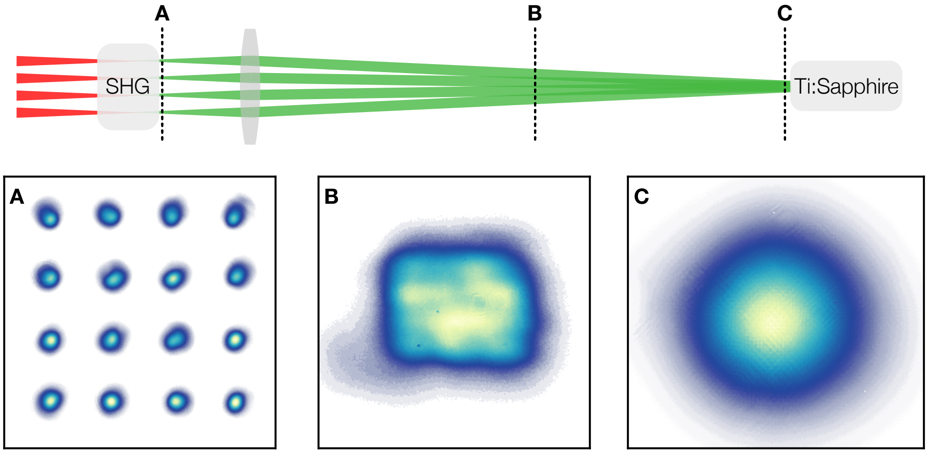

Figure 3.11 – Beam profiles of the frequency doubled MCF output. A: The array of beamlets imaged at the SHG crystals output, B: an intermediate image plane where a flattop beam profile is achieved and C: far-field beam profile of the incoherently combined beams. For comparison, see also the profiles of the fundamental beams in figures 3.3 and 3.4.

3.2.3 Frequency Conversion of a 2.5 kW MCF Fiber Laser

With the first demonstration of frequency doubling of an MCF laser's output, along with good agreement with theory, we can now consider a full-scale joule-level version of the setup with an envisioned MCF fiber setup of $16 \times 16 = 256$ cores and an output energy of 10 mJ, which is well within realistic limits for multi-mode fibers. After first looking at the slightly modified conversion process due to the higher pulse energy, we will proceed with some thermal considerations that need to be taken into account at the 2.5 kW average power of the entire MCF output.

Second Harmonic Generation

In particular the higher power per MCF core has significant advantages for second harmonic generation, which can result in greatly improved conversion efficiency because larger beam sizes can be used in the nonlinear crystal, largely eliminating the propagation effects that limited conversion efficiency in early experiments. For example, in the case of M=8.3 imaging from the MCF fiber to the SHG crystal – for which the peak intensity would remain approximately the same – the beam size and therefore the Rayleigh length would be more than doubled, resulting in an almost negligible beam size variation during propagation through the nonlinear crystal (see figure 3.12).

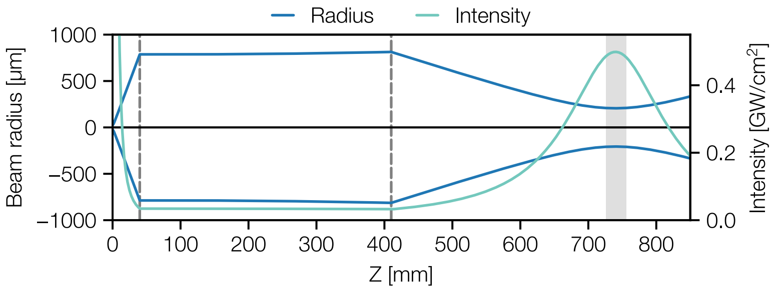

Figure 3.12 – Radius ($1/e^2$) of an individual beamlet in the relay imaging from the output facet of a fiber to the SHG. Compared to figure 3.5, the magnification is increased to M=8.3 to maintain an approximately equal peak intensity of 480 MW/cm^2. The variation of the intensity along the propagation through the LBO crystal is however decreased to only approximately 4.5%.

As a result of this reduced diffraction, the simulated conversion efficiency increases to 85% for ideal, Gaussian pulses and to 83% using the measured beam properties. Increasing the single-core energy is therefore an important step in increasing the efficiency to a level comparable to other high-energy nanosecond laser systems. If such an energy increase is achieved, it would also have a significant impact on the overall efficiency of the pump laser system. As a result, fewer pump lasers would be required for the Ti:sapphire amplifier, significantly reducing the overall cost of the laser system.

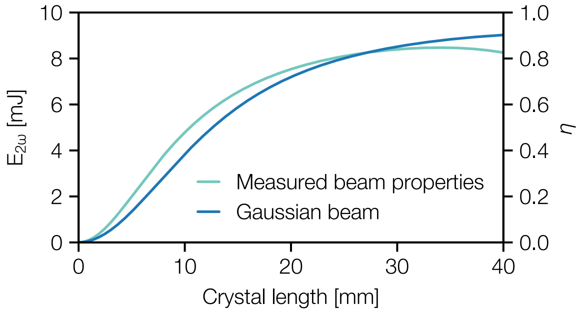

Figure 3.13 – Conversion efficiency of second harmonic generation in non-critically phase matched LBO with a peak intensity of 480 MW/cm^2. The pulse energy is 10 mJ, the pulse duration 20 ns FWHM and the beamsize is magnified by a factor of 8.3 from the fiber output facet. The minimal beam waist of the Gaussian beam is thus 206 μm.

Thermal Considerations at High Average Power

While the bulk absorption of LBO at both the 1030 nm and 515 nm wavelengths is low at approximately 2 ppm/cm and 8 ppm/cm, respectively, in high quality crystals [249], LBO also shows a strong thermal dependence of the phase matching conditions, and thus it is necessary to evaluate whether the high average power leads to a locally varying temperature increase in the crystal that may degrade the conversion efficiency. To estimate whether this is a limiting factor for the conversion efficiency of a high average power SHG, we simulate the thermal gradients in such an SHG crystal using COMSOL Multiphysics [250] with its heat transport module. As input parameters for the simulation we used the thermal properties of LBO published in [251] and a crystal aperture of 30 × 30 mm^2. The beam properties and crystal length are the same as in the previously described simulations of the second harmonic generation itself. We assume a room temperature of 300 K as the base temperature applied to the outer faces of the crystal, and consider radiative and convective cooling on the input and output faces of the crystal. The locally varying heat source was calculated from the locally absorbed power using the respective power of the fundamental and second harmonic at the values shown in figure 3.13 as well as the above mentioned absorption values for the fundamental and second harmonic.

At the maximum average power of 2.56 kW in the entire array of beamlets, we observe a peak-to-peak temperature difference of approximately 70 mK. The temperature distribution follows a radial symmetry with a peak reached towards the output side

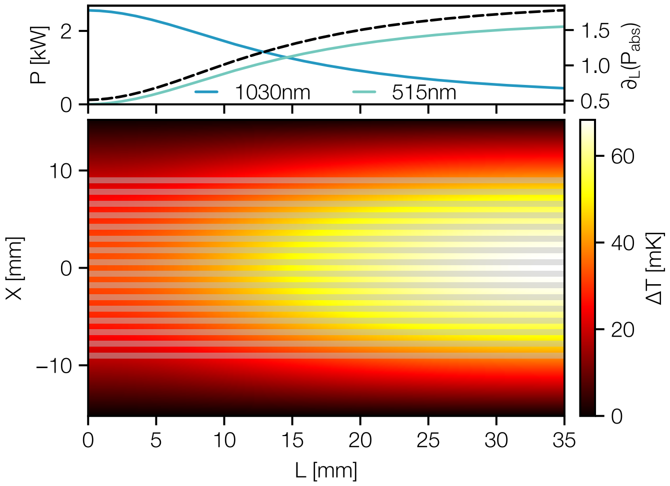

Figure 3.14 – Top: Total power (solid lines) of the fundamental and second harmonic beams, as well as locally absorbed power $\partial_\mathrm{L}(P_\mathrm{abs})$ in mW mm^{-1} (dashed line). The bottom shows a cut through the central portion of a non-critically phase matched SHG crystal and resulting temperature distribution. The shaded areas show the location and size of the beamlets as a reference. The peak-to-peak temperature difference is 70 mK.

of the crystal where the total absorbed power is high due to the high fraction of power at 515 nm (see Fig. 3.14). The temperature difference would result in a Δk of approximately 130 mrad, which would correspond to a reduction in conversion efficiency of about 1 %, and thus the induced thermal gradients are indeed negligible and LBO is a feasible nonlinear medium for generating second harmonic even at kW average power.

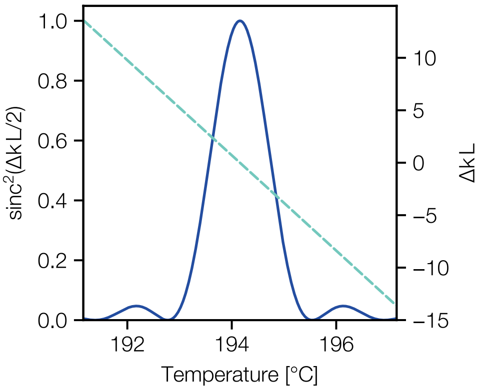

Figure 3.15 – SHG conversion efficiency (solid line) and accumulated wavevector mismatch $\Delta k\,\mathrm{L}$ (dashed line) as a function of temperature deviation for a 35 mm long LBO crystal for non-critical phase matching.

3.2.4 Outlook on High Average Power Pump Generation

Multi-core fiber-based lasers have been shown to be capable of delivering kW-level average power in a compact setup, and due to their scalability in the core count, they should also scale in pulse energy, resulting in a potential path toward the generation of Joule-level pulses at 1030 nm. In contrast to other high-energy Yb and Nd lasers [107, 252], the MCF approach is more compact and does not require complex cooling technologies such as cryogenic amplifiers.

The results we have presented in this section show the very first conversion of the multi-aperture beam of such a laser to 515 nm. In our experiments, we achieved a total output energy of 17 mJ, which can be converted into a smooth, high-quality beam profile suitable for pumping Ti:sapphire amplifiers. The measured output energy is well reproducible in simulations using a custom simulation code. In those simulations, we also see that the conversion efficiency in the experiment was limited by the properties of the MCF laser itself – in particular, the 2 mJ pulse energy of a single core. However, it has already been shown experimentally that scaling to higher energies is possible, which will make it possible to increase the conversion efficiency to a level comparable to other high-energy laser systems. In fact, new fibers with a higher number of cores and higher output energy per core are under development, bringing the average power closer to the ultimately desired kW level, which would be needed to pump a kW-level drive laser for laser wakefield acceleration.

Further simulations of the thermal gradients that develop in the LBO crystals, show that the described SHG-setup is scalable to multi-kW level average power. The thermal gradients that develop in a 2.5 kW laser will not have a significant influence on the phase matching conditions of the frequency conversion and will not limit the performance of such a potential future pump laser.

3.3 High Average Power Ti:sapphire Amplifiers

In a first phase of the development of the KALDERA laser system, an operation with at an on-target pulse energy above 500 mJ at 100 Hz repetition rate will be targeted. This has been simulated to be sufficient for the acceleration of high quality electron bunches to around 100 MeV at the unprecedented repetition rate of 100 Hz [253].

The planned layout of the laser system is shown in figure 3.16. Seed pulses will be delivered by the femtosecond OPCPA front-end described in chapter 2, which will then be stretched to about 400 ps duration in a four-pass opener stretcher based on transmission gratings [50], before being sent into an acousto-optical programmable dispersive filter (AOPDF) [103] to fine-tune the dispersion and precompensate for gain narrowing in the subsequent Ti:sapphire amplifiers. The first of these – a three-pass booster amplifier – will boost the pulse energy to approximately 500 μJ, with a

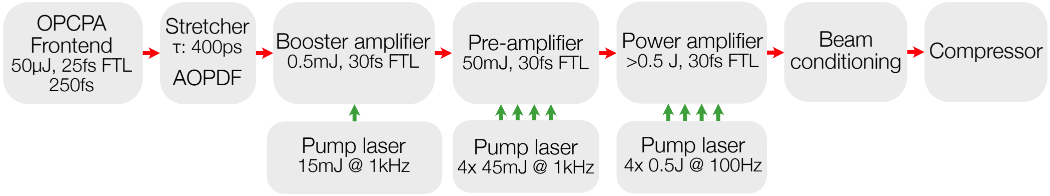

Figure 3.16 – Overview of the amplification chain of a first development stage of KALDERA.

maximum available pump energy of 15 mJ at a repetition rate of 1 kHz. The second amplifier will be pumped with a total of up to 180 mJ delivered by four pump lasers, also operating at 1 kHz. The amplifier will be a cryogenic seven-pass multipass amplifier with an output energy of approximately 50 mJ. The final amplifier – the focus of this chapter – will operate at 100 Hz and aim to deliver at least about 600 mJ to enable a pulse energy of about 500 mJ after compression in a four-grating compressor based in an out-of-plane configuration and multi-layer dielectric gratings [50], with an expected transmission of $> 80\%$. A beam conditioning section for fine tuning the pulse energy and correcting wavefront distortions using adaptive optics is planned between the final amplifier and the compressor.

The high power density in the amplifier crystal of COLIMA would – if not handled properly – result in significant thermal lensing and degradation of spatial beam quality. In the following sections, we will therefore first review some general challenges of high average power Ti:sapphire lasers and some solutions suggested in the literature, before discussing a possible design of COLIMA and how the amplifier is set up to achieve the planned output specifications.

3.3.1 High Average Power Amplification in Ti:sapphire

The main challenge in high average power laser systems is to maintain high wavefront quality, which is easily distorted by thermally induced optical path length differences in the amplifier medium. The main causes of these phase aberrations are the bulging of the amplifier medium due to thermal expansion and a thermally dependent refractive index $n(T) = n_0 + \Delta n_T + \Delta n_\epsilon$ [254], where Δn_T and Δn_ϵ are the temperature and stress dependent refractive index changes, respectively. Due to the typically radially varying temperature gradients in an amplifier medium, these pathlength differences result in a radial dependence that causes effective lensing of a beam passing through the amplifier medium. In typical pumping configurations, the temperature in an amplifier medium follows a roughly parabolic profile, resulting in an effective thermal focal length of [254]

$$f_{\text{therm}} = \frac{KA}{P_{\text{heat}}} \left(\underbrace{\frac{1}{2}\frac{dn}{dT}}_{\text{Temperature-dependent } n} + \overbrace{\alpha C_{\mathrm{r},\Phi} n_0^3}^{\text{Photo-elasticity}} + \underbrace{\frac{\alpha r_0 (n_0 - 1)}{l}}_{\text{Thermal expansion}} \right)^{-1} , \tag{3.3}$$

where A is the pumped area, K the thermal conductivity, P_{heat} is the dissipated heat, dn/dT is the temperature dependence of the refractive index, α the coefficient of thermal expansion, $C_{\mathrm{r},\Phi}$ the photo-elastic coefficient, r_0 the radius of the pumped area and l the length of the amplifier medium. The respective terms that describe the three main contributions to the thermal lens are marked in the above equation. Specifically in Ti:sapphire, the photo-refractive contribution is often negligible, while the temperature dependent refractive index and the thermal expansion of the medium have roughly equal contributions [255].

If we assume operation near the saturation fluence F_{sat}, equation 3.3 can be rewritten as

$$f_{\text{therm}} \propto \frac{K}{F_{\text{sat}} \mathrm{f}_{\text{rep}}} \left(\frac{1}{2}\frac{dn}{dT} + \alpha C_{\mathrm{r},\Phi} n_0^3 + \sqrt{\frac{E}{F_{\text{sat}}\pi}} \frac{\alpha (n_0 - 1)}{l} \right)^{-1} , \tag{3.4}$$

and we see that the thermal focal length scales according to $\propto 1/\mathrm{f}_{\text{rep}}$, while only the term corresponding to thermal expansion scales weakly with energy ($\propto \sqrt{E}$). This suggests that managing the thermal lens, and in general the thermal characteristics of a laser, is much more important when increasing the repetition rate than when increasing the pulse energy of a laser system.

A number of strategies have been developed to mitigate thermal lensing. The most widely used are based on optimizing the heat extraction from the amplifier medium by adjusting the geometry and optimizing the heat flow within the amplifier medium. The two most common geometries suitable for high-energy laser systems that utilize this approach for high energy lasers are disk amplifiers and slab amplifiers.

In slab amplifiers [256] (see figure 3.17 a) and b)), the size of the transverse dimensions of the amplifier crystal is minimized so that thermal transport - and thus thermal gradients - are primarily present in a direction perpendicular to the direction of beam propagation. Strictly speaking, this does not solve thermal lensing, but it limits it to one axis, making it somewhat easier to handle. The advantage of this approach is that the variation in beam size due to thermal lensing can be minimized by maintaining a small beam diameter in the fast axis - the direction of strong thermal lensing - so that diffraction and thermal lensing largely cancel each other out. The strong astigmatism and elliptical beam shape emitted from such an amplifier must be treated after the amplifier to maintain a uniform and high beam quality.

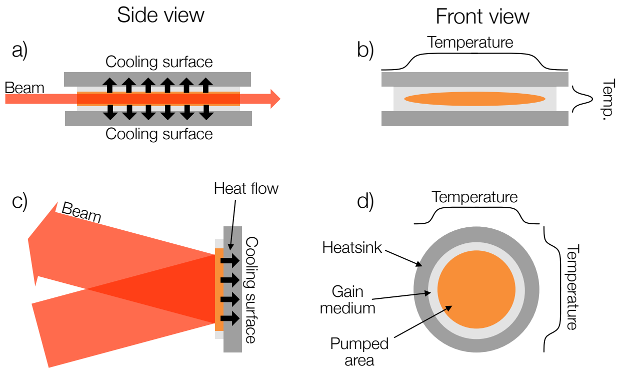

Figure 3.17 – Schematic overview of the cooling geometry of slab (a) and b)) and disk (c) and d)) amplifiers. The black arrows in a) and b) indicate the primary direction of heat flow and thermal gradients within the amplifier medium. c) and d) show a frontal view of the amplifier medium to illustrate the differences in beam shape and thermal gradients that lead to thermal lensing.

Disk amplifiers [257, 258] (see figure 3.17 c) and d)) minimize the longitudinal dimension of the amplifier crystal, such that thermal gradients are predominantly present in the direction parallel to the propagation of the beam. This leads to a more even temperature profile across the beam aperture and – due to the primarily longitudinal heat extraction – can eliminate the parabolic temperature gradients that cause the lensing.

However, this approach has a fundamental disadvantage for Ti:sapphire lasers with <1 J: To ensure the primarily longitudinal direction of thermal gradients, a high aspect ratio of the disk must be maintained, which means that the thickness of the disk must be small compared to the diameter – typically an aspect ratio of 1:10 or less is required. Since it is desirable for efficient energy extraction and stability to operate laser amplifiers at or above the saturation fluence of the gain medium, the beam diameter must be scaled according to the desired pulse energy after amplification. However, for Ti:sapphire amplifiers (with a saturation fluence around $0.7\,\mathrm{J/cm^2}$) operating at sub-joule energies, this results in disk thicknesses of less than a mm, leading to low single-pass gain and poor pump absorption. This is particularly limiting for Ti:sapphire, as the doping concentration cannot be arbitrarily increased without loss of crystal quality, whereas the low gain can be partially compensated for by exactly this method, e.g. in Yb:doped gain media.

Typically, such disk amplifiers are operated in an active mirror configuration with a highly reflective coating on the backside of the amplifier medium. This allows the backside of the disk to be used solely for cooling components such as a heat sink, but

the low single pass gain and low pump absorption result in the need for many passes of the pump and seed beams over the active mirror and thus complex beam routing of the pump and seed beams.
Concepts using a disk amplifier in a transmissive geometry have also been developed [259–264], but to ensure efficient heat removal from the disk, a liquid or gaseous coolant must be passed over the front and back surfaces of the disk so that the seed beam is transmitted through the coolant. For applications such as laser wakefield acceleration, where the highest possible wavefront stability is required, such an approach is not good because potential turbulence in the coolant can disturb the wavefront of the amplified beam. Mitigating such turbulence is possible, but requires a thorough understanding of the phenomenon and considerable engineering effort in the cooling assembly.

Slab amplifiers are more suitable for small aperture, low energy beams, but the need for complex beam conditioning to compensate for the elliptical beam profiles and astigmatism of the amplified beams makes this approach attractive only when no other approach is feasible. While both of these architectures have been implemented with Ti:sapphire as the amplifier medium [265–267], their scalability to kW average power with high-energy lasers is questionable.

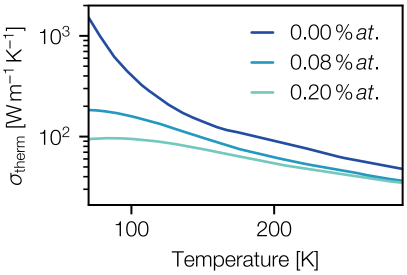

Figure 3.18 – Thermal conductivity of pure sapphire [268] and Ti:sapphire with doping concentrations of 0.08 % *at.* and 0.2 % *at.* [269]

Another approach that works particularly well for Ti:sapphire amplifiers is cryogenic cooling of the amplifier crystals [270–272]. At cryogenic temperatures, all relevant thermal properties of sapphire (see table 3.1) improve significantly, so that – using equation 3.3 – we can estimate an approximately 300-fold increase in the focal length at 100 K compared to room temperature.

While the corresponding improvements are slightly lower for doped Ti:sapphire (see e.g. figure 3.18), cryogenic cooling enabled the construction of high average power Ti:sapphire amplifiers at kHz repetition rate and millijoule level pulse energy [274–277] in simple bulk crystals.

As a side effect of cryogenic cooling, the fluorescence characteristics of Ti:sapphire are slightly changed, resulting in a slight blue shift and narrowing of the fluorescence

Table 3.1 – Parameters of the sapphire at cryogenic and room temperature [273]

	At 290 K	At 100 K
Thermal conductivity, K [$\mathrm{W\,m^{-1}\,K^{-1}}$]	47.8	405.6
Thermal dependence of the refractive index, dn/dT [$10^{-5}\,\mathrm{K^{-1}}$]	0.62	1.46
Coefficient of thermal expansion, α, $\parallel$C [$\cdot 10^{-6}\,\mathrm{K^{-1}}$]	4.87	0.6
α, $\perp$C [$\cdot 10^{-6}\,\mathrm{K^{-1}}$]	3.89	0.6
Heat capacity, c_p [$\mathrm{J\,kg^{-1}\,K^{-1}}$]	779	62.8

spectrum [278] as well as an increase in the emission cross section [279], which lowers the saturation fluence and thus allows a slightly increased efficiency of the Ti:sapphire laser [279].

3.3.2 Colima: Concept for a 100 Hz, 1 J Ti:sapphire Amplifier

Inspired by the results obtained with other cryogenic lasers, cryogenic cooling will also be implemented in the preamplifier and is a viable option for – COLIMA – the main amplifier (see fig. 3.16) of the first development stage of KALDERA. Experimental results [274] as well as simulation results on the kHz, 50 mJ preamplifier of KALDERA, operating at an average power similar to that expected from COLIMA, suggest that advanced heat removal methods such as a disk or slab-based amplifier geometry are not necessary. In fact, thermal lensing should become much more manageable due to the larger beam sizes (compare equation 3.3) needed for the desired higher pulse energy. Hence, the suitability of a cryogenically cooled bulk crystal will be investigated in this section. In the final section of this chapter, we will further explore the limitations of this chosen architecture and briefly investigate the scalability towards kHz-level repetition rates.

Using typical efficiencies of Ti:sapphire amplifiers, we can estimate that about 2 J of pump energy is needed to achieve the >600 mJ required as the output energy of COLIMA. There are currently no commercially available pump lasers capable of delivering such energy at a repetition rate of 100 Hz. However, a number of frequency-doubled, neodymium-based 100 Hz lasers with an output energy of 600-700 mJ are available from various manufacturers. 3 to 4 such lasers would be needed to pump an amplifier like COLIMA. With four lasers, the total output energy would be sufficient to additionally homogenize the beam profiles, which is often necessary in high energy pump lasers to ensure a smooth spatial profile in the gain of the amplifier crystal. This is typically done using diffractive optical elements with efficiencies in the order of 85%. This would result in a remaining pump energy of >500 mJ per laser and the required total of 2 J. We will keep the option to use this approach and assume the use of 4 500 mJ lasers in the following considerations.

The preamplifier that will supply the seed pulses for COLIMA was developed by J.B. Gonzalez and was in a build-up phase at the time of the design of COLIMA, so the seed parameters for COLIMA are derived from simulations of the preamplifier. As described above, it delivers approximately 50 mJ pulses at a repetition rate of 1 kHz, although an available seed energy of 40 mJ is assumed for the simulations described in the following to account for potential losses in beam transport and beam conditioning stages between the amplifiers. The pulses are centered at 800 nm with a bandwidth that supports compression down to 30 fs. For simplicity, the spectral shape is assumed to be Gaussian for the design of COLIMA, although the AOPDF installed earlier in the gain chain (see fig. 3.16) will allow optimization of the spectral shape to avoid excessive gain constriction and redshift of the spectrum. The beam profile of the seed is primarily defined by the pump profile in the Ti:sapphire of the preamplifier and is also expected to be approximately second order Supergaussian.

Gain Simulations

As a first step towards simulating the expected gain dynamics of COLIMA, we should estimate an appropriate seed beam size. Since a high extraction efficiency of the pump energy stored in the amplifier is desired, the amplifier is operated in saturation, which typically results in pump-to-seed efficiencies above 30 % in high energy Ti:sapphire amplifiers. This results in a rough estimate of the expected output energy of at least 600 mJ, which with a saturation fluence of about $0.6\,\mathrm{J\,cm^{-2}}$ results in a required beam diameter of 11 mm.

At high doping concentrations, Ti:sapphire can exhibit significant parasitic absorption at 800 nm, which is characterized by the figure of merit FOM $= \alpha_{\mathrm{pump}}/\alpha_{\mathrm{seed}}$. High quality crystals with FOM>400 are commercially available [280] with doping concentrations below about 0.14 % *wt.* [281] or a corresponding absorption coefficient of $\alpha_{532\,\mathrm{nm}} = 2/\mathrm{cm}$. To ensure a simple beam guiding for the pump beams, a single pass absorption of 95 % is desired, which would be achieved with a crystal length of 15 mm and $\alpha_{532\,\mathrm{nm}} = 2/\mathrm{cm}$.

The 3-dimensional gain dynamics were simulated using CommodPro [282]. Work by J.B. Gonzalez verified the validity of CommodPro by accurately reproducing the gain of the preamplifier and Amp1 (see section 1.2 for details) of the ANGUS laser system. For COLIMA, the 3D simulations include a crystal and an input beam with the above specifications. In addition, relay imaging with 5 % energy loss between passes is assumed. Noncollinear propagation through the amplifier medium in a multi-pass amplifier with angular multiplexing has been observed to cause only 1 % level changes in output energy and no change to the amplified beam profile for small non-collinear angles $< 4^\circ$, and is therefore neglected. The spatial profile of the pump beams was assumed to be a fifth-order Supergaussian.

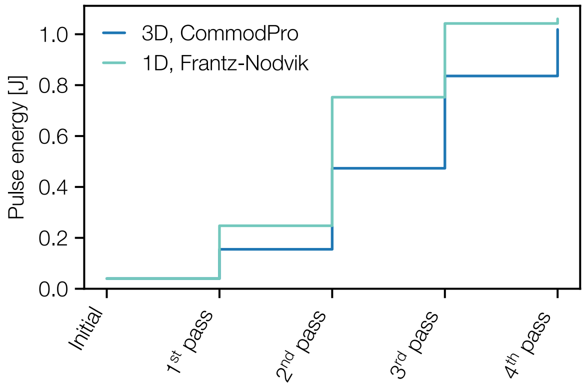

Figure 3.19 – Evolution of pulse energy in COLIMA

The resulting evolution of the pulse energy from the input to the output of the amplifier is shown in figure 3.19. The maximum pulse energy after four passes is 1.02 J, which agrees well with calculations done using a simple 1-dimensional Frantz-Nodvik-calculation [254], which predicts a final pulse energy of approximately 1.06 J. The 3D-model predicts slightly lower gain and therefore slower saturation than the 1D-model due to the lower fluence on the edges of the beam profile.

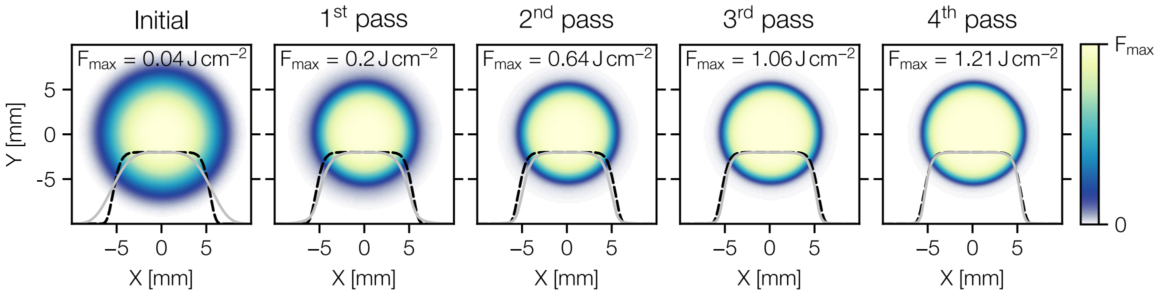

Figure 3.20 – Beamprofiles after the respective passes in COLIMA, as well as the respective peak fluence F_{max}. The grey lines show a central lineout through the beam profile, while the dashed lines indicate the intensity profile of the absorbed pump.

The accumulated B-integral [254] in the Ti:sapphire crystal is 0.13 rad, which is low enough to not cause significant problems with contrast degradation due to nonlinear couplings [94], or instability of the spatial or spectral phase of the pulse. For the calculation of the B-integral, a stretched pulse duration of 400 ps was assumed.

The Supergaussian beam profile of the pump is imprinted onto the seed pulse within the first 3 passes (see figure 3.20). The peak fluence of $1.21\,\mathrm{J\,cm^{-2}}$ is well below the damage threshold of all necessary optics of the multipass arrangement.

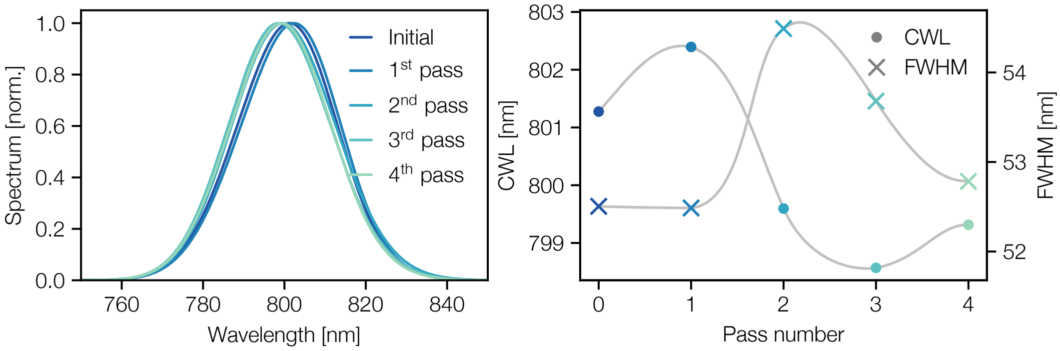

Figure 3.21 – Evolution of spectrum during amplification in Colima. The grey lines in the right pane are shown to guide the eye.

The evolution of the spectrum during the amplification is depicted in figure 3.21. In total, a shift of the spectrum by approximately 1.5 nm, and a minor change in FWHM bandwidth by only 0.4 % was observed as a consequence of spectral shaping in the amplifier. In contrast to most Ti:Sapphire amplifiers operated at room temperature, the slight blue-shifting of the gain spectrum in cryogenically cooled Ti:Sapphire [278] results in a decreased red-shift of the spectrum during amplification.

For pumping the Ti:sapphire crystal, a two-sided longitudinal pumping configuration is favored primarily because it leads to more homogeneous pump absorption throughout the crystal volume than a one-sided pumping scheme. This results in a more homogeneous heat distribution and therefore in smaller thermal gradients and in addition in a lower transverse gain in the amplifier and therefore smaller losses due to amplified spontaneous emission. The transverse gain along the longitudinal axis through the crystal can be estimated using [283]

$$G_T(z) = \exp\left(2r\frac{F_p(z)}{F_{\mathrm{sat}}}\frac{\lambda_{\mathrm{pump}}}{\lambda_{\mathrm{seed}}}\right), \tag{3.5}$$

where r is the radius of the pumped ares, $F_p(z)$ is the fluence of the absorbed pump along the longitudinal axis z, and λ_{pump} and λ_{pump} are the respective wavelengths of the pump and signal. For our crystal and pumping parameters, the maximum estimated to be about 170 for one-sided pumping and only 15 for two-sided pumping. The respective curves of $G_T(z)$ are shown in figure 3.22. However, neither of these values is expected to cause significant losses due to transverse amplified spontaneous emission [283]. In addition, with the four available pump beams, two-sided pumping can be realized in a more practical and space-efficient manner than one-sided pumping.

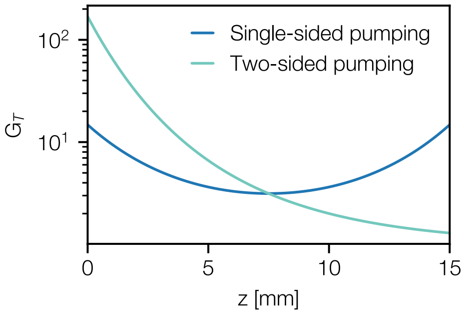

Figure 3.22 – Transverse gain for one-sided and two-sided pumping of the Ti:sapphire crystal. The pump diameter is 11 mm and the pump energy is 2 J.

All of these parameters lie well within limits that promise the generation of high quality, high energy pulses in Colima and we shall therefore turn our attention to the management of the heatload that is dissipated in the amplifier crystal.

Thermal Lensing

The heatsink of the cryogenic bulk Ti:sapphire crystal that we will assume in the following simulations the is inspired by a design developed at DESY for high average power Yb:doped lasers and its functionality has been demonstrated in several publications [284–289]. The design relies on one-sided cooling with the rectangular crystal being bonded to a heatspreader, which is connected to a cryocooler (similar to the design described in [290]).

In our specific case, the heatspreader consists of a cylindrical copper disk onto which the Ti:sapphire is bonded. The heatspreader is attached to the cold surface of a solid state cryocooler operating at 100 K. The crystal itself has a square aperture of 25 mm side length which was dimensioned to eliminate any potential diffraction of the fifth order Supergaussian seed beam with its 11 mm diameter, and is oriented with the C-axis perpendicular to the cold surface of the heatspreader.

The heat-transport and thermal expansion of the Ti:sapphire crystal under the previously described pumping conditions, were simulated using COMSOL Multiphysics. The heat source is given by the absorption of a flat-top pump beam with an absorption coefficient of 2/cm. Half of the pump power is sent into the crystal from each side, resulting in uniform absorption and local variation of the introduced heat, as shown in figure 3.24. We assume that 50 % of the total incident pump power of 200 W is converted into heat, which slightly overestimates the approximately 40 % that would be expected from the quantum defect and non-radiative decays.

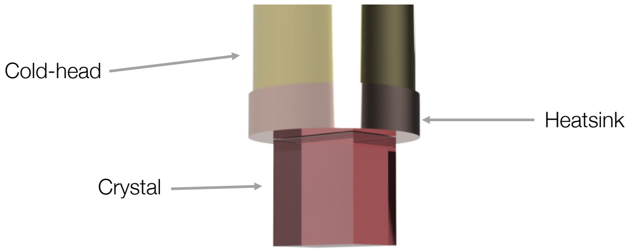

Figure 3.23 – Overview of the cooling assembly as it was used in the thermal simulations.

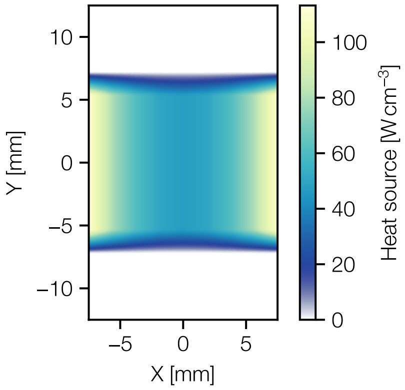

Figure 3.24 – Central cut of the crystal with the locally introduced heat due to the absorbed pump throughout the amplifier crystal. The local heatload is used as an input for the thermal simulations.

The surface of the heatspreader that is attached to the cold-head is set to a constant temperature of 100 K, which is well within the capabilities of cryo-coolers with high cooling capacity [291]. The heatspreader is assumed to be rigidly attached to the cold-head, which limits the thermal expansion in the plane of this surface. The used material properties of the Ti:sapphire are given in references [268, 269, 273, 292]. A boundary layer between the crystal and the heatspreader was included in the simulations to account for the thermal resistance at the bonding interface[1]. Equivalent simulations of the preamplier – which has a very similar heatsink design with slightly different dimensions – resulted in a deviation of <5 % ($f_{\mathrm{sim}} = 5\,\mathrm{m}$, $f_{\mathrm{exp}} = 5.2\,\mathrm{m}$) between the simulated and measured focal length of the thermal lens, confirming the general validity of the simulations[2].

---

[1] The exact parameters of the interface and bonding procedure are confidential and property of the FS-CFEL group at DESY

[2] Measurement of the thermal focal length done by J.B. Gonzales

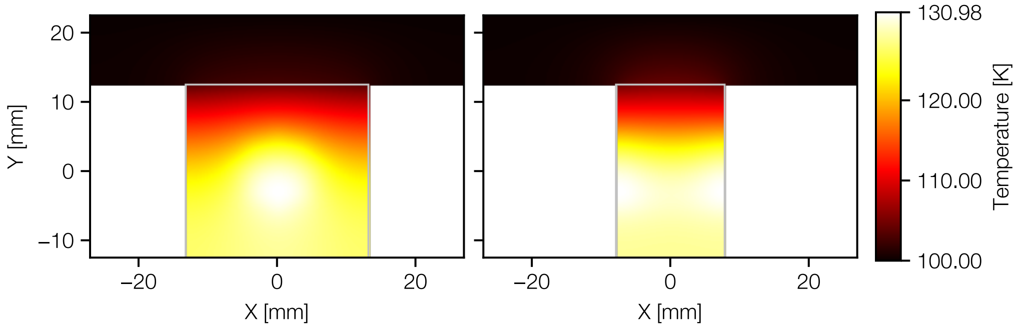

Figure 3.25 – Temperature distribution within the amplifier crystal and heatsink. The left image shows a front view in beam direction, while the right is a cut through along the axis of beam propagation. The grey rectangle shows the outline of the Ti:sapphire crystal

The temperature distribution that is reached in thermal equilibrium is shown in shown in figure 3.25. The peak-to-peak temperature difference within the crystal volume is 27.5 K.

This 3-dimensional temperature profile, and the resulting locally varying refractive index as well as the simulated deformation of the crystal was then used as the input to a ray-tracing simulation to calculate the propagation of the seed beam after a single pass through the crystal. The resulting evolution of the rms-beamsize is shown in figure 3.26, which shows that a focus is reached after approximately 56 m of propagation. This result is also in good agreement with the estimated focal length of 52.9 m, which can be derived using equation 3.3 and photo-elastic properties of Sapphire found in [293].

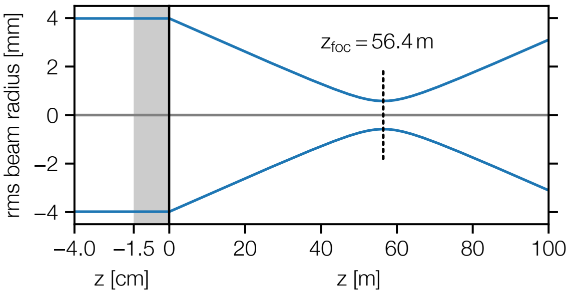

Figure 3.26 – Simulated caustic after single pass through amplifier crystal. The shaded area in the left part of the plot indicates the location and extent of the crystal.

Mainly due to the one-sided cooling of the crystal, the thermal lens does not lead to a clean, perfect lens, but some higher order wavefront aberrations are present, as shown in figure 3.27.

A Zernike analysis shows that the primary aberration is a 0° astigmatism due to the different temperature profiles in the vertical and horizontal directions. With its small amplitude of $-\lambda/69$, it however does not cause a significant degradation of the beam profile within the amplifier or during further propagation – even after multiple transmission through the crystal – and can be corrected with a deformable mirror in the beam conditioning section planned after COLIMA. The total peak-to-valley wavefront amplitude of a single pass of the higher order Zernike components is $\lambda/12$, comparable to the typical wavefront error of unpumped Ti:sapphire crystals [280]. The corresponding Strehl ratio of the transmitted wavefront is 0.985.

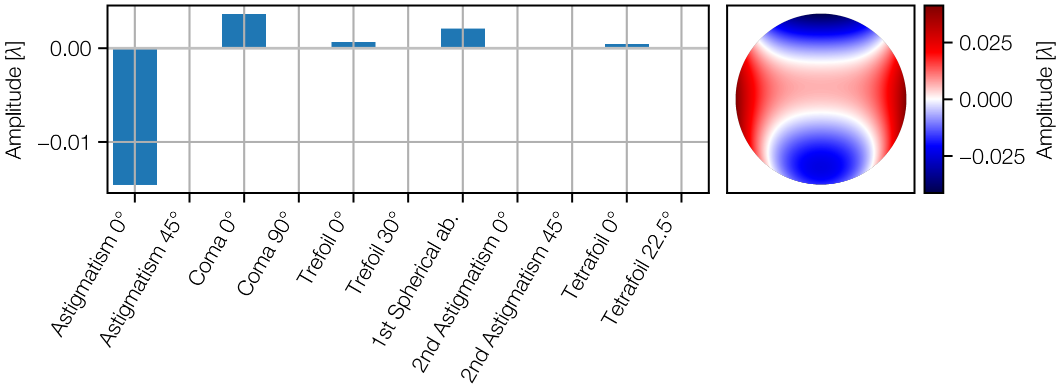

Figure 3.27 – Higher order wavefront after a single pass through amplifier crystal. The Zernike polynomials for defocus and tilts have been subtracted to emphasize the higher order wavefront aberrations.

We can therefore conclude that, according to our simulations, COLIMA should be able to deliver about 1 J of output energy without significant changes to the spectrum, and that a Supergaussian output beam profile and thermal gradients within the amplifier medium do not introduce aberrations that would degrade the quality of the beams. Without compensation of the thermal lens, repeated transmission through the amplifier crystal, with at least about 2 m propagation between each pass, would cause a reduction in beam diameter of at least 20% on the last pass for a collimated input beam. On the one hand, this means that the beam would be too small to extract the full pump energy stored in the crystal due to the worse spatial overlap, and on the other hand, the extracted energy is highly dependent on small changes in the thermal lens. It will therefore be necessary to compensate the lensing between each pass.

3.3.3 Proposed Optical Layout

While several methods have been developed to deal with thermal lensing and prevent it from negatively affecting the output of high-power multipass amplifiers, they can be broadly divided into two main approaches: The first uses a periodic arrangement of focusing and defocusing elements in the beam to maintain a roughly constant beam size as it propagates through the amplifier [294, 295]. The second relies on pass-to-pass relay imaging [296]. While the first approach can work well for high quality beams and a fixed operating point of the amplifier, any changes in the thermal lens will result in changes in beam size in subsequent passes, leading to complex couplings between output energy, wavefront, and possibly other parameters of the amplifier output. Since variations in pump laser parameters or laboratory conditions cannot be completely eliminated, such drifts in the characteristics of the amplified pulses will always be present to some degree. Relay imaging between passes offers a much more robust approach, as the beam profile remains constant in the amplifier crystal and only changes on the optics between passes through the amplifier medium.

A similarly robust approach based on a combination of relay imaging and optical Fourier transform has been proposed by Schuhmann *et al.* [297], and would have the additional advantage of passively compensating wavefront changes due to changes in thermal lens focal length. This approach has been considered, but due to the long thermal focal length and large beam size, would result in either impractically large setups with 100 m propagation between amplifier passes, or unsafe fluences on the optics. As a consequence, a relay imaging setup was chosen, which also prevents diffraction from affecting the beam profile with sharp intensity gradients, as in the final passes of COLIMA (see figure 3.20). The free propagation of such a beam profile leads to the formation of diffraction rings after only a few meters, making this issue highly relevant for the propagation between passes, which – in a conventional bowtie geometry with a small angle of incidence on the crystal – would have a length of at least 2-3 m.

To minimise chromatic aberrations of the broadband beam, the relay imaging is done using spherical mirrors. Figure 3.28 shows a proposed layout that includes relay imaging with spherical mirrors.

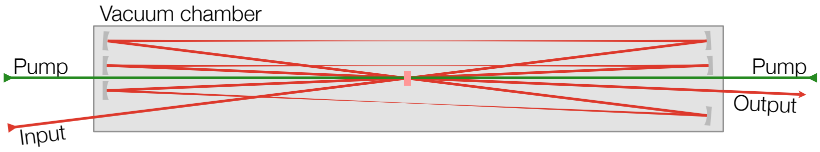

Figure 3.28 – Optical layout of the relay imaging multipass setup.

The off-axis use of spherical mirrors results in an astigmatism that gradually builds up during the repeated reflection, which can be minimized by choosing large focal lengths and small deflection angles. A reasonable compromise in terms of setup size and low astigmatism was found at a radius of curvature of 2 m for the spherical mirrors and an angle of incidence varying between 1° and 3°. The resulting caustic is shown in figure

3.29, where a thermal lens with $f = 56.4\,\mathrm{m}$ is included, resulting in a net focusing of the multipass setup. The total focal length can be compensated either by adjusting the separation of the focusing mirrors in the relay imaging telescopes, or in a separate telescope before or after the multipass amplifier.

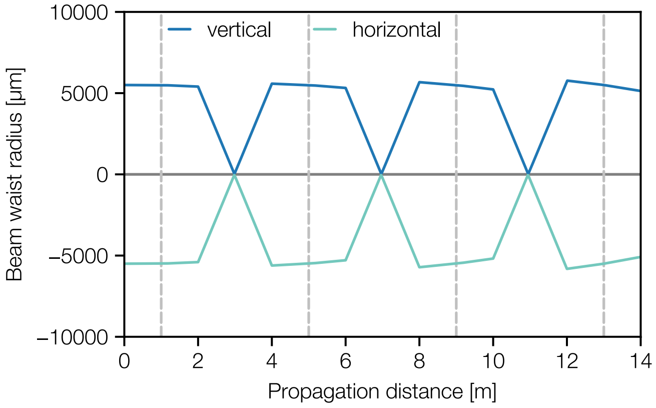

Figure 3.29 – Caustic through the relay imaged multipass amplifier. The dashed lines indicate the locations of the Ti:sapphire crystal.

The focal intensity in the relay imaging telescopes would be around $4.6\,\mathrm{TW\,cm^{-2}}$ on the last pass, making it necessary to have the focal area in reduced air pressure or vacuum to avoid nonlinearities and air breakdown. In order to keep the small angles of incidence as well as a compact setup, the best solution would be to house the entire multipass arrangement in the same vacuum vessel as the cryogenic crystal, as it is suggested in figure 3.28. The B-integral accumulated in the output window – assuming a 3 mm thick fused silica window [298] – is manageable at only 0.02 rad, but as a further improvement it would also be possible to include an output telescope inside the vacuum chamber to increase the beam diameter and reduce the intensity at the output window.

An equally compact approach with improved flexibility and constant access to all mirrors would be to place the relay imaging mirrors outside the vacuum chamber with the beam being transmitted through windows before and after each pass. The additional B-integral in that case would be around 0.15 rad, resulting in a moderate total B-integral of the full multipass arrangement of approximately 0.3 rad.

The relay imaging setup also provides a natural location for implementing spatial filtering between passes to further ensure high spatial homogeneity by filtering out high spatial frequency components of the beam. However, whether this is necessary depends strongly on the effectiveness of the pump homogenization, since inhomogeneities in the pump profile are expected to be the largest contributor to high spatial frequency intensity variations in the beam profile.

3.3.4 Concluding Remarks and Outlook towards first Experimental Results

Our simulations show that a cryogenically cooled Ti:sapphire crystal with a simple bulk geometry can be used to amplify 1 J pulses at a repetition rate of 100 Hz. A bandwidth supporting a 30 fs pulse duration is maintained during amplification. By cooling the crystals to a temperature of 100 K, thermal lensing can be mitigated so that a thermal focal length of >50 m is expected per pass. This focal length is predicted both by simple analytical estimates and by FEM simulation of the thermal transport and deformation of the Ti:sapphire crystal and subsequent ray tracing through the amplifier crystal. The ray tracing simulations also predict that some astigmatism is expected due to the temperature profiles in the Ti:sapphire crystal, but its amplitudes of only $\lambda/69$ is well manageable using adaptive optics. Nevertheless, we propose to use relay imaging between the passes in the amplifier to ensure stable operation and maintain a high quality beam profile.

Simulations indicate that pulses from such an amplifier are capable of accelerating electrons to the level of a few hundred MeV, which has not yet been done at the repetition rate of 100 Hz. To demonstrate this, an amplifier following the proposed optical setup is currently being built, and first experimental results of the amplifier's performance are expected in summer 2023.

This amplifier will also serve as a testbed for optimizing the cooling configuration, and the experience gained from operating the amplifier will be used to design future KALDERA amplifiers. These future amplifiers will run at a repetition rate of 1 kHz, which – as we have derived in equation 3.4 – will be another major challenge for the thermal design of the amplifier. While COLIMA is not designed to operate at 1 kHz, we can already look at how well the design would perform at higher repetition rates and what challenges to expect.

3.3.5 Scaling to Higher Repetition Rates

A relay imaging setup such as the one proposed for COLIMA is usable at focal lengths $f_{\text{therm}} \gg f_{\text{im}}$, where f_{im} is the focal length of the focusing elements in the relay imaging telescope. Since practical focal lengths are on the order of 1 m, this means that thermal focal lengths down to around 10 m could be handled. Looking at figure 3.30, we can see that the thermal lens power increases almost exponentially as a function of the incident pump power, and in the presented design, a focal length of 10 m would be reached at a pump power of 500 W. Even with a modular approach in which the total pump power is distributed across multiple amplifier modules, this approach would mean that – for a total pump power of 2 kW at 1 kHz operation – a total of 4 amplifier modules would be required. To ensure efficient extraction of the stored energy from the Ti:sapphire crystal, each crystal must be passed at least once with a fluence close to the saturation fluence, resulting in a total number of crystal passes of at least 8.

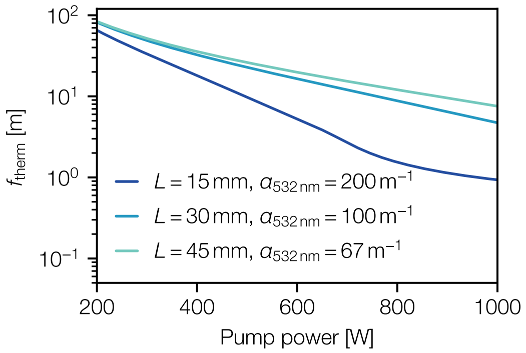

Figure 3.30 – Scaling of the thermal focal length as a function of incident pump power

A more scalable approach would be to optimize the thermal performance of each individual amplifier module. A simple way to do this is to reduce the absorption coefficient $\alpha_{532\,\mathrm{nm}}$ of the Ti:sapphire crystals and compensate for the reduced absorption by increasing the crystal length. This has several consequences, all of which contribute to reduced thermal gradients in the Ti:sapphire crystal. Most importantly, the more uniform pump absorption results in a more homogeneous heat load along the longitudinal axis of the crystal, and heat extraction is improved due to a larger contact area between the crystal and the heatsink, as well as the higher thermal conductivity of Ti:sapphire due to the reduced Ti^{+3}:doping (see figure 3.18).

As one can see in figure 3.30, a reduction of the absorption coefficient by a factor of 3 to $\alpha_{532\,\mathrm{nm}} = 67\,\mathrm{m}^{-1}$ and a corresponding increase of the crystal length to 45 mm would result in a manageable thermal focal length of 7.5 m at an incident pump power of 1 kW. The higher order wavefront content would deteriorate to a peak-to-peak value of $0.6\,\lambda$, with the most dominant aberrations still being astigmatism and coma with amplitudes of $-\lambda/15$ and $\lambda/12$, respectively. These aberrations are within the dynamic range of commercial adaptive optics and compensation in the image plane of the relay imaging telescopes would be possible, similar to what has been implemented in several other high power laser systems [299–302]. While correctable, these aberrations do have a clear impact on the beam quality and an optimisation of the cooling assembly should be done before using it at kW-level average power.
Further improvements in the temperature gradient can also be expected by reducing the single-pass absorption and recycling the pump in a second crystal pass, and by reducing the crystal temperature, e.g. to 80 K by liquid nitrogen cooling – in contrast to the 100 K temperature assumed in this section.

A potential drawback of this approach is the additional B-integral accumulated during the increased propagation length through the Ti:sapphire substrates. In the case of two crystals of 45 mm length, this would result in a total B-integral of about 0.8 rad, but could be counteracted by longer stretched pulse durations.

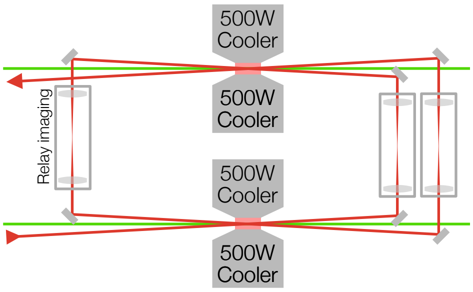

Figure 3.31 – Schematic overview of a potential adaptation of COLIMA for scaling to kW average power.

By combining two amplifier modules with these optimized crystal parameters into a single amplifier, the 2 kW power could in principle be handled by only two cold heads. Cryocoolers capable of handling the resulting 500 W heat load per cold head are commercially available [291], making this approach technically feasible. A sketch of a possible amplifier design suitable for kW average power is shown in figure 3.31. Here, the thermal load of the pump beams is distributed over two amplifier modules, each cooled by up to two 500 W cryocoolers. This would even result in some overhead in cooling capacity.

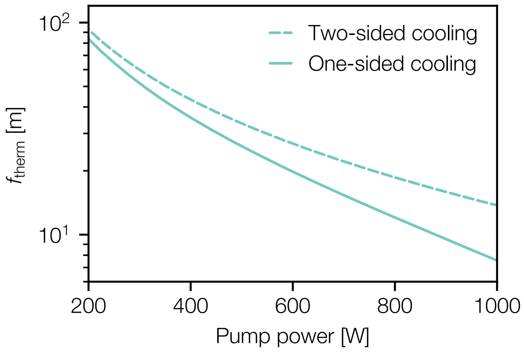

Figure 3.32 – Thermal focal length for one-sided vs two-sided cooling. The crystal parameters are the same as in the low-doping configuration shown in figure 3.30, i.e. a length of 45 mm and an absorption coefficient of $\alpha_{532\,\text{nm}} = 67\,\text{m}^{-1}$.

Such an approach could also be easily implemented in a way that would allow the heat to be extracted from both the top and bottom surfaces of the crystal, as it is sketched in figure 3.31. As indicated in figure 3.32, the resulting more efficient heat extraction would also allow to further increase the thermal focal length to about 14 m. The even more pronounced asymmetry of the thermal gradients in the vertical and horizontal axis would then resemble the gradients in a slab amplifier, and therefore result in a slightly stronger astigmatism of $\lambda/11$. However, this is still in a range that can be easily compensated, especially considering that other aberrations besides astigmatism are reduced compared to the one-sided cooling configuration.

In conclusion, these simulations suggest that the approach of using a cryogenically cooled bulk Ti:sapphire crystal would indeed be scalable to an incident pump power in the kW range by optimizing the crystal parameters and distributing the heat load over two amplifier crystals in a single multipass amplifier.

4 Heat-Induced Deformation and Thermal Management of Diffraction Gratings

The work presented in this chapter was partially published in Optics Express [44]. The groundwork was laid by Vincent Leroux, who performed initial Comsol simulations and wrote a majority of the spatio-spectral propagation code. The author of this thesis made final corrections to the code and Comsol models, that enabled the agreement with experimental results, and performed the comparison of different substrate materials as well as the investigation of potential mitigation strategies.

High peak power TW-class femtosecond laser systems require compression gratings that can support a spectral bandwidth of more than 100 nm. As a result, the vast majority of such laser systems designed over the past few decades have used gold-coated gratings for their broad diffraction bandwidth. While this approach has produced some impressive results and peak intensities, the current trend toward higher average power is pushing this technology to its limits. The gold coating absorbs about 3-4 % of the incident light at the 800 nm wavelength of Ti:sapphire laser systems [303]. In addition, the gratings must be operated in a vacuum environment to eliminate any nonlinear interaction between the high intensity pulses and the surrounding air. These two factors lead to the problem that a significant fraction of the average laser power is deposited in the grating and cannot be easily dissipated and is therefore stored in the grating substrate. The subsequent heating of the grating leads to thermal expansion and deformation of the grating, which is transferred to the wavefront of the laser pulse. This influence on the wavefront has been observed and characterized at several laser facilities [45, 304]. However, since the beam is spectrally dispersed within the compressor, the grating deformation additionally leads to a complex spectrally dependent wavefront deformation – i.e., spatio-spectral couplings (STCs) – that has a detrimental effect on the quality of the accelerated electrons in the LWFA and the focal intensity of the laser system. Such STCs cannot be easily compensated after they are introduced to the beam, and as a result, this problem represents a fundamental limitation on the average power at which gold-coated compressor gratings can be operated.

In the following sections, we will investigate this effect using simulations based on a formalism introduced by Li *et al.* [305, 306], which is used to derive the 3-dimensional in-focus pulse shape for a given deformation of the compression grating surfaces.

To verify the results of the code, we perform a case study of the 200 TW Angus laser system, in which we reproduce the spectrally integrated wavefront deformation published in [45], and derive bounds for the average power below which the deformation of the pulse remains negligible in the Angus laser system. To mitigate this problem, we will compare different substrate materials for the gratings, and propose ultra-low expansion glasses such as ULE and Zerodur as candidates for the grating substrate in gold-based grating compressors. Finally, we'll show that even these substrate materials have limitations due to the surface temperature that can be reached in high average power operation. Even with reasonable countermeasures, this temperature rise effectively limits the usability of gold-coated gratings to the low single-digit kW range.

4.1 Thermal Expansion of Compressor Gratings

4.1.1 Simulation of Grating Deformation

As already mentioned in the introduction of this chapter, an influence of the average power on the laser's wavefront quality has already previously [45] been observed in the Angus laser system. In order to benchmark the simulation code described in this chapter, we will reproduce those results by using the beam- and compressors parameters of Angus (see table 4.1) which are typical for modern 100 TW-class systems: The maximum energy sent into the compressor is 6 J, at a repetition rate of 5 Hz, resulting in a maximum average power of 30 W. The intensity profile of the collimated (near-field, NF) beam is a 6$^{\text{th}}$ order super-Gaussian profile with a 70 mm full width at half-maximum (FWHM). In order to focus on the aberrations introduced by thermal effects, static wavefront errors of the beam or the diffraction gratings are not considered. The holographic gratings consist of a gold-coated Pyrex substrate with a groove density of 1480 lines/mm, and are operated at an angle of incidence of 51.4°. The two gratings are used in a double pass configuration, and therefore a fraction of the laser beam is absorbed twice at each grating.

Using the complex refractive index of gold [307], we calculate that 3.74% of the incident power is absorbed in the coating in each pass. This fraction is included in the total diffraction efficiency, which was measured to be 92%, and is used to reduce the laser energy after each pass. A Gaussian spectrum with a FWHM bandwidth of 32 nm was used for the simulations.

Using these parameters, we simulate the deformation profile of the grating substrate with the COMSOL Multiphysics [250] thermal expansion module for different average powers of the laser, ranging from 0 W (no deformation) to 30 W (maximum deformation). Since the compressor is operated in vacuum and the gratings are installed in

Table 4.1 – Parameters of the ANGUS laser systems pulse compressor that were used as an input for the simulations presented in this work. These parameters are typical for a Ti:sapphire 100-TW class laser system.

Pulse energy before compressor	6 J
Pulse repetition rate	5 Hz
Fourier limited pulse duration (FWHM)	29 fs
Near field intensity profile	6th order super-Gaussian
Beam diameter (FWHM)	70mm
Angle of incidence on compressor gratings	51.4°
Groove density of compressor gratings	1480 lines/mm
Grating diffraction efficiency	92%
Coating absorption	3.74%

low-distortion mounts with minimal contact to the substrate, convective and conductive cooling can be neglected. As a result, we consider only radiative cooling in our simulations. The measurements in [45] were made after 30 minutes of irradiation, after which a state close to thermal equilibrium was reached. In our COMSOL simulations we therefore also calculate the deformation and heat distribution that is reached in thermal equilibrium.

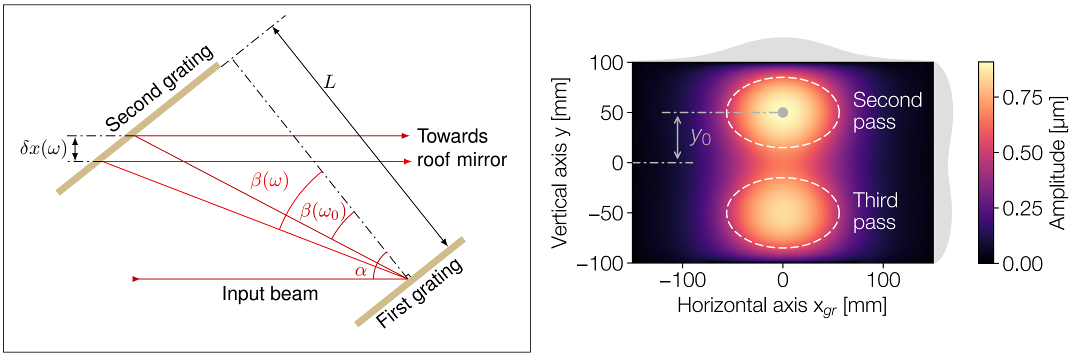

Figure 4.1 – The compressor layout with the notation used in the text (left), and the deformation profile of the second grating normal to the surface d_{G2} simulated with COMSOL. Simulations show the deformation of a Pyrex substrate after 30 minutes of laser operation at 30 W average power. The full width at half maximum of the second and third passes of the compressor are indicated in white dashed line. The shaded areas show the projected deformation profile.

Figure 4.1 shows the deformation profile simulated for the second grating at the maximum average power (30 W). We call the deformation profiles of the two gratings

$d_{\mathrm{G1}}(x_{\mathrm{gr}}, y)$ and $d_{\mathrm{G2}}(x_{gr}, y)$, with the horizontal coordinate x_{gr} in the plane of the grating surface and y, the vertical coordinate.

4.1.2 Spatio-Spectral Phase

Following [306], we can now use these deformation profiles of the gratings to introduce the projected deformation profiles $f_{\mathrm{G1}}(x, y, \omega)$ and $f_{\mathrm{G2}}(x, y, \omega)$ that are imprinted onto the laser wavefront as the pulse is diffracted on the grating surface. Here, x denotes the horizontal coordinate in the reference frame of the wavefront. These profiles represent the transversely resolved difference in path length that is caused by the bulging of the grating surface. To calculate them, we project the deformation profiles of the gratings to the plane of the laser wavefront. The projection consists of a scaling of a) the horizontal axis $x = x_{\mathrm{gr}} \cos\alpha$ of the grating according to the angle of incidence, and b) the amplitude of the deformation, to account for the fact that the deformation profiles d_{G1} and d_{G2} are normal to the grating surface and not along the direction of propagation:

$$f_{\mathrm{G1,\,G2}}(x, y, \omega) = \left[\frac{1}{\cos\alpha} + \frac{1}{\cos\beta(\omega)}\right] d_{\mathrm{G1,\,G2}}(x_{\mathrm{gr}} \cos\alpha, y) \tag{4.1}$$

Here, α is the angle of incidence on the gratings and $\beta(\omega)$ is the frequency dependent angle of diffraction, as is illustrated in fig. 4.1. The wavefront aberration added by each pass f_i can then be expressed as:

$$\begin{aligned} f_1(x,\, y) &= f_{\mathrm{G1}}(x,\, y - y_0,\, \omega), \\ f_2(x,\, y,\, \omega) &= f_{\mathrm{G2}}(x + \delta x(\omega),\, y - y_0,\, \omega), \\ f_3(x,\, y,\, \omega) &= f_{\mathrm{G2}}(x + \delta x(\omega),\, -y - y_0,\, \omega), \\ f_4(x,\, y) &= f_{\mathrm{G1}}(x,\, -y - y_0,\, \omega), \end{aligned} \tag{4.2}$$

with y_0 the vertical offset from the center of the grating, and $\delta x(\omega)$ the frequency-dependant horizontal shift of a frequency ω on the second grating with respect to the central frequency ω_0. This shift can be written as:

$$\delta x(\omega) = (\tan\beta(\omega_0) - \tan\beta(\omega))\, \cos\alpha\, L, \tag{4.3}$$

with β the diffraction angle, α the angle of incidence, and L the distance between the two gratings along the surface normal. We note that for the last two passes, the vertical axis is flipped, as our setup features a roof mirror.

For a compressor with a negligible change of beam properties during the propagation between the gratings, we can then write the total, frequency-resolved wavefront deformation $\phi_{\text{comp.}}$ as

$$\phi_{\text{comp.}}(x,y,\omega) = k(\omega)\left[f_1(x,y,\omega) + f_2(x,y,\omega) + f_3(x,y,\omega) + f_4(x,y,\omega)\right] \tag{4.4}$$

with the wave vector amplitude $k(\omega)$.

For an arbitrary input pulse $E_{\text{NF},in}(x,y,\omega) = A(x,y,\omega)e^{i\,\phi_0(x,y,\omega)}$, with an envelope $A(x,y,\omega)$ and an initial phase $\phi_0(x,y,\omega)$, we can now calculate the effect of the compressor by adding the deformation phase term to the initial pulse:

$$E_{\text{NF, out}}(x,y,\omega) = E_{\text{NF, in}}(x,y,\omega)\; e^{i\,\phi_{\text{comp.}}(x,y,\omega)}. \tag{4.5}$$

To calculate the beam properties of the pulse in the focus, we neglect a longitudinal shift of the focal plane and a detuning of the group delay dispersion (GDD) of the compressor that are caused by the deformation of the gratings. To do this, we first remove the frequency-averaged spherical curvature of the wavefront, which simply corresponds to the divergence of the beam, and thus a longitudinal shift of the focal plane. The curvature is determined through a parabolic fit to the frequency-averaged phase of the electric field. This resulting divergence is shown in fig. 4.3(a), where we compare it to the measured laser divergence. The GDD is determined from the quadratic component of the spectral phase on the beam axis and is removed from the pulse to mimic a compressor that is tuned for optimal compression. Then, by performing a 2D Fourier transform for each frequency, we obtain the focal spot in the space-frequency domain

$$E_{\text{FF}}(\xi,\eta,\omega) = FT_2\left[E_{\text{NF, out}}(x,y,\omega)\right], \tag{4.6}$$

with η and ξ denoting the vertical and horizontal coordinates in the focus. Finally, an inverse Fourier transform at each spatial position gives the 3D spatio-temporal focal spot

$$E_{\text{FF}}(\xi,\eta,t) = iFT\left[E_{\text{FF}}(\xi,\eta,\omega)\right], \tag{4.7}$$

from which we can derive the relevant information such as peak intensity, pulse duration, waist, but also pulse front tilt, or spatial chirp for instance.

Apart from the FEM simulations performed in COMSOL, this whole calculation is implemented in the Python language and available as an open source software package [308].

4.2 Case Study of the Angus Laser System

For the following calculations, we use the Angus laser parameters that were reported above and simulate the deformation of a Pyrex substrate to ensure comparability with previously published experimental data [45]. At the maximum average power, the deformation of the grating corresponds to a 0.9 λ peak-to-peak surface deformation at the 800 nm wavelength of the laser (compare fig. 4.1) and consequently to a severe degradation of the focus quality. The near field profile is focused by an optic with a focal length of 2 meters, which corresponds to the setup of the laser-plasma accelerator Lux [46].

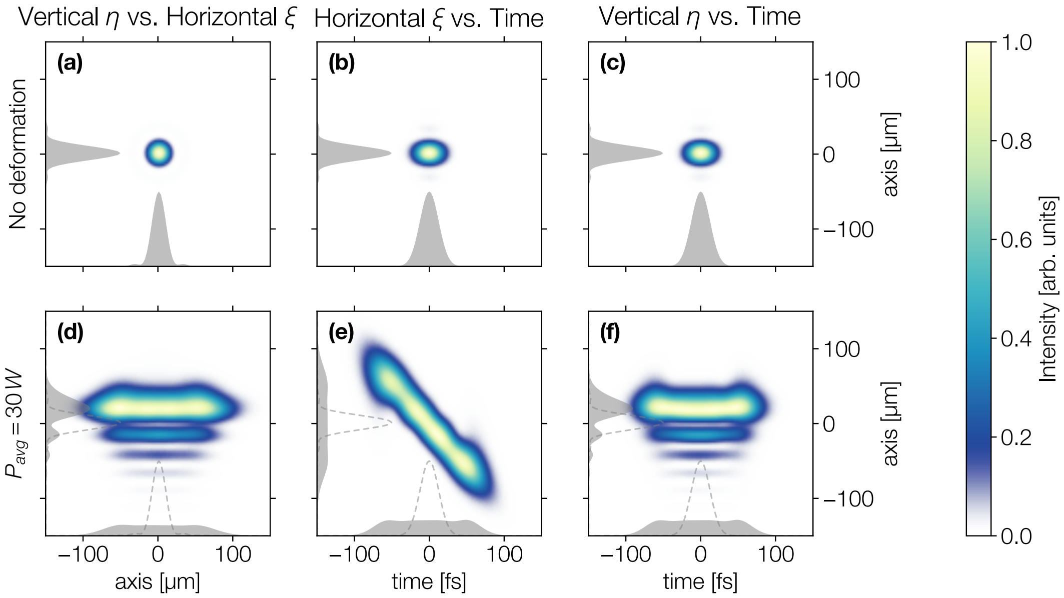

Figure 4.2 – Integrated horizontal-vertical (a, d), horizontal-temporal (b, e), and vertical-temporal (c, f) profiles, with no deformation (a–c), and with a 30 W average power deformation (d–f). One can see a strong wavefront deformation in the vertical plane, and a strong pulse front tilt and spatial chirp in the horizontal plane. The shaded areas show the respective projections, and the dashed lines show the projections of the Fourier limited focal spot. The initial beam size $\omega_{x,y}$ is 25.5 μm in both planes and the pulse duration is 29.5 fs. The intensity is normalised to the maximum in each individual subfigure.

To understand the effect of this deformation on focus quality, we can compare the pulses in the focal plane at the maximum average power of the Angus laser of 30 W (maximum deformation) with an undistorted pulse at an average power of 0 W. Figure 4.2 shows the integrated profiles of these two extreme cases. There is a strong tilt of the pulse front in the horizontal plane, which amounts to 0.83 fs/µm. The spatial profile is distorted by $\lambda/3$ of astigmatism at 0°, $\lambda/24$ of coma at 90°, and $\lambda/19$

of trefoil at 90°(all values are rms amplitude). In addition, the focal spot is broadened in the horizontal axis by spatial chirp, which amounts to about 0.52 mm/(rad·fs^{-1}) at maximum average power. We do not observe any significant higher order STC, such as pulse front curvature.

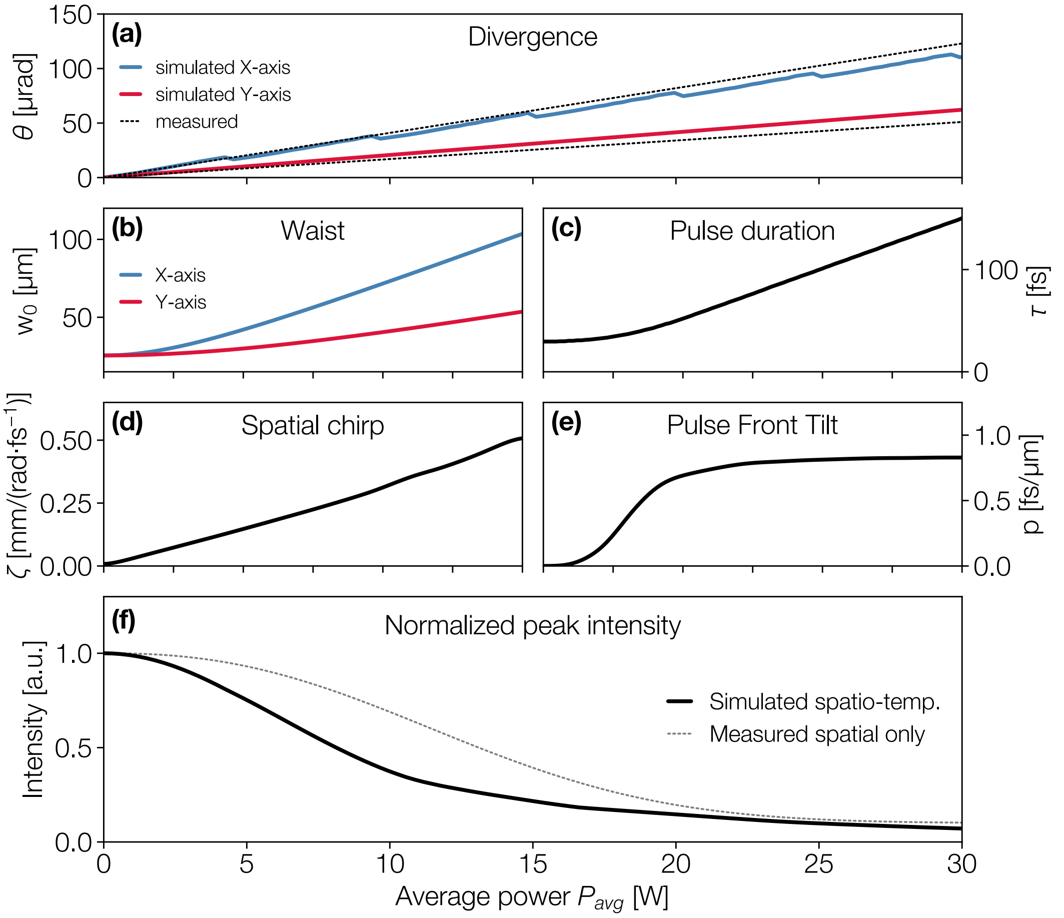

Figure 4.3 – Evolution of the main laser beam parameters as a function of the laser average power ranging from 0 W to 30 W. Divergence at the exit of the compressor (a) and waist in focus (b) are shown in the horizontal and vertical axes. The waist is integrated over time, and the pulse duration in focus (c) is integrated over the spatial dimensions. The spatial chirp (d) and pulse front tilt (e) correspond to STCs in the horizontal axis. The simulated peak intensity (f, solid) is compared to the measured Strehl ratio [45] (dotted). The step-like variation of the horizontal divergence in (a) is attributed to numerical errors of the simulation.

Following the notation of [81], we write the pulse front tilt p so that $E(x,t) = E_{\mathrm{x}}(x)E_{\mathrm{t}}(t-p{\cdot}x)$, and the spatial chirp ζ so that $E(x,\omega) = E_{\mathrm{x}}(x-\zeta{\cdot}\omega)E_{\omega}(\omega)$.

Figure 4.3 shows the evolution of the main spatio-temporal properties of the laser, namely the divergence of the beam in the near field (which we remove before simulating the focal spot as explained above), the time-integrated waist, the space-integrated pulse duration, the horizontal spatial chirp, the horizontal pulse front tilt, and the peak intensity normalized to the non-deformed focal spot peak intensity. We find that the beam divergence agrees well with the measured divergence reported in [45] and are therefore confident that our code provides a reasonable estimate of the in-focus STCs, even though we could not measure them directly with our experimental layout.

The spatial chirp scales linearly with average power, according to ζ [µm/(rad·fs^{-1})] $= 16.7 \times P$ [W]. The pulse front tilt remains nearly constant above an average power of 11 W. Above this value, the focal spot grows at similar rates in time and in the horizontal plane due to spatial chirp. Consequently, the two effects balance the growth of the pulse front tilt. Finally, we observe that the spatio-temporal couplings further reduce the available peak intensity compared to our previous measurements [45], which were limited to the Strehl ratio as a time-integrated property and thus did not consider the change in pulse length.

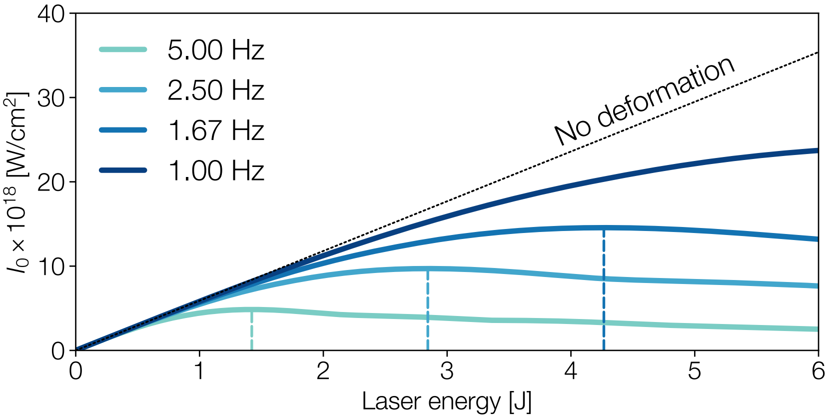

Figure 4.4 – Simulated peak intensity in focus for different repetition rates.

Using these simulations, we calculate that the maximum peak intensity is reached at an average power of 7.1 W (see Fig. 4.4). At this power, a further increase in laser energy is balanced by further deformation of the gratings and subsequent degradation of focal quality. The peak intensity at this average power is still 42 % lower than a pulse generated by an undistorted compressor, and the focal spot has a pulse front tilt of 0.52 fs/µm. For comparison, the projected beam profiles at this optimal average power are shown in fig. 4.5. Below an average power of 2.7 W, the pulse front tilt remains negligible (<0.01 fs/μm) and the peak intensity is reduced by only 6.7 % due to spatial chirp, which may be a superior configuration for applications that require the highest possible beam quality.

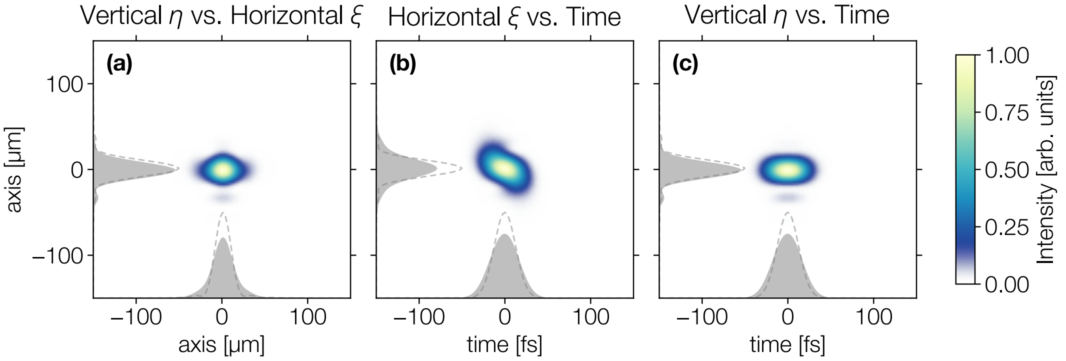

Figure 4.5 – Integrated horizontal-vertical (a), horizontal-temporal (b), and vertical-temporal (c) profiles, with a 7.1 W average power deformation. The shaded areas show the respective projections, and the dashed lines show the projections of the Fourier limited focal spot.

4.3 Comparison of Substrate Materials

One potential way to increase this strict limit on the average power below which a gold-based compressor can be operated is through the choice of substrate material. Materials with a lower coefficient of thermal expansion (CTE) should result in less significant grating deformation at the same temperature, i.e., approximately the same power deposited in the grating. In the following, we will look at the commonly used fused silica, as well as Zerodur, a popular material from the family of ultra-low expansion glasses and glass ceramics. Both materials have optical and mechanical properties that make them well suited for use as substrate materials for diffraction gratings. The relevant thermal material properties of both materials are compared with those of Pyrex in the table 4.2. The material properties of Zerodur are very similar to those of other low-expansion materials such as Corning ULE, and we will therefore use Zerodur as a representative of the entire family of low-expansion materials. Looking at table 4.2, it is immediately apparent that the coefficient of thermal expansion in particular varies greatly between the materials and is significantly higher for Pyrex than for fused silica and especially than for Zerodur.

Table 4.2 – Comparison of thermal material properties of Pyrex, Fused silica and Zerodur [309–311].

	Pyrex	Fused silica	Zerodur
Coefficient of thermal expansion α [1/K]	3.25×10^{-6}	0.55×10^{-6}	$0 \pm 7 \times 10^{-9}$
Thermal conductivity k [W/m K]	1.13	1.38	1.46
Heat capacity C_p [J/kg K]	1050	703	820

Using these material properties, we can perform the same analysis of the compressor performance described in section 4.1, and look at the focal properties of a laser pulse after passing through a compressor once thermal equilibrium has been reached in the gratings. Apart from the substrate material, we will keep the same beam and compressor parameters as in Angus, which represent a typical compromise between a low risk of damage due to high beam fluence and reasonable grating dimensions that help with the cost-effectiveness of the pulse compressor.

While the qualitative behavior of the individual STCs is very similar to what we observed in Angus, the trend of the peak intensity varies greatly between the different materials: From the normalized peak intensity shown in figure 4.6, it is clear that significant improvements can be expected from the use of fused silica. The figure also shows that – using the parameters of the Angus laser – the average power at which the highest peak intensity is reached is 27 W, which is already a significant improvement over Pyrex. However, at this power, the peak intensity is already reduced by 41%. If, in addition, the pulse front tilt is to be kept at a negligible level of less than 0.01 fs/μm, the average power must be limited to 10.8 W (as opposed to 2.7 W for Pyrex), which would correspond to a peak intensity reduction of 8.8%. This means that for many practical applications in modern laser systems, fused silica would allow improved, though still limited, performance.

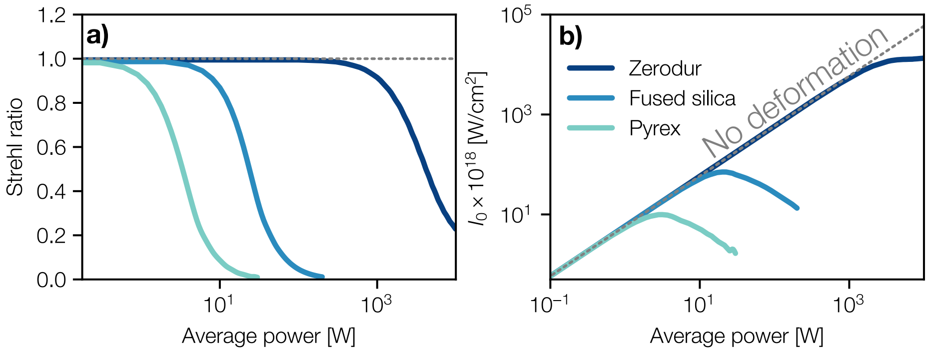

Figure 4.6 – Comparison of the degradation of beam quality for Pyrex, Fused silica and Zerodur. a) shows the degradation of the Strehl ratio, while b) shows the achievable peak intensity as a function of average power at a fixed repetition rate. All values are calculated for the beam and grating parameters of the Angus laser shown in table 4.1. For the simulation of Zerodur, a worst case-scenario with a coefficient of thermal expansion of $7 \times 10^{-9}\,\mathrm{K}^{-1}$ was assumed.

Scaling to kW-Level Average Power

If we take a further look at the respective performance of Zerodur, we can see that the pulse deformation is practically gone in the sub-100 W range. In fact – assuming a worst case scenario with a coefficient of thermal expansion of $7 \times 10^{-9}\,\mathrm{K}^{-1}$ – an influence of the thermally induced deformation only becomes visible above an average power of about 1 kW (see figure 4.6). In practice, however, operation at such an average power is not possible, since the surface temperature would reach values that would lead to coating damage. The power is therefore practically limited to below about 1 kW (see figure 4.7), where a surface temperature of 250°C is reached, which corresponds to the groove integrity limit of typical gold-based grating technologies [312].

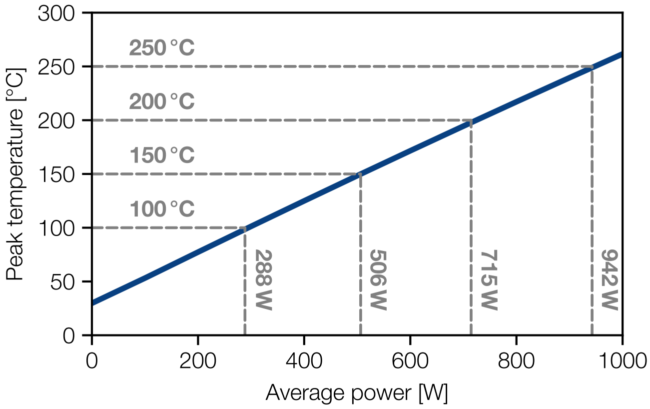

Figure 4.7 – Peak surface temperature as a function of laser average power. The groove integrity limit of gold gratings is around 250°C

From these results, it can be concluded that new technological advances are needed to increase the average power at which gold-based gratings can be operated beyond a few hundred watts, since even with negligible surface deformation of the grating substrates, the surface reaches temperatures that can lead to coating damage.

4.4 Mitigation Strategies

One possible approach to mitigate the surface temperature rise is active cooling of the grating, as first proposed by Alessi *et al.* [312]. In order to investigate the applicability of this approach for a compressor similar to the ANGUS design, we simulated the same method of cooling the top and bottom edges of the coating, which are well suited as they are also suitable points for mounting the gratings. A schematic overview of the gratings is shown in figure 4.8, where the temperature profiles on the front and back surfaces are shown.

While this cooling method indeed helps to reduce the peak temperature of the grating surface – as described by Alessi *et al.* – the configuration leads to an unfavorable temperature distribution in the grating substrate. The edges of the grating that are in contact with a cold head naturally have the lowest temperature, while the center of the grating has the highest temperature, resulting in a large temperature gradient across the grating surface. As a result, high stress and non-uniform deformation of the grating substrate will result in poorer wavefront quality than would be obtained in an uncooled configuration.

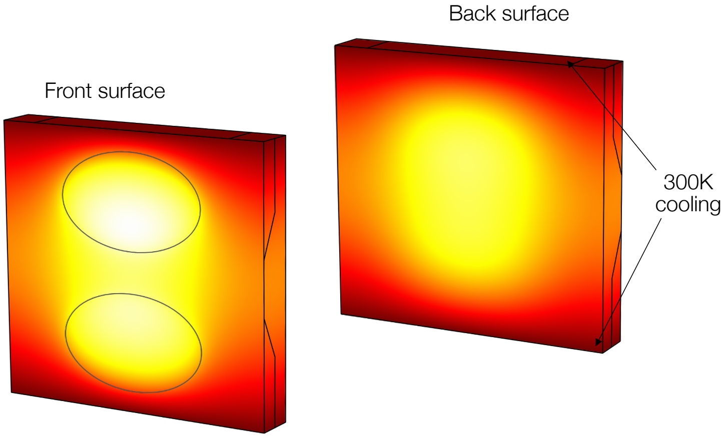

Figure 4.8 – Cooling configuration of the gratings, similar to the one investigated in [312]. The grey ellipses indicate the extent of the incident beam.

To prevent the development of temperature gradients across the grating surface, we instead propose a back-cooled configuration, as shown in figure 4.9. With a cooled patch on the backside of the grating – i.e., opposite the incident beam – one can efficiently remove heat from the substrate because the distance of heat transport through the substrate is minimized, and in addition, by limiting the cooling to an area roughly the size of the incident beam, one does not reduce the temperature in areas where no heat is being deposited. This results in a more uniform distribution of heat across the diffraction surface and consequently less stress and deformation.

Without further optimization of the grating dimensions – in particular, the thickness of the substrate, since it is equal to the thermal transport distance – it would be possible to approximately double the average power incident on the grating without reaching surface temperatures above the groove integrity limit (see figure 4.10). This is for a constant 300 K temperature of the cooled region, which would be achievable with water cooling – a technically feasible approach despite the challenges of integrating water cooling of in-vacuum components.

This estimate is consistent with results from Lawrence Livermore National Lab [313] and recent work by Power *et al.* [314], which proposes a more sophisticated cooling scheme consisting of a ceramic flow cell design in which the grating substrate is

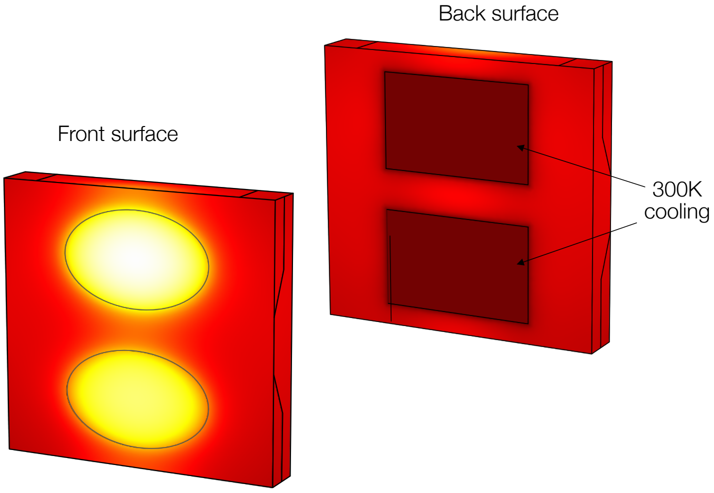

Figure 4.9 – Simple concept for cooling the gratings from the backside. The grey ellipses indicate the extent of the incident beam.

perforated with cooling channels that allow a further improvement in heat extraction efficiency. Combined with cordierite ceramics as a substrate material with particularly high thermal stability, this scheme allows a further improvement of about a factor of 2. This means that in the grating geometry of the Angus laser, operation at an average power of about 3-4 kW average power would be feasible. However, even this technologically advanced cooling scheme does not allow for easy scaling to the average power of laser systems such as Kaldera.

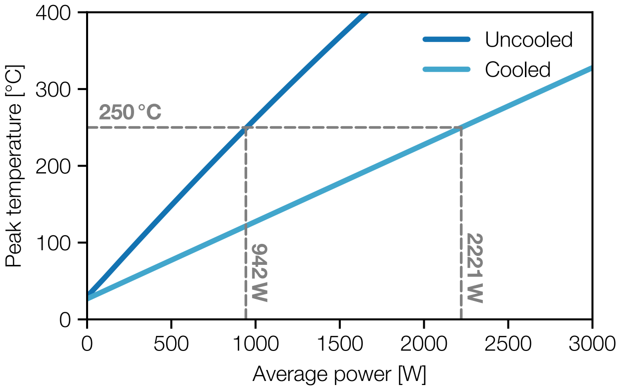

Figure 4.10 – Peak surface temperature with a cooled back-surface of the grating substrate.

4.5 Conclusion and Outlook

In this chapter, we have simulated the degradation of spatio-temporal beam quality as a result of heat-induced deformation of traditionally used gold-coated diffraction gratings. In a case study of the ANGUS laser system, we observed that this effect can severely limit the maximum average power at which the laser can be operated without degrading the beam quality. We further conclude that by appropriate selection of the grating substrate material – i.e., the use of low-expansion glasses such as ULE or Zerodur – the onset of severe focal quality degradation can be pushed into the single-digit kW range. At such high average power, however, the surface temperature of the gratings can rise above the groove integrity limit of typically 250°C for gold-coated gratings, resulting in grating damage. By actively cooling the gratings, the peak temperature of the gratings can be reduced to such an extent that the average power incident on the grating surface can be approximately doubled. However, even with further optimization of the cooling concept and compressor geometry, we conclude that the use of gold-coated gratings will be limited to the single-digit kW range.

Other grating technologies, such as multilayer dielectric coatings, may offer a way around this problem in future high average power ultrafast lasers. Their primary advantage over gold-based grating coatings is a greatly reduced surface absorption of tens of ppm instead of 3-4%. This difference already allows an increase of the average incident power by about three orders of magnitude for a given substrate material. In practice, this factor is slightly reduced as the bulk absorption of the substrate becomes more relevant, but since it is also in the ppm/cm range for typical materials such as fused silica, an improvement of about two orders of magnitude can still be expected. This conclusion is shared by [315].
An additional advantage of dielectric gratings is their increased diffraction efficiency, which can increase the overall compressor throughput from 60-70% to over 90%, thus reducing the required input pulse energy for a given on-target pulse energy. This reduces the requirements for the pump laser and the amplifier section of such laser systems.
In addition, dielectric coatings are generally more robust to laser-induced damage, although the advantage over gold coatings is somewhat diminished at short pulse durations of tens of femtoseconds [316].

While dielectric grating technology is widely used in high average power laser systems, such as those using ytterbium gain media, it has not yet been established for compression of Ti:sapphire lasers because the dielectric coating typically provides only a fraction of the reflection bandwidth of gold-based coatings. However, when combined with a compressor design that allows the gratings to be operated at a Littrow angle, the reflection bandwidth can be maximized to allow compression of pulses below 30 fs [315, 317]. In fact, stretching and recompression of 26 fs pulses has recently been demonstrated with an out-of-plane dielectric compressor and matched transmission grating stretcher [50], making the technology a viable alternative for high average power Ti:sapphire systems that is more scalable in average power than gold-based compression gratings.

5 Conclusion

This thesis outlines a potential path towards a drive laser for reliable, high-energy laser-wakefield acceleration (LWFA) at up to kHz repetition rates. This is done by demonstrating solutions to problems in key components of such laser systems that currently limit their average power and pulse quality.
Beginning with a review of the fundamental physics of LWFA, the first chapter explains why high quality Joule-level pulses lasting tens of femtoseconds are required to drive bright LWFA-based X-ray sources. From a comparison of several relevant laser technologies, it becomes evident that the currently most viable option for delivering such pulses is the use of Ti:sapphire-based laser systems. The required pulse energy and duration are routinely achieved in Ti:sapphire lasers, but the challenge for future systems is to further improve the pulse quality and increase the repetition rate to the kHz-level. Solving this challenge is at the core of the KALDERA project, which aims to build a 100 TW-class laser system with kHz repetition rate and kW average power dedicated to LWFA.

The main obstacles in developing such a laser system can be summarized in four key points. First, generating the seed pulse is crucial as it largely determines the final pulse's quality and stability. In laser-wakefield acceleration (LWFA), the properties of the driving laser pulse directly impact the properties of the accelerated electrons due to complex plasma dynamics. Hence, precise control of the seed properties is vital.
Second, the high average power in the main amplifiers creates a heat load that can degrade beam quality through thermal lensing. To prevent this, the amplifier must be designed to minimize thermal gradients in the laser crystal.
Pumping these amplifiers is the third major challenge. To achieve multi kW-level output power, Ti:sapphire amplifiers require high-brightness pump beams with an average power on the order of 10-15 kW in the blue/green spectral region, which is at the limit of what is currently possible.
Finally, compression of the pulses from high-intensity Ti:sapphire amplifiers requires compression gratings that can support their large bandwidth. Typically, gold-coated gratings are used, but the few percent absorption of the coatings leads to heating of the in-vacuum grating substrates. Previously published experimental work has shown that the resulting thermal deformation leads to a severe degradation of pulse quality, even in current laser systems with a few Hz repetition rate. Mitigating this effect will be even more important in future laser systems with up to kHz repetition rates.

This thesis has addressed all four of these challenges.

For generating high-quality seed pulses, a front-end laser system based on white-light seeded OPCPA was introduced. This approach provides flexibility in spectral properties while ensuring excellent temporal contrast and a compact design. The laser system was specifically designed to ensure long-term stability and spatio-spectral beam quality, which are crucial for reliable laser wakefield acceleration. It further meets the seeding requirements of subsequent Ti:sapphire amplifiers by delivering pulse energy of up to 50 μJ and a spectrum supporting a Fourier-limited pulse duration of 25 fs at a center wavelength of 800 nm.

In OPCPA, there is typically a trade-off between beam quality and output stability, as the damping of input fluctuations can be achieved by saturating the parametric amplifiers, but the back-conversion that causes the saturation also degrades the spatio-spectral beam profile and wavefront.
To understand and mitigate this issue, the behavior was studied through (3+1)D start-to-end simulations and experimental measurements of the spatio-spectral electric field of amplified laser pulses in chapter 2. Spatial filtering was identified as a simple and yet effective solution for recovering an excellent beam quality in highly saturated OPCPA, while maintaining high energy stability of the output pulses. In fact, the simulations indicate that stability can even be further improved by filtering out specific higher order modes. Understanding these saturation dynamics enables the generation of stable laser pulses with excellent spatio-spectral wavefront quality and an M^2 of 1.2 in both beam axes. The short-term, shot-to-shot energy stability of the OPCPA output was measured to be better than 0.15 % rms.

While OPCPA offers a high degree of flexibility in the characteristics of the amplified pulses, the complex and highly nonlinear interaction is sensitive to several difficult-to-control parameters, such as phase matching conditions and subtle changes in the characteristics of the input pulses. The resulting large number of adjustable parameters makes it difficult to precisely tune and control the properties of the amplified pulses, and results in sensitivity to changes in environmental conditions. This thesis demonstrates that evolutionary optimization can be used to automatically tune the pulse characteristics of an OPCPA system, making the fine-tuning of the laser system largely independent of the operator, and even allowing a slight improvement in laser performance over what can typically be achieved by manual tuning. In addition, full-state feedback control was used to simultaneously stabilize multiple output pulse characteristics that are highly coupled and where stabilizing one parameter independently would result in unwanted changes in another. This approach allows the excellent short-term stability to be maintained over several days of operation, which was confirmed in a 50 hour measurement during which the laser maintained an energy stability of better than 0.18% rms, a center wavelength stability of 25 pm rms, and a bandwidth stability of 0.19% rms using single-shot measurements.

This OPCPA system – Malcolm – has been used to seed the 200 TW Angus laser for over a year, and has consistently delivered pulses that have enabled reliable laser wakefield experiments at the Lux facility. This already demonstrates the real-world usefulness of automated control methods, but these initial results are expected to further improve applying further optimised control methods that better handle the nonlinearity of the laser system. Although the feedback loop has so far only been implemented as a slow drift compensation, its simplicity and low computational cost of make it suitable for use at high repetition rates, such as those planned for Kaldera. The approach can also be applied to other laser technologies beyond OPCPA to improve their long-term performance and fully exploit their capabilities.

Chapter 3 presents the development of Colima, a cryogenically cooled 100 Hz Ti:sapphire amplifier, capable of delivering 1 J pulses suitable for accelerating electrons to the few hundred MeV level. Simulations show that high-quality, 30 fs pulses can be amplified while effectively mitigating thermal-induced degradation of beam quality. The calculated thermal focal length of the pump crystal is 56 m, with a peak-to-peak wavefront error of $\lambda/12$ per pass. This is comparable to the typical transmitted wavefront quality of unpumped crystals and should therefore not be a limiting factor for the quality of the amplified beam.
A study on the amplifier design's scalability to higher repetition rates indicates that compensating for higher-order wavefront aberrations becomes necessary. However, with minor adjustments to the cooling configuration and splitting the pump-induced heat load between two amplifier heads, the design can be scaled to an average power of 1 kW, corresponding to an amplified pulse energy of 1 J at the desired 1 kHz repetition rate for future iterations of Kaldera.

Chapter 3 also addresses the generation of the multi-kW pump beams required for such amplifiers, by focusing on the frequency doubling of a multi-core fiber (MCF)-based laser system. Such fiber lasers have been demonstrated to handle multi-kW average power without complex cooling techniques, and the multi-core approach promises scalability to higher pulse energy. However, their multi-aperture beam profile poses challenges for beam transport and frequency conversion. In this thesis chapter, first results on a frequency-doubled, nanosecond MCF laser were presented. These intial experiments achieved a total output energy of 17 mJ at a repetition rate of 1 kHz. The measured peak SHG conversion efficiency of 52% could be reproduced in numerical simulations, which also show that the efficiency should improve with further optimization of the pulse characteristics of the MCF laser. Specifically, increasing the energy emitted from a single core to a realistic 10 mJ level should raise the conversion efficiency to over 80%, similar to that achieved in other high-energy laser systems. Further simulations of the thermal performance of the frequency conversion setup confirm that, even at multi-kW average power, the thermal gradients caused by absorption in LBO should not affect the conversion efficiency in such crystals.

These promising outcomes affirm that MCF-based lasers are indeed a viable option for providing high-energy pump pulses for high repetition rate Ti:sapphire lasers.

In order to understand the limitations of gold-based compression gratings, a numerical model was introduced in chapter 4 that allows to simulate thermally induced grating deformation and the spatio-temporal intensity profiles of pulses compressed in such a compromised compressor. The model was used to study pulse degradation in the ANGUS laser system, and the results indicate that absorption in the gratings coatings can limit the usable average power of such lasers to only a few Watts – especially if maintaining a low pulse front tilt is important for the application. Furthermore, the simulations show that the degradation of the pulse's peak intensity is more severe than previously published measurements of the spectrally integrated wavefront suggest.
However, the simulations also show that this behavior can be mitigated by an appropriate choice of substrate material, allowing the use of gold-coated gratings up to nearly 1 kW of incident power. Furthermore, cooling of the grating substrate allows to use gold-based grating technology at average power in the low single-digit kW range, a conclusion shared by several other publications [313, 314]. Nevertheless, considering of other compressor technologies, such as multilayer dielectric-coated gratings, will be necessary for future iterations of the KALDERA laser system, where average powers of up to 5 kW are expected. Indeed, recent experimental results [50] on pulse compressors based on dielectric gratings confirm that this technology is suitable for compressing sub-30 fs pulses. Such gratings are used in the highest average power Yb laser systems with multi-kW average power [107, 140], and the ability to use them in Ti:sapphire systems makes them a legitimate option for pulse compression in KALDERA.

Overall, the results presented in this thesis offer concrete solutions for constructing a reliable LWFA-drive lasers at 100 Hz with Joule-level energy, which is suitable for accelerating electrons to 100-200 MeV [253]. In fact, a laser system employing the OPCPA front-end and Ti:sapphire amplifier design proposed in this work is currently under construction.
The initial operation of this KALDERA prototype will provide valuable experience, especially concerning the amplifier design. The lessons learned during this phase will enable further refinement of the approach and scaling the technology to meet the targeted specifications of 100 TW peak power at a pulse repetition rate of 1 kHz. The key challenges for achieving those specifications remain the thermal design of the Ti:sapphire amplifiers and pump laser technology, but the thesis also highlights the necessary steps towards a solution: increasing the number of cores and single-core energy of MCF lasers and verifying the amplifier design's suitability for kHz repetition rates. Through experiments on the 100 Hz prototype, optimization of the amplifier design can be carried out, and it can be adapted for a further 3-5 J amplifier that will be required to reach the 100 TW peak power.

Also beyond the laser, the increased average power and repetition rate of future laser-wakefield acceleration (LWFA) light sources requires adaptations to various sub-components of the overall LWFA system: The plasma target must be capable of handling the deposited average power, while the diagnostic and control systems must cope with the increased data acquisition at kHz repetition rates. In addition, the electron optics and diagnostics must be optimized to accommodate the high repetition rate. However, this last point in particular can benefit from the decades of experience gained with conventional high repetition rate accelerators, and the experience can be transferred to the laser-wakefield domain, as it is already done for many aspects of the LUX facility. Similarly, the laser technology developed in this thesis and in other parts of the KALDERA project will aid in the development of other laser systems outside of laser-wakefield acceleration, as almost any application will benefit from reliable, stable, high-quality pulses at high repetition rates.

This combination of advances in laser systems and accelerator technology sets the stage for advances that pave the way for lasers and accelerators to continue their synergistic journey, as they have for the past half century. As these technologies evolve together, they will undoubtedly drive breakthroughs and innovation in various scientific disciplines.

Bibliography

[1] A. L. Schawlow and C. H. Townes, *Infrared and optical masers*, Phys. Rev. **112**, 1940 (1958).

[2] T. H. Maiman, *Stimulated Optical Radiation in Ruby*, Nature **187**, 493–494 (1960).

[3] A. H. Zewail, *Femtochemistry: Atomic-scale dynamics of the chemical bond*, J. Phys. Chem. A **104**, 5660 (2000).

[4] T. Udem, R. Holzwarth, and T. W. Hänsch, *Optical frequency metrology*, Nature **416**, 233–237 (2002).

[5] H. J. Metcalf and P. Van der Straten, *Laser cooling and trapping of neutral atoms*, in The Optics Encyclopedia: Basic Foundations and Practical Applications (Wiley Online Library, 2007).

[6] P. B. Corkum and F. Krausz, *Attosecond science*, Nat. phys. **3**, 381–387 (2007).

[7] J. Aasi, B. Abbott, R. Abbott, T. Abbott, M. Abernathy, K. Ackley, C. Adams, T. Adams, P. Addesso, R. Adhikari, *et al.*, *Advanced ligo*, Class. Quantum Gravity **32**, 074001 (2015).

[8] B. P. Abbott, R. Abbott, T. Abbott, M. Abernathy, F. Acernese, K. Ackley, C. Adams, T. Adams, P. Addesso, R. Adhikari, *et al.*, *Observation of gravitational waves from a binary black hole merger*, Phys. Rev. Lett **116**, 061102 (2016).

[9] R. Q. Fugate, D. L. Fried, G. A. Ameer, B. Boeke, S. Browne, P. H. Roberts, R. Ruane, G. A. Tyler, and L. Wopat, *Measurement of atmospheric wavefront distortion using scattered light from a laser guide-star*, Nature **353**, 144–146 (1991).

[10] R. Ragazzoni, E. Marchetti, and G. Valente, *Adaptive-optics corrections available for the whole sky*, Nature **403**, 54–56 (2000).

[11] L. Fletcher, H. Lee, T. Döppner, E. Galtier, B. Nagler, P. Heimann, C. Fortmann, S. LePape, T. Ma, M. Millot, *et al.*, *Ultrabright X-ray laser scattering for dynamic warm dense matter physics*, Nat. Photonics **9**, 274–279 (2015).

[12] M. Tabak, J. Hammer, M. E. Glinsky, W. L. Kruer, S. C. Wilks, J. Woodworth, E. M. Campbell, M. D. Perry, and R. J. Mason, *Ignition and high gain with ultrapowerful lasers*, Phys. Plasmas **1**, 1626–1634 (1994).

[13] A. Zylstra, O. Hurricane, D. Callahan, A. Kritcher, J. Ralph, H. Robey, J. Ross, C. Young, K. Baker, D. Casey, *et al.*, *Burning plasma achieved in inertial fusion*, Nature **601**, 542–548 (2022).

[14] T. Ishikawa, *Accelerator-based X-ray sources: synchrotron radiation, X-ray free electron lasers and beyond*, Philos. Trans. R. Soc. A **377**, 20180231 (2019).

[15] T. Ishikawa, H. Aoyagi, T. Asaka, Y. Asano, N. Azumi, T. Bizen, H. Ego, K. Fukami, T. Fukui, Y. Furukawa, *et al.*, *A compact X-ray free-electron laser emitting in the sub-ångström region*, Nat. Photonics **6**, 540–544 (2012).

[16] T. Gaumnitz, A. Jain, Y. Pertot, M. Huppert, I. Jordan, F. Ardana-Lamas, and H. J. Wörner, *Streaking of 43-attosecond soft-X-ray pulses generated by a passively CEP-stable mid-infrared driver*, Opt. Express **25**, 27506–27518 (2017).

[17] R. Neutze, R. Wouts, D. Van der Spoel, E. Weckert, and J. Hajdu, *Potential for biomolecular imaging with femtosecond X-ray pulses*, Nature **406**, 752–757 (2000).

[18] H. N. Chapman, A. Barty, M. J. Bogan, S. Boutet, M. Frank, S. P. Hau-Riege, S. Marchesini, B. W. Woods, S. Bajt, W. H. Benner, *et al.*, *Femtosecond diffractive imaging with a soft-X-ray free-electron laser*, Nat. Phys **2**, 839–843 (2006).

[19] L. Young, E. P. Kanter, B. Kraessig, Y. Li, A. March, S. Pratt, R. Santra, S. Southworth, N. Rohringer, L. DiMauro, *et al.*, *Femtosecond electronic response of atoms to ultra-intense X-rays*, Nature **466**, 56–61 (2010).

[20] H. N. Chapman, P. Fromme, A. Barty, T. A. White, R. A. Kirian, A. Aquila, M. S. Hunter, J. Schulz, D. P. DePonte, U. Weierstall, *et al.*, *Femtosecond X-ray protein nanocrystallography*, Nature **470**, 73–77 (2011).

[21] R. D. Miller, *Femtosecond crystallography with ultrabright electrons and x-rays: Capturing chemistry in action*, Science **343**, 1108–1116 (2014).

[22] M. Maiuri, M. Garavelli, and G. Cerullo, *Ultrafast spectroscopy: state of the art and open challenges*, J. Am. Chem. Soc **142**, 3–15 (2019).

[23] T. Tajima and J. M. Dawson, *Laser Electron Accelerator*, Phys. Rev. Lett. **43**, 267–270 (1979).

[24] K. Nakajima, *Towards a table-top free-electron laser*, Nat. Phys **4**, 92–93 (2008).

[25] D. Strickland and G. Mourou, *Compression of amplified chirped optical pulses*, Opt. Commun. **56**, 219–221 (1985).

[26] P. F. Moulton, *Spectroscopic and laser characteristics of Ti:Al_2O_3*, JOSA B **3**, 125–133 (1986).

[27] S. P. Mangles, C. Murphy, Z. Najmudin, A. G. R. Thomas, J. Collier, A. E. Dangor, E. Divall, P. Foster, J. Gallacher, C. Hooker, *et al.*, *Monoenergetic beams of relativistic electrons from intense laser–plasma interactions*, Nature **431**, 535–538 (2004).

[28] C. Geddes, C. Toth, J. Van Tilborg, E. Esarey, C. Schroeder, D. Bruhwiler, C. Nieter, J. Cary, and W. Leemans, *High-quality electron beams from a laser wakefield accelerator using plasma-channel guiding*, Nature **431**, 538–541 (2004).

[29] J. Faure, Y. Glinec, A. Pukhov, S. Kiselev, S. Gordienko, E. Lefebvre, J.-P. Rousseau, F. Burgy, and V. Malka, *A laser–plasma accelerator producing monoenergetic electron beams*, Nature **431**, 541–544 (2004).

[30] H.-P. Schlenvoigt, K. Haupt, A. Debus, F. Budde, O. Jäckel, S. Pfotenhauer, H. Schwoerer, E. Rohwer, J. Gallacher, E. Brunetti, *et al.*, *A compact synchrotron radiation source driven by a laser-plasma wakefield accelerator*, Nat. Phys **4**, 130–133 (2008).

[31] M. Fuchs, R. Weingartner, A. Popp, Z. Major, S. Becker, J. Osterhoff, I. Cortrie, B. Zeitler, R. Hörlein, G. D. Tsakiris, *et al.*, *Laser-driven soft-X-ray undulator source*, Nat. Phys **5**, 826–829 (2009).

[32] S. Kneip, C. McGuffey, J. L. Martins, S. Martins, C. Bellei, V. Chvykov, F. Dollar, R. Fonseca, C. Huntington, G. Kalintchenko, *et al.*, *Bright spatially coherent synchrotron X-rays from a table-top source*, Nat. Phys **6**, 980–983 (2010).

[33] S. Corde, K. T. Phuoc, G. Lambert, R. Fitour, V. Malka, A. Rousse, A. Beck, and E. Lefebvre, *Femtosecond x-rays from laser-plasma accelerators*, Rev. Mod. Phys **85**, 1 (2013).

[34] N. D. Powers, I. Ghebregziabher, G. Golovin, C. Liu, S. Chen, S. Banerjee, J. Zhang, and D. P. Umstadter, *Quasi-monoenergetic and tunable X-rays from a laser-driven Compton light source*, Nat. Photonics **8**, 28–31 (2014).

[35] A. R. Maier, N. Kajumba, A. Guggenmos, C. Werle, J. Wenz, N. Delbos, B. Zeitler, I. Dornmair, J. Schmidt, E. Gullikson, *et al.*, *Water-window x-ray pulses from a laser-plasma driven undulator*, Sci. Rep **10**, 1–8 (2020).

[36] W. Wang, K. Feng, L. Ke, C. Yu, Y. Xu, R. Qi, Y. Chen, Z. Qin, Z. Zhang, M. Fang, *et al.*, *Free-electron lasing at 27 nanometres based on a laser wakefield accelerator*, Nature **595**, 516–520 (2021).

[37] M. Labat, J. C. Cabadağ, A. Ghaith, A. Irman, A. Berlioux, P. Berteaud, F. Blache, S. Bock, F. Bouvet, F. Briquez, *et al.*, *Seeded free-electron laser driven by a compact laser plasma accelerator*, Nat. Photonics **17**, 150–156 (2022).

[38] European XFEL website: Comparison of current and future x-ray free-electron lasers, `https://www.xfel.eu/facility/comparison/index_eng.html`, accessed: 2022-12-12.

[39] A. Dubietis, G. Jonušauskas, and A. Piskarskas, *Powerful femtosecond pulse generation by chirped and stretched pulse parametric amplification in BBO crystal*, Opt. Commun. **88**, 437–440 (1992).

[40] S. Witte and K. S. Eikema, *Ultrafast optical parametric chirped-pulse amplification*, IEEE J. Sel. Top. Quantum Electron. **18**, 296–307 (2011).

[41] T. Eichner, T. Hülsenbusch, J. Dirkwinkel, T. Lang, L. Winkelmann, G. Palmer, and A. R. Maier, *Spatio-spectral couplings in saturated collinear OPCPA*, Opt. Express **30**, 3404–3415 (2022).

[42] T. Eichner, T. Hülsenbusch, G. Palmer, and A. R. Maier, *Evolutionary optimization and long-term stabilization of a white-light seeded two-stage OPCPA seed laser*, Opt. Express **31**, 36915–36927 (2023).

[43] C. Aleshire, T. Eichner, A. Steinkopff, A. Klenke, C. Jauregui, G. Palmer, S. Kuhn, N. Haarlammert, W. P. Leemans, T. Schreiber, *et al.*, *Frequency-doubled Q-switched 4× 4 multicore fiber laser system*, Opt. Lett. **48**, 2198–2201 (2023).

[44] V. Leroux, T. Eichner, and A. R. Maier, *Description of spatio-temporal couplings from heat-induced compressor grating deformation*, Opt. Express **28**, 8257–8265 (2020).

[45] V. Leroux, S. W. Jolly, M. Schnepp, T. Eichner, S. Jalas, M. Kirchen, P. Messner, C. Werle, P. Winkler, and A. R. Maier, *Wavefront degradation of a 200 TW laser from heat-induced deformation of in-vacuum compressor gratings*, Opt. Express **26**, 13061–13071 (2018).

[46] N. Delbos, C. Werle, I. Dornmair, T. Eichner, L. Hübner, S. Jalas, S. Jolly, M. Kirchen, V. Leroux, P. Messner, M. Schnepp, M. Trunk, P. Walker, P. Winkler, and A. Maier, *Lux – A laser–plasma driven undulator beamline*, Nucl. Instrum. Methods Phys. Res. A **909**, 318–322 (2018).

[47] A. R. Maier, N. M. Delbos, T. Eichner, L. Hübner, S. Jalas, L. Jeppe, S. W. Jolly, M. Kirchen, V. Leroux, P. Messner, M. Schnepp, M. Trunk, P. A. Walker, C. Werle, and P. Winkler, *Decoding Sources of Energy Variability in a Laser-Plasma Accelerator*, Phys. Rev. X **10**, 031039 (2020).

[48] M. Kirchen, S. Jalas, P. Messner, P. Winkler, T. Eichner, L. Hübner, T. Hülsenbusch, L. Jeppe, T. Parikh, M. Schnepp, and A. R. Maier, *Optimal Beam Loading in a Laser-Plasma Accelerator*, Phys. Rev. Lett **126**, 174801 (2021).

[49] S. Jalas, M. Kirchen, C. Braun, T. Eichner, J. B. Gonzalez, L. Hübner, T. Hülsenbusch, P. Messner, G. Palmer, M. Schnepp, C. Werle, P. Winkler, W. P. Leemans, and A. R. Maier, *Tuning curves for a laser-plasma accelerator*, Phys. Rev. Accel. Beams **26**, 071302 (2023).

[50] C. Werle, C. Braun, T. Eichner, T. Hülsenbusch, G. Palmer, and A. R. Maier, *Out-of-plane compressor for ultrafast Ti:sapphire pulses based on multilayer-dielectric gratings*, Opt. Express **31** (2023).

[51] S. W. Jolly, N. H. Matlis, F. Ahr, V. Leroux, T. Eichner, A.-L. Calendron, H. Ishizuki, T. Taira, F. X. Kärtner, and A. R. Maier, *Spectral phase control of interfering chirped pulses for high-energy narrowband terahertz generation*, Nat. Commun. **10**, 2591 (2019).

[52] N. Matlis, F. Ahr, A.-L. Calendron, H. Cankaya, G. Cirmi, T. Eichner, A. Fallahi, M. Fakhari, A. Hartin, M. Hemmer, *et al.*, *Acceleration of electrons in THz driven structures for AXSIS*, Nucl. Instrum. Methods Phys. Res. A **909**, 27–32 (2018).

[53] V. Berezhiani and I. Murusidze, *Interaction of highly relativistic short laser pulses with plasmas and nonlinear wake-field generation*, Phys. Scr. **45**, 87 (1992).

[54] P. Sprangle, E. Esarey, and A. Ting, *Nonlinear interaction of intense laser pulses in plasmas*, Phys. Rev. A **41**, 4463 (1990).

[55] R. Lehe, M. Kirchen, I. A. Andriyash, B. B. Godfrey, and J.-L. Vay, *A spectral, quasi-cylindrical and dispersion-free Particle-In-Cell algorithm*, Comput. Phys. Commun. **203**, 66–82 (2016).

[56] E. Esarey, C. B. Schroeder, and W. P. Leemans, *Physics of laser-driven plasma-based electron accelerators*, Rev. Mod. Phys. **81**, 1229–1285 (2009).

[57] A. I. Akhiezer and R. Polovin, *Theory of wave motion of an electron plasma*, Sov. phys. JETP **3** (1956).

[58] J. M. Dawson, *Nonlinear electron oscillations in a cold plasma*, Phys. Rev. **113**, 383 (1959).

[59] L. Lilje, E. Kako, D. Kostin, A. Matheisen, W.-D. Möller, D. Proch, D. Reschke, K. Saito, P. Schmüser, S. Simrock, *et al.*, *Achievement of 35 MV/m in the superconducting nine-cell cavities for TESLA*, Nucl. Instrum. Methods Phys. Res. A **524**, 1–12 (2004).

[60] S. Bulanov, N. Naumova, F. Pegoraro, and J. Sakai, *Particle injection into the wave acceleration phase due to nonlinear wake wave breaking*, Phys. Rev. E **58**, R5257 (1998).

[61] H. Suk, N. Barov, J. B. Rosenzweig, and E. Esarey, *Plasma electron trapping and acceleration in a plasma wake field using a density transition*, Phys. Rev. Lett **86**, 1011 (2001).

[62] L.-L. Yu, E. Esarey, C. Schroeder, J.-L. Vay, C. Benedetti, C. Geddes, M. Chen, and W. Leemans, *Two-color laser-ionization injection*, Phys. Rev. Lett **112**, 125001 (2014).

[63] M. Chen, E. Esarey, C. Schroeder, C. Geddes, and W. Leemans, *Theory of ionization-induced trapping in laser-plasma accelerators*, Phys. Plasmas **19**, 033101 (2012).

[64] E. Esarey, P. Sprangle, J. Krall, A. Ting, and G. Joyce, *Optically guided laser wake-field acceleration*, Physics of Fluids B: Plasma Physics **5**, 2690–2697 (1993).

[65] K. Nakamura, B. Nagler, C. Tóth, C. Geddes, C. Schroeder, E. Esarey, W. Leemans, A. Gonsalves, and S. Hooker, *GeV electron beams from a centimeter-scale channel guided laser wakefield accelerator*, Phys. Plasmas **14**, 056708 (2007).

[66] J. M. Madey, *Stimulated emission of bremsstrahlung in a periodic magnetic field*, J. Appl. Phys. **42**, 1906–1913 (1971).

[67] W. Decking, S. Abeghyan, P. Abramian, A. Abramsky, A. Aguirre, C. Albrecht, P. Alou, M. Altarelli, P. Altmann, K. Amyan, *et al.*, *A MHz-repetition-rate hard X-ray free-electron laser driven by a superconducting linear accelerator*, Nat. Photonics **14**, 391–397 (2020).

[68] P. Emma, R. Akre, J. Arthur, R. Bionta, C. Bostedt, J. Bozek, A. Brachmann, P. Bucksbaum, R. Coffee, F.-J. Decker, *et al.*, *First lasing and operation of an ångstrom-wavelength free-electron laser*, Nat. Photonics **4**, 641–647 (2010).

[69] E. Allaria, L. Badano, S. Bassanese, F. Capotondi, D. Castronovo, P. Cinquegrana, M. B. Danailov, G. D'Auria, A. Demidovich, R. De Monte, G. De Ninno, S. Di Mitri, B. Diviacco, W. M. Fawley, M. Ferianis, E. Ferrari, G. Gaio, D. Gauthier, L. Giannessi, F. Iazzourene, G. Kurdi, N. Mahne, I. Nikolov, F. Parmigiani, G. Penco, L. Raimondi, P. Rebernik, F. Rossi, E. Roussel, C. Scafuri, C. Serpico, P. Sigalotti, C. Spezzani, M. Svandrlik, C. Svetina, M. Trovó, M. Veronese, D. Zangrando, and M. Zangrando, *The FERMI free-electron lasers*, J. Synchrotron Radiat **22**, 485–491 (2015).

[70] W. a. Ackermann, G. Asova, V. Ayvazyan, A. Azima, N. Baboi, J. Bähr, V. Balandin, B. Beutner, A. Brandt, A. Bolzmann, *et al.*, *Operation of a free-electron laser from the extreme ultraviolet to the water window*, Nat. Photonics **1**, 336–342 (2007).

[71] P. Schmüser, M. Dohlus, J. Rossbach, and C. Behrens, *Free-electron lasers in the ultraviolet and X-ray regime*, Springer Tracts in Modern Physics **258** (2014).

[72] E. J. Jaeschke, S. Khan, J. R. Schneider, and J. B. Hastings, *Synchrotron light sources and free-electron lasers: accelerator physics, instrumentation and science applications* (Springer, 2016).

[73] O. Lundh, J. Lim, C. Rechatin, L. Ammoura, A. Ben-Ismaïl, X. Davoine, G. Gallot, J.-P. Goddet, E. Lefebvre, V. Malka, *et al.*, *Few femtosecond, few kiloampere electron bunch produced by a laser–plasma accelerator*, Nat. Phys **7**, 219–222 (2011).

[74] G. Plateau, C. Geddes, D. Thorn, M. Chen, C. Benedetti, E. Esarey, A. Gonsalves, N. Matlis, K. Nakamura, C. Schroeder, *et al.*, *Low-emittance electron bunches from a laser-plasma accelerator measured using single-shot x-ray spectroscopy*, Phys. Rev. Lett **109**, 064802 (2012).

[75] R. Weingartner, S. Raith, A. Popp, S. Chou, J. Wenz, K. Khrennikov, M. Heigoldt, A. R. Maier, N. Kajumba, M. Fuchs, *et al.*, *Ultralow emittance electron beams from a laser-wakefield accelerator*, Phys. Rev. Accel. Beams **15**, 111302 (2012).

[76] W. P. Leemans, B. Nagler, A. J. Gonsalves, C. Tóth, K. Nakamura, C. G. Geddes, E. Esarey, C. Schroeder, and S. Hooker, *GeV electron beams from a centimetre-scale accelerator*, Nat. Phys **2**, 696–699 (2006).

[77] X. Wang, R. Zgadzaj, N. Fazel, Z. Li, S. Yi, X. Zhang, W. Henderson, Y.-Y. Chang, R. Korzekwa, H.-E. Tsai, *et al.*, *Quasi-monoenergetic laser-plasma acceleration of electrons to 2 GeV*, Nat. Commun. **4**, 1–9 (2013).

[78] W. Lu, M. Tzoufras, C. Joshi, F. Tsung, W. Mori, J. Vieira, R. Fonseca, and L. Silva, *Generating multi-GeV electron bunches using single stage laser wakefield acceleration in a 3D nonlinear regime*, Phys. Rev. Accel. Beams **10**, 061301 (2007).

[79] Y. Glinec, J. Faure, A. Lifschitz, J. Vieira, R. A. Fonseca, L. Silva, and V. Malka, *Direct observation of betatron oscillations in a laser-plasma electron accelerator*, EPL **81**, 64001 (2008).

[80] S. Mangles, G. Genoud, S. Kneip, M. Burza, K. Cassou, B. Cros, N. Dover, C. Kamperidis, Z. Najmudin, A. Persson, *et al.*, *Controlling the spectrum of*

x-rays generated in a laser-plasma accelerator by tailoring the laser wavefront, Appl. Phys. Lett. **95**, 181106 (2009).

[81] S. Akturk, X. Gu, E. Zeek, and R. Trebino, *Pulse-front tilt caused by spatial and temporal chirp*, Opt. Express **12**, 4399 (2004).

[82] X. Gu, S. Akturk, and R. Trebino, *Spatial chirp in ultrafast optics*, Opt. Commun. **242**, 599–604 (2004).

[83] A. Jeandet, S. W. Jolly, A. Borot, B. Bussière, P. Dumont, J. Gautier, O. Gobert, J.-P. Goddet, A. Gonsalves, A. Irman, *et al.*, *Survey of spatio-temporal couplings throughout high-power ultrashort lasers*, Opt. Express **30**, 3262–3288 (2022).

[84] J. P. Zou, H. Coïc, and D. Papadopoulos, *Spatiotemporal coupling investigations for Ti:sapphire-based multi-PW lasers*, High Power Laser Sci. Eng. **10** (2022).

[85] M. Thévenet, D. E. Mittelberger, K. Nakamura, R. Lehe, C. B. Schroeder, J.-L. Vay, E. Esarey, and W. P. Leemans, *Pulse front tilt steering in laser plasma accelerators*, Phys. Rev. Accel. Beams **22**, 071301 (2019).

[86] A. Popp, J. Vieira, J. Osterhoff, Z. Major, R. Hörlein, M. Fuchs, R. Weingartner, T. P. Rowlands-Rees, M. Marti, R. A. Fonseca, S. F. Martins, L. O. Silva, S. M. Hooker, F. Krausz, F. Grüner, and S. Karsch, *All-Optical Steering of Laser-Wakefield-Accelerated Electron Beams*, Phys. Rev. Lett. **105**, 215001 (2010).

[87] D. E. Mittelberger, M. Thévenet, K. Nakamura, A. J. Gonsalves, C. Benedetti, J. Daniels, S. Steinke, R. Lehe, J.-L. Vay, C. B. Schroeder, E. Esarey, and W. P. Leemans, *Laser and electron deflection from transverse asymmetries in laser-plasma accelerators*, Phys. Rev. E **100**, 063208 (2019).

[88] C. qing Zhu, J. guang Wang, Y. fei Li, J. Feng, D. zhang Li, Y. hang He, J. hao Tan, J. long Ma, X. Lu, Y. tong Li, and L. ming Chen, *Optical steering of electron beam in laser plasma accelerators*, Opt. Express **28**, 11609–11617 (2020).

[89] A. Jullien, C. Durfee, A. Trisorio, L. Canova, J.-P. Rousseau, B. Mercier, L. Antonucci, G. Cheriaux, O. Albert, and R. Lopez-Martens, *Nonlinear spectral cleaning of few-cycle pulses via cross-polarized wave (XPW) generation*, Appl. Phys. B **96**, 293–299 (2009).

[90] D. Homoelle, A. L. Gaeta, V. Yanovsky, and G. Mourou, *Pulse contrast enhancement of high-energy pulses by use of a gas-filled hollow waveguide*, Opt. Lett. **27**, 1646–1648 (2002).

[91] J. H. Sung, S. K. Lee, T. M. Jeong, and C. H. Nam, *Enhancement of temporal contrast of high-power femtosecond laser pulses using two saturable absorbers in the picosecond regime*, Appl. Phys. B **116**, 287–292 (2014).

[92] B. Dromey, S. Kar, M. Zepf, and P. Foster, *The plasma mirror – a subpicosecond optical switch for ultrahigh power lasers*, Rev. Sci. Instrum **75**, 645–649 (2004).

[93] J. Ma, J. Wang, P. Yuan, G. Xie, K. Xiong, Y. Tu, X. Tu, E. Shi, Y. Zheng, and L. Qian, *Quasi-parametric amplification of chirped pulses based on a Sm^{3+}-doped yttrium calcium oxyborate crystal*, Optica **2**, 1006 (2015).

[94] H. Kiriyama, Y. Miyasaka, A. Kon, M. Nishiuchi, A. Sagisaka, H. Sasao, A. S. Pirozhkov, Y. Fukuda, K. Ogura, K. Kondo, *et al.*, *Enhancement of pre-pulse and picosecond pedestal contrast of the petawatt J-KAREN-P laser*, High Power Laser Sci. Eng. **9** (2021).

[95] M. Kalashnikov, K. Osvay, G. Priebe, L. Ehrentraut, S. Steinke, and W. Sandner, *Temporal contrast of high intensity laser systems above 10^{11} with double CPA technique*, in AIP Conference Proceedings, Vol. 1462 (American Institute of Physics, 2012) pp. 108–111.

[96] N. Khodakovskiy, M. Kalashnikov, E. Gontier, F. Falcoz, and P.-M. Paul, *Degradation of picosecond temporal contrast of Ti:sapphire lasers with coherent pedestals*, Opt. Lett. **41**, 4441–4444 (2016).

[97] J. Tan, N. Forget, A. Borot, D. Kaplan, P. Tournois, A. Muschet, and L. Veisz, *Dispersion control for temporal contrast optimization*, Opt. Express **26**, 25003–25012 (2018).

[98] J. Cupal, T. Spinka, E. Sistrunk, B. Rus, and C. Häfner, *Temporal prepulse contrast degradation in high-intensity CPA lasers from anisotropy of amplifier gain media*, Appl. Opt **60**, 8408–8418 (2021).

[99] Y. Tang, C. Hooker, O. Chekhlov, S. Hawkes, J. Collier, and P. Rajeev, *Transmission grating stretcher for contrast enhancement of high power lasers*, Opt. Express **22**, 29363–29374 (2014).

[100] L. Ranc, C. Le Blanc, N. Lebas, L. Martin, J.-P. Zou, F. Mathieu, C. Radier, S. Ricaud, F. Druon, and D. Papadopoulos, *Improvement in the temporal contrast in the tens of ps range of the multi-PW Apollon laser front-end*, Opt. Lett. **45**, 4599–4602 (2020).

[101] S. Jalas, M. Kirchen, P. Messner, P. Winkler, L. Hübner, J. Dirkwinkel, M. Schnepp, R. Lehe, and A. R. Maier, *Bayesian optimization of a laser-plasma accelerator*, Phys. Rev. Lett **126**, 104801 (2021).

[102] C. Le Blanc, P. Curley, and F. Salin, *Gain-narrowing and gain-shifting of ultra-short pulses in Ti:sapphire amplifiers*, Opt. Commun. **131**, 391–398 (1996).

[103] F. Verluise, V. Laude, Z. Cheng, C. Spielmann, and P. Tournois, *Amplitude and phase control of ultrashort pulses by use of an acousto-optic programmable dispersive filter: pulse compression and shaping*, Opt. Lett. **25**, 575–577 (2000).

[104] S. Goloboroko, G. Grygiel, O. Hensler, V. Kocharyan, K. Rehlich, and P. Shevtsov, *DOOCS: an Object-Oriented Control System as the Integrating Part for the TTF Linac*, in Proceedings of ICALEPCS, Vol. 97 (1997) p. 141.

[105] Website of the DOOCS control system at DESY, `https://doocs.desy.de`, accessed: 2022-12-08.

[106] M. Müller, C. Aleshire, A. Klenke, E. Haddad, F. Légaré, A. Tünnermann, and J. Limpert, *10.4 kW coherently combined ultrafast fiber laser*, Opt. Lett. **45**, 3083–3086 (2020).

[107] Y. Wang, H. Chi, C. Baumgarten, K. Dehne, A. R. Meadows, A. Davenport, G. Murray, B. A. Reagan, C. S. Menoni, and J. J. Rocca, *1.1 J Yb:YAG picosecond laser at 1 kHz repetition rate*, Opt. Lett. **45**, 6615 (2020).

[108] Y. Pfaff, G. Barbiero, M. Rampp, S. Klingebiel, J. Brons, C. Y. Teisset, H. Wang, R. Jung, J. Jaksic, A. H. Woldegeorgis, M. Trunk, A. R. Maier, C. J. Saraceno, and T. Metzger, *Nonlinear pulse compression of a 200 mJ and 1 kW ultrafast thin-disk amplifier*, Opt. Express **31**, 22740–22756 (2023).

[109] A.-L. Viotti, M. Seidel, E. Escoto, S. Rajhans, W. P. Leemans, I. Hartl, and C. M. Heyl, *Multi-pass cells for post-compression of ultrashort laser pulses*, Optica **9**, 197 (2022).

[110] Y. Pfaff, C. Forster, G. Barbiero, M. Rampp, S. Klingebiel, J. Brons, C. Y. Teisset, H. Wang, R. Jung, J. Jaksic, A. H. Woldegeorgis, C. J. Saraceno, and T. Metzger, *Nonlinear pulse compression of a thin-disk amplifier and contrast enhancement via nonlinear ellipse rotation*, Opt. Express **30**, 10981–10990 (2022).

[111] E. Escoto, A.-L. Viotti, S. Alisauskas, H. Tünnermann, I. Hartl, and C. M. Heyl, *Temporal quality of post-compressed pulses at large compression factors*, J. Opt. Soc. Am. B **39**, 1694 (2022).

[112] H. Stark, M. Benner, J. Buldt, A. Klenke, and J. Limpert, *32 mJ, 158 fs pulses at 20 kHz repetition rate from a spatio-temporally combined*, Opt. Express **23**, 7442 (2015).

[113] N. Flemens, N. Swenson, and J. Moses, *Efficient parametric amplification via simultaneous second harmonic generation*, Opt. Express **29**, 30590–30609 (2021).

[114] Z. Hong, H. Zhang, and S. Ke, *Efficient Generation of Spectrum-Manipulated Few-Cycle Laser Pulses through Cascaded Dual-Chirped OPA*, International Journal of Molecular Sciences **22**, 6887 (2021).

[115] R. Riedel, J. Rothhardt, K. Beil, B. Gronloh, A. Klenke, H. Höppner, M. Schulz, U. Teubner, C. Kränkel, J. Limpert, *et al.*, *Thermal properties of borate crystals for high power optical parametric chirped-pulse amplification*, Opt. Express **22**, 17607–17619 (2014).

[116] A. Zaukevičius, V. Jukna, R. Antipenkov, V. Martinėnaitė, A. Varanavičius, A. P. Piskarskas, and G. Valiulis, *Manifestation of spatial chirp in femtosecond noncollinear optical parametric chirped-pulse amplifier*, J. Opt. Soc. Am. B **28**, 2902 (2011).

[117] I. Jovanovic, C. A. Ebbers, and C. P. J. Barty, *Hybrid chirped-pulse amplification*, Opt. Lett. **27**, 1622 (2002).

[118] I. Jovanovic, B. J. Comaskey, C. A. Ebbers, R. A. Bonner, D. M. Pennington, and E. C. Morse, *Optical parametric chirped-pulse amplifier as an alternative to Ti:sapphire regenerative amplifiers*, Appl. Opt **41**, 2923 (2002).

[119] I. Tamer, B. A. Reagan, T. Galvin, J. Galbraith, E. Sistrunk, A. Church, G. Huete, H. Neurath, and T. Spinka, *Demonstration of a compact, multi-joule, diode-pumped Tm:YLF laser*, Opt. Lett. **46**, 5096–5099 (2021).

[120] I. Tamer, B. A. Reagan, T. Galvin, F. Batysta, E. Sistrunk, D. Willard, A. Church, H. Neurath, J. Galbraith, G. Huete, *et al.*, *1 GW peak power and 100 J pulsed operation of a diode-pumped Tm:YLF laser*, Opt. Express **30**, 46336–46343 (2022).

[121] W. Leemans, *Laser technology for k-BELLA and beyond* (2017).

[122] V. Petrov, Y. Wang, W. Chen, Z. Pan, Y. Zhao, L. Wang, M. Mero, S. Y. Choi, F. Rotermund, W. B. Cho, W. Jing, H. Huang, H. Yuan, H. Cai, L. Zhang, Z. Lin, P. Loiko, X. Mateos, X. Xu, J. Xu, H. Yu, H. Zhang, S. Suomalainen, M. Guina, A. Härkönen, and U. Griebner, *Sub-100-fs bulk solid-state lasers near 2-micron*, in Eleventh International Conference on Information Optics and Photonics (CIOP 2019), Vol. 11209, edited by H. Wang, International Society for Optics and Photonics (SPIE, 2019) p. 112094G.

[123] Wang, Ziyao, Heuermann, Tobias, Gebhardt, Martin, Lenski, Mathias, Gierschke, Philipp, Klas, Robert, Jauregui, Cesar, and Limpert, Jens, *100W, 1 mJ, few-cycle pulses at 2 velength*, EPJ Web Conf. **267**, 02025 (2022).

[124] Z. Wang, T. Heuermann, M. Gebhardt, M. Lenski, P. Gierschke, R. Klas, J. Rothhardt, C. Jauregui, and J. Limpert, *Nonlinear pulse compression to sub-two-cycle, 1.3 mJ pulses at 1.9 μm wavelength with 132 W average power*, Opt. Lett. **48**, 2647–2650 (2023).

[125] C. Danson, D. Hillier, N. Hopps, and D. Neely, *Petawatt class lasers worldwide*, High Power Laser Sci. Eng. **3**, e3 (2015).

[126] C. Radier, O. Chalus, M. Charbonneau, S. Thambirajah, G. Deschamps, S. David, J. Barbe, E. Etter, G. Matras, S. Ricaud, and et al., *10 PW peak power femtosecond laser pulses at ELI-NP*, High Power Laser Sci. Eng. **10**, e21 (2022).

[127] K. Mecseki, M. K. R. Windeler, A. Miahnahri, J. S. Robinson, J. M. Fraser, A. R. Fry, and F. Tavella, *High average power 88W OPCPA system for high-repetition-rate experiments at the LCLS x-ray free-electron laser*, Opt. Lett. **44**, 1257–1260 (2019).

[128] M. K. R. Windeler, K. Mecseki, A. Miahnahri, J. S. Robinson, J. M. Fraser, A. R. Fry, and F. Tavella, *100W high-repetition-rate near-infrared optical parametric chirped pulse amplifier*, Opt. Lett. **44**, 4287–4290 (2019).

[129] R. Budriūnas, T. Stanislauskas, J. Adamonis, A. Aleknavičius, G. Veitas, D. Gadonas, S. Balickas, A. Michailovas, and A. Varanavičius, *53 W average power CEP-stabilized OPCPA system delivering 5.5 TW few cycle pulses at 1 kHz repetition rate*, Opt. Express **25**, 5797–5806 (2017).

[130] V. V. Lozhkarev, G. I. Freidman, V. N. Ginzburg, E. V. Katin, E. A. Khazanov, A. V. Kirsanov, G. A. Luchinin, A. N. Mal'shakov, M. A. Martyanov, O. V. Palashov, A. K. Poteomkin, A. M. Sergeev, A. A. Shaykin, and I. V. Yakovlev, *Compact 0.56 Petawatt laser system based on optical parametric chirped pulse amplification in KD*P crystals*, Laser Phys. Lett **4**, 421 (2007).

[131] X. Zeng, K. Zhou, Y. Zuo, Q. Zhu, J. Su, X. Wang, X. Wang, X. Huang, X. Jiang, D. Jiang, Y. Guo, N. Xie, S. Zhou, Z. Wu, J. Mu, H. Peng, and F. Jing, *Multi-petawatt laser facility fully based on optical parametric chirped-pulse amplification*, Opt. Lett. **42**, 2014–2017 (2017).

[132] T. Heuermann, Z. Wang, M. Lenski, M. Gebhardt, C. Gaida, M. Abdelaal, J. Buldt, M. Müller, A. Klenke, and J. Limpert, *188 W average power coherently combined Tm-doped fiber laser system delivering ultrashort pulses with 1.86 mJ energy*, in Fiber Lasers XX: Technology and Systems, Vol. 12400, edited by V. R. Supradeepa, International Society for Optics and Photonics (SPIE, 2023) p. 124000E.

[133] T. Heuermann, Z. Wang, M. Lenski, M. Gebhardt, C. Gaida, M. Abdelaal, J. Buldt, M. Müller, A. Klenke, and J. Limpert, *Ultrafast Tm-doped fiber laser system delivering 1.65-mJ, sub-100-fs pulses at a 100-kHz repetition rate*, Opt. Lett. **47**, 3095–3098 (2022).

[134] H. Stark, J. Buldt, M. Müller, A. Klenke, A. Tünnermann, and J. Limpert, *23mJ high-power fiber CPA system using electro-optically controlled divided-pulse amplification*, Opt. Lett. **44**, 5529–5532 (2019).

[135] H. Stark, J. Buldt, M. Müller, A. Klenke, and J. Limpert, *1kW, 10mJ, 120fs coherently combined fiber CPA laser system*, Opt. Lett. **46**, 969–972 (2021).

[136] M. Müller, C. Aleshire, A. Klenke, E. Haddad, F. Légaré, A. Tünnermann, and J. Limpert, *10.4kW coherently combined ultrafast fiber laser*, Opt. Lett. **45**, 3083–3086 (2020).

[137] J.-P. Negel, A. Loescher, A. Voss, D. Bauer, D. Sutter, A. Killi, M. A. Ahmed, and T. Graf, *Ultrafast thin-disk multipass laser amplifier delivering 1.4 kW (4.7 mJ, 1030 nm) average power converted to 820 W at 515 nm and 234 W at 343 nm*, Opt. Express **23**, 21064–21077 (2015).

[138] T. Dietz, M. Jenne, D. Bauer, M. Scharun, D. Sutter, and A. Killi, *Ultrafast thin-disk multi-pass amplifier system providing 1.9 kW of average output power and pulse energies in the 10 mJ range at 1 ps of pulse duration for glass-cleaving applications*, Opt. Express **28**, 11415–11423 (2020).

[139] T. Nubbemeyer, M. Kaumanns, M. Ueffing, M. Gorjan, A. Alismail, H. Fattahi, J. Brons, O. Pronin, H. G. Barros, Z. Major, T. Metzger, D. Sutter, and F. Krausz, *1kW, 200mJ picosecond thin-disk laser system*, Opt. Lett. **42**, 1381–1384 (2017).

[140] M. Müller, A. Klenke, A. Steinkopff, H. Stark, A. Tünnermann, and J. Limpert, *3.5kW coherently combined ultrafast fiber laser*, Opt. Lett. **43**, 6037–6040 (2018).

[141] L. Zapata, M. Pergament, M. Schust, S. Reuter, J. Thesinga, C. Zapata, M. Kellert, U. Demirbas, A.-L. Calendron, Y. Liu, *et al.*, *One-joule 500-Hz cryogenic Yb: YAG laser driver of composite thin-disk design*, Opt. Lett. **47**, 6385–6388 (2022).

[142] M. Divoký, J. Pilař, M. Hanuš, P. Navrátil, O. Denk, P. Severová, P. Mason, T. Butcher, S. Banerjee, M. De Vido, *et al.*, *150J DPSSL operating at 1.5kW level*, Opt. Lett. **46**, 5771–5773 (2021).

[143] C. Grebing, M. Müller, J. Buldt, H. Stark, and J. Limpert, *Kilowatt-average-power compression of millijoule pulses in a gas-filled multi-pass cell*, Opt. Lett. **45**, 6250–6253 (2020).

[144] M. Kaumanns, V. Pervak, D. Kormin, V. Leshchenko, A. Kessel, M. Ueffing, Y. Chen, and T. Nubbemeyer, *Multipass spectral broadening of 18 mJ pulses compressible from 1.3 ps to 41 fs*, Opt. Lett. **43**, 5877–5880 (2018).

[145] M. Kaumanns, D. Kormin, T. Nubbemeyer, V. Pervak, and S. Karsch, *Spectral broadening of 112 mJ, 1.3 ps pulses at 5 kHz in a LG 10 multipass cell with compressibility to 37 fs*, Opt. Lett. **46**, 929–932 (2021).

[146] J. Bromage, S.-W. Bahk, M. Bedzyk, I. Begishev, S. Bucht, C. Dorrer, C. Feng, C. Jeon, C. Mileham, R. Roides, *et al.*, *MTW-OPAL: a technology development platform for ultra-intense optical parametric chirped-pulse amplification systems*, High Power Laser Sci. Eng. **9**, e63 (2021).

[147] M. Pergament, G. Palmer, M. Kellert, K. Kruse, J. Wang, L. Wissmann, U. Wegner, M. Emons, D. Kane, G. Priebe, *et al.*, *Versatile optical laser system for experiments at the European X-ray free-electron laser facility*, Opt. Express **24**, 29349–29359 (2016).

[148] L. Gizzi, P. Koester, L. Labate, F. Mathieu, Z. Mazzotta, G. Toci, and M. Vannini, *Lasers for novel accelerators*, in Journal of Physics: Conference Series, Vol. 1350 (IOP Publishing, 2019) p. 012157.

[149] L. Kiani, T. Zhou, S.-W. Bahk, J. Bromage, D. Bruhwiler, E. M. Campbell, Z. Chang, E. Chowdhury, M. Downer, Q. Du, *et al.*, *High average power ultrafast laser technologies for driving future advanced accelerators*, arXiv preprint arXiv:2204.10774 (2022).

[150] C. Benedetti, S. Bulanov, E. Esarey, C. Geddes, A. Gonsalves, A. Huebl, R. Lehe, K. Nakamura, C. Schroeder, D. Terzani, *et al.*, *Linear colliders based on laser-plasma accelerators*, arXiv preprint arXiv:2203.08366 (2022).

[151] R. Baumgartner and R. Byer, *Optical parametric amplification*, IEEE J. Sel. Top. Quantum Electron **15**, 432–444 (1979).

[152] X. Liang, X. Xie, J. Kang, Q. Yang, H. Wei, M. Sun, and J. Zhu, *Design and experimental demonstration of a high conversion efficiency OPCPA pre-amplifier for petawatt laser facility*, High Power Laser Sci. Eng. **6** (2018).

[153] C. Dorrer, A. Consentino, D. Irwin, J. Qiao, and J. Zuegel, *OPCPA front end and contrast optimization for the OMEGA EP kilojoule, picosecond laser*, J. Opt. **17**, 094007 (2015).

[154] I. Ahmad, S. A. Trushin, Z. Major, C. Wandt, S. Klingebiel, T.-J. Wang, V. Pervak, A. Popp, M. Siebold, F. Krausz, *et al.*, *Frontend light source for short-pulse pumped OPCPA system*, Appl. Phys. B **97**, 529–536 (2009).

[155] E. Hugonnot, G. Deschaseaux, O. Hartmann, and H. Coïc, *Design of PETAL multipetawatt high-energy laser front end based on optical parametric chirped pulse amplification*, Appl. Opt **46**, 8181–8187 (2007).

[156] C. N. Danson, C. Haefner, J. Bromage, T. Butcher, J.-C. F. Chanteloup, E. A. Chowdhury, A. Galvanauskas, L. A. Gizzi, J. Hein, D. I. Hillier, N. W. Hopps, Y. Kato, E. A. Khazanov, R. Kodama, G. Korn, R. Li, Y. Li, J. Limpert, J. Ma, C. H. Nam, D. Neely, D. Papadopoulos, R. R. Penman, L. Qian, J. J. Rocca, A. A. Shaykin, C. W. Siders, C. Spindloe, S. Szantmári, R. M. G. M. Trines,

J. Zhu, P. Zhu, and J. D. Zuegel, *Petawatt and exawatt class lasers worldwide*, High Power Laser Sci. Eng. **7**, e54 (2019).

[157] R. W. Boyd, *Nonlinear optics* (Academic press, 2020).

[158] H. Fattahi, *Third-generation Femtosecond Technology, Springer theses* (Springer International Publishing Cham, 2015).

[159] C. Manzoni and G. Cerullo, *Design criteria for ultrafast optical parametric amplifiers*, J. Opt. **18**, 103501 (2016).

[160] F. Zernike and J. E. Midwinter, *Applied nonlinear optics* (Courier Corporation, 2006).

[161] G. New, *Introduction to nonlinear optics* (Cambridge University Press, 2011).

[162] Y.-R. Shen, *The Principles of Nonlinear Optics. 3rd edn, 576* (Wiley-Interscience, New York, 2002).

[163] V. Pyragaite, A. Stabinis, R. Butkus, R. Antipenkov, and A. Varanavičius, *Parametric amplification of chirped optical pulses under pump depletion*, Opt. Commun. **283**, 1144–1151 (2010).

[164] T. Lang, A. Harth, J. Matyschok, T. Binhammer, M. Schultze, and U. Morgner, *Impact of temporal, spatial and cascaded effects on the pulse formation in ultrabroadband parametric amplifiers*, Opt. Express **21**, 949 (2013).

[165] T. Lang, *Chi23D* (2022), www.chi23d.com.

[166] T. Lang, *Ultrashort laser pulses from optical parametric amplifiers and oscillators*, Ph.D. thesis (2014).

[167] I. N. Ross, P. Matousek, G. H. New, and K. Osvay, *Analysis and optimization of optical parametric chirped pulse amplification*, JOSA B **19**, 2945–2956 (2002).

[168] J. Moses, C. Manzoni, S.-W. Huang, G. Cerullo, and F. X. Kaertner, *Temporal optimization of ultrabroadband high-energy OPCPA*, Opt. Express **17**, 5540 (2009).

[169] D. Eimerl, *High average power harmonic generation*, IEEE J. Sel. Top. Quantum Electron. **23**, 575–592 (1987).

[170] A. Sharma, R. Patidar, P. Naik, and P. Gupta, *Theoretical studies on optimization of a broadband optical parametric amplifier for enhanced output stability*, Opt. Commun. **309**, 139–147 (2013).

[171] S. Zhang, M. Fujita, M. Yamanaka, M. Nakatsuka, Y. Izawa, and C. Yamanaka, *Study of the stability of optical parametric amplification*, Opt. Commun. **184**, 451–455 (2000).

[172] M. Guardalben, J. Keegan, L. Waxer, V. Bagnoud, I. Begishev, J. Puth, and J. Zuegel, *Design of a highly stable, high-conversion-efficiency, optical parametric chirped-pulse amplification system with good beam quality*, Opt. Express **11**, 2511 (2003).

[173] S. Prinz, M. Häfner, M. Schultze, C. Y. Teisset, R. Bessing, K. Michel, R. Kienberger, and T. Metzger, *Active pump-seed-pulse synchronization for OPCPA with sub-2-fs residual timing jitter*, Opt. Express **22**, 31050 (2014).

[174] R. Riedel, M. Schulz, M. J. Prandolini, A. Hage, H. Höppner, T. Gottschall, J. Limpert, M. Drescher, and F. Tavella, *Long-term stabilization of high power optical parametric chirped-pulse amplifiers*, Opt. Express **21**, 28987 (2013).

[175] C. Homann and E. Riedle, *Direct measurement of the effective input noise power of an optical parametric amplifier*, Laser Photonics Rev **7**, 580–588 (2013).

[176] F. Tavella, A. Marcinkevičius, and F. Krausz, *Investigation of the superfluorescence and signal amplification in an ultrabroadband multiterawatt optical parametric chirped pulse amplifier system*, New J. Phys. **8**, 219–219 (2006).

[177] C. Manzoni, J. Moses, F. X. Kärtner, and G. Cerullo, *Excess quantum noise in optical parametric chirped-pulse amplification*, Opt. Express **19**, 8357–8366 (2011).

[178] W. Chen, J. Fan, A. Ge, H. Song, Y. Song, B. Liu, L. Chai, C. Wang, and M. Hu, *Intensity and temporal noise characteristics in femtosecond optical parametric amplifiers*, Opt. Express **25**, 31263 (2017).

[179] L. J. Waxer, V. Bagnoud, I. A. Begishev, M. J. Guardalben, J. Puth, and J. D. Zuegel, *High-conversion-efficiency optical parametric chirped-pulse amplification system using spatiotemporally shaped pump pulses*, Opt. Lett. **28**, 1245 (2003).

[180] J. Bromage, C. Dorrer, and J. D. Zuegel, *Angular-dispersion-induced spatiotemporal aberrations in noncollinear optical parametric amplifiers*, Opt. Lett. **35**, 2251 (2010).

[181] R. Danielius, A. Piskarskas, P. Di Trapani, A. Andreoni, C. Solcia, and P. Foggi, *Matching of group velocities by spatial walk-off in collinear three-wave interaction with tilted pulses*, Opt. Lett. **21**, 973–975 (1996).

[182] A. Baltuška and T. Kobayashi, *Adaptive shaping of two-cycle visible pulses using a flexible mirror*, Appl. Phys. B **75**, 427–443 (2002).

[183] A.-L. Calendron, H. Çankaya, G. Cirmi, and F. X. Kärtner, *White-light generation with sub-ps pulses*, Opt. Express **23**, 13866 (2015).

[184] A. Dubietis, G. Tamošauskas, R. Šuminas, V. Jukna, and A. Couairon, *Ultrafast supercontinuum generation in bulk condensed media*, Lithuanian Journal of Physics **57** (2017).

[185] M. Bradler, P. Baum, and E. Riedle, *Femtosecond continuum generation in bulk laser host materials with sub-J pump pulses*, Appl. Phys. B **97**, 561–574 (2009).

[186] A. Špaček, L. Indra, F. Batysta, P. Hříbek, J. T. Green, J. Novák, R. Antipenkov, P. Bakule, and B. Rus, *Stability mechanism of picosecond supercontinuum in YAG*, Opt. Express **28**, 20205 (2020).

[187] T. Hülsenbusch, *TBD*, (2023), in preparation.

[188] T. Hülsenbusch, *TBD*, Ph.D. thesis (2023).

[189] R. Akbari and A. Major, *Optical, spectral and phase-matching properties of BIBO, BBO and LBO crystals for optical parametric oscillation in the visible and near-infrared wavelength ranges*, Laser Phys **23**, 035401 (2013).

[190] D. N. Nikogosyan, *Lithium triborate (LBO)*, Appl. Phys. A **58**, 181–190 (1994).

[191] Ultrafast Innovations, *Datasheet of Tundra 800nm* (2022).

[192] A. Giree, M. Mero, G. Arisholm, M. J. J. Vrakking, and F. J. Furch, *Numerical study of spatiotemporal distortions in noncollinear optical parametric chirped-pulse amplifiers*, Opt. Express **25**, 3104 (2017).

[193] A. Borot and F. Quéré, *Spatio-spectral metrology at focus of ultrashort lasers: a phase-retrieval approach*, Opt. Express **26**, 26444–26461 (2018).

[194] Y. Wang, J. Wang, B. Zhou, J. Ma, P. Yuan, and L. Qian, *Spatiotemporal couplings through a nonlinear phase in broadband optical parametric amplification*, Opt. Lett. **46**, 5743–5746 (2021).

[195] H. J. Bakker, P. C. M. Planken, L. Kuipers, and A. Lagendijk, *Phase modulation in second-order nonlinear-optical processes*, Phys. Rev. A **42**, 4085–4101 (1990).

[196] V. Leroux, `https://github.com/VincentLeroux/Laser`.

[197] A. Jeandet, A. Borot, K. Nakamura, S. W. Jolly, A. J. Gonsalves, C. Tóth, H.-S. Mao, W. P. Leemans, and F. Quéré, *Spatio-temporal structure of a petawatt femtosecond laser beam*, JPhys photonics **1**, 035001 (2019).

[198] V. N. Mahajan, *Strehl ratio for primary aberrations in terms of their aberration variance*, J. Opt. Soc. Am. **73**, 860–861 (1983).

[199] B. J. Meers, *On the suppression of laser beam geometry fluctuations by spatial filtering*, Opt. Commun. **47**, 237–242 (1983).

[200] G. Genty, L. Salmela, J. M. Dudley, D. Brunner, A. Kokhanovskiy, S. Kobtsev, and S. K. Turitsyn, *Machine learning and applications in ultrafast photonics*, Nat. Photonics **15**, 91–101 (2021).

[201] R. Woodward and E. J. Kelleher, *Towards 'smart lasers': self-optimisation of an ultrafast pulse source using a genetic algorithm*, Sci. Rep **6**, 1–9 (2016).

[202] C. Sun, E. Kaiser, S. L. Brunton, and J. N. Kutz, *Deep reinforcement learning for optical systems: A case study of mode-locked lasers*, Machine Learning: Science and Technology **1**, 045013 (2020).

[203] C. M. Valensise, A. Giuseppi, G. Cerullo, and D. Polli, *Deep reinforcement learning control of white-light continuum generation*, Optica **8**, 239–242 (2021).

[204] N. Hansen, A. Auger, R. Ros, S. Finck, and P. Pošík, *Comparing results of 31 algorithms from the black-box optimization benchmarking*, in Proceedings of the 12th annual conference companion on Genetic and evolutionary computation (2010) pp. 1689–1696.

[205] O. Kramer, *Genetic algorithms*, in Genetic algorithm essentials (Springer, 2017) pp. 11–19.

[206] N. Hansen and A. Ostermeier, *Completely derandomized self-adaptation in evolution strategies*, Evolutionary Computation **9**, 159–195 (2001).

[207] N. Hansen, *The CMA evolution strategy: a comparing review*, Towards a new evolutionary computation , 75–102 (2006).

[208] N. Hansen, *The CMA evolution strategy: A tutorial*, arXiv preprint arXiv:1604.00772 (2016).

[209] *List of references to applications of CMA-ES*, `http://www.cmap.polytechnique.fr/~nikolaus.hansen/cmaapplications.pdf`, accessed: 2022-12-07.

[210] D. V. Arnold and H.-G. Beyer, *Noisy optimization with evolution strategies*, Vol. 8 (Springer Science & Business Media, 2002).

[211] M. J. Powell, *The NEWUOA software for unconstrained optimization without derivatives*, in Large-scale nonlinear optimization (Springer, 2006) pp. 255–297.

[212] R. Ros and N. Hansen, *Black-Box Optimization Benchmarking of NEWUOA compared to BIPOP-CMA-ES*, in Genetic and Evolutionary Computation Conference 2010 (2010).

[213] J. Blank and K. Deb, *pymoo: Multi-Objective Optimization in Python*, IEEE Access **8**, 89497–89509 (2020).

[214] B. Friedland, *Control system design: an introduction to state-space methods* (Courier Corporation, 2012).

[215] D. Sundararajan, *Control Systems: An Introduction* (Springer Nature, 2022).

[216] S. J. Dodds *et al.*, *Feedback control*, London: Springer , 5 (2015).

[217] H. Cao, S. Tóth, M. Kalashnikov, V. Chvykov, and K. Osvay, *Highly efficient, cascaded extraction optical parametric amplifier*, Opt. Express **26**, 7516 (2018).

[218] R. Budriūnas, D. Kučinskas, G. Valiulis, and A. Varanavičius, *Increasing the Efficiency of Optical Parametric Amplifiers With Polarization-Based Idler Elimination*, in OSA Nonlinear Optics 2021 (Optica Publishing Group, 2021).

[219] J. Ma, J. Wang, B. Zhou, P. Yuan, G. Xie, K. Xiong, Y. Zheng, H. Zhu, and L. Qian, *Broadband, efficient, and robust quasi-parametric chirped-pulse amplification*, Opt. Express **25**, 25149 (2017).

[220] R. Ell, U. Morgner, F. X. Kärtner, J. G. Fujimoto, E. P. Ippen, V. Scheuer, G. Angelow, T. Tschudi, M. J. Lederer, A. Boiko, *et al.*, *Generation of 5-fs pulses and octave-spanning spectra directly from a Ti:Sapphire laser*, Opt. Lett. **26**, 373–375 (2001).

[221] T. Steele, D. Gerstenberger, A. Drobshoff, and R. Wallace, *Broadly tunable high-power operation of an all-solid-state titanium-doped sapphire laser system*, Opt. Lett. **16**, 399–401 (1991).

[222] K. F. Wall and A. Sanchez, *Titanium sapphire lasers*, The Lincoln laboratory journal **3**, 447–462 (1990).

[223] P. F. Moulton, J. G. Cederberg, K. T. Stevens, G. Foundos, M. Koselja, and J. Preclikova, *Characterization of absorption bands in Ti:sapphire crystals*, Opt. Mater. Express **9**, 2216–2251 (2019).

[224] Minties Kvantas UAB, *Datasheet of PS5070 series flashlamp drivers* (2022).

[225] E. Sistrunk, T. Spinka, A. Bayramian, S. Betts, R. Bopp, S. Buck, K. Charron, J. Cupal, R. Deri, M. Drouin, *et al.*, *All diode-pumped, high-repetition-rate advanced petawatt laser system (HAPLS)*, in CLEO: Science and Innovations (Optica Publishing Group, 2017) pp. STh1L–2.

[226] R. Lera, P. Bellido, I. Sanchez, P. Mur, M. Seimetz, J. M. Benlloch, L. Roso, and A. R. de-la Cruz, *Development of a few TW Ti:Sa laser system at 100 Hz for proton acceleration*, Appl. Phys. B **125** (2018).

[227] C. G. Durfee, T. Storz, J. Garlick, S. Hill, J. A. Squier, M. Kirchner, G. Taft, K. Shea, H. Kapteyn, M. Murnane, *et al.*, *Direct diode-pumped Kerr-lens mode-locked Ti:sapphire laser*, Opt. Express **20**, 13677–13683 (2012).

[228] S. Backus, M. Kirchner, R. Lemons, D. Schmidt, C. Durfee, M. Murnane, and H. Kapteyn, *Direct diode pumped Ti:sapphire ultrafast regenerative amplifier system*, Opt. Express **25**, 3666–3674 (2017).

[229] Laserline GmbH, *Datasheet Laserline LDMblue laser diodes* (2022).

[230] A. J. Maclean, P. W. Roth, D. Burns, A. J. Kemp, and P. F. Moulton, *Pump Induced Loss in Directly-Diode Laser Pumped Ti:Sapphire Lasers*, in Lasers, Sources and Related Photonic Devices (Optica Publishing Group, 2010) p. AWB16.

[231] H. Liu, S. Sun, L. Zheng, G. Wang, W. Tian, D. Zhang, H. Han, J. Zhu, and Z. Wei, *Review of laser-diode pumped Ti:sapphire laser*, Microw. Opt. Technol. Lett. **63**, 2135–2144 (2021).

[232] A. Klenke, A. Steinkopff, C. Aleshire, C. Jauregui, S. Kuhn, J. Nold, C. Hupel, S. Hein, S. Schulze, N. Haarlammert, *et al.*, *500 W rod-type 4× 4 multicore ultrafast fiber laser*, Opt. Lett. **47**, 345–348 (2022).

[233] C. Aleshire, A. Steinkopff, A. Klenke, C. Jáuregui, S. Kuhn, J. Nold, N. Haarlammert, T. Schreiber, and J. Limpert, *High-energy Q-switched 16-core tapered rod-type fiber laser system*, Opt. Lett. **47**, 1725–1728 (2022).

[234] A. Steinkopff, C. Jauregui, C. Aleshire, A. Klenke, and J. Limpert, *Impact of thermo-optical effects in coherently combined multicore fiber amplifiers*, Opt. Express **28**, 38093–38105 (2020).

[235] A. Klenke, A. Steinkopff, C. Aleshire, C. Jauregui, S. Kuhn, J. Nold, N. Haarlammert, T. Schreiber, A. Tünnermann, and J. Limpert, *1 kW average power emission from an in-house 4x4 multicore rod-type fiber*, in 2021 Conference on Lasers and Electro-Optics Europe & European Quantum Electronics Conference (CLEO/Europe-EQEC) (IEEE, 2021) pp. 1–1.

[236] M.-Y. Cheng, Y.-C. Chang, A. Galvanauskas, P. Mamidipudi, R. Changkakoti, and P. Gatchell, *High-energy and high-peak-power nanosecond pulse generation with beam quality control in 200-µm core highly multimode Yb-doped fiber amplifiers* (The Optical Society, 2005) p. 358.

[237] R. Dinger, F.-P. Grundmann, C. Hapke, P. Kallage, W. Rath, and S. Ruppik, *Short-pulse MOPA fiber laser with kilowatt average power and multi-megawatt peak power, applying advanced XLMA fiber amplifiers*, in Fiber Lasers XIV: Technology and Systems, Vol. 10083 (SPIE, 2017) pp. 262–268.

[238] I. P. Coorporation, *Specifications of YLPN-100-100-500-R high energy nanosecond fiber lasers* (2023).

[239] C. Röcker, A. Loescher, F. Bienert, P. Villeval, D. Lupinski, D. Bauer, A. Killi, T. Graf, and M. A. Ahmed, *Ultrafast green thin-disk laser exceeding 1.4 kW of average power*, Opt. Lett. **45**, 5522–5525 (2020).

[240] Z. Hubka, R. Antipenkov, R. Boge, E. Erdman, M. Greco, J. T. Green, M. Horáček, K. Majer, T. Mazanec, P. Mazrek, *et al.*, *120 mJ, 1 kHz, picosecond laser at 515 nm*, Opt. Lett. **46**, 5655–5658 (2021).

[241] J. P. Phillips, S. Banerjee, P. Mason, J. Smith, J. Spear, M. De Vido, K. Ertel, T. Butcher, G. Quinn, D. Clarke, *et al.*, *Second and third harmonic conversion of a kilowatt average power, 100-J-level diode pumped Yb: YAG laser in large aperture LBO*, Opt. Lett. **46**, 1808–1811 (2021).

[242] C. Aparajit, K. Jana, A. D. Lad, Y. M. Ved, A. Couairon, and G. R. Kumar, *Efficient second-harmonic generation of a high-energy, femtosecond laser pulse in a lithium triborate crystal*, Opt. Lett. **46**, 3540–3543 (2021).

[243] J. P. Phillips, S. Banerjee, J. Smith, M. Fitton, T. Davenne, K. Ertel, P. Mason, T. Butcher, M. De Vido, J. Greenhalgh, *et al.*, *High energy, high repetition rate, second harmonic generation in large aperture DKDP, YCOB, and LBO crystals*, Opt. Express **24**, 19682–19694 (2016).

[244] RAICOL, *Product catalogue on non-linear crystals* (2023).

[245] SNLO, `https://as-photonics.com/products/snlo/`, version: v76.

[246] B. E. Saleh and M. C. Teich, *Fundamentals of photonics* (john Wiley & sons, 2019).

[247] T. Eichner, *Github: long-pulse-shg*, `https://github.com/TimoEichner/long-pulse-shg`.

[248] A. Klenke, personal communication.

[249] RAICOL, *Technical data sheet on LBO crystals* (2022).

[250] COMSOL Multiphysics v6.0. www.comsol.com. COMSOL AB, Stockholm, Sweden.

[251] S. G. Grechin, A. V. Zuev, A. E. Kokh, N. V. Moiseev, P. A. Popov, A. A. Sidorov, and A. S. Fokin, *Thermophysical parameters of the LBO crystal*, Quantum Electronics **40**, 509–512 (2010).

[252] C. Herkommer, P. Krötz, R. Jung, S. Klingebiel, C. Wandt, R. Bessing, P. Walch, T. Produit, K. Michel, D. Bauer, *et al.*, *Ultrafast thin-disk multipass amplifier with 720 mJ operating at kilohertz repetition rate for applications in atmospheric research*, Opt. Express **28**, 30164–30173 (2020).

[253] M. Kirchen, personal communication.

[254] W. Koechner, *Solid-state laser engineering*, Vol. 1 (Springer, 2013).

[255] T. Planchon, F. Burgy, J.-P. Rousseau, and J.-P. Chambaret, *3D Modeling of amplification processes in CPA laser amplifiers*, Appl. Phys. B **80**, 661–667 (2005).

[256] P. Russbueldt, D. Hoffmann, M. Höfer, J. Löhring, J. Luttmann, A. Meissner, J. Weitenberg, M. Traub, T. Sartorius, D. Esser, *et al.*, *Innoslab amplifiers*, IEEE J. Sel. Top. Quantum Electron. **21**, 447–463 (2014).

[257] A. Giesen, H. Hügel, A. Voss, K. Wittig, U. Brauch, and H. Opower, *Scalable concept for diode-pumped high-power solid-state lasers*, Appl. Phys. B **58**, 365–372 (1994).

[258] C. J. Saraceno, D. Sutter, T. Metzger, and M. Abdou Ahmed, *The amazing progress of high-power ultrafast thin-disk lasers*, J. Eur. Opt. Soc.: Rapid Publ **15**, 1–7 (2019).

[259] R. Nagymihaly, H. Cao, D. Papp, G. Hajas, M. Kalashnikov, K. Osvay, and V. Chvykov, *Liquid-cooled Ti: Sapphire thin disk amplifiers for high average power 100-TW systems*, Opt. Express **25**, 6664–6677 (2017).

[260] K. Ertel, S. Banerjee, P. Mason, P. Phillips, M. Siebold, C. Hernandez-Gomez, and J. Collier, *Optimising the efficiency of pulsed diode pumped Yb: YAG laser amplifiers for ns pulse generation.*, Opt. Express **19**, 26610–26626 (2011).

[261] P. Mason, M. Fitton, A. Lintern, S. Banerjee, K. Ertel, T. Davenne, J. Hill, S. Blake, P. Phillips, T. Butcher, *et al.*, *Scalable design for a high energy cryogenic gas cooled diode pumped laser amplifier*, Appl. Opt **54**, 4227–4238 (2015).

[262] T. Sekine, T. Kurita, Y. Hatano, Y. Muramatsu, M. Kurata, T. Morita, T. Watari, T. Iguchi, R. Yoshimura, Y. Tamaoki, *et al.*, *253 J at 0.2 Hz, LD pumped cryogenic helium gas cooled Yb: YAG ceramics laser*, Opt. Express **30**, 44385–44394 (2022).

[263] G. F. Albrecht, S. B. Sutton, H. F. Robey, and B. L. Freitas, *Flow, heat transfer, and wavefront distortion in a gas cooled disk amplifier*, in High Power and Solid State Lasers II, Vol. 1040 (SPIE, 1989) pp. 37–55.

[264] A. Bayramian, P. Armstrong, E. Ault, R. Beach, C. Bibeau, J. Caird, R. Campbell, B. Chai, J. Dawson, C. Ebbers, *et al.*, *The Mercury project: A high average power, gas-cooled laser for inertial fusion energy development*, Fusion Science and Technology **52**, 383–387 (2007).

[265] M. Jiang, H. Wu, Y. An, T. Hou, Q. Chang, L. Huang, J. Li, R. Su, and P. Zhou, *Fiber laser development enabled by machine learning: review and prospect*, PhotoniX **3**, 1–27 (2022).

[266] J.-H. Wolter, M. A. Ahmed, and T. Graf, *Thin-disk laser operation of Ti: sapphire*, Opt. Lett. **42**, 1624–1627 (2017).

[267] V. Chvykov, H. Chi, Y. Wang, K. Dehne, M. Berrill, and J. J. Rocca, *Demonstration of a side-pumped cross-seeded thin-slab pre-amplifier for high-power Ti:Sa laser systems*, Opt. Lett. **47**, 3463–3466 (2022).

[268] E. R. Dobrovinskaya, L. A. Lytvynov, and V. Pishchik, *Sapphire: material, manufacturing, applications* (Springer Science & Business Media, 2009).

[269] P. Popov, V. Solomennik, P. Belyaev, L. Lytvynov, and V. Puzikov, *Thermal conductivity of pure and* Cr^3 *and* Ti^3 *doped AlO crystals in 50-300 K temperature range*, Functional materials (2011).

[270] P. A. Schulz and S. R. Henion, *Liquid-nitrogen-cooled* $Ti{:}Al_2O_3$ *laser*, IEEE J. Sel. Top. Quantum Electron **27**, 1039–1047 (1991).

[271] C. Durfee, S. Backus, M. M. Murnane, and H. C. Kapteyn, *Design and implementation of a TW-class high-average power laser system*, IEEE J. Sel. Top. Quantum Electron. **4**, 395–406 (1998).

[272] D. C. Brown, *The promise of cryogenic solid-state lasers*, IEEE J. Sel. Top. Quantum Electron. **11**, 587–599 (2005).

[273] Y. Touloukian, R. Powell, C. Ho, and M. Nioolsou, *Thermophysical Properties of Matter. Vol. 10. New York-Washington: IFI* (1973).

[274] M. Büscher, R. Adam, C. Tusche, A. Hützen, C. Wiemann, Y.-J. Chen, and C. M. Schneider, *JuSPARC-The Jülich Short-Pulsed Particle and Radiation Center*, Journal of large-scale research facilities **6**, A138–A138 (2020).

[275] S. Backus, C. G. Durfee, G. Mourou, H. C. Kapteyn, and M. M. Murnane, *0.2-TW laser system at 1 kHz*, Opt. Lett. **22**, 1256–1258 (1997).

[276] S. Backus, J. Peatross, C. Huang, M. Murnane, and H. Kapteyn, *Ti: sapphire amplifier producing millijoule-level, 21-fs pulses at 1 kHz*, Opt. Lett. **20**, 2000–2002 (1995).

[277] S. Backus, R. Bartels, S. Thompson, R. Dollinger, H. C. Kapteyn, and M. M. Murnane, *High-efficiency, single-stage 7-kHz high-average-power ultrafast laser system*, Opt. Lett. **26**, 465–467 (2001).

[278] H. Burton, C. Debardelaben, W. Amir, and T. A. Planchon, *Temperature dependence of Ti:Sapphire fluorescence spectra for the design of cryogenic cooled Ti: Sapphire CPA laser*, Opt. Express **25**, 6954–6962 (2017).

[279] M. Fibrich, J. Šulc, M. Jelínek, H. Jelínková, and V. Kubeček, *Influence of temperature on Ti:sapphire spectroscopic and laser characteristics*, Laser Phys **28**, 085801 (2018).

[280] *Crystal Systems Datasheet on HEM Ti:Sapphire*, `https://crystalsystems.com/products/ti-sapphire/`, accessed: 2022-12-01.

[281] *Altechna whitepaper on Ti:Sapphire*, `https://www.altechna.com/white-papers/`, accessed: 2021-03-05.

[282] Oxalis-Laser: CommodPro, `https://www.oxalis-laser.com/commodpro.php`.

[283] K. Ertel, C. Hooker, S. J. Hawkes, B. T. Parry, and J. L. Collier, *ASE suppression in a high energy Titanium sapphire amplifier*, Opt. Express **16**, 8039–8049 (2008).

[284] U. Demirbas, J. Thesinga, H. Cankaya, M. Kellert, F. X. Kärtner, and M. Pergament, *High-power passively mode-locked cryogenic Yb:YLF laser*, Opt. Lett. **45**, 2050–2053 (2020).

[285] U. Demirbas, H. Cankaya, J. Thesinga, F. X. Kärtner, and M. Pergament, *Efficient, diode-pumped, high-power (>300W) cryogenic Yb:YLF laser with broad-tunability (995-1020.5 nm): investigation of E//a-axis for lasing*, Opt. Express **27**, 36562–36579 (2019).

[286] U. Demirbas, J. Thesinga, M. Kellert, F. X. Kärtner, and M. Pergament, *Comparison of different in situ optical temperature probing techniques for cryogenic Yb:YLF*, Opt. Mater. Express **10**, 3403–3413 (2020).

[287] U. Demirbas, H. Cankaya, Y. Hua, J. Thesinga, M. Pergament, and F. X. Kärtner, *20-mJ, sub-ps pulses at up to 70 W average power from a cryogenic Yb:YLF regenerative amplifier*, Opt. Express **28**, 2466–2479 (2020).

[288] H. Cankaya, U. Demirbas, Y. Hua, M. Hemmer, L. E. Zapata, M. Pergament, and F. X. Kaertner, *190-mJ cryogenically-cooled Yb:YLF amplifier system at 1019.7 nm*, OSA Continuum **2**, 3547–3553 (2019).

[289] U. Demirbas, M. Kellert, J. Thesinga, Y. Hua, S. Reuter, M. Pergament, and F. X. Kärtner, *Highly efficient cryogenic Yb:YLF regenerative amplifier with 250 W average power*, Opt. Lett. **46**, 3865–3868 (2021).

[290] L. E. Zapata, H. Lin, A.-L. Calendron, H. Cankaya, M. Hemmer, F. Reichert, W. R. Huang, E. Granados, K.-H. Hong, and F. X. Kärtner, *Cryogenic Yb:YAG composite-thin-disk for high energy and average power amplifiers*, Opt. Lett. **40**, 2610–2613 (2015).

[291] *CryoSpectra GmbH: Specifications of K100-series cryo-coolers*, `https://www.cryospectra.com/cryocooler-k100-series/`, accessed: 2022-12-04.

[292] A. C. DeFranzo and B. G. Pazol, *Index of refraction measurement on sapphire at low temperatures and visible wavelengths*, Appl. Opt. **32**, 2224–2234 (1993).

[293] S. Cho, J. Jeong, S. Hwang, and T. J. Yu, *Thermal lens effect model of Ti: sapphire for use in high-power laser amplifiers*, Appl. Phys. Express **11**, 092701 (2018).

[294] J.-P. Negel, A. Loescher, B. Dannecker, P. Oldorf, S. Reichel, R. Peters, M. Abdou Ahmed, and T. Graf, *Thin-disk multipass amplifier for fs pulses delivering 400 W of average and 2.0 GW of peak power for linear polarization as well as 235 W and 1.2 GW for radial polarization*, Appl. Phys. B **123**, 1–8 (2017).

[295] T. Dietz, M. Jenne, D. Bauer, M. Scharun, D. Sutter, and A. Killi, *Ultrafast thin-disk multi-pass amplifier system providing 1.9 kW of average output power and pulse energies in the 10 mJ range at 1 ps of pulse duration for glass-cleaving applications*, Opt. Express **28**, 11415–11423 (2020).

[296] J. Körner, J. Hein, and M. C. Kaluza, *Compact aberration-free relay-imaging multi-pass layouts for high-energy laser amplifiers*, Appl. Sci **6**, 353 (2016).

[297] K. Schuhmann, K. Kirch, M. Marszalek, F. Nez, R. Pohl, I. Schulthess, L. Sinkunaite, G. Wichmann, M. Zeyen, and A. Antognini, *Multipass amplifiers with self-compensation of the thermal lens*, Appl. Opt **57**, 10323–10333 (2018).

[298] *VAb Vakuum-Anlagenbau GmbH, Catalogue of vacuum components*, `http://www.vab-vakuum.com/uploads/pdf/VAb-Katalog_2015-16.pdf`, accessed: 2022-12-05.

[299] P. Mason, S. Banerjee, J. Smith, T. Butcher, J. Phillips, H. Höppner, D. Möller, K. Ertel, M. De Vido, I. Hollingham, *et al.*, *Development of a 100 J, 10 Hz laser for compression experiments at the High Energy Density instrument at the European XFEL*, High Power Laser Sci. Eng. **6** (2018).

[300] J. Schwarz, M. Geissel, P. Rambo, J. Porter, D. Headley, and M. Ramsey, *Development of a variable focal length concave mirror for on-shot thermal lens correction in rod amplifiers*, Opt. Express **14**, 10957–10969 (2006).

[301] S. Piehler, B. Weichelt, A. Voss, M. A. Ahmed, and T. Graf, *Power scaling of fundamental-mode thin-disk lasers using intracavity deformable mirrors*, Opt. Lett. **37**, 5033–5035 (2012).

[302] K. Schmidt, T. Dietrich, B. Dannecker, T. Graf, M. A. Ahmed, and O. Sawodny, *On compensating thermal lensing in high-power lasers using intra-cavity deformable mirrors*, IFAC-PapersOnLine **52**, 1–6 (2019).

[303] O. Loebich, *The optical properties of gold*, Gold Bull. **5**, 2–10 (1972).

[304] R. Clady, Y. Azamoum, L. Charmasson, A. Ferré, O. Utéza, and M. Sentis, *22 W average power multiterawatt femtosecond laser chain enabling 10*^{19} *W/cm*^{2} *at 100 Hz*, Appl. Phys. B **124**, 89 (2018).

[305] Z. Li, K. Tsubakimoto, H. Yoshida, Y. Nakata, and N. Miyanaga, *Degradation of femtosecond petawatt laser beams: Spatio-temporal/spectral coupling induced by wavefront errors of compression gratings*, Appl. Phys. Express **10**, 102702 (2017).

[306] Z. Li and N. Miyanaga, *Simulating ultra-intense femtosecond lasers in the 3-dimensional space-time domain*, Opt. Express **26**, 8453–8469 (2018).

[307] P. B. Johnson and R. W. Christy, *Optical Constants of the Noble Metals*, Phys. Rev. B **6**, 4370–4379 (1972).

[308] V. Leroux and T. Eichner, *Github: spatio-temporal-couplings*, `https://github.com/VincentLeroux/spatio-temporal-couplings`.

[309] Specialty Glass Products, Technical Details on Corning Pyrex 7740 Glass, Accessed January 2020, `https://www.sgpinc.com/materials/borosilicate/pyrex7740-glass/`.

[310] Heraeus GmbH, Technical knowledge base on Fused Silica, Accessed February 2022, `https://www.heraeus.com/en/hca/fused_silica_quartz_knowledge_base_1/properties_1/properties_hca.html#tabs-608478-5`.

[311] Schott GmbH, Technical details on Zerodur, Accessed February 2022, `https://www.schott.com/en-gb/products/zerodur-p1000269/technical-details?tab=94a500186e9c4dc88469136f9c65fa4a`.

[312] D. A. Alessi, P. A. Rosso, H. T. Nguyen, M. D. Aasen, J. A. Britten, and C. Haefner, *Active cooling of pulse compression diffraction gratings for high energy, high average power ultrafast lasers*, Opt. Express **24**, 30015–30023 (2016).

[313] H. Nguyen, J. Britten, E. Sistrunk, M. Aasen, P. Rosso, T. Spinka, and C. Haefner, *Pulse Compression Gratings for High Average Power Petawatt-Class Lasers*, Tech. Rep. (Lawrence Livermore National Lab.(LLNL), Livermore, CA (United States), 2018).

[314] E. P. Power, S. Bucht, K. R. P. Kafka, J. Bromage, and J. D. Zuegel, *Design and characterization of "flow-cell" integrated-flow active cooling for high-average-power ceramic optics*, Opt. Express **30**, 42525–42540 (2022).

[315] D. A. Alessi, H. T. Nguyen, J. A. Britten, P. A. Rosso, and C. Haefner, *Low-dispersion low-loss dielectric gratings for efficient ultrafast laser pulse compression at high average powers*, Opt Laser Technol. **117**, 239–243 (2019).

[316] *Technical note on differences between common grating technologies*, `https://www.plymouthgrating.com/guidance/technical-notes/applications/how-to-choose-the-right-diffraction-grating/`, accessed: 2023-05-25.

[317] T. Erdogan, *PGL, Tech. Note: Gratings for High-average-power Ti:Sapphire Laser Systems* (2018).

Acknowledgements

First and foremost, I would like to thank Andi Maier for giving me the opportunity to join the LUX group at the University of Hamburg, and for repeatedly motivating me to stick around and take part in the group's new challenges in KALDERA. His way of providing just the right amount of freedom to explore topics out of pure interest, and support and advice when needed, resulted in a highly productive and enjoyable working environment that makes it a pleasure to be part of the MLS/KALDERA/LUX team.

I would also like to thank Franz Kärtner, Jens Osterhoff, Nina Rohringer, and Jochen Liske for agreeing to be part of the dissertation committee.

Guido Palmer has always been a great support in all sorts of questions and provided excellent guidance on the technical part of the KALDERA project. Thank you Guido! It is an incredible opportunity to be a part of this project and I would like to thank him for his trust in allowing me to be involved in so many parts of this huge project.

The by far largest part of this thesis, the design and construction of MALCOLM, would not have been possible alone, and especially not without sharing this project with Thomas Hülsenbusch. Without sharing this project with him, his contributions at all stages of development, and his far greater practical experience, MALCOLM would not have turned out as nice as it did in the end. It is a pleasure to have such a colleague to discuss such a wide range of (often stupid) laser-related ideas with.

Getting MALCOLM to its final form would also not have been possible without the help of Julian Dirkwinkel, whose support in coordinating the technical efforts of MALCOLM-v2 was indispensable. He and many of the technical groups at DESY – MCS, ZM2, ZE, the MEA workshop, and many others in the background – have been a huge help.

Especially in the very early stages of the development of MALCOLM, the entire FS-LA group has been a huge help through many fruitful discussions at the weekly Laser R'n'D meetings and by lending us equipment to start our OPA experiments. In particular, Tino Lang has been a tremendous help in providing the chi2D and chi3D codes that helped getting a feel for OPCPA physics and getting started on the design of MALCOLM. His continued support with the simulations and also with various other questions on NLO-related topics certainly helped us get a good and quick start on OPCPA development.

Juan Gonzales did a terrific job in deciphering the intricacies of CommodPro so that the ”CommodPro fun” was much more productive than it would otherwise have been, and in his thermal lens measurements without which the design of the Colima would not have been possible. Thank you Juan!

Vincent Leroux should be thanked for all the work he put into the foundations of the grating deformation simulation on which I was able to build and get a nice finish to the thesis. Spencer Jolly should be thanked for helpful discussions on the Insight measurements of Malcolm. Spencer, Vincent, and Matthias Schnepp were also the key guys who introduced me to the laser field when I first joined the LUX team, intriguing me enough to stick with it for the last few years and hopefully many more.

Christopher Aleshire, Arno Klenke, Cesar Jauregui and Jens Limpert should be thanked for working together on the multi-core fiber project, hosting me in Jena for a few days and making our first MCF experiments a great experience.

Caterina Vidoli and Lutz Winkelmann should be thanked for taking on the challenge of building another, third, iteration of Malcolm – Masubi – and polishing out all the little problems we stumbled across in the setup of the first iteration of the laser. Similarly, Man Jiang (JJ) should be thanked for accepting the challenge of turning my simulations and initial plans of Colima into a real amplifier that will hopefully work after all the practical details that were not yet relevant in the simulations have been worked out. I'm really excited to see how Colima turns out!

In particular Heike Kaminski and Diana Barlag have been an excellent support in all sorts of organisational tasks, but especially their help in planning various conference trips has been indispensible.

Thomas, Guido, Juan, Lutz, Sören Jalas, Frida Brogren, and Chris Werle should also be thanked for the work they put into reading parts of this thesis at various stages of its completion and providing lots of valuable feedback.

The rest of the Lux/MLS team – especially the laser team: Thomas, Julian, Chris, Cora, Juan, Caterina, Leonie, JJ, Matthias, Guido and Lutz – should be thanked for a lot of fun times at work, after work, during ”Feierabendbier”, and on many other occasions.

Und natürlich gab es auch viele liebe Menschen außerhalb vom DESY, die einen unersetzlichen Ausgleich zum Alltag geschaffen haben und durch Ablenkung, Motivation, ein offenes Ohr und auf unzählige andere Weisen die Wochenenden, Abende und sonstige Freizeit versüßt haben. Ja lopuksi tietenkin myös valtavan iso kiitos Helsinkiin ja Tšekkiin. Kiitos kuuntelemisesta, kannatuksesta, ymmärryksestä, ja niin monesta muusta.

Thanks to all of you!